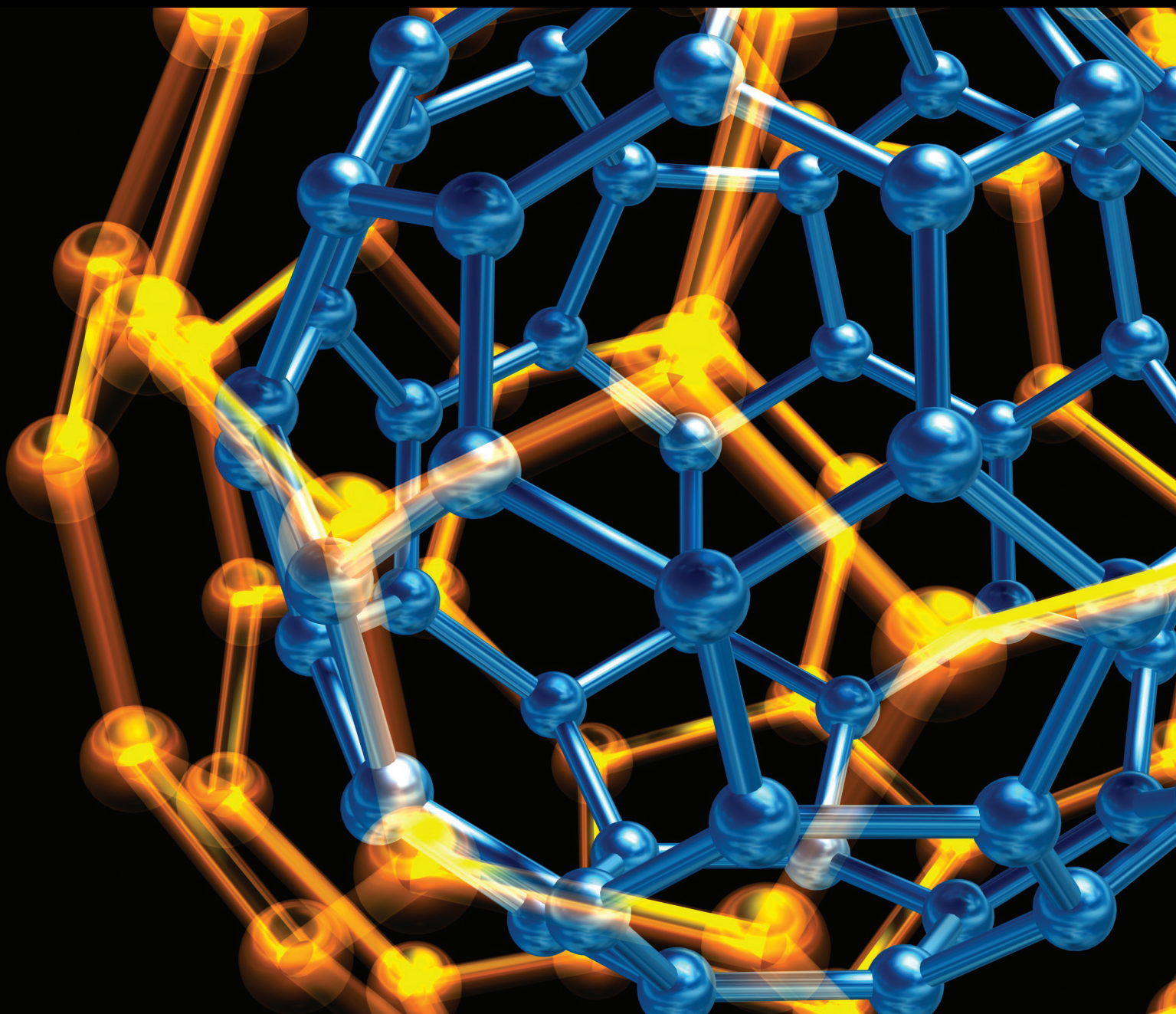


Journal of Nanotechnology

Nanoparticles for Environment, Engineering, and Nanomedicine

Lead Guest Editor: Rachid Seqqat

Guest Editors: Jamboor K. Vishwanatha, Lee Blaney, David Quesada,
Brajesh Kumar, and Luis Cumbal





Nanoparticles for Environment, Engineering, and Nanomedicine

Journal of Nanotechnology

Nanoparticles for Environment, Engineering, and Nanomedicine

Lead Guest Editor: Rachid Seqqat

Guest Editors: Jamboor K. Vishwanatha, Lee Blaney,
David Quesada, Brajesh Kumar, and Luis Cumbal



Copyright © 2019 Hindawi. All rights reserved.

This is a special issue published in "Journal of Nanotechnology." All articles are open access articles distributed under the Creative Commons Attribution License, which permits unrestricted use, distribution, and reproduction in any medium, provided the original work is properly cited.

Editorial Board

Simon Joseph Antony, UK
Raul Arenal, Spain
Thierry Baron, France
Carlos R. Cabrera, Puerto Rico
Enkeleda Dervishi, USA
Dmitriy A. Dikin, USA
Dimitris Drikakis, UK
Thomas Fischer, Germany
Noritada Kaji, Japan

Joanna Kargul, Poland
Valery Khabashesku, USA
María J. Lázaro, Spain
Eduard Llobet, Spain
Oleg Lupan, Moldova
Abdel Salam H. Makhlouf, USA
Paolo Milani, Italy
A. E. Miroshnichenko, Australia
Tomonori Ohba, Japan

Ramakrishna Podila, USA
Paresh Chandra Ray, USA
Marco Rossi, Italy
Jorge M. Seminario, USA
Xiaowei Sun, Singapore
Boris I. Yakobson, USA
Yoke K. Yap, USA
Chuan Jian Zhong, USA

Contents

Nanoparticles for Environment, Engineering, and Nanomedicine

Rachid Seqqat , Lee Blaney, David Quesada, Brajesh Kumar , and Luis Cumbal 
Editorial (2 pages), Article ID 2850723, Volume 2019 (2019)

Green Synthesis of Iron Nanoparticles: Application on the Removal of Petroleum Oil from Contaminated Water and Soils

Erika Murgueitio , Luis Cumbal , Mayra Abril, Andrés Izquierdo , Alexis Debut , and Oscar Tinoco
Research Article (8 pages), Article ID 4184769, Volume 2018 (2019)

Biological Effect of Organically Coated *Grias neuberthii* and *Persea americana* Silver Nanoparticles on HeLa and MCF-7 Cancer Cell Lines

Lizeth Salazar, María José Vallejo López, Marcelo Grijalva , Luis Castillo, and Alexander Maldonado
Research Article (11 pages), Article ID 9689131, Volume 2018 (2019)

Biological Impact of Exposure to Extremely Fine-Grained Volcanic Ash

Cristina Aguilera, Marco Viteri, Rachid Seqqat , Ligia Ayala Navarrette, Theofilos Toulkeridis, Ana Ruano, and Marbel Torres Arias 
Research Article (12 pages), Article ID 7543859, Volume 2018 (2019)

Assessing the Static and Dynamic Sensitivity of a Commercial Off-the-Shelf Multicore Processor for Noncritical Avionic Applications

Pablo F. Ramos , Vanessa C. Vargas , Nacer-Eddine Zergainoh, and Raoul Velazco
Research Article (8 pages), Article ID 2926392, Volume 2018 (2019)

Improvement of N-Acetylcysteine Loaded in PLGA Nanoparticles by Nanoprecipitation Method

Ruth Lancheros , Carlos A. Guerrero, and Rubén D. Godoy-Silva
Research Article (11 pages), Article ID 3620373, Volume 2018 (2019)

Arsenic Retention on Technosols Prepared with Nanoparticles and Ferric Soil from Mine Drainage Water

Darío R. Bolaños-Guerrón , Viviana P. Sánchez-Gómez, Johanna Paz, Andrés R. Izquierdo , Carina Stael, and María Balseiro-Romero
Research Article (8 pages), Article ID 6840856, Volume 2018 (2019)

Computational Modeling of the Interaction of Silver Nanoparticles with the Lipid Layer of the Skin

Andrea Fabara, Sebastián Cuesta , Fernanda Pilaquinga, and Lorena Meneses 
Research Article (9 pages), Article ID 4927017, Volume 2018 (2019)

Improvement of Cochineal Extract (*Dactylopius coccus* Costa) Properties Based on the Green Synthesis of Silver Nanoparticles for Application in Organic Devices

Carina Stael, Ricardo Cruz, Blanca Naranjo, Alexis Debut , and Yolanda Angulo 
Research Article (11 pages), Article ID 3751419, Volume 2018 (2019)

Larvicidal Activity of Silver Nanoparticles Synthesized Using Extracts of *Ambrosia arborescens* (Asteraceae) to Control *Aedes aegypti* L. (Diptera: Culicidae)

Bianca Morejón, Fernanda Pilaquina, Flavia Domenech, Danny Ganchala, Alexis Debut , and Marco Neira 

Research Article (8 pages), Article ID 6917938, Volume 2018 (2019)

Biosynthesis of Multicomponent Nanoparticles with Extract of Mortiño (*Vaccinium floribundum* Kunth) Berry: Application on Heavy Metals Removal from Water and Immobilization in Soils

Mayra Abril, Hugo Ruiz, and Luis H. Cumbal 

Research Article (10 pages), Article ID 9504807, Volume 2018 (2019)

Curcumin-Loaded Mixed Micelles: Preparation, Characterization, and *In Vitro* Antitumor Activity

Suping Ji, Xiao Lin, Enjiang Yu, Chengyang Dian, Xiong Yan, Liangyao Li, Meimei Zhang, Wenchang Zhao, and Linghui Dian 

Research Article (9 pages), Article ID 9103120, Volume 2018 (2019)

Editorial

Nanoparticles for Environment, Engineering, and Nanomedicine

Rachid Seqqat ^{1,2}, Lee Blaney,³ David Quesada,^{4,5} Brajesh Kumar ⁶, and Luis Cumbal ²

¹*Departamento de Ciencias de la Vida, Laboratorio de Inmunología y Virología, Universidad de las Fuerzas Armadas ESPE, Av. Gral. Rumiñahui s/n, P.O. Box 171-5-231B, Sangolquí, Ecuador*

²*Centro de Nanociencia y Nanotecnología, Universidad de las Fuerzas Armadas ESPE, Av. Gral. Rumiñahui s/n, P.O. Box 171-5-231B, Sangolquí, Ecuador*

³*University of Maryland, Baltimore County (UMBC) Department of Chemical, Biochemical and Environmental Engineering, 1000 Hilltop Circle, Engineering 314 Baltimore, Baltimore, MD 21250-0002, USA*

⁴*Mathematics Department, Miami Dade College, Wolfson Campus, Miami, FL 33132, USA*

⁵*School of Science, Technology and Health Science, St. Thomas University, Miami Gardens, FL 33054, USA*

⁶*Department of Chemistry, TATA College, Kolhan University, Chaibasa 833202, Jharkhand, India*

Correspondence should be addressed to Rachid Seqqat; rseqqat@espe.edu.ec

Received 24 December 2018; Accepted 5 January 2019; Published 30 January 2019

Copyright © 2019 Rachid Seqqat et al. This is an open access article distributed under the Creative Commons Attribution License, which permits unrestricted use, distribution, and reproduction in any medium, provided the original work is properly cited.

In recent years, the nanoscience and nanotechnology community has moved toward a more comprehensive integration of nanosciences and nanotechnologies with other emergent technologies and topics of interests such as biotechnology, biomedical engineering, environmental remediation, molecular communication networks, quantum computing, and data-driven design of new materials (materials informatics). Nanoinformatics along with materials science modeling has caught the attention of materials scientists because of several reasons: (1) it is aimed at creating comprehensive databases of physical and chemical properties of materials based on which quantitative structure-activity (QSAR) and structure-properties (QSPR) relationships might be advanced; (2) by incorporating optimization methods (Monte Carlo, genetic algorithms, neural networks) and data analytics techniques (data mining, network analysis, k-clustering, machine learning, and deep learning), it helps to optimize quantum mechanical calculations aimed at designing new molecules and materials, and (3) it is permitting to reduce the time of design and translation into applications as well as the cost of new materials. Nanoinformatics is proving itself as a very successful tool assisting bioinformatics, drug design, photovoltaic materials science design, superconducting materials, and topological insulators discoveries for quantum computing, catalytic converters for environmental remediation, and magnetic nanoparticles for biomedical applications and computer memories.

The nanomedicine has been generally defined as the medical application of nanotechnology. This application leads to a better repair, protection, and improvement of a great majority of human biological systems. The integration of nanotechnology in medicine, more commonly known as nanomedicine, allows new hope in the field of health. As an emerging discipline, nanomedicine is gradually being created by opening up new perspectives on key issues: optimizing drug delivery, specifically targeting tissues or cells, more optimal controlling the rate of release of the drug into the body, and providing early and accurate detection of diseases.

Nanomedicine uses nanodevices and nanostructures for tissue engineering and diagnosis and prevention of various diseases. The nanomedicine devices, which build “nanoparticles and nanotubes, for example,” depend on chemistry and chemical engineering. However, the application of nanomedicine devices for disease treatment is strongly dependent on molecular biology, biochemistry, and medically related disciplines. Therefore, the nanomedicine requires a collaborative effort from a high variety of other disciplines.

By interacting with biological molecules at the nanoscale level, nanotechnology has opened a large field of research and subsequent application. Synthetic nanoscale devices and biomolecules interactions have been able to be designed both in the extracellular environment and inside the cells of the human body. The physical properties have been able to be

explored better at the nanoscale level than those observed at the microscopic scale, such as the surface/volume ratio.

The medical applications of nanotechnologies are very promising, due to the possibility offered by miniaturization and ultraminiaturization in order to interact in a targeted way with biological entities such as tissues, cells, and even molecules. Nanotechnology is therefore a real hope in the development of new medical techniques for diagnosis, therapy, or patient follow-up. Currently, nanomedicine is involved in several areas: (1) the diagnosis that leads to the identification of a disease through the detection of specific symptoms of the pathology; (2) therapy and specific treatment of a disease; (3) regenerative medicine that aims to allow regeneration of damaged human tissue or organs; and (4) the sensor systems, which is a set of interfaces detecting, in the form of an electrical signal, a physical phenomenon in order to represent it and to acquire data on it.

On the other hand, due to their high surface area and enhanced reactivity, nanomaterials offer a profound potential for remediation of various contaminants in the environment. Importantly, the small size and corresponding ability for subsurface transport provide opportunities for in situ remediation of contaminated sites. Over the last two decades, research endeavors have focused on producing, characterizing, and applying various nanomaterials for treatment of a multitude of organic and inorganic contaminants in water and soils. Nevertheless, several areas require further investigation. For instance, the production of nanomaterials remains costly, employs hazardous chemicals, and requires downstream cleanup for size and composition control. In this regard, we need to develop, optimize, and validate innovative green synthesis techniques to sustainably scale-up production of novel nanomaterials. Recent research has shown opportunities for multispecies nanocomposites to outperform monometal nanomaterials. We need to continue efforts to explore and understand novel composites to improve sorption and photocatalysis of traditional and emerging contaminants in water/wastewater treatment and environmental remediation scenarios. Finally, as nanomaterials are incorporated into more consumer and industrial products, the impacts of synthesis techniques and nanomaterial properties on bacterial and animal cells must be evaluated to ensure the responsible manufacture and deployment of these exciting materials. The articles included in this special issue touch on these areas and more.

These days, green synthesis of nanoparticles using biodegradable materials, especially phytochemicals, has drawn a new and exciting area of research in the field of nanotechnology. Due to their vast range of applications, the synthesis of metal nanoparticles of different shapes and sizes is of great interest. The phytosynthetic approach provides various advantages, including cost-effectiveness, being simple, being green, being eco-friendly, and biocompatibility. However, little attention has been paid to the morphological effects of the organic-coated nanoparticles on engineering and medical fields. This special issue highlights the synthesis of various nanoparticles using mortiño berry, avocado leaves, cochineal, *Ambrosia arborescens*, curcumin,

N-acetylcysteine, and so on and their application in environmental remediation, nanomedicine, insecticide, and organic devices.

Conflicts of Interest

The editors declare that they have no conflicts of interest regarding the publication of this Special Issue.

Rachid Seqqat
Lee Blaney
David Quesada
Brajesh Kumar
Luis Cumbal

Research Article

Green Synthesis of Iron Nanoparticles: Application on the Removal of Petroleum Oil from Contaminated Water and Soils

Erika Murgueitio ^{1,2} Luis Cumbal ^{1,3} Mayra Abril,¹ Andrés Izquierdo ^{1,3}
Alexis Debut ^{1,3} and Oscar Tinoco²

¹Centro de Nanociencia y Nanotecnología, Universidad de las Fuerzas Armadas ESPE, Av. Gral. Rumiñahui s/n, P.O. Box 171-5-231B, Sangolquí, Ecuador

²Unidad de Posgrado, Facultad de Ingeniería Geológica, Minera, Metalúrgica y Geográfica, Doctorado en Ciencias Ambientales, Universidad Nacional Mayor de San Marcos, Lima, Peru

³Departamento de Ciencias de la Vida y de la Agricultura, Universidad de las Fuerzas Armadas ESPE, Av. Gral. Rumiñahui s/n, P.O. Box 171-5-231B, Sangolquí, Ecuador

Correspondence should be addressed to Erika Murgueitio; esmurgueitio@espe.edu.ec

Received 4 March 2018; Revised 20 June 2018; Accepted 14 July 2018; Published 2 September 2018

Academic Editor: Carlos R. Cabrera

Copyright © 2018 Erika Murgueitio et al. This is an open access article distributed under the Creative Commons Attribution License, which permits unrestricted use, distribution, and reproduction in any medium, provided the original work is properly cited.

Iron nanoparticles were produced using the extract of mortiño berry (*Vaccinium floribundum*) (vZVI) as reducing and stabilizer agent. Fresh nanoparticles were characterized using TEM, XRD, and FTIR techniques, while laboratory experiments were conducted to assess the removal of total petroleum hydrocarbons (TPHs) from water and soil after treatment with synthesized nanoscale iron particles. Nanoparticles as produced were spherical in the range of 5–10 nm. After treatment with vZVI nanoparticles, water contaminated with two concentrations of TPHs (9.32 mg/L and 94.20 mg/L) showed removals of 85.94% and 88.34%, respectively, whereas a contaminated soil with a TPHs concentration of 5000 mg/kg treated during 32 h with nanoparticles reached a removal of 81.90%. Results indicate that the addition of vZVI nanoparticles produced strong reducing conditions, which accelerate removal of TPHs and suggest that these nanoparticles might be a promising technology to clean up TPHs contaminated water and soils.

1. Introduction

Total petroleum hydrocarbons (TPHs) encompass a broad family of several hundreds of chemical compounds that originally come from crude oil [1]. These nature-based hydrocarbons embody a group of persistent organic contaminants [2], which pollute different environmental compartments such as air, water, soils, and sediments, and cause a probable toxic impact on different biological receptors [3]. The strategies employed to remediate soils contaminated with hydrocarbons can be physical, chemical, and biological processes [4, 5]. However, these techniques have shown drawbacks due to high cost, long-term treatment, difficulty in reducing the concentration of pollutants to the regulated levels, and ability to reach the contaminant

in the subsurface [6, 7]. Recently, a new experimental setup has been proposed using iron nanoparticles [8]. Remediation of soils with engineered nanomaterials (ENMs) promises more effective and cheaper approaches than conventional methods because of the increased reactivity of nanoparticles and the possibility of *in situ* treatment [9]. Microscale granular metallic iron (mZVI) has been widely used as a reducing agent for the remediation of a variety of contaminants in permeable reactive barriers. However, the cost of this method is deemed high and the process extent could be approximately 15 years [10]. Also, zerovalent iron nanoparticles have been successfully used in the past to remediate groundwater. Due to its small size and large surface area per unit mass, properties of the nanoparticles can be useful in hazardous waste site remediation and

contaminant reduction [11, 12]. Nevertheless, almost all tiny particles are prepared with toxic chemicals or require high capital costs and also generate hazardous toxic wastes. To overcome these shortcomings, this study examines an environmental friendly way to synthesize zerovalent iron nanoparticles using an endemic fruit from Ecuador, mortiño berry (*Vaccinium floribundum*). This fruit contains large amounts of polyphenols that are biodegradable and soluble in water at room temperature and have molecules carrying alcoholic functional groups that can be used for the reduction as well as for the stabilization of the nanoparticles [13]. In this work, peel and pulp of the fruits were used to obtain high concentration of polyphenols and high antioxidant capacity. The iron nanoparticles were synthesized by a simple procedure using the extract of mortiño berry to produce zerovalent nanoparticles iron from solutions of ferric ions. As-fabricated nanoparticles were then applied for the degradation of TPHs from contaminated water and soils.

2. Materials and Methods

2.1. Materials. In this study, a soil from the Ecuadorian Amazon region, La Joya de los Sachas County, Francisco de Orellana province, was collected to investigate TPHs remediation using vZI. For soil sampling, the protocol suggested in [14] was used. Concisely, a 500 m² of soil surface was divided into 5 × 5 m² squares. At the center point of each square, using an auger for soil drilling, 0.5 kg of soil was taken at a depth of 30 cm. Plant materials and stones were removed before mixing all soil samples. Then 4 kg of the mixed soil were taken for the study, stored in labeled ziploc plastic bags, and transported to the laboratory in a freezer at 4°C. Absolute ethanol and iron chloride (FeCl₃·6H₂O, 99.8%) were purchased from Scharlau and Fisher Scientific, respectively. A sample of petroleum hydrocarbons (22° API (American Petroleum Institute)) was obtained from the Joya de los Sachas Petroleum Storage Station, Ecuador. Double deionized water was produced using a Thermo Scientific Smart 2 pure deionized system.

2.2. Fabrication of Nanoparticles

2.2.1. Extraction of Liquid Mortiño. Fruit extract of *V. floribundum* (peel and pulp) was prepared by maceration with ethanol and magnetic stirring for 48 h in darkness. To minimize the passage of particles, the fruit extract was filtered three times through a filter paper of 1 mm diameter and a filter millipore millex-GV hydrophilic PVDF of 0.22 μm. Lastly, the extract was concentrated on a rotary evaporator (Buchi-850) removing the solvent.

2.2.2. Polyphenol and Antioxidant Capacity Tests. The polyphenol concentration of the extract was found with the Folin-Ciocalteu method. Briefly, the extract was sonicated on a CV33-Daigger ultrasonic processor and concentrated on a rotary evaporator. Thereafter, the polyphenol concentration was estimated. The antioxidant capacity was obtained, following the protocol developed by Brand-Williams et al. [15].

This method is based on the absorbance reduction of the antioxidant, measured at 515 nm for the DPPH radical. The concentration of DPPH in the reaction medium was calculated from a calibration curve obtained by linear regression. The results were expressed as activity equivalent to trolox (AET) (μM/g of fresh weight sample).

2.2.3. Synthesis of Zerovalent Nanoparticles Using *V. floribundum* (vZVI). Solutions of 0.5, 0.1, and 0.001 M of FeCl₃ were prepared as precursors of zerovalent iron. The extract of *V. floribundum* with a fixed pH between 9 and 10 was added to solutions of FeCl₃ at the volume ratio of 2:1 under sonication. The development of a black precipitate in the flask was an indication of the zerovalent nanoparticle formation, in all cases. Moreover, powder zerovalent nanoparticles were prepared by water evaporation, placing the liquid solution on a hot plate (D Lab M57-H550-5). Additional drying of the wet solution was performed with a line of nitrogen gas in a fume hood for two hours. Finally, the solid sample was washed several times with deionized water to remove sodium chloride crystals.

2.3. Characterization of Iron Nanoparticles. Mineral composition of the nanoparticles was analyzed with a X-ray diffractometer (EMPYREAN, PANalytical) with 2θ configuration (generator-detector) wherein a copper disc emits X-rays at a wavelength of λ = 1.54 Å. For size distribution of nanoparticles, a submicron particle analyzer (HORIBA LB-550) was employed. Transmission electron microscope (TEM) images were digitally recorded for morphological studies (Tecnaï G2 Spirit TWIN, FEI, Netherlands). The functional groups of the extract and the nanoparticles covered with the extract were recorded on a Spectra Two IR spectrometer (PerkinElmer, USA) and by UV-Vis (Analytik Jena).

2.4. Batch Experiments to Remove TPHs from Contaminated Water and Soil Using vZVI Nanoparticles. Laboratory experiments were performed following published protocols [16–18]. For the removal of TPHs dissolved in water, 1 g of vZVI was placed in amber-colored Boeco bottles filled with 100 mL of water containing 10 and 100 mg/L of TPHs in triplicate. Samples were stirred for 10 min in a Branson 3510 sonicator at amplitude of 70%. The supernatant was centrifuged, filtered, and sent for TPHs analysis in an accredited laboratory. TPHs removal from soils was performed following the procedure developed by Chang et al. [17] with some modifications. First, a series of 10 g soil samples were placed into 250 mL amber borosilicate glass bottles sealed with Teflon-lined screw caps. Petroleum was dissolved completely in hexane, and the solution was immediately poured into the bottles and then mixed for 2 h. Vial caps were left open in a fume hood for 8 h at ambient temperature to allow hexane evaporation thus resulting in homogeneous distribution of petroleum in the soil samples with 5000 mg TPHs/kg soil. Immediately, a solution of vZVI was added into the bottles containing the petroleum-spiked

soil at a ratio of 1 : 9 (w/v). Subsequently, the samples were sonicated for 20 min and shaken for 64 h, and the aqueous supernatant was decanted. The extraction of the petroleum residual was performed mixing the treated soil with dichloromethane (125 mL) and sonicated (Cole-Parmer, Model 08855-10). The extract was then filtered and analyzed for TPHs.

2.5. Analytical Methods. Total petroleum hydrocarbons were analyzed using a gas chromatograph (PerkinElmer Clarus, Model 400) equipped with a flame detection system (FID), capillary columns, and electronic pressure control split/splitless. Sample injection was carried out manually, and the running time for samples was fixed in 27 min. Equipment preparation and measurements were performed with Software Navigator TotalChrom Ver 6.3.1. For analytical validation, some samples were sent to an accredited laboratory for TPHs analysis.

3. Results and Discussion

3.1. Polyphenol Content and Antioxidant Capacity. Polyphenols in mortiño berry extract was found to be 2127 ± 805 mg GAE/100 g sample. The content of polyphenols is similar to those found by Murgueitio et al. [19]. The antioxidant capacity of the fruit extract was measured as $50 \mu\text{mol}$ trolox/g of sample (fresh weight), and this value is similar to those found by other authors [20–22].

3.2. Visual and UV-Vis Study. Figure 1 shows the absorption spectrum of the mortiño extract and the nanoparticles formation versus time. For the extract alone, it is observed a broaden peak between 570–585 and 610 nm due to the presence of anthocyanins (galloyl esters, hydroxybenzoic acid derivatives, flavan-3-ols, proanthocyanidins, flavonols, hydroxycinnamic acid derivatives, and anthocyanins) [23]. The biosynthesis of vZVI was monitored periodically at 2, 4, 6, and 8 h. It is observed that, in comparison with the brown-yellow FeCl_3 , the color of the colloidal solution changed to blackish after the addition of the fruit extract. This is a direct proof for the reduction of Fe^{3+} to Fe^0 and the formation of vZVI. The UV-Vis spectra indicate the disappearance of the extract peak when this interacts with the inorganic reagents during the growth of the nanoparticles as the time increases. This is because the structure of the polyphenols of the mortiño extract underwent changes throughout the synthesis of nanoparticles, forming aggregates of vZVINPs in the range of 5–35 nm. This trend is also associated with the high pH used in the preparation process of the nanoparticles [24, 25].

3.3. Characterization of Nanoparticles. Figure 2 shows TEM images of nanoparticles prepared with mortiño. As seen in the figure, particle sizes are in between 5 and 35 nm in diameter. Using statistical and algorithmic calculations developed by Arroyo et al. [26], nanoparticle diameters were also estimated. The highest percentage of formed vZVI

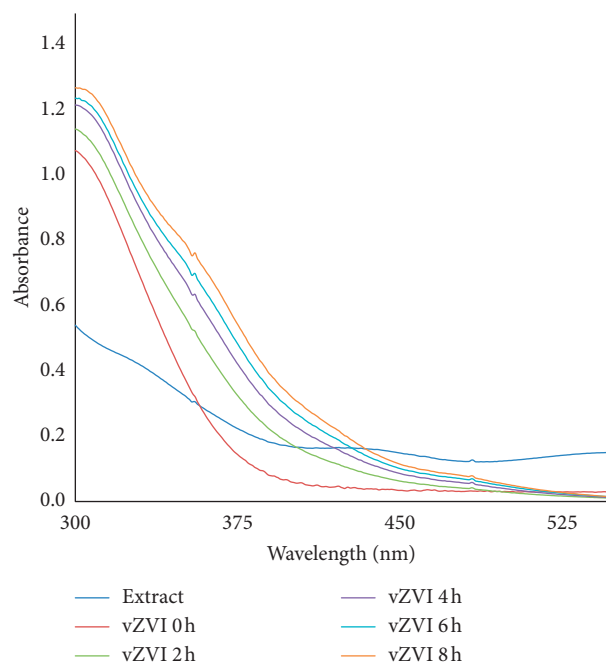


FIGURE 1: UV spectra of extract (*V. floribundum*) and vZVI.

nanoparticles in relation to 0.001 M FeCl_3 is 61% for 5–10 nm in diameter while the lowest percentage is 3% for 30–35 nm (Table 1). On the contrary, with 0.1 M FeCl_3 , the highest percentage is 45% for 15–20 nm and the lowest is 2% for 30–35 nm. Thus, calculated sizes of nanoparticles are in the range of 5 to 35 nm as well.

The mineral structure of the nanomaterials was characterized using XRD. Figure 3 shows the XRD pattern of synthesized vZVI nanoparticles. The major Bragg reflection at 2θ values are 45.2537° , 65.9598° , and 83.6821° which correspond to the planes (110), (200), and (211) of αFe crystalline (code 98-042-6989 Fe1) with a body-centered cube crystal structure (bcc). The mineral composition of the fabricated nanoparticles is similar to those reported before by Murgueitio et al. [19]. Besides, XRD results revealed the as-produced nanoparticles contain 24% of metallic iron.

Finally, FTIR measurements were carried out to understand the contribution of the mortiño berry extract molecules in the formation of nanoparticles. As seen in Figure 4(a) and Table 2, peaks in the range of $3650\text{--}3200\text{ cm}^{-1}$ are related to the vibrations of the --OH groups of the phenolic moiety of mortiño berry extract, positions from 1620 to 1690 cm^{-1} are attributed to the aldehydes (C=O) of an ester sugar [27]. These peaks in conjunction with the 1089 cm^{-1} peak (CO stretching) represent the amount of carbon that belongs to the extract [28]. Conversely, for the nanoparticles, peaks of C=C alkene conjugate cis and benzene ring 1634.98 cm^{-1} can be seen [23]. In addition, bands belonging to the goethite phase ($\alpha\text{-FeO}$ (OH)) with its vibration of the Fe-O bond in stretching mode are seen at 630 cm^{-1} [29]. Thus, these groups may have participated in the nanoparticles synthesis. Hence, FTIR analysis confirms the presence of phenolic compounds and anthocyanins in mortiño berry extract, and

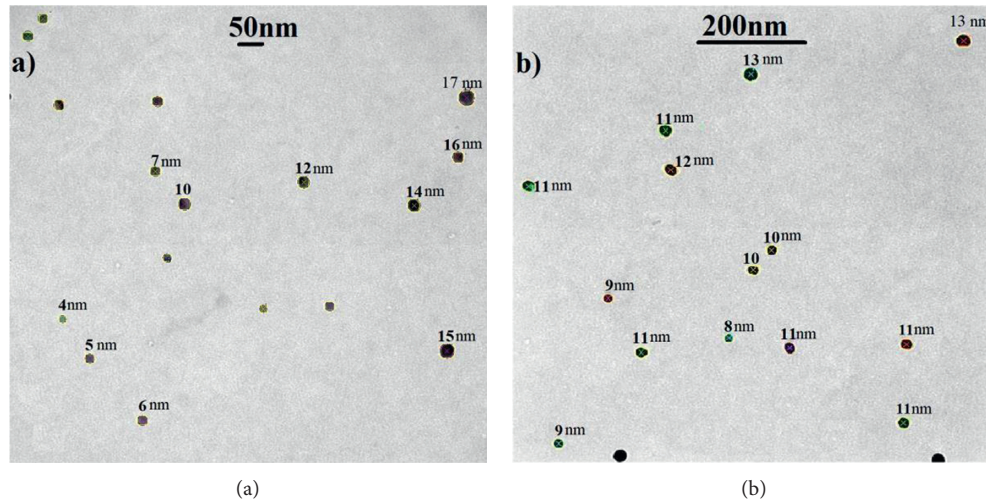


FIGURE 2: TEM images of vZVI.

TABLE 1: Percentage of vZVI produced in relation to the FeCl_3 concentration.

Diameter range	0.001 M FeCl_3 (%)	0.1 M FeCl_3 (%)
5–10	61	3
10–15	12	21
15–20	9	45
20–25	12	19
25–30	4	10
30–35	3	2

further it acts as reducing/capping agents for the functionalization of vZVI.

3.4. Treatment of Water Contaminated with TPHs Using vZVI Nanoparticles. The chromatograms in Figures 5(a)–5(d) show the distribution of TPHs peaks in water before and after treatment with vZVI, respectively. Calculated percentages of TPHs removal are 85.94% ($C_{\text{TPHs},i} = 9.32$ mg/L and $C_{\text{TPHs},f} = 1.31$ mg/L) and 88.34% ($C_{\text{TPHs},i} = 94.20$ mg/L and $C_{\text{TPHs},f} = 26.80$ mg/L). It is observed in Figure 5(b) that peaks in the range of 7.5 min to 8 min and beyond 8.2 min disappear, compared to Figure 5(a). Besides, the long peak at 8.2 min remains after treatment because this corresponds to ortho-terphenyl, the compound that is used as a surrogate for quality control. The same tendency is observed in Figures 5(c) and 5(d) (for high TPHs concentration); however, peaks in Figure 5(d) (after treatment) are shorter compared to peaks in Figure 5(c) (before treatment). It is further observed in Figures 5(a) and 5(b) that compounds with C7–C10 carbons may volatilize because peaks are absent. The performance of nanomaterials in the removal of TPHs can be attributed to their increased surface area, and higher reactivity, and the possibility of in situ treatment.

3.5. Treatment of Soils Contaminated with TPHs Using vZVI Nanoparticles. Results show that vZVI with 24% of zerovalent iron removed 81.90% of petroleum hydrocarbons from soil after 32 h of treatment ($C_{\text{TPHs},i} = 5000$ mg/kg and

$C_{\text{TPHs},f} = 931.8$ mg/kg). Removal of TPHs from soils can be attributed to the high reactivity and sorption of the nanoparticles [9], as shown in Figure 6, zone a. The reducing power of the iron nanoparticles is provided by its core, which is mainly composed of zerovalent iron. The coverage of the nanoscale particles contains iron oxides and hydroxides that supply reactive sites for the immobilization of large petroleum hydrocarbons and the formation of chemical complexes (Figure 6, zone b). Measurements of TPHs in soil after 40, 56, and 64 h of treatment were also performed (inset Figure 6). It shows no more TPHs removal, indicating that the treatment reached steady state. A previous study has shown that 70% reduction of pyrene contained in soil samples was achieved in 60 min by contacting the soil with nanoscale ZVI powders in aqueous solution under ambient conditions with no pH control (Chang et al. [16]). Our treatment takes more time because TPHs are a cocktail of hundred derivatives with different molecular weight, size, viscosity, solubility, hydrophobicity, and so on, which may influence in the removal.

The removal mechanism of TPHs from water and soils using the vZVI could be a Fenton reaction. In the preparation of nanoparticles, it was used ultrasonication, as a result of this process, water of the iron solution could be splitted and produce hydrogen peroxide, although in small quantities [30, 31] (Equation (1)):



Fenton oxidation process starts when oxygenated water is activated with ferrous ions (Fe^{2+}) coming from the oxidation of Fe^0 nanoparticles. Fe^{2+} is in turn is oxidized to Fe^{3+} , producing hydroxyl ions and radicals. Then, Fe^{3+} is reduced to Fe^{2+} with hydrogen peroxide producing hydronium ions and peroxydril radicals, OH_2^* (Equations (2) and (3)). The radicals oxidize organics by abstraction of protons and producing organic radicals (R^*) as shown in (4), which are highly reactive and can be further oxidized (Equations (5)–(7)) [32].

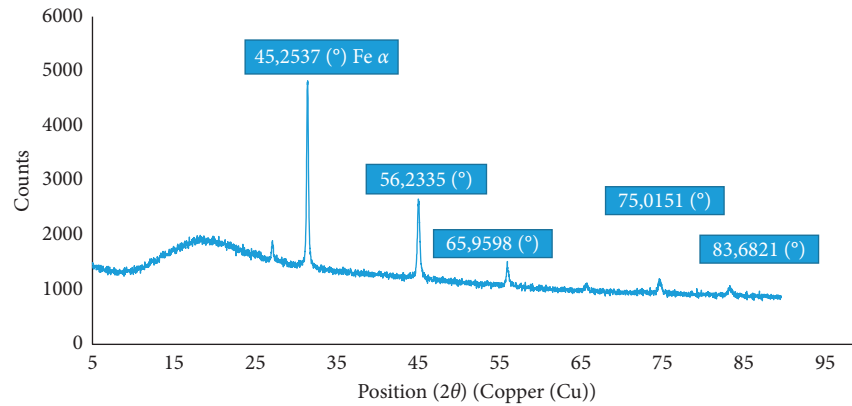


FIGURE 3: XRD pattern of iron nanoparticles prepared with mortiño berry (vZVI).

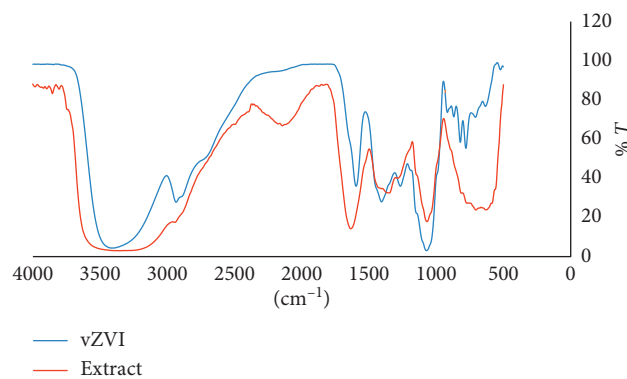
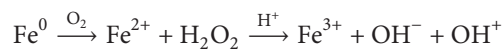
FIGURE 4: FTIR spectra of vZVI nanoparticles and *V. floribundum* extract.

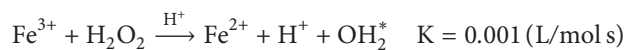
TABLE 2: FTIR peaks for extract and nanoparticles.

Extract		Nanoparticles	
Peak name	cm ⁻¹	Peak name	cm ⁻¹
1	3409.72	a	3354.02
	Vibrations of the -OH groups of phenolic moiety		Vibrations (inter o intramolecular) of -OH groups of the phenolic
3	1594.46	b	1634.98
	C=C ring stretching in polyphenols		C=C alkene conjugate cis and benzene ring
4	1405.43	c	1068.42
	In-plane bending vibration of -OH in phenol		v sim. C-O ether forming ring or aryl ether
5	1070.42	d	630.23
	v sim. C-O ether forming ring or aryl ether		Fe-O bond in stretching mode (tension)



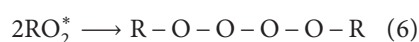
$$K = 76 (\text{L/mol s})$$

(2)



(3)

The route of the petroleum hydrocarbon transformation can be as follows (Equations (4)–(8)) [33]:



where RH is the petroleum hydrocarbon compound with H⁺ as the extractable proton and TPH* and TPH are fraction of hydrocarbon radical and fraction of stable hydrocarbon, respectively.

4. Conclusions

According to TEM images, around 90% of nanoparticles prepared with *V. floribundum* show 5 to 25 nm in diameter regardless of the iron precursor concentration. The mineral content of the vZVI nanoparticles is 24% of alpha iron with a body-centered cubic crystal structure, and the remaining

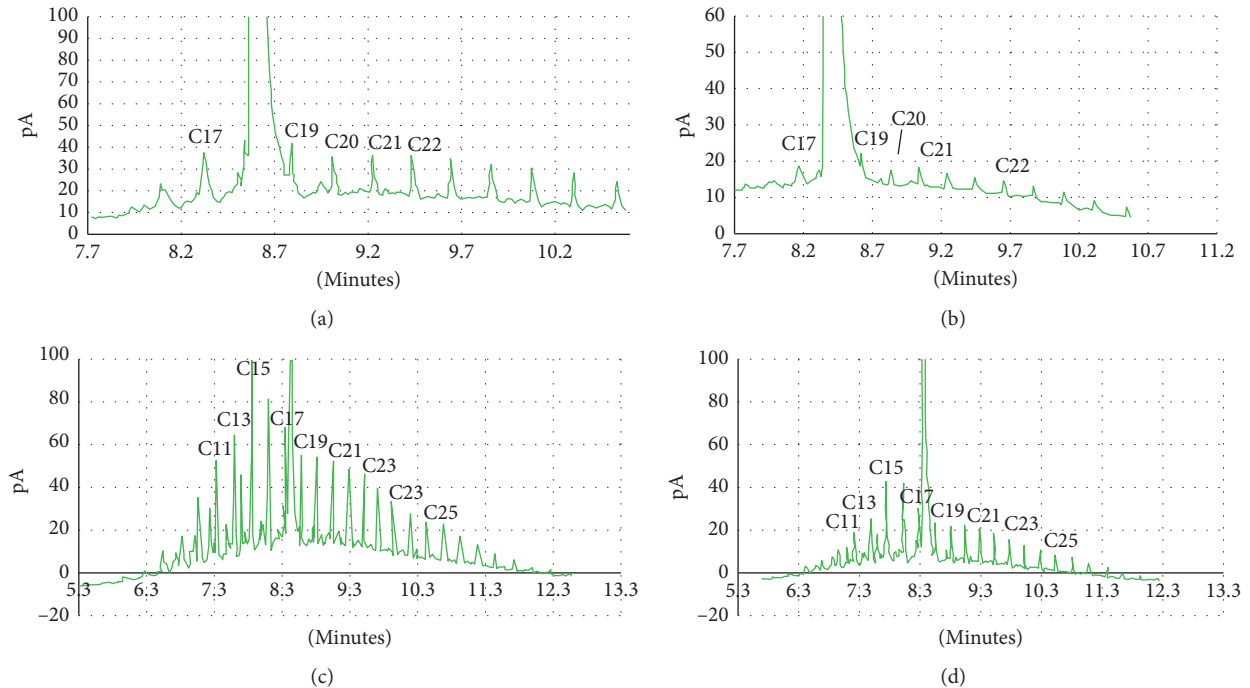


FIGURE 5: Chromatograms of TPHs derivatives in water before and after treatment with vZVI: (a) initial concentration = 9.32 ppm, (b) final concentration = 1.31 ppm, (c) initial concentration = 94.20 ppm, and (d) final concentration = 26.80 ppm.

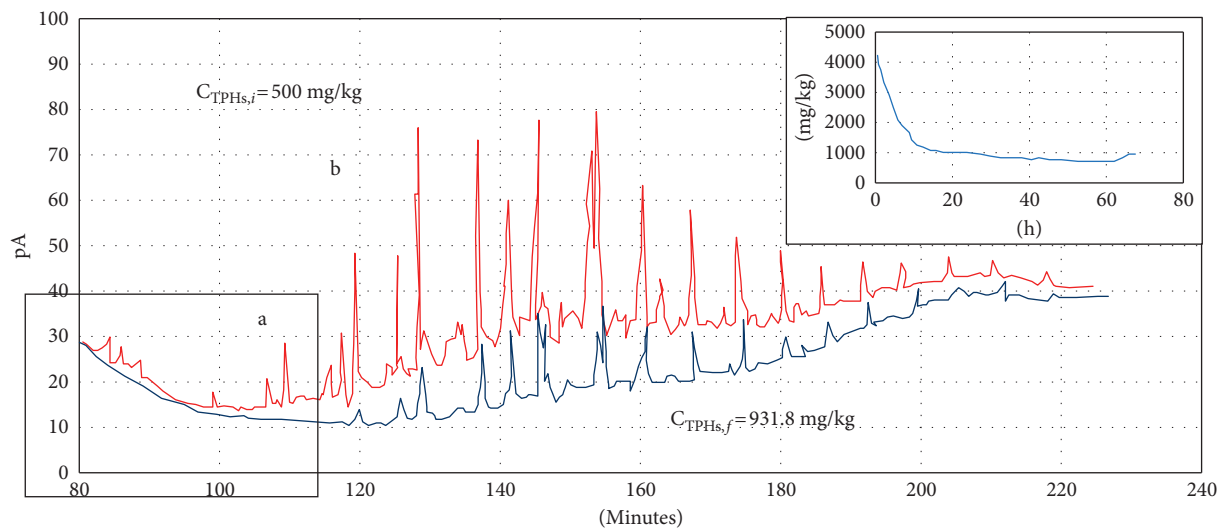


FIGURE 6: Chromatogram of TPHs derivatives: before and after treatment with vZVI.

fraction is composed of iron oxides. FTIR studies indicate $-\text{OH}$ and $\text{C}=\text{C}$ groups of the mortiño berry extract could have participated in the formation and stabilization of the iron nanoparticles. In general, the removal of TPHs with the Fe nanoparticles was successful as demonstrated by the chromatographic peaks of TPHs derivatives. Nevertheless, the treatment is strongly influenced by the content of iron in the nanoscale particles. Removals of 88.24% and 81.90% of petroleum hydrocarbons from water and soil samples were achieved after 12 min and 32 h of treatment with the vZVI particles, respectively. The good performance of vZVI

particles can be associated with their increased surface area, higher reactivity, the possibility of *in situ* treatment. Thus, this technique may be efficacious to be used in the remediation water and soil contaminated with petroleum hydrocarbons in less time compared to a conventional bioremediation process.

Data Availability

The data used to support the findings of this study are available from the corresponding author upon request.

Conflicts of Interest

The authors declare that they have no conflicts of interest.

Acknowledgments

The authors acknowledge the assistance of Andrea Vaca with the TEM images, data processing, and XRD analysis. They thank Dr. Miguel Angel Bustamante Domínguez for his help in interpreting XRD spectra and the Universidad de las Fuerzas Armadas-ESPE for funding Project 2015PIC-004. Also, they show gratitude to all other contributors for providing us with the early data presented in the III International Congress of Nanoscience and Nanotechnology (ICNN'2017) held in Quito, Ecuador.

References

- [1] G. Todd, R. Chessin, and J. Colman, *Toxicological Profile for Total Petroleum Hydrocarbons (TPH)*, U.S. Department of Health and Human Services, Washington, DC, USA, 1999.
- [2] X. Huang, Y. El-Alawi, J. Gurska, B. Glick, and B. Greenberg, "A multi-process phytoremediation system for decontamination of persistent total petroleum hydrocarbons (TPHs) from soils," *Microchemical Journal*, vol. 81, no. 1, pp. 139–147, 2005.
- [3] K. Masakorala, J. Yao, H. Guo et al., "Phytotoxicity of long-term total petroleum hydrocarbon-contaminated soil—a comparative and combined approach," *Water, Air, and Soil Pollution*, vol. 224, no. 5, p. 1553, 2013.
- [4] S. Gan, E. Lau, and H. Ng, "Remediation of soils contaminated with polycyclic aromatic hydrocarbons (PHAs)," *Journal of Hazardous Materials*, vol. 172, no. 2-3, pp. 532–549, 2009.
- [5] M. Chang, C. Huang, and H. Shu, "Effects of surfactants on extraction of phenanthrene in spiked sand," *Chemosphere*, vol. 41, no. 8, pp. 1295–1300, 2000.
- [6] M. Litter, A. Sancha, and A. Ingallinella, "Tecnologías económicas para el abatimiento de arsénico en aguas," in *Proceedings of Programa Iberoamericano de Ciencia y Tecnología para el Desarrollo*, Buenos Aires, Argentina, 2010.
- [7] B. Schrick, W. Hydutsky, J. Blough, and T. Mallouk, "Delivery vehicles for zerovalent metal nanoparticles in soil and groundwater," *Chemistry of Materials*, vol. 16, no. 11, pp. 2187–2193, 2004.
- [8] H. Gomes, L. Ottosen, A. Ribeiro, and C. Dias-Ferreira, "Treatment of a suspension of PCB contaminated soil using iron nanoparticles and electric current," *Journal Environmental Management*, vol. 151, pp. 550–555, 2015.
- [9] N. Mueller and B. Nowack, "Nanoparticles for remediation: solving big problems with little particles," *Elements*, vol. 6, no. 6, pp. 395–400, 2010.
- [10] D. O'Carroll, B. Sleep, M. Krol, H. Boparai, and C. Kocur, "Nanoscale zero valent iron and bimetallic particles for contaminated site of remediation," *Advances in Water Resources*, vol. 51, pp. 104–122, 2013.
- [11] S. Cook, *Assessing the Use and Application of Zero Valent Iron Nanoparticle Technology for Remediation at Contaminated Sites*, Jackson State University, Jackson, MS, USA, 2009.
- [12] C. Barreto, *Visión General de la Nanotecnología y Sus Posibilidades en la Industria de Alimentos*, ReCiTeIA, Cali, Colombia, 2011.
- [13] M. N. Nadagouda, A. B. Castle, R. C. Murdck, S. M. Hussain, and R. S. Varma, "In vitro biocompatibility of nanoscale zerovalent iron particles (NZVI) synthesized using tea polyphenols," *Green Chemistry*, vol. 12, pp. 114–122, 2010.
- [14] TULSMA, *Anexo 2 del libro VI del Texto Unificado de Legislación Secundaria del Ministerio del Ambiente: Norma de Calidad Ambiental del Recurso suelo y Criterios de Remediación para suelos contaminados*, TULSMA, Ecuador, 2015.
- [15] W. Brand-Williams, M. Cuvelier, and C. Berset, "Use of a free radical method to evaluate antioxidant activity," *LWT-Food Science and Technology*, vol. 28, no. 1, pp. 25–30, 1995.
- [16] M.-C. Chang, H.-Y. Shu, W.-P. Hsieh, and M.-C. Wang, "Using nanoscale zero-valent iron for the remediation of polycyclic aromatic hydrocarbons contaminated soil," *Journal of the Air and Waste Management Association*, vol. 55, no. 8, pp. 1200–1207, 2005.
- [17] M. Chang, H. Shu, W. Hsieh, and M. Wang, "Remediation of soil contaminated with pyrene using ground nanoscale zero-valent iron," *Journal of the Air and Waste Management Association*, vol. 57, no. 2, pp. 221–227, 2007.
- [18] M. C. Chang and H. Y. Kang, "Remediation of pyrene contaminated soil by synthesized nanoscale zero valent iron particles," *Journal of Environmental Science and Health Part A*, vol. 44, no. 6, pp. 576–582, 2009.
- [19] E. Murgueitio, L. Cumbal, A. Debut, and J. Landívar, "Synthesis of iron nanoparticles through extracts of natives fruits of Ecuador as capulí (*Prunus serotina*) and mortiño (*Vaccinium floribundum*)," *Biology and Medicine*, vol. 8, no. 3, p. 1, 2016.
- [20] C. Vasco, J. Ruales, and A. Kaml-Eldin, "Total phenolic compounds and antioxidant capacities of major fruits from Ecuador," *Food Chemistry*, vol. 111, no. 4, pp. 816–823, 2008.
- [21] S. Roldan, *Caracterización Molecular, Funcional y Estudio del Comportamiento Post Cosecha del Mortiño (Vaccinium floribundum Kunth) de la Comunidad de Quinticusig del Cantón Sigchos de la Provincia de Cotopaxi*, Escuela Politécnica Nacional, Quito, Ecuador, 2012.
- [22] S. Zapata, A. M. Piedrahita, and B. Rojano, "Capacidad atrapadora de radicales oxígeno(ORAC) y fenoles totales de frutas y hortalizas de Colombia," *Perspectivas en Nutrición Humana*, vol. 16, no. 1, pp. 25–36, 2014.
- [23] V. Roshchina, *Model Systems to Study the Excretory Function of Higher Plants*, Springer, Berlin, Germany, 2014.
- [24] G. Ortega, A. Bermello, M. Guerra, G. Castillo, S. Armenteros, and G. Miere, "Estudios de separación y caracterización de pigmento en caldo de fermentación Botryodiplodia theobromae," *ICIDCA. Sobre los Derivados de la Caña de Azúcar*, vol. 41, no. 3, pp. 27–34, 2007.
- [25] A. Castañeda-Sanchez and J. Guerrero-Beltrán, *En los Espectros FTIR de Ambas Fracciones*, Tema Selectos de Ingeniería en Alimentos, Puebla, PUE, Mexico, 2015.
- [26] C. Arroyo, A. Debut, C. Stael, K. Guzman, and B. Kumar, "Reliable tools for quantifying the morphological properties at the nanoscale," *Biology and Medicine*, vol. 8, no. 3, p. 281, 2016.
- [27] S. Steven, H. Genuino, M. Nashaat, S. Mohammad, L. Zhu, and G. Hoag, "Green synthesis of iron nanomaterials for oxidative catalysis of organic environmental pollutants," in *New and Future Developments in Catalysis: Catalysis for Remediation and Environmental Concerns*, Elsevier, New York, NY, USA, 2013.
- [28] M. Abril, H. Ruiz, and L. H. Cumbal, "Biosynthesis of multicomponent nanoparticles with extract of mortiño (*Vaccinium floribundum Kunth*) berry: application on heavy metals removal from water and immobilization in soils," *Journal of Nanotechnology*, vol. 2018, Article ID 9504807, 10 pages, 2018.

- [29] P. Palacios, L. De los Santos Valladares, A. Bustamante, and J. González, "Estudio de la deshidroxilación en el óxido férrico hidratado denominado limonita," *Revista Sociedad Química del Perú*, vol. 78, no. 3, pp. 198–207, 2012.
- [30] F. Osorio, J. Torres, and M. Sánchez, *Tratamiento de Aguas Para la Eliminación de Microorganismos y Agentes Contaminantes*, Dias de Santos, Madrid, Spain, 2010.
- [31] S. Chitra, K. Paramasivan, P. Sinha, and K. Lal, "Ultrasonic treatment of liquid waste containing EDTA," *Journal of Cleaner Production*, vol. 12, no. 4, pp. 429–435, 2004.
- [32] P. Ghosh, A. Samanta, and S. Ray, "COD reduction of petrochemical industry wastewater using Fenton's oxidation," *Canadian Journal of Chemical Engineering*, vol. 88, no. 6, pp. 1021–1026, 2010.
- [33] A. Rubio, E. Chica, and G. Peñuela, "Aplicación del proceso Fenton en el tratamiento de aguas residuales de origen petroquímico," *Ingeniería y Competitividad*, vol. 12, no. 2, pp. 211–223, 2014.

Research Article

Biological Effect of Organically Coated *Grias neuberthii* and *Persea americana* Silver Nanoparticles on HeLa and MCF-7 Cancer Cell Lines

Lizeth Salazar,¹ María José Vallejo López,² Marcelo Grijalva ^{1,2} Luis Castillo,³ and Alexander Maldonado¹

¹Centro de Nanociencia y Nanotecnología, Universidad de las Fuerzas Armadas ESPE, Avenida General Rumiñahui S/N y Ambato, P.O. Box 171-5-231B, Sangolquí, Ecuador

²Departamento de Ciencias de la Vida, Universidad de las Fuerzas Armadas ESPE, Avenida General Rumiñahui S/N y Ambato, P.O. Box 171-5-231B, Sangolquí, Ecuador

³Facultad de Ingeniería, Ciencias Físicas y Matemáticas, Universidad Central del Ecuador, P.O. Box 1701521, Quito, Ecuador

Correspondence should be addressed to Marcelo Grijalva; rmgrijalva@espe.edu.ec

Received 8 March 2018; Revised 5 June 2018; Accepted 2 July 2018; Published 1 August 2018

Academic Editor: Lee Blaney

Copyright © 2018 Lizeth Salazar et al. This is an open access article distributed under the Creative Commons Attribution License, which permits unrestricted use, distribution, and reproduction in any medium, provided the original work is properly cited.

The aim of this study was to assess the biological effect of organically coated *Grias neuberthii* (*piton*) fruit and *Persea americana* (*avocado*) leaves nanoparticles (NPs) on cervical cancer (HeLa) and breast adenocarcinoma (MCF-7) cells with an emphasis on gene expression (p53 transcription factor and glutathione-S-transferase *GST*) and cell viability. UV-Vis spectroscopy analysis showed that synthesized AgNPs remained partially stable under cell culture conditions. HeLa cells remained viable when exposed to *piton* and *avocado* AgNPs. A statistically significant, dose-dependent cytotoxic response to both AgNPs was found on the breast cancer (MCF-7) cell line at concentrations above 50 μM . While expression levels of transcription factor p53 showed down-regulation in treated MCF-7 and HeLa cells, *GST* expression was not affected in both cell lines treated. Cell viability assays along with gene expression levels in treated MCF-7 cells support a cancer cell population undergoing cell cycle arrest. The selective toxicity of biosynthesized *piton/avocado* AgNPs on MCF-7 cells might be of value for novel therapeutics.

1. Introduction

Breast and cervical cancers are the most common malignancies among females in low- and middle-income countries (LMICs). The two malignancies are associated with high mortality rates and represent a considerable burden for public health systems [1]. Currently available cancer therapeutics, such as chemotherapy and radiotherapy, exhibit limitations that must be overcome to improve their efficacy and patient's life expectancy. Since cancer is a world health problem, emerging drug preparations that can pass through tumor barriers and enhance anticancer drug delivery are potentially useful [2]. In this context, a lot of research has been done to synthesize new classes of materials, including

those at nanoscale, and test their anticancer properties and/or their application in cancer early detection approaches [3, 4]. Silver nanoparticles (AgNPs) are widely applied in cancer research due to their potent *in vitro* antitumor effects on cancer cell lines including breast and cervical cancer models [5, 6]. The cytotoxic response that a nanoparticle could trigger in cells depends not only on its physical and chemical characteristics [3], but also, since different cell lines do not respond identically to stimuli with the same nanoparticles, on the cell type [7].

The synthesis of AgNPs through different physical, chemical, and biological methods and with well-defined parameters of size and shape has been reported by several authors [8]. Recent studies suggest that biosynthetic

approaches for AgNPs fabrication may improve some limitations found with commonly used physical and chemical methods, namely, high-energy consumption, negative environmental impact, and significant production costs [3, 8]. Plant extracts are commonly used as reducing and stabilizing agents for the biosynthesis of AgNPs. The cytotoxic and antiproliferative effects of plant-based AgNPs against different cancer cell models have been extensively investigated [9]. A study using green synthesis with traditional plants is the one performed by Barua et al., where *Thuja occidentalis* leaf extract was used to synthesize AgNPs that displayed anticancer properties against MCF-7, MDA-MB-231, KB, and HeLa cell lines. NPs also showed antibacterial properties against *Bacillus subtilis*, *Staphylococcus aureus*, *Listeria monocytogenes*, *Salmonella typhimurium*, and *Pseudomonas aeruginosa* [29].

An interesting finding has been an upregulation of proapoptotic genes following AgNPs exposure [10–12]. A recent study found that AgNPs may induce cell death through the p53 apoptotic pathway in a time- and dose-dependent manner [13, 14]. The tumor suppressor p53 gene induces cell cycle arrest and triggers apoptosis initiation in cells with extensive DNA damage. In some types of cancer, however, p53 inactivation functions as a drug-resistance mechanism [15]. Thus, *in vitro* expression studies of p53 are important to evaluate AgNPs cytotoxicity.

Oxidative stress is another harmful effect of AgNPs. In response to high rates of reactive oxygen species (ROS), oxidative stress-related genes (catalase, mu class of glutathione-S-transferase) are reported to be overexpressed [16]. The last one, glutathione-S-transferase (GST), is an antioxidant defense enzyme that catalyzes the coupling of reduced glutathione to a variety of damaging compounds to activate cellular outflow of these contaminants [17].

P. americana (avocado) is a member of the *Lauraceae* family, which has been used in herbal medicine in Central and South America due to its pharmacological properties [18, 19]. It is well known that avocado could exert antioxidant, anti-inflammatory, and other beneficial effects [19]. The avocado pulp, seeds, and leaves contain lipophilic phytochemicals [20] and phenolic compounds [21]. Anitha and Sakthivel have reported the biosynthesis of AgNPs using aqueous leaf extract of avocado as reducing agent and demonstrated an anti-inflammatory effect on red blood cells [22]. Another study showed that biosynthesized AgNPs from avocado showed strong antimicrobial effect against gram-positive and gram-negative bacteria [23].

G. neuberthii (Sachamango, piton) is a medicinal tree, belonging to the *Lecythidaceae* family, that grows in the Amazon regions of Peru, Brazil, and Ecuador [24–26]. Traditional medicine in local indigenous communities uses piton properties for treatment of several pathological conditions including sinusitis, uterine bleeding, diarrhea, constipation, among others [27]. Recently, Vásquez-Ocmín and coworkers demonstrated that a *G. neuberthii* bark extract had antiparasitic activity *in vitro* [28]. The application, however, of *G. neuberthii* extract in the synthesis of AgNPs has not been reported yet.

The present study aimed at evaluating the effects of two types of biosynthesized AgNPs using *G. neuberthii* fruit and *P. americana* leaf extracts (as stabilizing and reducing agents) on breast (MCF-7) and cervical (HeLa) cancer cell lines. NPs' cytotoxicity was assessed using an MTT colorimetric assay. The study also assessed the AgNPs modulation properties in two metabolic pathways: apoptosis and oxidative stress. For this purpose, gene expression assays were used for relative quantification of the expression of p53 and GST genes.

2. Materials and Methods

2.1. Silver Nanoparticles (AgNPs). *G. neuberthii* fruit AgNPs and *P. americana* leaf AgNPs were biosynthesized and kindly provided by Dr. Brajesh Kumar from the Advanced Materials Laboratory at CENCINAT, Universidad de las Fuerzas Armadas ESPE, Ecuador. AgNPs were characterized by transmission electron microscopy (TEM) (FEI-TECNAI G20 SPIRIT TWIN, USA), UV-visible spectroscopy (Analytik Jena SPECORD® S 600, Germany), and dynamic light scattering (DLS) (HORIBA LB-550, Japan). *G. neuberthii* and *P. americana* AgNPs were spherical, and their hydrodynamic diameters were 38.9 ± 19.0 nm and 41.1 ± 19.1 nm, respectively.

2.2. Cell Culture. MCF-7 (human breast adenocarcinoma) and HeLa cell (cervix adenocarcinoma) lines were kindly provided by Dr. Javier Camacho, CINVSTAV-IPN, Mexico. The cell lines were cultivated in Dulbecco's Modified Eagle's Medium/Nutrient Mixture F-12 (DMEM/F-12) (Gibco), supplemented with 10% fetal bovine serum (FBS) (Gibco), and 1% penicillin-streptomycin (Gibco). Additionally, 1% sodium pyruvate (Gibco) was added to HeLa cell medium. Cell cultures were maintained at 37°C and 5% CO₂ in a humidified atmosphere. Subcultures were obtained when cells reached 85–90% confluence. Cells were washed three consecutive times with phosphate-buffered saline (PBS) (Gibco) and then detached with trypsin-EDTA 0.25% solution (Gibco). Cellular suspensions were centrifuged at 1000 rpm at 22°C for 10 minutes. Pellets were resuspended in medium, and cells were counted on Neubauer chambers with an inverted microscope (MICROS Austria MCX-1600, Austria). Cells were seeded on 6-well plates or 60 mm × 15 mm Petri dishes at specific densities.

2.3. Nanoparticles' Stability under Cell Culture Conditions. Prior to *in vitro* biological testing, the stability of the two types of biosynthesized AgNPs (*G. neuberthii* and *P. americana*) under cell culture conditions was assessed by UV-visible spectroscopy (Analytik Jena SPECORD S 600, Germany). Stock AgNPs preparations (1 mM) were diluted in complete culture medium and distilled water. AgNPs solutions were placed in 60 mm × 15 mm Petri dishes and incubated at 37°C and 5% CO₂ for 0, 24, and 48 hours. An additional control was included to evaluate the influence of cellular debris. For this control, MCF-7- HeLa cell lines were grown for 24 hours and then exposed to NPs. The supernatant was later collected

to determine the presence of agglomeration. For noncontrols, MCF-7 and HeLa cell lines were seeded (1.5×10^5 cells) and maintained for 24 hours, followed by exposure to different AgNPs concentration and incubation times. Finally, UV-visible absorption spectra were measured at 350–800 nm.

2.4. MTT Assay for Cytotoxicity Assessment of Nanoparticles. MCF-7 and HeLa cells were seeded in 96-well plates in 200 μ L of complete culture medium at a density of 4×10^3 cells per well and 2×10^3 cells per well, respectively. Cells were maintained under culture conditions as described above. Different concentrations of *G. neuberthii* and *P. americana* AgNPs were used. Dilutions of AgNPs were obtained adding complete culture medium to final exposure concentrations of 1–80 μ M for MCF-7 cells and 0.001–50 μ M for HeLa cells. For each cell line and AgNPs type, six technical replicates were performed. The complete experiment was carried out three times (biological replicates). Blank wells containing only medium and untreated cells were included in every experiment, as appropriate controls. After an exposure time of 48 hours, cell viability was measured by a 3-(4, 5-dimethyl-2-thiazolyl)-2, 5-diphenyl-2H-tetrazolium bromide (MTT), colorimetric assay (Molecular Probes), following the manufacturer's recommendations.

For the MTT assay, supernatants were removed, and 100 μ L of Dulbecco's Modified Eagle's Medium (DMEM) without red phenol was placed in each well. A 12 mM MTT stock solution was prepared by adding 1 mL of sterile PBS. Next, 10 μ L of this stock was added to each well. Cells were then incubated protected from light for 4 hours, followed by addition of 100 μ L of SDS-HCl and homogenization and another 4-hour incubation, in order to dissolve intracellular formazan products. Finally, absorbance was measured at 570 nm using a microplate reader (Perlong, Beijing). Cell viability was calculated as the ratio of the mean absorbance obtained for the treatment wells to the mean absorbance of the control wells (untreated cells) as follows:

$$\text{cell viability (\%)} = \frac{\text{mean absorbance of treatment}}{\text{mean absorbance of control}} \times 100\%. \quad (1)$$

2.5. Quantitative Real-Time PCR Analysis. MCF-7 and HeLa cells were seeded into 6-well plates at a cell density of 1.5×10^5 per well. After a 24-hour culture period, cells were exposed to different concentrations of AgNPs for 48 hours. Tested AgNPs concentrations were 0, 40, 80, and 160 μ M for the MCF-7 cell line, and 0, 25, 50, and 100 μ M for the HeLa cell line. After 48 hours of exposure to either piton or avocado AgNPs, cells were collected and diluted in 200 μ L PBS. Total RNA was then extracted using *PureLink® RNA Mini Kit* (Ambion) and purified with *TURBO DNA-free™ Kit* (Ambion) in order to remove contaminant genomic DNA. Purified RNA was quantified with a NanoDrop 2000 spectrophotometer (Thermo Scientific) and also separated by electrophoresis in an agarose gel (1%) with 1X

Tris-borate-EDTA buffer (TBE) at 100 V and 300 mA for 55 minutes to check for integrity.

Purified RNAs were used in one-step qRT-PCR assays on a LightCycler® Nano Instrument (Roche Diagnostics), with TaqMan probes chemistry to determine relative quantification of p53 and *GST* genes in MCF-7 and HeLa cell lines. Primers and probes used in the present study are listed in Table 1. TaqMan probes (Invitrogen) were end-labeled with the fluorophore 6-carboxyfluorescein (6-FAM) and the quencher tetramethylrhodamine (TAMRA) at 5' and 3', respectively. Each PCR mix included 1X TaqMan® RT-PCR Mix, 0.5 μ M of forward primer, 0.5 μ M of reverse primer, 0.15 μ M of TaqMan probe, 1X TaqMan RT Enzyme Mix, DEPC-treated water (Invitrogen), and 20 ng RNA template in a total volume of 10 μ L. The qRT-PCR thermocycling program was as follows: cDNA synthesis at 48°C for 15 min, followed by a polymerase activation step at 95°C for 10 minutes. Then, 40 cycles of thermal amplification were carried out at 95°C for 15 s (denaturation), 50°C or 56°C for 15 s (for primer annealing of *ACTB* and *GST* genes, resp.), and a last step of 45 s at 60°C (extension). For p53 gene amplification, annealing and extension were performed in a single step at 61°C for 60 s. For PCR efficiency and correlation coefficient (R^2) calculations, 10-fold RNA dilutions were used. A semilogarithmic graph was constructed with Ct values plotted on the X-axis and log values of the RNA concentration, on the Y-axis. qRT-PCR efficiencies were calculated according to the following equation:

$$E = 10^{-1/\text{slope}}. \quad (2)$$

p53 and *GST* expression levels were normalized with actin beta gene (housekeeping gene) expression levels according to the methodology developed by Pfaffl (2001) [30]. RNA expression levels from untreated cells were used as calibrators to calculate the relative expression ratios.

2.6. Statistical Analysis. Six replicates of each treatment were done for cytotoxicity experiments. For gene expression qRT-PCR, experiments were performed in triplicate. Data are presented as the mean \pm standard deviation (SD). The Kruskal–Wallis, Dunn's, and Tukey's multiple comparison tests were performed to determine any significant difference between controls and treatments. A p value < 0.05 was set for statistical significance.

3. Results

3.1. AgNPs Stability. Stability of biosynthesized *G. neuberthii* AgNPs and *P. americana* AgNPs in biological medium and distilled water was evaluated by UV-visible spectroscopy for 3 incubation times under standard conditions of 37°C and 5% CO₂ in a humidified atmosphere (see supplementary data (available here)). Results showed that absorbance values were higher when AgNPs were diluted in culture medium in comparison with AgNPs diluted in distilled water. UV-Vis spectra of all samples showed a broad peak at the maximum absorption wavelength between 400 and 420 nm due to the surface plasmon resonance (SPR) band of spherical AgNPs.

TABLE 1: Oligonucleotide sequences for quantitative, real-time PCR analysis.

Gene name	Sequences (5'-3')	T _m (°C)	GenBank (accession code)	Amplicon size (bp)	Efficiency	Reference
Glutathione-S-transferase (<i>GST</i>)	Forward: GATACTGGGGTACTGGGACATCC	61.58	NM_146421.2	130	1.87	[31]
	Reverse: CCACTGGCTTCTGTCATAATCAGG	61.22				
	Probe: CCCACGCCATCCGCCTGCTCCT	68.9				
Tumor suppressor p53	Forward: TAACAGTTCCTGCATGGGCGGC	65.66	NM_000546.5	121	1.96	[32]
	Reverse: AGGACAGGCACAAACACGCACC	66.01				
	Probe: CGGAGGCCCATCCTCACCATCATCA	67.97				
Actin beta (<i>ACTB</i>)	Forward: CCTCGCCTTGCCGA	56.04	NM_001101.3	171	2.23	[33]
	Reverse: TGGTGCCTGGGGCG	58.15				
	Probe: CCGCCGCCCGTCCACACCCGCC	69.7				

AgNPs diluted in DMEM/F12 medium showed a second peak between 550 and 560 nm. The absorption spectra of AgNPs incubated with HeLa and MCF-7 cell lines did not present any other modification. Incubation at 37°C and 5% CO₂ for 24 and 48 hours did not produce any significant change in the UV-visible spectra as compared to 0 hours of incubation.

3.2. Cell Viability of HeLa and MCF-7 Cell Lines Exposed to Piton and Avocado AgNPs. The MTT colorimetric assay was used to assess the *in vitro* cytotoxic effect of the two types of AgNPs on MCF-7 and HeLa cancer cell lines. Absorbance data were transformed to cell viability rates using (1). Untreated cells without exposure to AgNPs (control) represented 100% of cell viability. Results showed that MCF-7 cell viability rates decreased when piton and avocado AgNPs concentration increased. In comparison with the control, this dose-dependent cytotoxicity was statistically significant at the concentration of 50 μM ($p = 0.0203$) and 80 μM ($p = 0.0003$) for piton AgNPs, showing a cell viability decrease of approximately 16% and 25%, respectively (Figure 1(a)). The effect of avocado AgNPs on MCF-7 cell line was significant at 50 μM ($p = 0.0097$) and 80 μM ($p < 0.0001$) causing a decrease of 19% and 27% in cell viability, respectively (Figure 1(b)). Tukey's multiple comparison tests were used to determine which treatments were different from each other. The viability means of 1 μM and 80 μM treatments for both types of AgNPs showed a p-value of 0.0249 for piton AgNPs and 0.0371 for avocado AgNPs. Figures 2(a) and 2(b) show that the confidence intervals (95% confidence level) for the difference between the means of 1 μM and 80 μM do not contain zero. Consequently, a statistically significant difference for these means is supported. Conversely, HeLa cells treated with piton and avocado AgNPs in concentrations up to 50 μM did not show a statistically significant cytotoxic response ($p > 0.05$). The viability of treated HeLa cells remained similar to nonexposure

control (Figures 1(c) and 1(d)), and no relevant differences were obtained with Tukey's multiple comparison tests and confidence intervals (data not shown).

3.3. Relative Quantification of *GST* and *p53* Genes. *GST* and *p53* genes are important in mounting cellular defense responses against harmful stimuli causing, for instance, DNA damage [34, 35]. We conducted *GST* and *p53* relative mRNA expression analysis by qRT-PCR from RNA extracted from MCF-7 and HeLa cells exposed to *G. neuberthii* and *P. americana* AgNPs. Cells were treated with various concentrations of NPs (0, 40, 80, and 160 μM for MCF-7 cell line, and 0, 25, 50, and 100 μM for HeLa cell line) for 48 h, then RNAs were isolated, and qRT-PCR assays were conducted as described in Methods. Exposure of MCF-7 cells to 40 μM of *G. neuberthii* and *P. americana* AgNPs resulted in a statistically significant downregulation of *p53* with relative expression levels of 0.527 ($p = 0.0499$) and 0.560 ($p = 0.0499$), respectively (Figure 3(a)). In HeLa cells, *G. neuberthii* AgNPs at 100 μM and *P. americana* AgNPs at 25 μM also decreased *p53* expression (to a relative expression of 0.331, $p = 0.0499$ and 0.234, $p = 0.0062$, resp.) (Figure 3(b)). For both cell lines, *GST* gene expression was not significantly affected by AgNPs treatment at any tested concentration (Figures 3(a) and 3(b)). Although we found some AgNPs treatments to slightly higher *GST* expression levels, these results were not statistically relevant.

4. Discussion

There is a considerable amount of literature on naked silver nanoparticles that show their antimicrobial [23], anti-inflammatory [22], anticancer, antiangiogenic [38], antiviral [39–41], and antiproliferative [42] properties. However, toxicity evaluation of silver NPs in mammalian cells has shown adverse effects [43]. Several *in vitro* assays have reported that Zn and Fe nanoparticles induce oxidative stress, DNA damage, and apoptosis in human hepatoma cells,

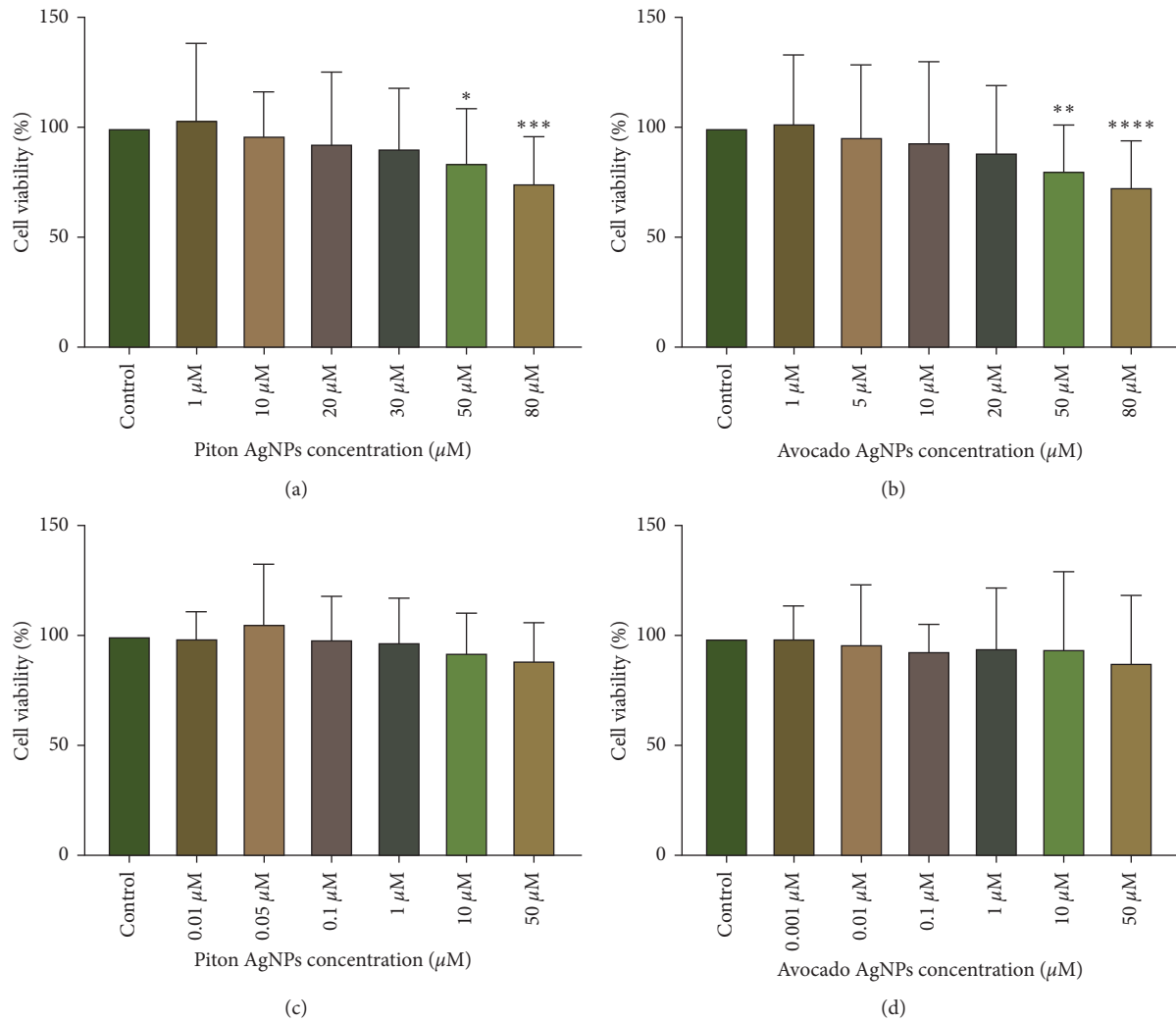


FIGURE 1: Viability of MCF-7 (a, b) and HeLa (c, d) cells treated with piton AgNPs or avocado AgNPs relative to viability of the control (untreated cells). Cells were treated with several concentrations of AgNPs for 48 hours. Data are presented as mean \pm SD from three independent experiments (* $p \leq 0.05$, ** $p \leq 0.01$, *** $p \leq 0.001$, and **** $p \leq 0.0001$).

hepatocytes, and lymphocytes [44]. *In vivo* experiments on Crl:CD(SD)IGS BR 344 rats showed pulmonary inflammation and cytotoxicity following exposure to single-wall carbon nanotubes [45].

When studying organically coated nanoparticles (OC-NPs), it is important to understand their chemistry, dissolution rate, surface properties, and determine their physical properties to evaluate their *in vivo* and *in vitro* effects. For instance, OC-AgNPs interact with aqueous solutions and form Ag⁺ which leads to membrane and sub-cellular components damage [46]. However, it is essential to evaluate all the different coatings in order to explore new applications.

To the best of our knowledge, the present study is the first one that evaluates both *P. americana* and *G. neuberthii*-coated AgNPs biological *in vitro* effects on MCF-7 and HeLa cells. After bio-synthesized AgNPs physical characterization, stability under culture conditions was assessed using UV-Vis absorption spectrometry which provided information on the

structural conformation of organic or inorganic elements in eluted solutions [47]. The principle of localized surface plasmon resonance (LSPR) states that when light interacts with conductive nanoparticles (i.e., AgNPs) which are smaller than the incident wavelength, the resultant electric field excites electrons and generates plasmon oscillations which are dependent on the composition, size, geometry, dielectric environment, and separation distance of NPs [48]. UV-Vis analysis of spectra of organically coated nanoparticles suspended in DI water for HeLa in our study did not show an absorbance peak due to the fact that it was highly diluted, whereas for MCF-7, a small peak was present at 400–420 nm. Stability assays on complete medium showed the presence of the previously described peak and a second one between 550 and 560 nm. Since AgNPs absorbance is in the range of 390–430 nm [49, 50], our results confirm the presence of nanoparticles. However, synthesized NPs lacked uniformity, suggesting that the obtained NPs have different shapes, sizes [49], and were not completely monodispersed

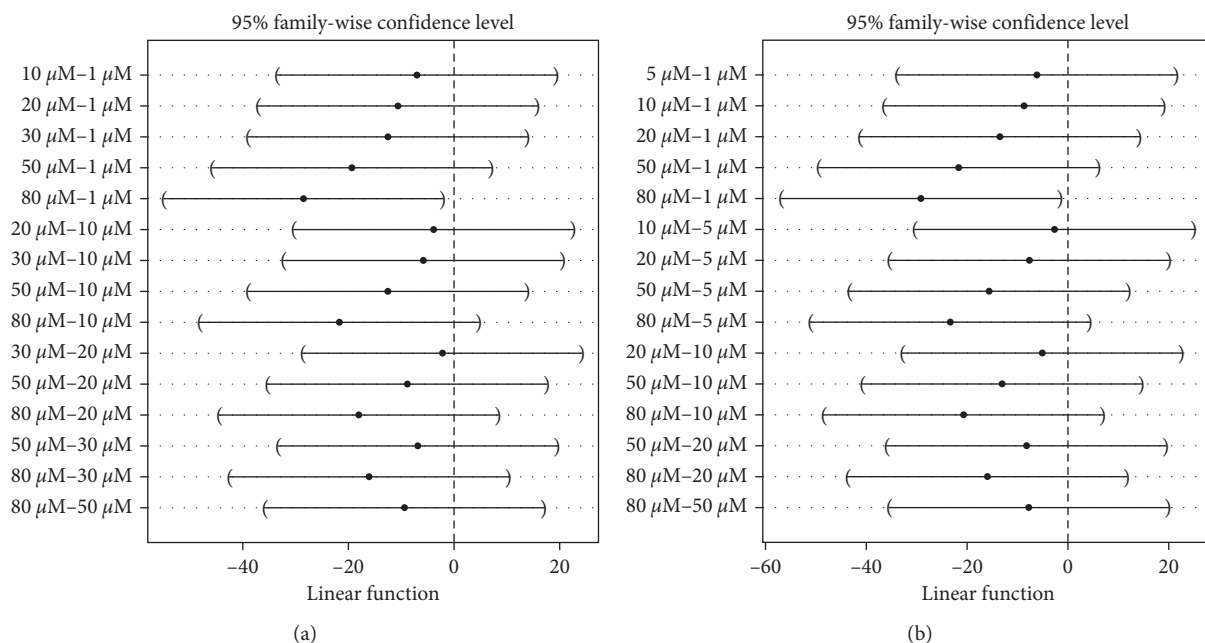


FIGURE 2: Interval plots for differences of means with 95% confidence levels for (a) piton AgNPs treatments and (b) avocado AgNPs treatments on MCF-7 cell line viability. The confidence intervals for the pairs of means that include zero represent that the differences are not statistically significant.

(agglomeration) [51]. The second peak clearly corresponded to DMEM, which absorbs at wavelengths from 440 to 560 nm depending on the solution's pH [52]. Although this peak corresponds to the growth medium, a related point to consider is the presence of diverse amino acids, growth factors, and FBS that might also contribute to cause AgNPs aggregation [53].

An important point to note is that HeLa cells showed a reduced cellular uptake in comparison with MCF-7 cells. Biosynthesized AgNPs in our study became aggregated, but endocytosis depends not only on aggregation status but also on multiple factors such as size, charge, surface coating, interactions with the culture media, and cell-specific uptake properties [54].

Gliga and collaborators studied the importance of agglomeration in the cellular uptake of coated AgNPs, concluding that the primary particle size is the most important factor that contributes to Ag⁺ release and subsequently cellular toxicity [55]. For instance, hydrophobically modified glycol CS (HGCS) nanoparticles were evaluated on HeLa cells where most of them were internalized by the non-destructive mechanism of micropinocytosis (used for agglomerated NPs) instead of the clathrin-mediated endocytosis route. These internalization pathways exhibit diverse intracellular behaviors and trigger different levels of cytotoxicity, including inhibition of lysosome degradation [56].

Cytotoxicity MTT assays showed a dose-dependent toxicity in the MCF-7 cell line with a statistically significant reduction in cell viability at concentrations of 50 μM and 80 μM for both nanoparticles. The cytotoxic effect found in the present study is in agreement with findings from other studies. For instance, green biosynthesized AgNPs (*Tanacetum vulgare*, phycocyanin) can exert a lethal effect on

MCF-7 cells [57, 58]. Further analysis from Figure 1(a) (*G. neuberthii*) and Figure 1(b) (*P. americana*) in MCF-7 cells indicates a reduction of viability of up to 25% and 27%, respectively. However, high toxicity levels (above 50%) have been previously reported by Gurunathan et al. [59] using biologically synthesized AgNPs on the same cell line with toxicity being mediated via micropinocytosis and clathrin-dependent endocytosis [60]. However, the morphology, size, and surface chemical groups of nanoparticles affect the above mechanisms [61] and our bio-AgNPs lacked monodispersity. According to El-Naggar et al. [58], AgNPs action mechanisms involve the release of silver cations and further interaction with biomolecules such as DNA and proteins, affecting cell membrane integrity, lactate dehydrogenase (LDH) levels and mitochondrial permeability and leading finally to oxidative stress and apoptosis.

In contrast, HeLa cells MTT viability assessments (Figures 1(c) and 1(d)) suggest that non-monodispersed nanoparticles interfered with Ag⁺ ion release. Furthermore, the agglomeration/aggregation state of AgNPs influences cellular uptake depending mainly on cell types and their properties, as being reported by Lankoff et al. [62] whose results are similar to ours. To sum up, HeLa cells exhibited a reduced uptake in the presence of agglomerated AgNPs, conversely to MCF-7 cells, which showed a higher uptake rate for this type of NPs.

An interesting aspect to address is the interaction among AgNPs coating with cell membranes which are negatively charged in mammalian cells at pH = 7. Electric variations of this layer affect the transport of substrates, as reported by Dobrzyńska et al., who described electrical membrane variations of MCF-7 cells according to their media pHs [63]. The authors showed a shift of the isoelectric point at low pH

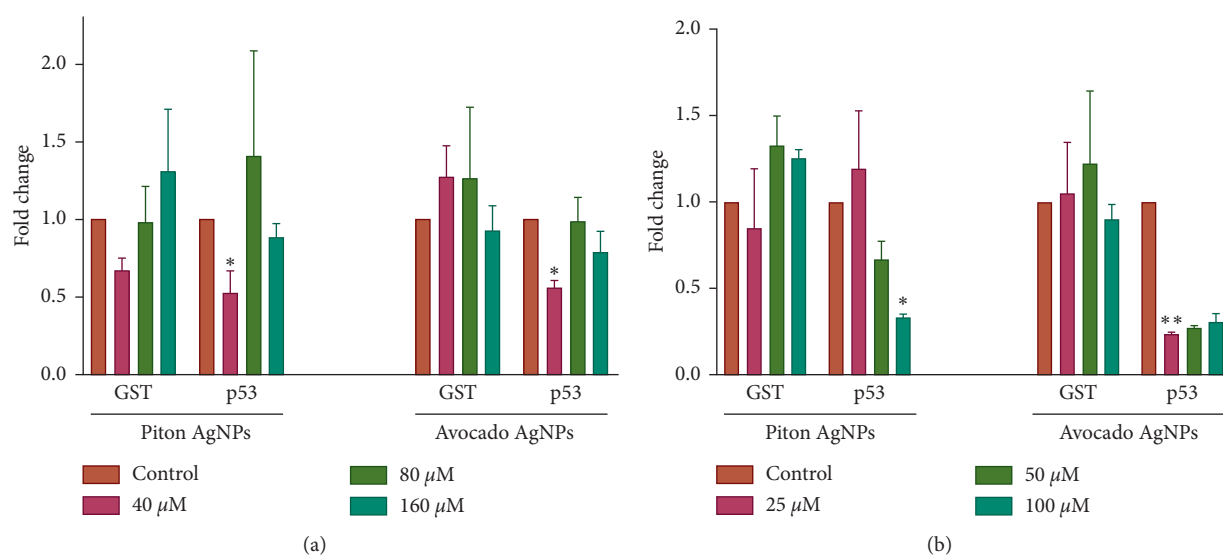


FIGURE 3: Relative expression of *GST* and *p53* genes in (a) MCF-7 and (b) HeLa cells treated with piton and avocado AgNPs. Actin beta was used as the reference gene for data normalization. Untreated cells were used as calibrators to calculate the fold changes. Data are presented as mean \pm SD from three independent experiments (* $p \leq 0.05$, ** $p \leq 0.01$, *** $p \leq 0.001$, and **** $p \leq 0.0001$).

values and a positive charge was evidenced at low pH, with negative charge at high pH. In the case of HeLa cells, a study by Warren and Payne found that nanoparticles do not permeabilize the membrane but allow depolarization by increasing potassium channels, which leads to stabilization of the resting membrane potential [64]. In the present study, different responses in the studied cell lines suggest that intrinsic differences affect the uptake and internalization of nanoparticles. Cell culture components (media and serum) affect nanoparticles and cause aggregation, which might affect the intracellular behavior of NPs but not necessarily inhibit their effect [63]. This is due to the fact that NPs cellular uptake is always mediated by a biocorona, which affects NPs biodistribution, activation, and interaction with cell surface receptors. As reported by Asharani et al., NPs size affects binding and activation of membrane receptors and gene expression in cancer cell lines [42].

Although AgNPs cytotoxicity has been found in several studies [14,66–69], the molecular mechanisms involved are not completely understood [16]. AgNPs may trigger oxidative stress by reactive oxygen species (ROS) production [70, 71] causing a variety of intracellular responses and alterations in antioxidant systems [72], which finally could lead to apoptosis or necrosis [73].

Recent studies have reported a remarkable increase in expression levels of *GST* in different *in vitro* [16] [31] and *in vivo* [74, 75] models treated with AgNPs, showing that *GST* is an important factor to balance intracellular oxidative status [76]. We found, however, that exposure to bio-synthesized AgNPs did not elicit statistically significant variations in gene expression in treated cancer cells after 48 hours of incubation/exposure. This lack of response regarding *GST* expression might be explained by the presence of bioactive compounds that may counteract the formation of intracellular free radicals. It has been previously reported by Owolabi et al. [77] that phytochemicals such as quercetin

have strong antioxidant activity in extracts from *P. americana* leaves. Alva et al. [27] found that *G. neuberthii* fruit contains monounsaturated and polyunsaturated fatty acids, which are known for their capacity to scavenge free radicals, for example, superoxide [78]. However, further experiments are required to confirm the presence of antioxidants in the nanoparticles and inside the cells.

An analysis of the expression levels of genes coding for detoxifying enzymes by Aueviriyavit et al. [79] found that *GST* expression levels remained unchanged after Caco-2 cells were exposed to AgNPs, despite the fact that expression levels of other stress-responsive genes were significantly affected. Kumaran et al. [31] found that *GST* expression in MCF-7 cells became altered after 24 hours of exposure to NPs rather than 48 hours. This phenomenon was explained by a higher NPs: cell ratio at 24 hours in comparison with the proliferation rate at 48 hours, where intracellular amounts of NPs decrease, resulting in less cytotoxicity.

Another interesting study showed that a possible mechanism of death induced by NPs in cell lines is p53-mediated apoptosis, mechanism that depends, among other things, on the size of the nanomaterial studied [80–82]. Blanco et al. suggested that p53 expression might be downregulated when smaller NPs and longer incubation times are assayed [14]. In the present study, p53 gene expression decreased significantly at different concentrations after 48 hours of incubation with *G. neuberthii* and *P. americana* AgNPs (around 40 nm in diameter), which is in agreement with the study by Blanco et al. We found that *P. americana* AgNPs induced a statistically significant p53 downregulation after 48 hours of exposure to concentrations of 25 μ M and 40 μ M. Throughout, *G. neuberthii* AgNPs exhibited the same pattern for 40 μ M and 100 μ M. Our findings are in agreement with other studies, such as a recent one by Asharani et al. in which the authors found p53 to become downregulated along with low levels of p21 protein in normal human lung cells (IMR-90) and human

brain cancer cells (U251) after exposure to AgNPs [83]. Zhang et al. [65] found that AgNPs (400 µg/ml) in several cancer cell lines induced downregulation of p53 expression and cell cycle arrest at S/G2/M phases.

In our study, HeLa cells line showed a p53 significant downregulation at 25 µM and 100 µM. However, at any concentration, relevant toxicity was absent. This finding might be explained by the role of p53 as a crucial regulator of cell proliferation and genome stability. p53 induces the expression of p21 transcription factor in presence of stress signals in order to trigger cell cycle arrest and senescence [36]. In primary tumors, however, p53 might be mutated with inhibition of its normal function as a result or might become degraded by ubiquitin-protein ligase targeting. Engeland found that p53 activation leads to cell cycle arrest by the p53-DREAM pathway. This network involves the downregulation of several genes including the major checkpoint p53 [37]

A correlation between mRNA p53 levels and cell viability was found in a study by Kovács and collaborators. The authors found a decrease in osteosarcoma U-2 OS cell viability when they were treated with AgNPs, with p53 significantly upregulated [15]. However, there are other primary mechanisms that are involved in apoptosis triggering, for example, mitochondrial stress. Our findings are in agreement with Kovács' study, as we observed a downregulation of p53 gene while cell viability was not significantly affected, thus supporting the notion that p53 downregulation might induce proliferation arrest.

In summary, MCF-7 cells underwent cycle arrest when exposed to our biosynthesized AgNPs, while HeLa cells were not affected. This finding might be of use when designing novel therapeutic strategies in cancer, specifically in breast cancer.

5. Conclusions

In the present study, we tested the cytotoxic/antiproliferative effect of biosynthesized AgNPs from *P. americana* and *G. neuberthii* on MCF-7 and HeLa cell lines. Expression of p53 and GST genes was also assessed for NPs' apoptosis triggering and oxidative stress modulation properties, respectively. Biosynthesized AgNPs were toxic in a concentration-dependent manner on MCF-7 cells but not on HeLa cells. GST expression was not affected, while p53 was downregulated in treated MCF-7 cells. Our findings demonstrate a net cytotoxic effect of both AgNPs on MCF-7 cells with a possible small apoptotic population and a large cell population going into proliferation arrest. While there is a clear need of mechanistic studies on the above cell responses, synthesized AgNPs might be useful when designing future therapeutic applications in breast cancer.

Data Availability

The data supporting this research article are available from the corresponding author upon request.

Conflicts of Interest

The authors declare that there are no conflicts of interest regarding the publication of this paper.

Acknowledgments

The authors are thankful to Dr. Brajesh Kumar for provision of biosynthesized NPs and to Dr. Rachid Seqqat for valuable help with preliminary experiments. This work was supported by Universidad de las Fuerzas Armadas ESPE Research Grant 2014-PIT-044 (to Marcelo Grijalva).

Supplementary Materials

UV-visible spectra analysis of piton/avocado AgNPs under biological conditions. (*Supplementary Materials*)

References

- [1] L. A. Torre, F. Islami, R. L. Siegel, E. M. Ward, and A. Jemal, "Global cancer in women: burden and trends," *Cancer Epidemiology, Biomarkers & Prevention*, vol. 26, no. 4, pp. 444–457, 2017.
- [2] Y. J. Ho, T. C. Wang, C. H. Fan, and C. K. Yeh, "Current progress in antivasculature tumor therapy," *Drug Discovery Today*, vol. 22, no. 10, pp. 1503–1515, 2017.
- [3] X.-F. Zhang, Z.-G. Liu, W. Shen, and S. Gurunathan, "Silver nanoparticles: synthesis, characterization, properties, applications, and therapeutic approaches," *International Journal of Molecular Sciences*, vol. 17, no. 9, p. 1534, 2016.
- [4] J. Elgqvist, "Nanoparticles as theranostic vehicles in experimental and clinical applications-focus on prostate and breast cancer," *International Journal of Molecular Sciences*, vol. 18, no. 5, p. 1102, 2017.
- [5] F. Ordikhani, M. Erdem Arslan, R. Marcelo et al., "Drug delivery approaches for the treatment of cervical cancer," *Pharmaceutics*, vol. 8, no. 3, p. 23, 2016.
- [6] K. Juarez-Moreno, E. B. Gonzalez, N. Giron-Vazquez et al., "Comparison of cytotoxicity and genotoxicity effects of silver nanoparticles on human cervix and breast cancer cell lines," *Human & Experimental Toxicology*, vol. 36, no. 9, pp. 931–948, 2017.
- [7] D. Sahu, G. M. Kannan, M. Tailang, and R. Vijayaraghavan, "In vitro cytotoxicity of nanoparticles: a comparison between particle size and cell type," *Journal of Nanoscience*, vol. 2016, Article ID 4023852, 9 pages, 2016.
- [8] S. Irvani, H. Korbekandi, S. V. Mirmohammadi, and B. Zolfaghari, "Synthesis of silver nanoparticles: chemical, physical and biological methods," *Research in Pharmaceutical Sciences*, vol. 9, no. 6, pp. 385–406, 2014.
- [9] M. Grijalva, M. J. Vallejo, L. Salazar, J. Camacho, and B. Kumar, "Cytotoxic and antiproliferative effects of nanomaterials on cancer cell lines: a review," in A. Gomes, Ed., *Unraveling the Safety Profile of Nanoscale Particles and Materials*, InTech, Rijeka, Croatia, 2018.
- [10] A. M. Yassin, N. M. El-Deeb, A. M. Metwaly, G. F. El Fawal, M. M. Radwan, and E. E. Hafez, "Induction of apoptosis in human cancer cells through extrinsic and intrinsic pathways by *Balanites aegyptiaca* Furostanol saponins and saponin-coated silvernanoparticles," *Applied Biochemistry and Biotechnology*, vol. 182, no. 4, pp. 1675–1693, 2017.

- [11] S. Dehghanizade, J. Arasteh, and A. Mirzaie, "Green synthesis of silver nanoparticles using *Anthemis atropatana* extract: characterization and in vitro biological activities," *Artificial Cells, Nanomedicine, and Biotechnology*, vol. 46, no. 1, pp. 160–168, 2018.
- [12] P. P. Banerjee, A. Bandyopadhyay, S. N. Harsha et al., "*Mentha arvensis* (Linn.)-mediated green silver nanoparticles trigger caspase 9-dependent cell death in MCF7 and MDA-MB-231 cells," *Breast Cancer*, vol. 9, pp. 265–278, 2017.
- [13] Y.-J. Choi, J.-H. Park, J. W. Han et al., "Differential cytotoxic potential of silver nanoparticles in human ovarian cancer cells and ovarian cancer stem cells," *International Journal of Molecular Sciences*, vol. 17, no. 12, p. 2077, 2016.
- [14] J. Blanco, D. Lafuente, M. Gomez, T. Garcia, J. L. Domingo, and D. J. Sanchez, "Polyvinyl pyrrolidone-coated silver nanoparticles in a human lung cancer cells: time- and dose-dependent influence over p53 and caspase-3 protein expression and epigenetic effects," *Archives of Toxicology*, vol. 91, no. 2, pp. 651–666, 2017.
- [15] D. Kovács, N. Igaz, C. Keskeny et al., "Silver nanoparticles defeat p53-positive and p53-negative osteosarcoma cells by triggering mitochondrial stress and apoptosis," *Scientific Reports*, vol. 6, no. 1, article 27902, 2016.
- [16] M. Zuberek, D. Wojciechowska, D. Krzyzanowski, S. Meczynska-Wielgosz, M. Kruszewski, and A. Grzelak, "Glucose availability determines silver nanoparticles toxicity in HepG2," *Journal of Nanobiotechnology*, vol. 13, no. 1, p. 72, 2015.
- [17] C. Licciardello, N. D'Agostino, A. Traini, G. R. Recupero, L. Frusciante, and M. L. Chiusano, "Characterization of the glutathione S-transferase gene family through ESTs and expression analyses within common and pigmented cultivars of *Citrus sinensis* (L.) Osbeck," *BMC Plant Biology*, vol. 14, no. 1, p. 39, 2014.
- [18] D. Dabas, R. M. Shegog, G. R. Ziegler, and J. D. Lambert, "Avocado (*Persea americana*) seed as a source of bioactive phytochemicals," *Current Pharmaceutical Design*, vol. 19, no. 34, pp. 6133–6140, 2013.
- [19] M. Yasir, S. Das, and M. D. Kharya, "The phytochemical and pharmacological profile of *Persea americana* Mill," *Pharmacognosy Reviews*, vol. 4, no. 7, pp. 77–84, 2010.
- [20] D. Rodriguez-Sanchez, C. Silva-Platas, R. P. Rojo et al., "Activity-guided identification of acetogenins as novel lipophilic antioxidants present in avocado pulp (*Persea americana*)," *Journal of Chromatography B*, vol. 942–943, pp. 37–45, 2013.
- [21] A. Kosińska, M. Karamać, I. Estrella, T. Hernández, B. Bartolomé, and G. A. Dykes, "Phenolic compound profiles and antioxidant capacity of *Persea americana* mill. peels and seeds of two varieties," *Journal of Agricultural and Food Chemistry*, vol. 60, no. 18, pp. 4613–4619, 2012.
- [22] P. Anitha and P. Sakthivel, "Synthesis and characterization of silver nanoparticles using *Persea americana* (Avocado) and its anti-inflammatory effects on human blood cells," *International Journal of Pharmaceutical Sciences Review and Research*, vol. 35, no. 2, pp. 173–177, 2015.
- [23] S. P. Vinay, N. Chandrashekar, and C. P. Chandrappa, "Silver nanoparticles: synthesized by leaves extract of Avocado and their antibacterial activity," *International Journal of Engineering Development and Research*, vol. 5, no. 2, pp. 1608–1613, 2017.
- [24] J. León, *Botánica de los Cultivos Tropicales*, 2000.
- [25] M. S. Gachet, J. S. Lecaro, M. Kaiser et al., "Assessment of anti-protozoal activity of plants traditionally used in Ecuador in the treatment of leishmaniasis," *Journal of Ethnopharmacology*, vol. 128, no. 1, pp. 184–197, 2010.
- [26] M. M. Grandtner and J. Chevrette, *Dictionary of Trees: Nomenclature, Taxonomy and Ecology*, Elsevier Science, Vol. 2, Elsevier Science, New York, NY, USA, 2013.
- [27] A. Alva, O. Vásquez, R. Cuniberti, A. Castillo, and W. Guerra, "Extracción y Caracterización de Ácidos Grasos de la especie *Grias neuberthii* Macht (Sachamango)," *Revista Amazónica de Investigación Alimentaria*, vol. 2, no. 1, pp. 103–106, 2002.
- [28] P. Vásquez-Ocmín, S. Cojean, E. Rengifo et al., "Anti-protozoal activity of medicinal plants used by Iquitos-Nauta road communities in Loreto (Peru)," *Journal of Ethnopharmacology*, vol. 210, pp. 372–385, 2017.
- [29] S. Barua, P. P. Banerjee, A. Sadhu et al., "Silver nanoparticles as antibacterial and anticancer materials against human breast, cervical and oral cancer cells," *Journal of Nanoscience and Nanotechnology*, vol. 17, no. 2, pp. 968–976, 2017.
- [30] M. W. Pfaffl, "A new mathematical model for relative quantification in real-time RT-PCR," *Nucleic Acids Research*, vol. 29, no. 9, p. e45, 2001.
- [31] R. S. Kumaran, Y.-K. Choi, H. J. Kim, and K. J. Kim, "Quantitation of oxidative stress gene expression in MCF-7 human cell lines treated with water-dispersible CuO nanoparticles," *Applied Biochemistry and Biotechnology*, vol. 173, no. 3, pp. 731–740, 2014.
- [32] Y. C. Chew, G. Adhikary, G. M. Wilson, W. Xu, and R. L. Eckert, "Sulforaphane induction of p21(Cip1) cyclin-dependent kinase inhibitor expression requires p53 and Sp1 Transcription Factors and Is p53-dependent," *Journal of Biological Chemistry*, vol. 287, no. 20, pp. 16168–16178, 2012.
- [33] K. Andrea Kreß, *The Tax Protein of Human T Cell Lymphotropic Virus Type 1 as a Multifunctional Oncoprotein*, 2011.
- [34] Z. Lei, T. Liu, X. Li, X. Xu, and D. Fan, "Contribution of glutathione S-transferase gene polymorphisms to development of skin cancer," *International Journal of Clinical and Experimental Medicine*, vol. 8, no. 1, pp. 377–389, 2015.
- [35] T. Ozaki and A. Nakagawara, "Role of p53 in cell death and human cancers," *Cancers*, vol. 3, no. 1, pp. 994–1013, 2011.
- [36] R. A. Shamanna, M. Hoque, T. Pe'ery, and M. B. Mathews, "Induction of p53, p21 and apoptosis by silencing the NF90/NF45 complex in human papilloma virus-transformed cervical carcinoma cells," *Oncogene*, vol. 32, p. 5176, 2012.
- [37] K. Engeland, "Cell cycle arrest through indirect transcriptional repression by p53: I have a DREAM," *Cell Death and Differentiation*, vol. 25, no. 1, pp. 114–132, 2018.
- [38] S. Gurunathan, K.-J. Lee, K. Kalishwaralal, S. Sheikpranbabu, R. Vaidyanathan, and S. H. Eom, "Antiangiogenic properties of silver nanoparticles," *Biomaterials*, vol. 30, no. 31, pp. 6341–6350, 2009.
- [39] H. R. Kim, D. Y. Shin, Y. J. Park, C. W. Park, S. M. Oh, and K. H. Chung, "Silver nanoparticles induce p53-mediated apoptosis in human bronchial epithelial (BEAS-2B) cells," *Journal of Toxicological Sciences*, vol. 39, no. 3, pp. 401–412, 2014.
- [40] L. Sun, A. K. Singh, K. Vig, S. R. Pillai, and S. R. Singh, "Silver nanoparticles inhibit replication of respiratory syncytial virus," *Journal of Biomedical Nanotechnology*, vol. 4, no. 2, pp. 149–158, 2008.
- [41] D. Baram-Pinto, S. Shukla, N. Perkas, A. Gedanken, and R. Sarid, "Inhibition of herpes simplex virus type 1 infection by silver nanoparticles capped with mercaptoethane sulfonate," *Bioconjugate Chemistry*, vol. 20, no. 8, pp. 1497–1502, 2009.

- [42] P. V. Asharani, M. P. Hande, and S. Valiyaveetil, "Anti-proliferative activity of silver nanoparticles," *BMC Cell Biology*, vol. 10, p. 65, 2009.
- [43] M. Ahamed, M. S. AlSalhi, and M. K. J. Siddiqui, "Silver nanoparticle applications and human health," *Clinica Chimica Acta*, vol. 411, no. 23-24, pp. 1841-1848, 2010.
- [44] V. Kumar, N. Sharma, and S. S. Maitra, "In vitro and in vivo toxicity assessment of nanoparticles," *International Nano Letters*, vol. 7, no. 4, pp. 243-256, 2017.
- [45] D. B. Warheit, B. R. Laurence, K. L. Reed, D. H. Roach, G. A. M. Reynolds, and T. R. Webb, "Comparative pulmonary toxicity assessment of single-wall carbon nanotubes in rats," *Toxicological Sciences*, vol. 77, no. 1, pp. 117-125, 2004.
- [46] V. K. Sharma, K. M. Siskova, R. Zboril, and J. L. Gardea-Torresdey, "Organic-coated silver nanoparticles in biological and environmental conditions: fate, stability and toxicity," *Advances in Colloid and Interface Science*, vol. 204, pp. 15-34, 2014.
- [47] V. Williamson and S. Kumar, "Spectroscopy of organic compounds," *Department of Chemistry*, vol. 66, pp. 1-36, 2006.
- [48] E. Petryayeva and U. J. Krull, "Localized surface plasmon resonance: Nanostructures, bioassays and biosensing—a review," *Analytica Chimica Acta*, vol. 706, no. 1, pp. 8-24, 2011.
- [49] A. Mubayi, S. Chatterji, P. M. Rai, and G. Watal, "Evidence based green synthesis of nanoparticles," *Advanced Materials Letters*, vol. 3, no. 6, pp. 519-525, 2012.
- [50] A. Saxena, R. M. Tripathi, F. Zafar, and P. Singh, "Green synthesis of silver nanoparticles using aqueous solution of *Ficus benghalensis* leaf extract and characterization of their antibacterial activity," *Materials Letters*, vol. 67, no. 1, pp. 91-94, 2012.
- [51] A. N. Geraldes, A. A. da Silva, J. Leal et al., "Green nanotechnology from plant extracts: synthesis and characterization of gold nanoparticles," *Advanced in Nanoparticles*, vol. 5, no. 3, pp. 176-185, 2016.
- [52] I. Tasset, F. J. Medina, J. Peña et al., "Olfactory bulbectomy induced oxidative and cell damage in rat: protective effect of melatonin," *Physiological Research*, vol. 59, no. 1, pp. 105-112, 2010.
- [53] A. C. Sabuncu, J. Grubbs, S. Qian, T. M. Abdel-Fattah, M. W. Stacey, and A. Beskok, "Probing nanoparticle interactions in cell culture media," *Colloids and Surfaces B: Biointerfaces*, vol. 95, pp. 96-102, 2012.
- [54] S. Salatin and A. Yari Khosroushahi, "Overviews on the cellular uptake mechanism of polysaccharide colloidal nanoparticles," *Journal of Cellular and Molecular Medicine*, vol. 21, no. 9, pp. 1668-1686, 2017.
- [55] A. R. Gliga, S. Skoglund, I. O. Wallinder, B. Fadeel, and H. L. Karlsson, "Size-dependent cytotoxicity of silver nanoparticles in human lung cells: the role of cellular uptake, agglomeration and Ag release," *Particle and Fibre Toxicology*, vol. 11, no. 1, p. 11, 2014.
- [56] S. Park, S. J. Lee, H. Chung et al., "Cellular uptake pathway and drug release characteristics of drug-encapsulated glycol chitosan nanoparticles in live cells," *Microscopy Research and Technique*, vol. 73, no. 9, pp. 857-865, 2010.
- [57] Q. Liu and H. Jiang, "In vitro cytotoxicity of *Tanacetum vulgare* mediated silver nanoparticles against breast cancer (MCF-7) cell lines," *Biomedical Research*, vol. 28, no. 3, pp. 1354-1358, 2017.
- [58] N. E.-A. El-Naggar, M. H. Hussein, and A. A. El-Sawah, "Bio-fabrication of silver nanoparticles by phycocyanin, characterization, in vitro anticancer activity against breast cancer cell line and in vivo cytotoxicity," *Scientific Reports*, vol. 7, no. 1, article 10844, 2017.
- [59] S. Gurunathan, J. W. Han, A. A. Dayem et al., "Green synthesis of anisotropic silver nanoparticles and its potential cytotoxicity in human breast cancer cells (MCF-7)," *Journal of Industrial and Engineering Chemistry*, vol. 19, no. 5, pp. 1600-1605, 2013.
- [60] M. Milić, G. Leitinger, I. Pavičić et al., "Cellular uptake and toxicity effects of silver nanoparticles in mammalian kidney cells," *Journal of Applied Toxicology*, vol. 35, no. 6, pp. 581-592, 2014.
- [61] A. Nel, T. Xia, L. Mädler, and N. Li, "Toxic potential of materials at the nanolevel," *Science*, vol. 311, no. 5761, pp. 622-627, 2006.
- [62] A. Lankoff, W. J. Sandberg, A. Wegierek-Ciuk et al., "The effect of agglomeration state of silver and titanium dioxide nanoparticles on cellular response of HepG2, A549 and THP-1 cells," *Toxicology Letters*, vol. 208, no. 3, pp. 197-213, 2012.
- [63] I. Dobrzyńska, E. Skrzydlewska, and Z. A. Figaszewski, "Changes in electric properties of human breast cancer cells," *Journal of Membrane Biology*, vol. 246, no. 2, pp. 161-166, 2013.
- [64] E. A.K. Warren and C. K. Payne, "Cellular binding of nanoparticles disrupts the membrane potential," *RSC Advances*, vol. 5, no. 18, pp. 13660-13666, 2015.
- [65] X.-F. Zhang, W. Shen, and S. Gurunathan, "Silver nanoparticle-mediated cellular responses in various cell lines: an in vitro model," *International Journal of Molecular Sciences*, vol. 17, no. 10, p. 1603, 2016.
- [66] M. Wypij, J. Czarnecka, M. Swiecimska, H. Dahm, M. Rai, and P. Golinska, "Synthesis, characterization and evaluation of antimicrobial and cytotoxic activities of biogenic silver nanoparticles synthesized from *Streptomyces xinghaiensis* OF1 strain," *World Journal of Microbiology & Biotechnology*, vol. 34, no. 2, p. 23, 2018.
- [67] A. P. Kanjekar, A. L. Hugar, and R. L. Londonkar, "Characterization of phyto-nanoparticles from *Ficus krishnae* for their antibacterial and anticancer activities," *Drug Development and Industrial Pharmacy*, vol. 44, no. 3, pp. 377-384, 2018.
- [68] L. Qiu, J.-W. Li, C.-Y. Hong, and C.-Y. Pan, "Silver nanoparticles covered with pH-sensitive camptothecin-loaded polymer prodrugs: switchable fluorescence 'off' or 'on' and drug delivery dynamics in living cells," *ACS Applied Materials & Interfaces*, vol. 9, no. 46, pp. 40887-40897, 2017.
- [69] J. S. Park, E.-Y. Ahn, and Y. Park, "Asymmetric dumbbell-shaped silver nanoparticles and spherical gold nanoparticles green-synthesized by mangosteen (*Garcinia mangostana*) pericarp waste extracts," *International Journal of Nanomedicine*, vol. 12, pp. 6895-6908, 2017.
- [70] X.-F. Zhang and S. Gurunathan, "Combination of salinomycin and silver nanoparticles enhances apoptosis and autophagy in human ovarian cancer cells: an effective anticancer therapy," *International Journal of Nanomedicine*, vol. 11, pp. 3655-3675, 2016.
- [71] J. W. Han, S. Gurunathan, J.-K. Jeong et al., "Oxidative stress mediated cytotoxicity of biologically synthesized silver nanoparticles in human lung epithelial adenocarcinoma cell line," *Nanoscale Research Letters*, vol. 9, no. 1, p. 459, 2014.
- [72] D. B. Zorov, M. Juhaszova, and S. J. Sollott, "Mitochondrial reactive oxygen species (ROS) and ROS-induced ROS release," *Physiological Reviews*, vol. 94, no. 3, pp. 909-950, 2014.

- [73] T. Zhang, L. Wang, Q. Chen, and C. Chen, "Cytotoxic potential of silver nanoparticles," *Yonsei Medical Journal*, vol. 55, no. 2, pp. 283–291, 2014.
- [74] S. Saddick, M. Afifi, and O. A. A. Zinada, "Effect of Zinc nanoparticles on oxidative stress-related genes and antioxidant enzymes activity in the brain of *Oreochromis niloticus* and *Tilapia zillii*," *Saudi Journal of Biological Sciences*, vol. 24, no. 7, pp. 1672–1678, 2017.
- [75] T. Coccini, R. Gornati, F. Rossi et al., "Gene expression changes in rat liver and testes after lung instillation of a low dose of silver nanoparticles," *Journal of Nanomedicine & Nanotechnology*, vol. 5, no. 5, 2014.
- [76] P. M.G. Nair and J. Choi, "Identification, characterization and expression profiles of *Chironomus riparius* glutathione S-transferase (GST) genes in response to cadmium and silver nanoparticles exposure," *Aquatic Toxicology*, vol. 101, no. 3-4, pp. 550–560, 2011.
- [77] M. A. Owolabi, H. A B Coker, and S. Jaja, "Bioactivity of the phytoconstituents of the leaves of *Persea americana*," *Journal of Medicinal Plants Research*, vol. 4, no. 12, 2010.
- [78] D. Richard, K. Kefi, U. Barbe, P. Bausero, and F. Visioli, "Polyunsaturated fatty acids as antioxidants," *Pharmacological Research*, vol. 57, no. 6, pp. 451–455, 2008.
- [79] S. Aueviriyavit, D. Phummiratch, and R. Maniratanachote, "Mechanistic study on the biological effects of silver and gold nanoparticles in Caco-2 cells—induction of the Nrf2/HO-1 pathway by high concentrations of silver nanoparticles," *Toxicology Letters*, vol. 224, no. 1, pp. 73–83, 2014.
- [80] S. Park, H. H. Park, S. Y. Kim, S. J. Kim, K. Woo, and G. Ko, "Antiviral properties of silver nanoparticles on a magnetic hybrid colloid," *Applied and Environmental Microbiology*, vol. 80, no. 8, pp. 2343–2350, 2014.
- [81] S. R. Satapathy, P. Mohapatra, R. Preet et al., "Silver-based nanoparticles induce apoptosis in human colon cancer cells mediated through p53," *Nanomedicine*, vol. 8, no. 8, pp. 1307–1322, 2013.
- [82] W. Wang, C. Zeng, Y. Feng et al., "The size-dependent effects of silica nanoparticles on endothelial cell apoptosis through activating the p53-caspase pathway," *Environmental Pollution*, vol. 233, pp. 218–225, 2018.
- [83] P. V. Asharani, S. Sethu, H. K. Lim, G. Balaji, S. Valiyaveetil, and M. P. Hande, "Differential regulation of intracellular factors mediating cell cycle, DNA repair and inflammation following exposure to silver nanoparticles in human cells," *Genome Integrity*, vol. 3, no. 1, pp. 1–14, 2012.

Research Article

Biological Impact of Exposure to Extremely Fine-Grained Volcanic Ash

Cristina Aguilera,¹ Marco Viteri,¹ Rachid Seqqat ,^{1,2} Ligia Ayala Navarrette,¹ Theofilos Toulkeridis,¹ Ana Ruano,³ and Marbel Torres Arias ^{1,2}

¹Departamento de Ciencias de la Vida, Laboratorio de Inmunología y Virología, Universidad de las Fuerzas Armadas ESPE, Av. Gral. Rumiñahui s/n, P.O. Box 171-5-231B, Sangolquí, Ecuador

²Centro de Nanociencia y Nanotecnología, Universidad de las Fuerzas Armadas ESPE, Av. Gral. Rumiñahui s/n, P.O. Box 171-5-231B, Sangolquí, Ecuador

³National Institute of Public Health Research (INSPI), Quito, Ecuador

Correspondence should be addressed to Marbel Torres Arias; mmtorres@espe.edu.ec

Received 8 March 2018; Revised 17 May 2018; Accepted 10 June 2018; Published 16 July 2018

Academic Editor: Paresh Chandra Ray

Copyright © 2018 Cristina Aguilera et al. This is an open access article distributed under the Creative Commons Attribution License, which permits unrestricted use, distribution, and reproduction in any medium, provided the original work is properly cited.

At the northwestern edge of South America is located Ecuador. This place is a classical example of an active continental margin with widespread active volcanism. Detailed studies about the impact of volcanic ash on human health are still lacking. Therefore, the disease of exposed populations is unknown. The objective of the present investigation was to assess the biological impact of Pichincha volcanic ash on cell culture and inflammation in murine lung tissues that will contribute to the understanding of the hazards. In this study, the *in vivo* phase was performed in mice C57BL/6 exposed to several doses of volcanic ash (0.5, 1, and 3.75 mg/100 g mouse body weight). The body weight and survival were controlled during seven days of treatment. The expression of inflammation markers NRLP 3, caspase-1, pro-IL-1, IL-1 β , IL-6, IL-8, and h-HPRT was analyzed. The *in vitro* phase was performed in lung cancer cells A549, peritoneal macrophages, and McCoy cells exposing them to different concentrations of volcanic ash (80, 320, and 1280 $\mu\text{g}/\text{cm}^3$) to determine the cytotoxicity and the production of reactive oxygen species. The ash initiated activation of the inflammasome complex NRLP 3 and the initiation of a proinflammatory activity in the murine lung tissue depending on the concentration of this agent. The viability of A549 and McCoy cell decreased with the length of exposure and increased with the concentration of volcanic ash. The activity in superoxide dismutase decreased by about 60%, leading to the formation of reactive oxygen species. These results associated with compounds contained in Pichincha volcanic ash are considered hazardous elements which induce inflammation leading to activate inflammasome NRLP, releasing reactive oxygen species, and producing changes in cell morphology and density, all of which are expression of cytotoxicity.

1. Introduction

The Pichincha volcanic complex (PVC) is located on the Western Cordillera of the Ecuadorian Andes, some 11 km west of the city of Quito. This PVC consists of five successive volcanoes inside of two major volcanic edifices, named Rucu Pichincha and the younger Guagua Pichincha, which have been active since approximately 1.1 Ma ago [1]. The youngest lava dome complex within the Guagua Pichincha volcanic edifice has been active since the Early Holocene, evidenced by a series of eruptive phases within the last 3,000 years,

where domes have been formed and collapsed, while eruptions have been from phreatic, vulcanian, and subplinian up to plinian [2]. Ash emissions have been witnessed on various occasions, especially during the volcanic crisis of 1998–2001, when four strong and independent events (on the 05th and 7th of October, 26th of November, and 10th of December of 1999) covered the city of Quito with a mantle of very fine-grained, nanosized, fractured ash particles [2].

As any eruption of a volcano emits ash and gases that contain particulate material of different sizes from nanoscale to microns, the amount released from these particles has

been able to reach 30×10^6 tons of pyroclastic material represented by ash [3]. Volcanic ash of Guagua Pichincha is a thin material (<2 mm in diameter), and the main products found are dacitic, andesitic, and high-Rb acid [4] including sulfur dioxide, silicon oxide (SiO_2), and aluminum oxide (Al_2O_3) [5]. Moreover, volcanic activity is a natural source of respirable nanoparticles. The formation of crystals in volcanic ash is due to the abundance of short-range minerals among the main nanoscale materials, including imogolite (tubular nanotubes), allophane (nanospheres), ferrihydrite, and iron-humic complexes [6].

Previous studies indicated that both particle size and the percentage of crystalline-free silica play a crucial part in the development of respiratory diseases such as silicosis and tuberculosis. *In vivo* studies have shown that cristobalite present fibrogenicity and may cause silicosis and cancer [7]. Silicosis is caused by the inhalation of crystalline silica particles for extended periods of time. Silica presents different crystalline forms which vary in levels of fibrogenicity according to the degree of crystallization but not with crystalline silica concentration [8, 9]. Fibrogenicity increases from the less organized crystal structure to the more organized crystal structures of cristobalite [8]. The inhalation of silica can also lead to the development of bronchogenic carcinoma [10].

A recent study indicated an association between chronic exposure to volcanically active environments and the occurrence of DNA damage in human buccal epithelial cells, revealing that noneruptive active volcanism is a risk factor of carcinogenesis [11]. In a further study, when mice have been exposed to volcanogenic air pollution, alveolar space, alveolar perimeter, and lung structural functionality ratio decreased, while their alveolar septal thickness increased [12].

Additionally, the ash is markedly hemolytic, exhibiting an activity like chrysotile asbestos, a known fibrogenic agent. The results of these studies have been taken in conjunction with the results of animal studies indicating a fibrogenic potential of volcanic ash in heavily exposed humans [9]. However, a variety of studies suggest that the volcanic ash may pose a risk for pneumoconiosis in heavily exposed human populations [9].

Furthermore, cristobalite may cause inflammation in the lung and granuloma in the hilar lymph nodes of rats associated with significant size augmentation at 13 weeks postinstillation, while the same mineral induced fibrosis in the lung at 49 weeks postexposure [13]. Besides, ash respirable fractions have been used to investigate the *in vitro* response of THP-1 and A549 cells in cytotoxicity, cellular stress, and proinflammatory assays associated with toxicity. Macrophages experienced minimal ash-induced cytotoxicity and intracellular reduction of glutathione. However, production of IL- 1β , IL-6, and IL-8 has been sample dependent. Lung epithelial cells experienced moderate apoptosis, sample-dependent reduction of glutathione, and minimal cytokine production [14].

On the contrary, exposure to SiO_2 nanoparticles results in dose-dependent cytotoxicity in cultural human bronchoalveolar carcinoma-derived cells which is closely correlated to increased oxidative stress [15]. Crystallization

plays a role in fibrogenicity, and the large surface area per mass of silica nanoparticles allows for a greater production of reactive oxygen species [10]. The fine-grained character of volcanic ash generated in the long-lived eruption raises the issue of its possible health hazards. Surface- and free-radical production has been closely linked to bioreactivity of dusts within the lung. Concentrations of hydroxyl radicals (HO) in respirable ash are two to three times higher than a toxic quartz standard [16]. One investigation indicated that *in vitro* exposure to volcanic ash had little effect on the O_2 consumption of rabbit type II cells [17]. The toxic effect has been discovered after both *in vitro* and *in vivo* exposure and has not been due to a soluble component of the ash. This implies that inhalation of volcanic ash may adversely affect alveolar macrophages. Therefore, inhibition of superoxide release by volcanic ash may interfere with the ability of alveolar macrophages to protect the lung from some types of respiratory infections [17].

In Ecuador, published data on the effects on human health in the face of the exposure of volcanic ash are rare. Therefore, the main aim of this study was to assess the biological impact of the Pichincha volcanic ash, which certainly will be able to contribute significantly to the understanding of the hazards on cell cultures and inflammation in murine lung tissues. Such data will allow an extrapolation towards the affected populations during exposure to this agent.

2. Materials and Methods

2.1. Volcanic Ash Sample. Volcanic ash sample was collected from one of the two strongest eruptions of the PVC of the last 300 years on the 5th of October 1999. The health hazards of this eruption was previously documented [18], while the physical and chemical analyses of the sample used here have been analyzed in the same detailed way as other volcanic ashes of Ecuador [19–22]. In these studies, the volcanic ash has been dried, sedimented, and stored in undisturbed containers at a temperature of 18°C until being processed.

2.2. Sample Preparation. The dry volcanic ash samples were suspended in the appropriate cell-line media and sonicated with heating (37°C) for one hour to disaggregate the particles.

2.3. Animals Experiment. C57BL/6 mice from 12 to 14 weeks of age were obtained from the National Institute of Public Health Research (INSPI), where they have been housed in an environmentally controlled room (temperature: $22 \pm 3^\circ\text{C}$, relative humidity: $30 \pm 10\%$, programmed ventilation, and 12:12 h light-dark cycle). The volcanic ash was weighed, sonicated, and diluted in PBS for the administration of the mice, in such way that the applied concentrations were 0.5, 1, and 3.75 mg/100 g of corporal weight. These concentrations of volcanic ash were taken from related studies [23]. The control group administered PBS.

A total of thirty mice were treated to which intraperitoneal anesthesia was applied with Dormi-Xyl® 2

TABLE 1: Designed primers for inflammation study.

Protein	Primer forward and reverse	Product length
NLRP3	Forward: TCTGCACCCGGACTGTAAAC Reverse: TTCCGAAGGCTGTGGTTGTG	111
Caspase-1	Forward: GGAGATGGTGAAGAGAGGTGAA Reverse: GGTGTTGAAGAGCAGAAAGCA	375
Pro-IL-1	Forward: GTCGGGAGGAGACGACTCTAA Reverse: GCAACTCCTTCAGCAACACG	107
IL-8	Forward: GGCAAACGAAAATGTGGATGGG Reverse: TCAGAACGTGGCGGTATCTCT	125
IL-1 β	Forward: ACAACAAAAAGCCTCGTGCTGTC Reverse: ACAGGTATTTTGTGCGTTGCTTGG	135
IL-6	Forward: TCACAGAAGGAGTGGCTAAGGA Reverse: AGTGAGGAATGTCCACAACTGA	141
h-HPRT	Forward: TCAGTCAACGGGGGACATAAAAG Reverse: GCTTAACCAGGGAAAGCAAAG	131

(Agrovet Market Animal Health-30 mL); 0.15 mL/kg of mouse and a single dose via transtracheal of 100 μ L of the ash diluted in PBS was administered and 100 μ L PBS for the control group. On day 7, after exposure to volcanic ash, the mice were euthanized by cervical dislocation, and then each mouse was excised, the lungs were weighed, and stored at -80°C for RNA extraction from the protocol suggested by Chomzynski and Sacchi [24]. The positive control group was injected by a single dose of lipopolysaccharide (LPS, from *E. coli* at L2630-25MG).

2.3.1. Cytokine Release. The inflammatory response has been studied by cytokines released from the murine lungs exposed to volcanic ash via real-time PCR (CFX96 real-time system, Bio-Rad) according to the manufacturer's protocol. The applied analysis method for the results is the double delta C_t ($\Delta\Delta C_t$). The endogenous gene selected was h-HPRT. The primers used in the amplification of the genetic expression were designed through the online program primer 3 (<http://bioinfo.ut.ee/primer3-0.4.0/>) based on sequences published on NCBI (National Center for Biotechnology Information) Table 1.

2.4. Cell Culture Experiment. McCoy, mice fibroblast cell line, and A549 a human adenocarcinoma-derived type II alveolar epithelial cell line were maintained in continuous culture in EMEM growth media and Ham's F-12K (Kaighn's) growth media, respectively, with 10% of FBS and supplemented with penicillin (100 units·mL⁻¹) and streptomycin (100 mg·mL⁻¹). To prepare cells for particle treatment, cells were trypsinized using a 0.25% Tris-EDTA solution and allowed to readhere overnight. Treatments were performed on 100 μ L of cells at a density of 1×10^5 cells·mL⁻¹ in each well of a 96-well plate. Both cell lines were maintained at 37°C , in a 5% CO₂ environment.

Murine peritoneal macrophages were collected in the RPMI medium from the peritoneal cavity. *In vitro* adhesion of macrophages was maintained in continuous culture in RPMI growth media with 10% of FBS supplemented with

penicillin (100 units·mL⁻¹) and streptomycin (100 mg·mL⁻¹). Treatment was performed on 1 mL of cells at a density of 5×10^5 cells·mL⁻¹ in each well of a 24-well plate, while cells were maintained at 37°C in a 5% CO₂ environment.

Cells were treated for 24 h with five concentrations of volcanic ash and control particles: 80, 160, 320, 640, and 1280 $\mu\text{g}\cdot\text{mL}^{-1}$, and positive control oxide of titanium TiO₂ (400 $\mu\text{g}\cdot\text{mL}^{-1}$) reported elsewhere [25]. Oxidative stress was assessed by releasing NO (nitrogen oxide) using the Griess test and superoxide dismutase assay to evaluate anion superoxide.

2.4.1. Cytotoxicity Test. Volcanic ash at the final mineral concentrations of 80, 320, and 1280 $\mu\text{g}/\text{cm}^3$ was added to McCoy and A549 monolayer cells cultures. MTT assay was performed at 72, 120, 168, and 240 hours after volcanic ash particles application. For this purpose, MTT solution was prepared at 1 mg/ml in 100% acetone. Then, 10 μ L of MTT plus 100 μ L of cell-line media was added to each well. Cells were incubated for 4 hours at 37°C with 5% CO₂. After 4 hours, the MTT solution was removed and replaced with 100 μ L of DMSO. The plate was further incubated for 3 min at room temperature, and the optical density (OD) of the wells has been determined using a plate reader (Thermo Fisher) at a test wavelength of 570 nm.

Titanium oxide was used as a positive control, and its toxicity is well established in reported studies [7, 25–29].

2.4.2. Reactive Oxygen Species (ROS)

(1) Griess Test. The extent of cellular stress was determined by the Griess test, which was used to determine the quantity of nitrite oxide (NO) released in the cell supernatants. Treatment was performed on 1 mL of McCoy and A549 cells at a density of 2.5×10^5 cells·mL⁻¹ in each well of a 24-well plate and 1 mL of murine peritoneal macrophages at a density of 5×10^5 cells·mL⁻¹ in each well of a 24-well plate. Cells were maintained at 37°C in a 5% CO₂ environment.

Volcanic ash at the final mineral concentrations of 80, 320, and 1280 $\mu\text{g}/\text{cm}^3$ was added to McCoy, A549 monolayer

cells cultures, and macrophages. After 24 and 144 hours with volcanic ash particles, the supernatant of each well was collected. Murine peritoneal macrophages were exposed only 24 hours. The Griess assay was performed with sulfanilamide solution and *N*-1-naphthylethylenediamine dihydrochloride (NED) solution at 1:1 dilution. Then, 100 μ l of this dilution plus 100 μ l of cell supernatant was added to each well of a 96-well plate. The microplate was incubated for 30 minutes in the dark at room temperature, and the optical density of the wells was determined using a plate reader at a test wavelength of 540 nm.

The titanium oxide (TiO₂) at a final concentration of 400 μ g/cm³ and hydrogen peroxide (3%) were used as positive controls.

(2) *SOD Activity*. Treatment was performed on 1 mL of McCoy and A549 cells each one at a density of 2.5×10^5 cells·mL⁻¹ in each well of a 24-well plate and 1 mL of murine peritoneal macrophages at a density of 5×10^5 cells·mL⁻¹ in each well of a 24-well plate. Cells were maintained at 37°C in a 5% CO₂ environment.

Volcanic ash at the final mineral concentrations of 80, 320, and 1280 μ g/cm³ was added to McCoy and A549 monolayer cells cultures individually. Macrophages were exposed to concentrations of 80, 160, 320, 640, and 1280 μ g/mL of volcanic ash. After 24 and 144 hours, the supernatant was collected from each well. Murine peritoneal macrophages were exposed only 24 hours. The superoxide dismutase (SOD) activity was assessed in the fresh supernatant of the cell cultures with a SOD determination kit (Sigma-Aldrich). The microplate was incubated at 37°C for 20 minutes, and the absorbance read at 450 nm.

The SOD activity was calculated as follows:

SOD activity (inhibition rate %)

$$= \left\{ \frac{[(A_{\text{blank}} - A_{\text{blank3}}) - (A_{\text{sample}} - A_{\text{blank2}})]}{(A_{\text{blank1}} - A_{\text{blank3}})} \right\} * 100. \quad (1)$$

The negative control was the culture cells without any exposition. The titanium oxide (TiO₂) at a final concentration of 400 μ g/mL and hydrogen peroxide (3%) were used as positive controls.

2.5. Statistical Analysis. Statistical analysis has been performed using GraphPad PRISM 6 software (San Diego, CA). The comparisons were conducted using Student's *t*-test and one-way analysis of variance (ANOVA) with the Dunnett and Sidak posttest where appropriate.

3. Results and Discussion

3.1. Volcanic Ash Characterization. The photographs taken with SEM indicate the presence of pumice rock (central rounded particle) as result of a very violent magmatic explosion, surrounded by fragmented volcanic glass and some minor minerals such as quartz and plagioclase (Figure 1(a)).

Moreover, Figure 1(b) is a typical angular-shaped plagioclase (big grain), as well as quartz (above grain) and surrounding fresh (un-reworked) volcanic glass. Figure 1(c) illustrates the diameter particle histogram obtained from the analysis of the sample, using the MIRA3 SEM software. We have calculated the size distribution of the particles from manual diameter determination over a 1000 particles.

Table 2 represents the chemical compositions by energy dispersive spectroscopy (EDS) performed on some one hundred ash particles revealed on average typical geochemical ratios known of andesites and dacites of the region with Al/Mg of 9.85, Si/Mg of 24.97, and Na/Al ratios of about 0.29, with a sigma mean error between 0.26 and 0.97, pending of the particular element.

3.2. Effect of Volcanic Ash on Mice Body Weight and Survival.

Mice were once inoculated via transtracheal with a 100 μ L solution of volcanic ash and PBS at a final mineral concentration of 0.5 mg, 1 mg, and 3.75 mg per 100 g of body weight. Body weight has been recorded on day seven postinfection. Mice exposed to a concentration of volcanic ash of 3.75 mg indicate a constant and significant weight loss on day 7. Mice infected with 0.5 and 1 mg of volcanic ash gained weight as did in the uninfected group postinfection (Figure 2(a)). Likewise, during the exposure of the animals to the volcanic ash, the weight of the food that each group of mice consumed was recorded, demonstrating a reduction in the quantity of food consumed by the animal treated with volcanic ash.

Seven days after infection, all animals exposed to volcanic ash did not entirely die. In contrast, all animals not infected or infected with LPS survived for a 7-day period. Nevertheless, the groups that received the highest concentrations of ash 1 and 3.75 mg perished by 25% (Figure 2(b)).

The volcanic ash concentrations could overt toxicity as indicated by a change in body weight from animals exposed to 3.75 mg, which has often been an indicator of overt or systemic toxicity [30]. In the current study, we observed 25% of mouse mortality in the groups which have been exposed to highest concentrations of volcanic ash 1 and 3.75 mg (Figure 2(b)). The statistical reduction of body weights in the exposed group of 3.75 mg of volcanic ash indicated a level of malaise, which indicates that volcanic ash may interfere in the welfare and homeostasis of the murine organism [31].

3.3. Volcanic Ash Induce Expression of Inflammatory Factors in Mice Lung.

Volcanic eruptions increase concern about the potential adverse effects of volcanic ash in the lung [32]. The results from studies in laboratories suggest that volcanic ash is moderately toxic and has the potential to cause fibrosis in the lung of rodents when inhaled in high doses [33].

The term inflammasome is used to define the activation of caspase-1 characteristic of innate immunity and represents the response directed to suppress pathogenic microorganisms and to avoid tissue damage [34]. It is composed of the receptor with oligomerization domain and nucleotide binding (NLR3), ASC (apoptosis-associated speck-like) protein, and caspase-1. NLRP 3 inflammasome is the only

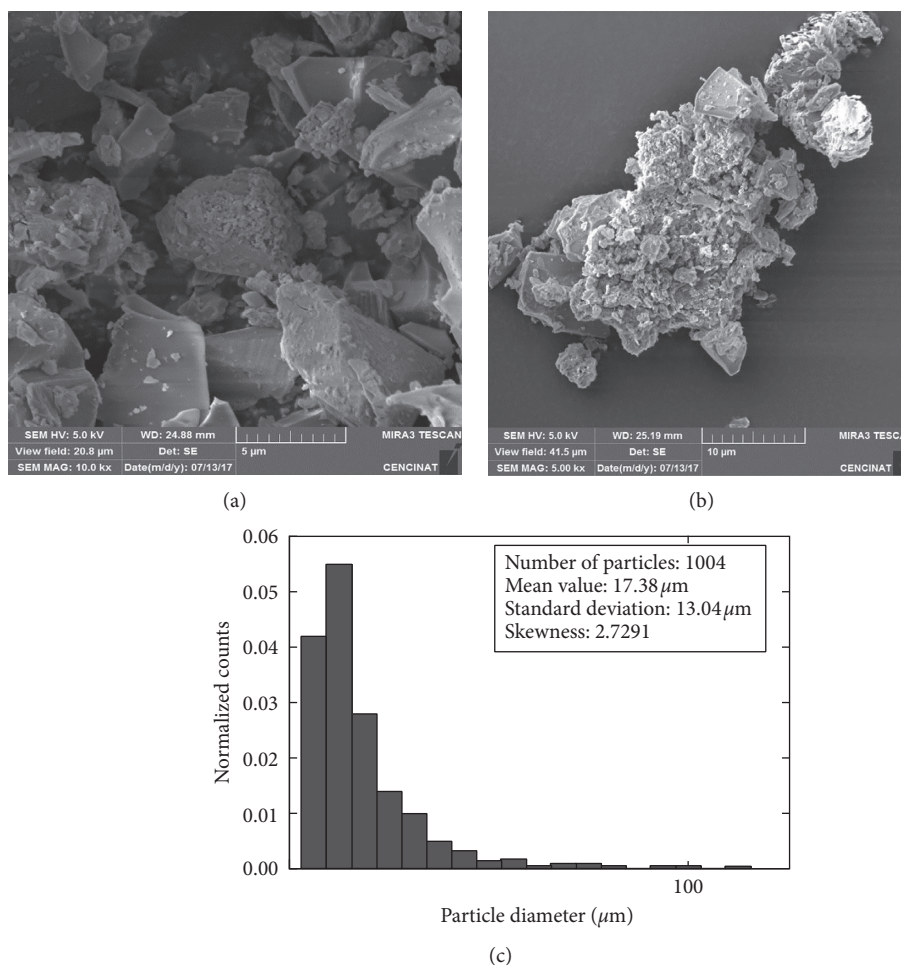


FIGURE 1: Representative SEM image of Pichincha's volcanic ash: (a) at 10000x magnifications; (b) at 5000 magnifications. The images illustrate angular- and round-shaped particles. (c) Granulometry of fine-grained volcanic ash of the 5th of October 1999 eruption of the PVC, using the MIRA3 SEM software based on 1004 particles.

TABLE 2: Chemical composition expressed as mass percent of major elements of 100 ash particles from the ash samples of the 5th of October 1999 eruption of the PVC (see Table S1 for details).

Element	Na	Mg	Al	Si	P	S	K	Ca	Ti	Mn	Fe
Mean value	5.07	1.76	17.29	43.83	1.52	2.42	5.11	10.02	2.34	0.16	10.49
Sigma	2.60	3.08	4.95	9.67	1.26	4.48	2.63	5.72	7.62	0.16	10.65
Sigma mean	0.26	0.31	0.49	0.97	0.13	0.45	0.26	0.57	0.76	0.02	1.06

one activated by several stimuli like molecule effectors produced or released by the mitochondria such as reactive mitochondrial oxygen species, mitochondrial DNA, and cardiolipin phospholipid [35]. The NLRP3 inflammasome is a signaling complex that activates procaspase-1 and induces the processing of caspase-1-dependent inflammatory cytokines (particularly IL-1 and IL-18) [36]. This inflammasome has been found in cells of the innate immune system such as macrophages and dendritic cells and has been able to be activated in response to a variety of intrinsic factors of the host, as well as a significant number of environmental substances such as silica, asbestos, and hydroxide adjuvant of aluminum [37]. Mice exposed to 0.5, 1, and 3.75 mg of Pichincha's ash produced more NLRP3 than the untreated control (Figure 3(a)).

The mechanisms of activation of caspase-1 that triggers different types of inflammasomes are diverse and leads to the induction and secretion of IL-1 β , generating inflammation and cell death of the proptosis type [38]. Caspases are proteins with cysteine-protease activity, which hydrolyzes in specific aspartate residues, and some of them are involved in inflammatory processes such as caspases 1, 2, 5, and 12 [39]. The inflammatory response in murine pulmonary tissue has been sampled and was determined to be cytokine dependent. The highest dose (3.75 mg) of volcanic ash resulted in the production of caspase-1 above threefold in the untreated control (Figure 3(b)), as observed by Lee et al. [40] where the mechanism that governs the expression of caspase-1 is determined and indicates the

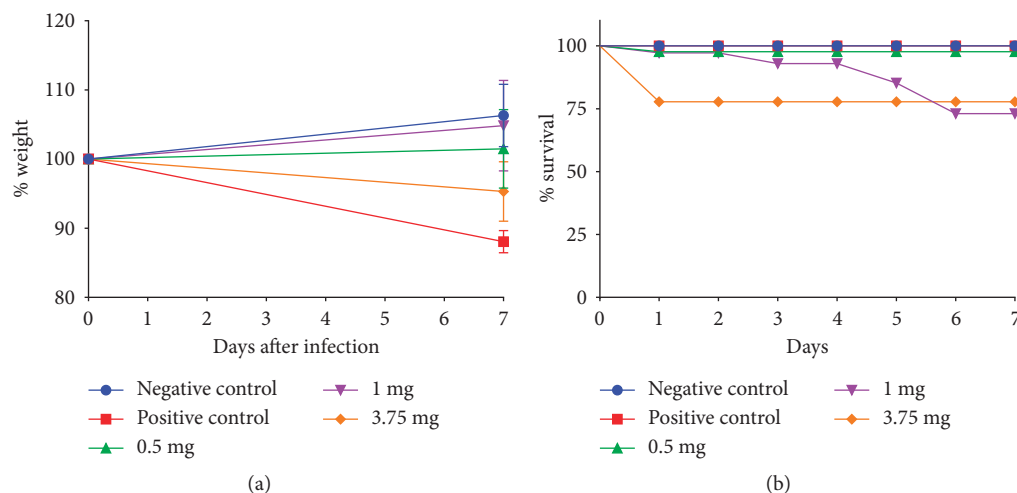


FIGURE 2: Graph of weight change and survival in infected mice: (a) graphic representation of the body weight (g) of C57BL/6 mice after 7 days postinfection with volcanic ash at concentrations of 0.5 mg (green), 1 mg (purple), and 3.75 mg (orange); negative control (PBS, blue); and positive control (LPS, red). (b) Five groups of mice were uninfected (blue) and infected with volcanic ash at concentrations of 0.5 mg (green), 1 mg (purple), and 3.75 mg (orange) of volcanic ash or intraperitoneally infected with LPS (red), and survival were monitored daily for seven days. All data points for mice not infected or infected with LPS are in the same horizontal line.

hypothesis that the simple increase in caspase-1 levels is sufficient to induce inflammation.

Cytokine pro-IL-1 is produced by macrophages and monocytes as well as nonimmunological cells, such as fibroblasts and activated endothelial cells during cell injury, infection, invasion, and inflammation. IL-1 β is synthesized as a precursor protein (pro-IL-1 β), which is not secreted in the active form until it is metabolized by the enzyme caspase-1 [35]. Levels for the highest dose (3.75 and 1 mg) of volcanic ash have been greater than that induced by the inflammation produced by lipopolysaccharide (LPS) in pro-IL-1 released.

IL-1 is a key cytokine in diverse responses of the immune system, and once it is secreted, it participates in the generation of local and systemic immune response against diverse classes of pathogens, and its implication in the pathophysiology of diverse inflammatory diseases highlights its role in the evolution of an inflammatory process [41]. Mice injected with lipopolysaccharide (LPS) present an expression >10 times more than the negative control. Although exposed groups to volcanic ash lack significant expression, the release of IL-1 β is greater and concentration dependent.

IL-6 is a proinflammatory cytokine that generates the maturity and activation of neutrophils, the maturation of macrophages, and the differentiation/maintenance of cytotoxic T lymphocytes and natural killer cells [35]. To identify an inflammatory response induced by the ash of PVC, the gene expression of the proinflammatory cytokine (IL-6) was measured in the murine lung tissues after treatment (Figure 3(e)). The secretion of the proinflammatory cytokine (IL-6) increased in a dose-dependent manner of volcanic ash as reported in the study of Park et al. [23].

Interleukin-8 (IL-8) has been identified as a chemotactic and leukocyte activating factor produced by activated tissue cells, as well as monocytes/macrophages. IL-1 β or IL-12 causes the production and release of IL-8 from neutrophils

in the presence of LPS [42]. In a study reported earlier [43], the amounts of protein in IL-1b or IL-12 have been correlated with the amounts of chemokine or with the number of neutrophils, suggesting that the increase in IL-12 and IL-1 β leads to the increase in chemokine followed by neutrophilic inflammation. Figure 3(f) demonstrates that the volcanic ash at high concentrations (1 and 3.75 mg) induce a significant increase of the inflammatory marker IL-8 over the control.

3.4. Cell Morphology Modification after Volcanic Ash Exposition. The changes in cellular morphology have been considered as a direct indicator of cytotoxicity [16]. This is directly reflected in cell viability, cell mechanisms, and cellular morphology [44]. We examined the morphology of A549 and McCoy cells exposed to different ash particle concentrations for 72 hours by optical microscopy. Cell proliferation is significantly reduced, and morphology shows irregular shape when increasing the ash concentrations (Figure 4). Duan et al. [44] observed that SiO₂ produces irregular shape in epithelial cells and density reduction at 24 hours of exposition which is directly reflecting cell injuries. These data indicate the big capacity of silica to be levels of mutagenicity which could contribute too many chronic pulmonary diseases. The deposition of nanoparticles in the lung could lead to chronic inflammation, epithelial injury, and pulmonary fibrosis [45].

A marked vacuolization and ash particles adhered or internalization in the cytoplasm have been observed after the ash treatment of peritoneal macrophages (Figure 5) in A549 cells and McCoy cells with 320 $\mu\text{g}/\text{cm}^3$ for 24 hours. Voicu et al. [46] observed a vacuolization in human lung fibroblast exposed to SiO₂ nanoparticles (NPs) after 24 hours exposure. Moreover, Duan et al. [44] observed in TEM that silica NPs have been internalized into endothelial cells after 24

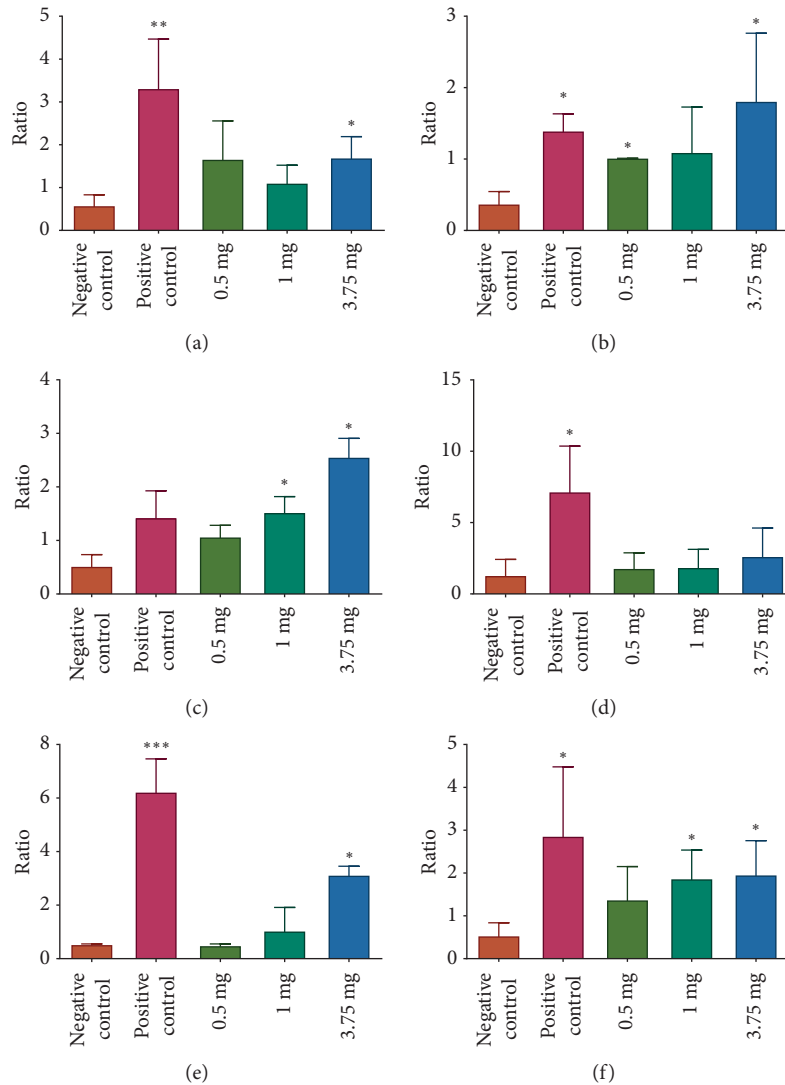


FIGURE 3: Cytokine production by C57BL/6 mice exposed to Pichincha's volcanic ash: production of the inflammatory markers (a) NLRP 3, (b) caspase I, (c) pro-IL-1, (d) IL-1 β , (e) IL-6, and (f) IL-8 at 7 days after treatment with 0.5, 1, and 3.75 mg/100 g body weights. * $p < 0.05$, ** $p < 0.01$, and *** $p < 0.001$ (Student's t -test).

hours. Additionally, previous study confirmed that the silica nanoparticles may be internalized into the cells and dispersed in the cytoplasm and inside the mitochondria [47]. In rat alveolar epithelial cells exposed to volcanic ash in culture, Monick et al. [48] observed with SEM and TEM ash particles on the cell surface, while in human alveolar macrophages exposed to volcanic ash, ash particles adhered to the surface or were internalized by alveolar macrophages and vesicles within the cell at cytosol.

3.5. Volcanic Ash Induce Cell Cytotoxicity In Vitro. The MTT assay which provides an indication of mitochondrial activity and cell viability [49] indicates the volcanic ash cytotoxicity. A549 and McCoy cells demonstrated a significant reduction in cell viability in response to the duration of exposure and volcanic ash concentration (Figure 6). In both cases, cells presented a decrease in viability at a concentration

of 320 and 1280 $\mu\text{g}/\text{cm}^3$ to 72 hours from 240 hours. The same occurred with the positive control, titanium oxide (Figures 6(a) and 6(b)). These data are comparable with another study where A549 cells were exposed for 24 hours to three different respirable ash particles and titanium oxide from Soufrière Hills [9]. As well, Lin et al. [15] demonstrated that SiO₂ reduces A549 cellular viability in a dose- and time-dependent manner. On the contrary, human lung fibroblasts have been exposed to different concentrations of SiO₂ NPs which demonstrated a decrease in a time- and dose-dependent manner [46].

3.6. Volcanic Ash Effect on the Reactive Oxygen Species Production in the Cells

3.6.1. Nitric Oxide. Nitric oxide synthase (NOS) is the enzyme responsible for generation of nitric oxide (NO), a fundamental mediator molecule produced by a variety of

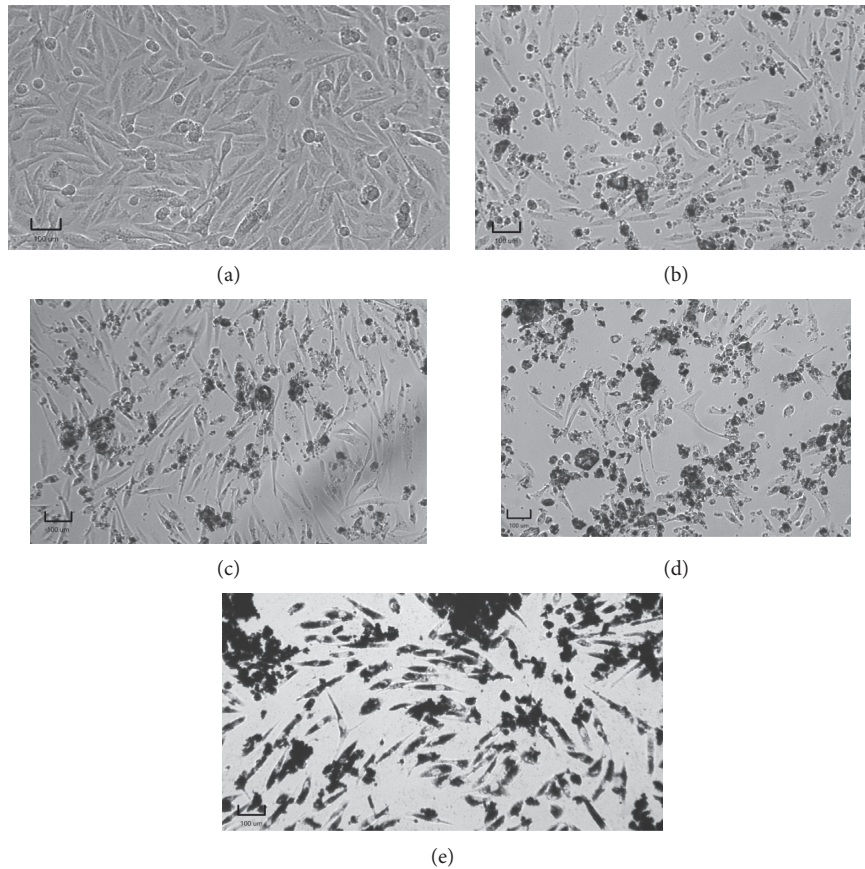


FIGURE 4: Morphology of A549 cells with different ash concentrations: (a) cells; (b) cells with $80 \mu\text{g}/\text{cm}^3$; (c) cells with $320 \mu\text{g}/\text{cm}^3$; (d) cells with $1280 \mu\text{g}/\text{cm}^3$; (e) cells with titanium oxide (TiO_2 , positive control). Images are representative of all samples. Scale: $100 \mu\text{m}$.

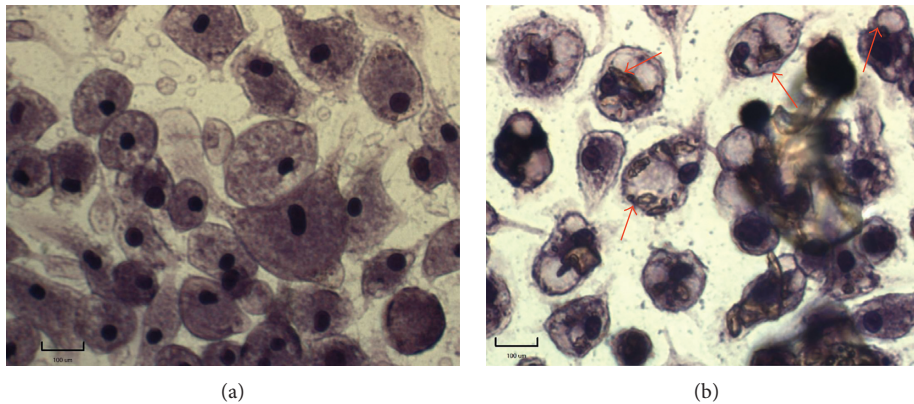


FIGURE 5: Uptake of ash and vacuolization by peritoneal macrophages: (a) untreated cells and (b) cells treated with $320 \mu\text{g}/\text{cm}^3$ and view of cells with internalized and vacuolization of ash particles (arrows). Images are representative of all samples. Staining: hematoxylin and eosin. Scale: $100 \mu\text{m}$.

diverse cell types. Three distinct NOS enzymes have been identified, being the neuronal form (nNOS), the endothelial (eNOS), and the macrophage forms (iNOS). The brain and endothelial forms are constitutive products, while macrophage NOS is present after induction by endotoxins. However, inducible NOS is also upregulated in various types of inflammatory disease, and the NO generated by the enzyme mediates various symptoms of inflammation [50, 51].

A549, McCoy cells, and peritoneal macrophages have been treated with concentrations of 80, 320, and $1280 \mu\text{g}/\text{cm}^3$ of volcanic ash for 24 hours. The absorbance of nitric oxide in the spent medium has been determined using the Griess test. The results yielded in peritoneal macrophages an increase in NO absorbance with different ash concentrations, with a statistically significant increase at the ash concentration $320 \mu\text{g}/\text{cm}^3$ compared to cells without any

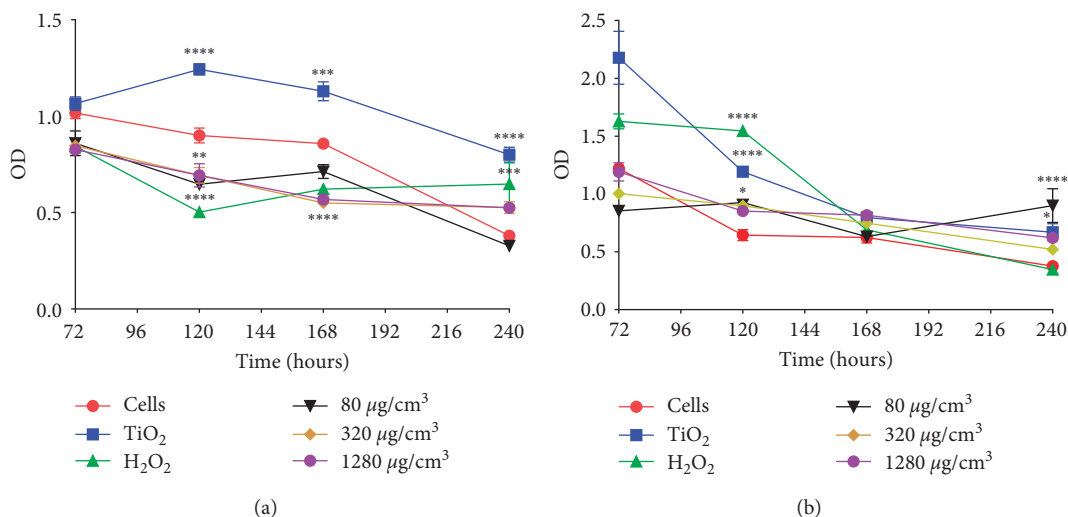


FIGURE 6: Cell viability, as assessed by MTT assay, of Pichincha volcanic ash in (a) A549 and (b) McCoy cells with ash treatments after 72, 120, 168, and 240 hours. The monolayer cell cultures were exposed to 80 µg/cm³ (black), 320 µg/cm³ (yellow), and 1280 µg/cm³ (purple) of volcanic ash and 400 µg/cm³ titanium dioxide (blue). The negative control (red) was cell without any treatment. * $p < 0.05$; ** $p < 0.01$ (two-way ANOVA with Dunnett's posttest).

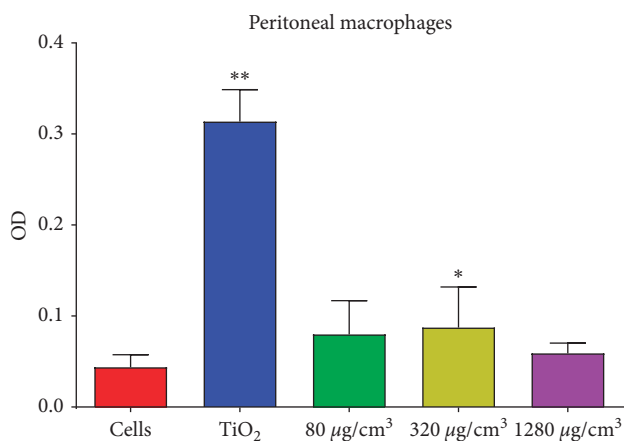


FIGURE 7: Nitric oxide production on peritoneal macrophages by volcanic ash after 24 hours. Macrophages were exposed to 80 µg/cm³ (green), 320 µg/cm³ (yellow), and 1280 µg/cm³ (purple) of volcanic ash and 400 µg/cm³ of titanium dioxide (blue). The negative control was cells without any treatment (red). * $p < 0.05$; ** $p < 0.01$ (one-way ANOVA with Dunnett's posttest).

treatment (Figure 7). The lack of the dose response effect can be justified by the fact that NO which is normally produced after activation of the macrophage by pathogens, in the case of volcanic ash, the cellular mechanism of activation in macrophages is unknown. However, titanium oxide induced significantly nitric oxide production in macrophages. The study from Kobzik et al. [50] reported a strong inducible NO in rat macrophages after the exposition of LPS by immunostaining, while the control macrophages have been negative. Nonetheless, A549 and McCoy cells did not present statistical difference in NO absorbance. This can be explained by the fact that NO is a constitutive product. Besides, a fundamental mode of inactivation of NO is its reaction with superoxide anion (O_2^-) to form the potent

oxidant peroxynitrite ($ONOO^-$) [52]. However, results from the hepatocellular carcinoma cell line indicate that the silica NPs may lead to increased cellular reactive oxygen species (ROS) production for 24 hours exposure [47].

3.6.2. Superoxide Dismutases. The superoxide dismutases (SODs) are a family of enzymes that effectively catalyze the dismutation of superoxide anion (O_2^-). The superoxide anion (O_2^-) generated in the mitochondria or in the other systems is converted by the SOD into hydrogen peroxide (H_2O_2), which in turn is also converted into water (H_2O) by catalase or glutathione peroxidase (GPx) [53]. Therefore, this antioxidant enzyme is very important to maintain the balance between the production of reactive oxygen species and antioxidants, since it can initiate oxidative chain reactions and lipid peroxidation that cause serious cellular damage [54].

Spectrophotometric studies documented that treatment of A549 cells with volcanic ash indicated a considerable decrease (<60%) in superoxide dismutase activity leading to the formation of reactive oxygen species in cells exposed to 80, 320, and 1280 µg/cm³ compared to the control cells (Figure 8(a)) in 24 hours. After hydrogen peroxide exposure, the SOD activity has been decreased significantly, reaching 40% in A549 cells (Figure 8(a)). In contrast to Lu et al. [54] study, the SOD activity has not been statistically altered by lung cells exposed to nano-SiO₂ alone compared with control cells.

Similarly, as seen in lung A549 cells, McCoy cells also revealed a statistically significant increase in the formation of ROS when exposed to volcanic ash at a concentration of 80, 320, and 1280 µg/cm³ for 24 hours (Figure 8(b)). The activity of the SOD enzyme in McCoy cell line reaches the lowest point (62%) in 24 hours where cells have been exposed to 80 µg/cm³ (Figure 8(b)). However, the absence of the dose

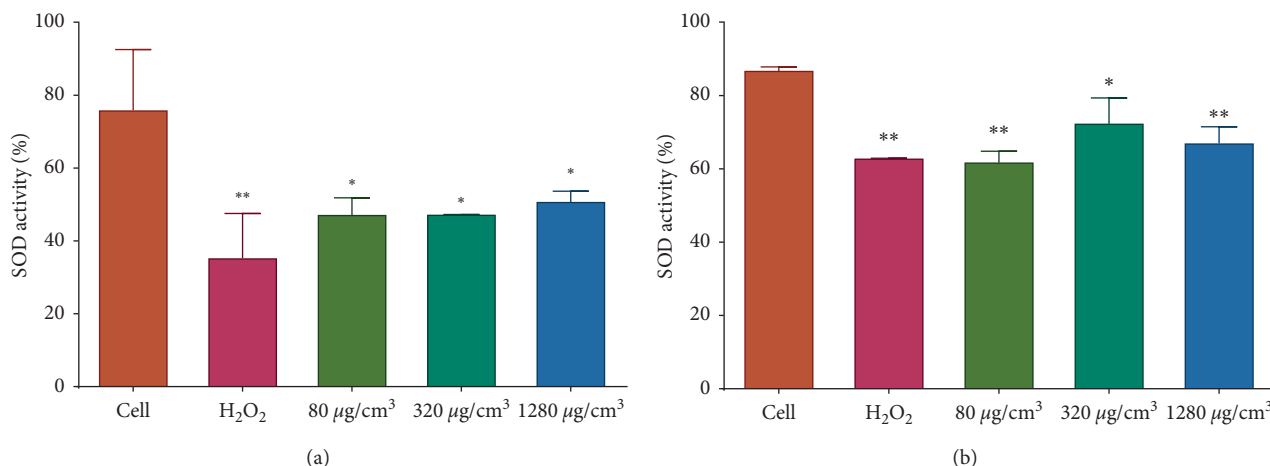


FIGURE 8: Effect of Pichincha's volcanic ash on the activity of the superoxide dismutase enzyme (SOD) in (a) A549 and (b) McCoy cell lines at 24 hours after treatment with 80, 320, and 1280 $\mu\text{g}/\text{cm}^3$ of volcanic ash. * $p < 0.05$; ** $p < 0.01$ (one-way ANOVA with Sidak's post hoc test).

response effect can be explained by the saturation in the secretion of the antioxidant enzyme superóxido dismutasa after volcanic ash exposition.

4. Conclusions

The ash of the Pichincha volcano induces an inflammatory response in the murine lung by activating the inflammasome NLRP 3 complex that can precipitate cellular pyrolysis and compromise the health of the animals exposed to this agent evidenced in the change in body weight and mortality. While after the *in vitro* tests, it is determined that the morphology of the cells changes, there is a reduction in the density, and the vacuolization is evident in peritoneal macrophages. Likewise, the effects of volcanic ash are the marked cellular toxicity dependent on the concentration of ash and the time of exposure and the imbalance of the regulation of reactive oxygen species by deactivating the activity of the antioxidant enzyme. The volcanic ash in peritoneal macrophages is toxic because it induces the production of nitric oxide or is a response to the inflammation produced. It is the first report of the biological effects or impacts produced by the ashes of the Pichincha volcano, so it is the guide to continue with future investigations that will clarify the effect of volcanic ash on Ecuadorian population.

Data Availability

The data used to support the findings of this study are available from the corresponding author upon request.

Conflicts of Interest

The authors declare that they have no conflicts of interest.

Authors' Contributions

Cristina Aguilera and Marco Viteri contributed equally to this work.

Acknowledgments

This work has been supported by the staff of the National Institute of Public Health Research (INSPI) as well as by the Laboratory of Immunology and Virology at the Universidad de las Fuerzas Armadas ESPE. The authors thank Dr. Alexis Debut and Dr. Carlos Arroyo for the SEM images and analysis at UFA-ESPE. McCoy cells were gently provided by Dr. Judith Torres. The authors thank Dr. Sandeep Kumar from Emory University for proofreading the manuscript.

Supplementary Materials

Table S1: the detail of chemical composition expressed as mass percent of major elements of 100 ash particles from the ash samples of the 5th of October 1999 eruption of the PVC. (*Supplementary Materials*)

References

- [1] R. D'Ercole, P. Metzger, and A. Sierra, "Alerta volcánica y erupción del volcán Pichincha en Quito (1998-1999)," *Bulletin de l'Institut Français d'Études Andines*, vol. 38, no. 3, pp. 487–499, 2009.
- [2] Global Volcanism Program, "Report on Guagua Pichincha (Ecuador)," *Bulletin of the Global Volcanism Network*, vol. 24, no. 12, 1999.
- [3] C. Buzea, I. I. Pacheco, and K. Robbie, "Nanomaterials and nanoparticles: sources and toxicity," *Biointerphases*, vol. 2, no. 4, pp. MR17–MR71, 2007.
- [4] M. Monzier, P. Samaniego, C. Robin et al., "Evolution of the Pichincha volcano complex (Ecuador)," in *Proceedings of the Fifth International Symposium on Andean Geodynamics*, Toulouse, France, September 2002.
- [5] M. Alvarez and J. Avilés, *Consideraciones Químicas y Medioambientales 2. Unidad Prep para Desastres Químicos*, Ministro Salud Pública, Ecuador, 1999.
- [6] B. K. G. Theng and G. Yuan, "Nanoparticles in the soil environment," *Elements*, vol. 4, no. 6, pp. 395–399, 2008.
- [7] M. R. Wilson, V. Stone, R. T. Cullen, A. Searl, R. L. Maynard, and K. Donaldson, "In vitro toxicology of respirable

- Montserrat volcanic ash," *Occupational and Environmental Medicine*, vol. 57, no. 11, pp. 727–733, 2000.
- [8] A. G. Heppleston, "Minerals, fibrosis, and the lung," *Environmental Health Perspectives*, vol. 94, pp. 149–168, 1991.
- [9] V. Vallyathan, M. S. Mentnech, L. E. Stettler, D. D. Dollberg, and F. H. Green, "Mount St. Helens' volcanic ash: hemolytic activity," *Environmental Research*, vol. 30, no. 2, pp. 349–360, 1983.
- [10] N. Fujimura, "Pathology and pathophysiology of pneumoconiosis," *Current Opinion in Pulmonary Medicine*, vol. 6, no. 2, pp. 140–144, 2000.
- [11] A. S. Rodrigues, M. S. C. Arruda, and P. V. Garcia, "Evidence of DNA damage in humans inhabiting a volcanically active environment: a useful tool for biomonitoring," *Environment International*, vol. 49, pp. 51–56, 2012.
- [12] R. Camarinho, P. V. Garcia, and A. S. Rodrigues, "Chronic exposure to volcanogenic air pollution as cause of lung injury," *Environmental Pollution*, vol. 181, pp. 24–30, 2013.
- [13] S. H. Lee and R. J. Richards, "Montserrat volcanic ash induces lymph node granuloma and delayed lung inflammation," *Toxicology*, vol. 195, no. 2–3, pp. 155–165, 2004.
- [14] D. E. Damby, F. A. Murphy, C. J. Horwell, J. Raftis, and K. Donaldson, "The in vitro respiratory toxicity of cristobalite-bearing volcanic ash," *Environmental Research*, vol. 145, pp. 74–84, 2016.
- [15] W. Lin, Y. Huang, X. D. Zhou, and Y. Ma, "In vitro toxicity of silica nanoparticles in human lung cancer cells," *Toxicology and Applied Pharmacology*, vol. 217, no. 3, pp. 252–259, 2006.
- [16] C. J. Horwell, I. Fenoglio, K. Vala Ragnarsdottir, R. S. J. Sparks, and B. Fubini, "Surface reactivity of volcanic ash from the eruption of Soufrière Hills volcano, Montserrat, West Indies with implications for health hazards," *Environmental Research*, vol. 93, no. 2, pp. 202–215, 2003.
- [17] V. Castranova, L. Bowman, J. M. Shreve, G. S. Jones, and P. R. Miles, "Volcanic ash: toxicity to isolated lung cells," *Journal of Toxicology and Environmental Health*, vol. 9, no. 2, pp. 317–325, 1982.
- [18] E. N. Naumova, H. Yepes, K. Griffiths et al., "Emergency room visits for respiratory conditions in children increased after Guagua Pichincha volcanic eruptions in April 2000 in Quito, Ecuador observational study: time series analysis," *Environmental Health*, vol. 6, no. 1, p. 111, 2007.
- [19] V. A. Vaca, R. C. Arroyo, A. Debut, and T. Toulkeridis, "The 2015 volcanic activity of Cotopaxi volcano ash data set," in *Proceedings of the Imprenta ESPE*, vol. 1, p. 214, Sangolqui, Ecuador, August–September 2016.
- [20] V. A. Vaca, R. C. Arroyo, A. Debut, and T. Toulkeridis, "The 2015 volcanic activity of Cotopaxi volcano ash data set," in *Proceedings of the Imprenta ESPE*, vol. 2, p. 214, Sangolqui, Ecuador, September 2016.
- [21] V. A. Vaca, R. C. Arroyo, A. Debut, and T. Toulkeridis, "The 2015 volcanic activity of Cotopaxi volcano ash data set," in *Proceedings of the Imprenta ESPE*, vol. 3, p. 210, Sangolqui, Ecuador, September–October 2016.
- [22] V. A. Vaca, R. C. Arroyo, A. Debut, and T. Toulkeridis, "The 2015 volcanic activity of Cotopaxi volcano ash data set," in *Proceedings of the Imprenta ESPE*, vol. 4, p. 220, Sangolqui, Ecuador, October–November 2016.
- [23] E. J. Park, H. Kim, Y. Kim, J. Yi, K. Choi, and K. Park, "Carbon fullerenes (C60s) can induce inflammatory responses in the lung of mice," *Toxicology and Applied Pharmacology*, vol. 244, no. 2, pp. 226–233, 2010.
- [24] P. Chomzynski and N. Sacchi, "Single-step method of RNA isolation by acid guanidinium thiocyanate-phenol-chloroform extraction," *Analytical Biochemistry*, vol. 162, no. 1, pp. 156–159, 1987.
- [25] E. Yano, A. Takeuchi, S. Nishii et al., "In vitro biological effects of volcanic ash from Mount Sakurajima," *Journal of Toxicology and Environmental Health*, vol. 16, no. 1, pp. 127–135, 1985.
- [26] B. Trouiller, R. Reliene, A. Westbrook, P. Solaimani, and R. H. Schiestl, "Titanium dioxide nanoparticles induce DNA damage and genetic instability *in vivo* in mice," *Cancer Research*, vol. 69, pp. 8784–8789, 2009.
- [27] M. Ghosh, M. Bandyopadhyay, and A. Mukherjee, "Genotoxicity of titanium dioxide (TiO₂) nanoparticles at two trophic levels: plant and human lymphocytes," *Chemosphere*, vol. 81, pp. 1253–1262, 2010.
- [28] J. C. Lai, M. B. Lai, S. Jandhyam et al., "Exposure to titanium dioxide and other metallic oxide nanoparticles induces cytotoxicity on human neural cells and fibroblasts," *International Journal of Nanomedicine*, vol. 2008, no. 4, pp. 533–545, 2008.
- [29] J. Zhao, L. Bowman, X. Zhang et al., "Titanium dioxide (TiO₂) nanoparticles induce JB6 cell apoptosis through activation of the caspase-8/Bid and mitochondrial pathways," *Journal of Toxicology and Environmental Health, Part A*, vol. 72, no. 19, pp. 1141–1149, 2009.
- [30] D. E. Keil, B. Buck, D. Goossens et al., "Health effects from exposure to atmospheric mineral dust near Las Vegas, NV, USA," *Toxicol Reports*, vol. 3, pp. 785–795, 2016.
- [31] M. L. McCaskill, D. J. Romberger, J. DeVasure et al., "Alcohol exposure alters mouse lung inflammation in response to inhaled dust," *Nutrients*, vol. 4, no. 7, pp. 695–710, 2012.
- [32] T. R. Martin, G. Ayars, J. Butler, and L. C. Altman, "The comparative toxicity of volcanic ash and quartz effects on cells derived from the human lung," *American Review of Respiratory Disease*, vol. 130, no. 5, pp. 778–782, 1984.
- [33] T. R. Martin, E. Y. Chi, D. S. Covert et al., "Comparative effects of inhaled volcanic ash and quartz in rats 1–4," *American Review of Respiratory Disease*, vol. 128, no. 1, pp. 144–152, 1983.
- [34] F. Martinon, K. Burns, and J. Tschopp, "The inflammasome: a molecular platform triggering activation of inflammatory caspases and processing of proIL- β ," *Molecular Cell*, vol. 10, no. 2, pp. 417–426, 2002.
- [35] R. Suárez and N. Buelvas, *El Inflammasoma: Mecanismos de Activación*, Investigación Clínica, Maracaibo, Venezuela, 2015.
- [36] C. D. Savage, G. Lopez-Castejon, A. Denes, and D. Brough, "NLRP3-inflammasome activating DAMPs stimulate an inflammatory response in glia in the absence of priming which contributes to brain inflammation after injury," *Frontiers in Immunology*, vol. 3, p. 288, 2012.
- [37] V. Hornung, F. Bauernfeind, A. Halle et al., "Silica crystals and aluminum salts activate the NALP3 inflammasome through phagosomal destabilization," *Nature Immunology*, vol. 9, no. 8, pp. 847–856, 2008.
- [38] K. Schroder and J. Tschopp, "The Inflammasomes," *Cell*, vol. 140, no. 6, pp. 821–832, 2010.
- [39] A. Akhter, K. Caution, A. Abu Khweek et al., "Caspase-11 promotes the fusion of phagosomes harboring pathogenic bacteria with lysosomes by modulating actin polymerization," *Immunity*, vol. 37, no. 1, pp. 35–47, 2012.
- [40] D. J. Lee, F. Du, S. W. Chen et al., "Regulation and function of the caspase-1 in an inflammatory microenvironment," *Journal of Investigative Dermatology*, vol. 135, no. 8, pp. 2012–2020, 2015.

- [41] T. T. Huang, K. Y. Chong, D. M. Ojcius et al., "Hirsutella sinensis mycelium suppresses interleukin-1 β and interleukin-18 secretion by inhibiting both canonical and non-canonical," *Scientific Reports*, vol. 3, no. 1, p. 1374, 2013.
- [42] F. Ethuin, C. Delarche, S. Benslama, M. A. Gougerot-Pocidalo, L. Jacob, and S. Chollet-Martin, "Interleukin-12 increases interleukin 8 production and release by human polymorphonuclear neutrophils," *Journal of Leukocyte Biology*, vol. 70, no. 3, pp. 439–446, 2001.
- [43] T. Ichinose, M. Nishikawa, H. Takano et al., "Pulmonary toxicity induced by intratracheal instillation of Asian yellow dust (Kosa) in mice," *Environmental Toxicology and Pharmacology*, vol. 20, no. 1, pp. 48–56, 2005.
- [44] J. Duan, Y. Yu, Y. Li et al., "Toxic effect of silica nanoparticles on endothelial cells through DNA damage response via Chk1-dependent G2/M checkpoint," *PLoS One*, vol. 8, no. 4, Article ID e62087, 2013.
- [45] J. D. Byrne and J. A. Baugh, "The significance of nanoparticles in particle-induced pulmonary fibrosis," *McGill Journal of Medicine*, vol. 11, no. 1, pp. 43–50, 2008.
- [46] S. N. P. Voicu, D. Dinu, C. Sima et al., "Silica nanoparticles induce oxidative stress and autophagy but not apoptosis in the MRC-5 cell line," *International Journal of Molecular Sciences*, vol. 16, no. 12, pp. 29398–29416, 2015.
- [47] L. Sun, Y. Li, X. Liu et al., "Cytotoxicity and mitochondrial damage caused by silica nanoparticles," *Toxicology in Vitro*, vol. 25, no. 8, pp. 1619–1629, 2011.
- [48] M. M. Monick, J. Baltrusaitis, L. S. Powers et al., "Effects of Eyjafjallajökull volcanic ash on innate immune system responses and bacterial growth in vitro," *Environmental Health Perspectives*, vol. 121, no. 6, pp. 691–698, 2013.
- [49] M. V. Berridge and A. S. Tan, "Characterization of the cellular reduction of 3-(4,5-dimethylthiazol-2-yl)-2,5-diphenyltetrazolium bromide (MTT): subcellular localization, substrate dependence, and involvement of mitochondrial electron transport in MTT reduction," *Archives of Biochemistry and Biophysics*, vol. 303, no. 2, pp. 474–482, 1993.
- [50] L. Kobzik, D. S. Bredt, C. J. Lowenstein et al., "Nitric oxide synthase in human and rat lung: immunocytochemical and histochemical localization," *American Journal of Respiratory Cell and Molecular Biology*, vol. 9, no. 4, pp. 371–377, 1993.
- [51] U. Förstermann and W. C. Sessa, "Nitric oxide synthases: regulation and function," *European Heart Journal*, vol. 33, no. 7, pp. 829–837, 2012.
- [52] R. G. Alscher, N. Erturk, and L. S. Heath, "Role of superoxide dismutases (SODs) in controlling oxidative stress in plants," *Journal of Experimental Botany*, vol. 53, pp. 1331–1341, 2002.
- [53] S. Jaramillo, A. Villa, A. F. Pineda, Á. B. Gallego, P. Tabares, and A. Ceballos, "Blood activity of superoxide dismutase and glutathione peroxidase in grazing dairy heifers," *Pesquisa Agropecuária Brasileira*, vol. 40, no. 11, pp. 1115–1121, 2005.
- [54] C. F. Lu, X. Y. Yuan, L. Z. Li et al., "Combined exposure to nano-silica and lead-induced potentiation of oxidative stress and DNA damage in human lung epithelial cells," *Ecotoxicology and Environmental Safety*, vol. 122, pp. 537–544, 2015.

Research Article

Assessing the Static and Dynamic Sensitivity of a Commercial Off-the-Shelf Multicore Processor for Noncritical Avionic Applications

Pablo F. Ramos ¹, Vanessa C. Vargas ¹, Nacer-Eddine Zergainoh,²
and Raoul Velazco²

¹DEEE, Universidad de las Fuerzas Armadas ESPE, Sangolquí 170501, Ecuador

²Laboratoire TIMA, Université Grenoble-Alpes, Grenoble 38400, France

Correspondence should be addressed to Pablo F. Ramos; pframos@espe.edu.ec

Received 9 March 2018; Revised 30 May 2018; Accepted 13 June 2018; Published 8 July 2018

Academic Editor: David Quesada

Copyright © 2018 Pablo F. Ramos et al. This is an open access article distributed under the Creative Commons Attribution License, which permits unrestricted use, distribution, and reproduction in any medium, provided the original work is properly cited.

The present work assesses the radiation sensitivity of an affordable and performant COTS multicore processor for noncritical avionic applications. The target device is the Epiphany E16G301 multicore manufactured in 65 nm CMOS which integrates 16 processor cores. This device was selected due to its high performance, low power consumption, and affordability, allowing general public accessing to parallel computing. Additionally, the E16G301 is the coprocessor for parallel processing of the Parallella platform, which was considered by NASA researchers for onboard health management of the DragonEye UAS. The evaluation of the device is done using quantitative theory by means of radiation experiments with 14 MeV neutrons to emulate the effects of high-energy neutrons present at avionic altitudes. Static and dynamic cross sections are obtained to evaluate the intrinsic sensitivity of the device as well as its dynamic response. Results show that the failure rate of the E16G301 running a matrix multiplication as application reaches level D of the DO-178B/C guideline, being the device well suited for minor failure conditions of avionic applications.

1. Introduction

Multicore processors are a suitable solution for achieving high performance and reliability without increasing significantly the power consumption. Its processing capacity and redundancy capabilities make them appropriate devices for implementing fault-tolerant mechanisms [1, 2]. Hence, avionic industries are interested in incorporating these devices in their systems [3]. However, the high degree of miniaturization (nanometer-scale) of multicores increases their vulnerability to the effects of natural radiation. This radiation may result in transient and permanent failures called single event effects (SEEs). Among them, the single event upset (SEU) is the most representative, since it may produce the modification of the content of a memory cell [4]. For this reason, manufacturers are enhancing fabrication processes and architectural designs. Silicon-on-Insulator (SOI) is a clear example

of technology improvements, implemented to face traditional bulk CMOS drawbacks [5, 6]. Radiation hardening by design (RHBD) techniques are also used to mitigate SEU consequences [7]. The implementation of error correcting codes (ECCs) and parity to protect the internal memory of the processors is useful but not enough in presence of multiple bit upsets (MBUs). Another well-known RHBD technique is the triple modular redundancy (TMR) which significantly improves the reliability of the system. Nevertheless, having more robust or dedicated components implies a considerable increase in costs. Consequently, an important challenge for aircraft industries is the integration of commercial-off-the-shelf (COTS) multicore processors due to budget and availability issues [8]. The current work assesses the effects of neutron radiation on a multicore processor which does not implement protection mechanisms in its internal memories. This is achieved by means of two accelerated

radiation experiments. The first one aims at evaluating the device (hardware) sensitivity, while the second one evaluates the application (software) sensitivity. Part of the results of current research has been presented in [9].

2. Related Work

There are some works in the literature regarding accelerated radiation experiments on multi-/manycore processors. The most representative ones are given below.

Stolt and Norman established a dynamic cross section model for a multicore server based on quadcore processors built in 45 nm bulk CMOS technology. The target multicore was an HP c7000 BladeSystem designed for aircraft altitudes. Radiation experiments on the multicore server were conducted with the 14 MeV neutron in order to simulate the effects of high energy particles present at avionic altitude. The server is composed by six Intel X5570-based HP server blades and six interconnect modules. For the test, it is possible to select the operating system, the BIOS setting, the processor, and the input/output utilization. Results estimate that the cross section per bit for 45 nm CMOS technology at 14 MeV neutrons is 1×10^{-14} cm²/bit [10].

Guertin presents radiation experiments on the 49-core Maestro processor, which is a radiation hardened by design (RHBD) device for space applications based on the Tiler TILE64 processor. This 90 nm manycore is produced by the onboard processing expandable reconfigurable architecture (OPERA) program and built by the Boeing Solid State Electronics Development (SSED). Experimental tests have been conducted at the Texas A/M University's (TAMU) cyclotron facility using 15 and 25 MeV ions. During the tests, internal registers as well as the L1 and L2 cache memories of the tile core were targeted. The main observed events were upsets in the L1 and L2 caches which were handled by an effective error correction and detection (EDAC) included in the Maestro design [11].

Santini et al. proposed a generic metric (mean workload between failures) to evaluate the reliability of an embedded processor intended to execute safety-critical applications. This study considers both cross section and exposure time for demonstrating that, on modern embedded processors, enabling the cache memories may provide benefits to critical systems in terms of reliability. This is possible since the larger exposed sensitive area may be compensated by a shorter exposure time of the application. The proposed metric is validated through extensive radiation test campaigns targeting a 28 nm COTS ARM-based SoC. The experiments were performed at the Los Alamos National Laboratory (LANL) and Los Alamos Neutron Science Center (LANSCE) with white neutrons source that emulates the energy spectrum of the atmospheric neutron flux. The failure probability of a bare-metal application is decreased when L1 cache is enabled. Consequently, it is not enough to rely only upon the cross section to ponder reliability [12].

Oliveira et al. presented the radiation sensitivity evaluation of cache memories and internal resources of modern graphic processing units (GPUs) designed in a 28 nm technology node. In addition, several hardening strategies

based on duplication with comparison (DWC) to reduce GPU radiation sensitivity are presented and validated through radiation experiments. The device under test was NVIDIA K20 that contains a compute unified device architecture (CUDA-) -based GPU. The cross section per bit of the L2 cache and shared memories were experimentally obtained at the Los Alamos facility using 14 MeV energy neutrons. Three different DWC strategies were designed to mitigate radiation-induced effects on GPU's used in safety-critical and high-performance computing (HPC) applications. The efficiency of the proposed strategies was experimentally evaluated and compared with chip's ECC protection mechanism. It was demonstrated that DWC strategies can be more effective than ECC when input data are duplicated [13].

Ramos et al. illustrated the radiation experiments on a quadcore processor built in a 45 nm SOI. The target device was the Freescale QorIQ P2041 processor, which is a high-performance device designed for communications. Experimental tests were conducted in the GENEPI2 (GEnerator of NEutron Pulsed and Intense) particle accelerator located in Grenoble, France. The results show that the SOI technology is between three and five times less sensitive to SEE than its CMOS counterpart. The dynamic asymmetric multiprocessing (AMP) tests have demonstrated that in spite of parity and ECC protection mechanisms, errors have been occurred in the result of the application. In addition, it can be seen that the dynamic sensitivity of the device strongly depends on the implemented multiprocessing mode [14].

Vargas et al. evaluated the SEE static and dynamic sensitivity of a manycore processor built in 28 nm CMOS. The target device was the Kalray MPPA-256 processor which is a power efficient device implementing a clustered architecture with 16 compute clusters each one with 16 processing elements. Radiation experiments were conducted in a GENEPI2 particle accelerator located in Grenoble, France. The evaluation of the device's dynamic response shows that, by enabling the cache memories, it is possible to gain in performance of the application without compromising reliability. Additionally, the results suggest that ECC and interleaving implemented in the static memories of the targeted clusters are very effective to mitigate SEUs since all detected events were corrected [15].

3. Methodology and Materials

Accelerated radiation ground testing allows performing the analysis of the sensitivity to radiation of electronic devices through artificial radiation environments. It is the fastest way to obtain statistically meaningful data in a short period of time, since the more particles hit the component, the more SEEs are observed [16]. The reproducibility of the experiment is also another major advantage of this strategy. Consequently, this work considers two models of tests for evaluating the sensitivity of a multicore processor: a static test in order to obtain the intrinsic sensitivity of the device's memory cells and a dynamic test for evaluating the dynamic response of the implemented application [17]. Figure 1 illustrates the proposed methodology.

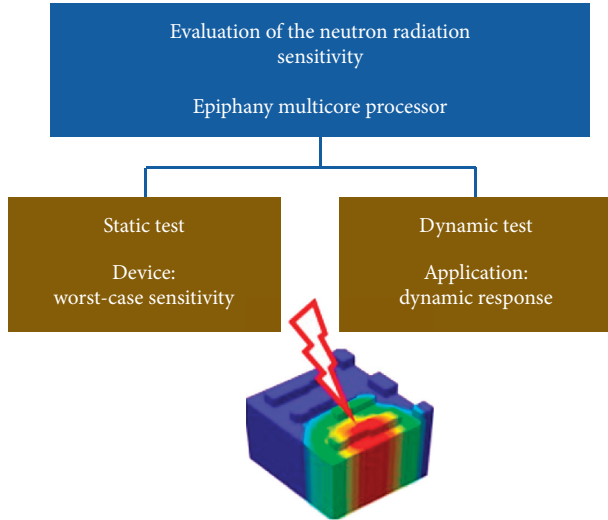


FIGURE 1: Multicore processor neutron sensitivity evaluation.

In this work, experimental tests have been conducted with 14 MeV neutron radiation to emulate the effects of high-energy neutrons present at avionic altitudes, since neutrons are the most representative particles in the Earth's atmosphere. Reference [18] discusses the relevance of using the 14 MeV neutron test to characterize the SEU sensitivity of digital devices. Sections 3 and 6 of the JEDEC89A document of the *JEDEC standard* were used as a base protocol for the experimental tests [19].

3.1. Identification of the Variables. Radiation tests are experiments that can be addressed using quantitative theory. Consequently, the first task is to identify the variables involved in the experiment. Table 1 lists the independent and dependent variables for the static and dynamic tests. Note that the dynamic test also depends on the system configuration and the implemented application.

The independent variables are divided in two groups: variables depending on the system (exclusive for the dynamic test) and variables to be manipulated during the radiation experiments.

Dependent variables represent the errors observed during the tests. They can be classified into single errors, multiple errors, and sequence interruption errors. It is important to consider that, depending on the memory architecture of the multicore, single and double errors can be corrected and detected, respectively, by the protection mechanisms.

3.2. Static Test. This test aims at estimating the intrinsic sensitivity to SEE of the memory cells of a processor. The device under test (DUT) is placed facing the center of the target perpendicularly to the beam axis at a distance depending on the required radiation flux. Typically, the method consists in writing a predefined pattern in the memory and accessible registers of the processor via the instruction set (load and store). Once finished the initialization, the DUT is irradiated and the program checks

TABLE 1: Independent and dependent variables for radiation tests.

	Independent variables	Dependent variables
Manipulated (static and dynamic tests)	Neutron flux	Single-bit upset (SBU) Multiple-bit upset (MBU) Multiple-cell upset (MCU)
	Distance DUT to target	
	Exposure time	
System dependent (dynamic test)	Implemented application	Single-event functional interruption (SEFI)
	Multiprocessing mode	
	Programming model	

periodically the memory locations along the radiation test to detect upset events. If an upset is detected, the program writes the correct pattern in the associated memory location and logs the results to an external host via Ethernet ports. During the static test, all the sensitive zones are exposed to radiation at the same time, which do not represent the real behavior of the circuit since not all the memory resources are used simultaneously when an application is executed. For this reason, the static test provides the worst-case estimation of the device sensitivity [20].

As a result of this test, the static cross section (σ_{STATIC}) of the device is obtained. It is defined as the number of detected upset events divided by the fluence, which is the neutron flux integrated in time, as expressed in the following equation:

$$\sigma = \frac{\text{number of SEE}}{\text{fluence}}. \quad (1)$$

The elementary data pattern for memory circuits is a logical checkerboard [19]. All zeros and all ones is also a common pattern used during the radiation test. However, some memories such as DRAMs usually have a favorite error failure, either 0→1 or 1→0. For this reason, for testing when there is no a priori information about the component, the test pattern have to balance the number of 0's and 1's. Thus, the selected pattern for the static test was 0x55AA55AA. Regarding the exposure time to radiation of the device, it is important to consider that the probability of having an upset event during a given period of time is a stochastic process that follows a Poisson distribution. Thus, the waiting time between the read operations in the static test can be validated by analyzing the distribution of the number of events per unit of time. If the obtained distribution does not follow the Poisson law, the waiting time should be adjusted.

3.3. Dynamic Test. The goal of this test is to estimate the SEE dynamic response of an application running on a processor. As a result of the experiment, the dynamic cross section (σ_{DYN}) is obtained. Unlike the static test, it only evaluates the memory cells used by the application. The method consists in the periodical execution of an application while the processor is being irradiated to induce SEE. Once finished each execution of the program, results are compared with a set of correct values previously obtained, in order to detect errors. The experiment is launched and monitored using a *host* computer located outside the armored chamber. The



FIGURE 2: GENEPI2 particle accelerator.

communication between the external host and the Parallella host is achieved by means of the Ethernet port using the Linux *ssh* communication command. All detected errors are logged and transmitted to the external host which stores the results.

3.4. Neutron Radiation Facility. Accelerated radiation ground tests were conducted at the GENEPI2 (GEnerator of NEutron Pulsed and Intense) facility located at the LPSC (Laboratoire de Physique Subatomique et Cosmologie) in Grenoble, France. This accelerator was originally developed for nuclear physics experiments, and since 2014, it has been used to irradiate integrated circuits from different technologies. GENEPI2 is an electrostatic accelerator producing neutrons by impinging a deuteron beam onto a tritium (T) target. After acceleration at 220 keV, deuterons (d) produce neutrons (n) by the fusion reaction $d + T \rightarrow n + 4He$ [21].

Neutrons are emitted omnidirectionally to the DUT with an average energy of 14 MeV. The DUT is set facing directly the target at a distance depending on the required neutron flux. Experimental radiation campaigns consider that only neutrons emitted fully forward will impact the DUT. For protecting the readout electronic platform other than the DUT, a dedicated neutron shielding is used.

A new T target providing a maximum neutron flux of $4.5 \times 10^7 \text{ n}\cdot\text{cm}^{-2}\cdot\text{s}^{-1}$ was installed in 2015 aiming at increasing the neutron production while improving the accelerator reliability. The major modification consists in replacing the current deuterium ion source by a new one, based on the electron cyclotron resonance (ECR) technique, delivering higher-beam intensity. Figure 2 illustrates GENEPI2 particle accelerator.

3.5. Device under Test. The selected device for this study was the Adapteva Epiphany E16G301 which is a 16-core processor designed for parallel computing of the Parallella board. This board is a high-performance computing platform based on a dual core ARM A9 processor, used as host, and the Epiphany E16G301 used as coprocessor. The Epiphany is a scalable multicore architecture with up to 4095 processors sharing a common 32-bits memory space. It defines a parallel computing fabric comprised of a 2D array of processors nodes connected by a low-latency mesh

network-on-chip. The E16G301, which is based on 3rd generation of the Epiphany multicore IP, is a 16-core system-on-chip implemented in a 65 nm CMOS technology [22]. Each processor core is a 32-bit superscalar floating point RISC CPUs, capable of performing two floating point operations per clock cycle and one integer calculation per clock cycle. The device has a peak performance of 32 Gflops (2 Gflops per core). The maximum chip power consumption is less than 2 W. Each CPU has an efficient general-purpose instruction set that excels at compute-intensive applications while being efficiently programmable in C/C++. Figure 3 shows the implementation of the E16G301 architecture.

The memory architecture of the E16G301 multicore is based on a flat shared memory map. Each compute core has up to 1 MB of local memory as a unique addressable part of the total 32-bit address space. The core processor can access its own local memory as well as other processors' memory by means of standard load/store instructions. The local memory is comprised of 4 independent banks, each one of 8 KB for a total of 32 KB for each CPU core. For the particular case of the Epiphany E16G301 that implements 16-cores, the chip has a 512 KB distributed shared memory [23]. This multicore processor does not implement any protection mechanisms in its internal memory.

3.6. Benchmark Application. A standard 45×45 matrix multiplication (MM), which is a memory-bound application, was selected to be tested throughout this work. It was considered since the matrix multiplication is one of the most essential algorithms in numerical algebra as well as in distributed, scientific, and high-performance computing [24]. Concerning avionic applications, MM is used for image processing, filtering, adaptive control, and navigation and tracking. The input matrix A was filled up with the decimal number "5," while matrix B was filled up with 6 s; thus the expected result was 1350 for all the elements of the resulting matrix C. The total number of variables used for the implementation of the matrix multiplication is 6078, distributed in 4050 input variables, 2025 output variables, and 3 indexes for loop operations. Each variable was implemented in 32-bit, being the targeted sensitive area about 24 KB that perfectly fits in the 32 KB local memory of each core. The size of the matrix was selected so that data occupy as much memory space as possible, leaving enough space for the program's code.

4. Results and Discussion

Radiation experiments performed on the Epiphany E16G301 are very interesting compared to similar works targeting other multicore processors, since errors produced by SEE are clearly identified as they are not masked by protection mechanisms such as ECC or parity. This fact allows a better analysis of the behavior of the device in presence of SEEs.

Concerning the limitations of the experiments, there are two points to consider:

- (i) The E16G301 processor does not have direct access to *printf* function for logging results. For this reason,

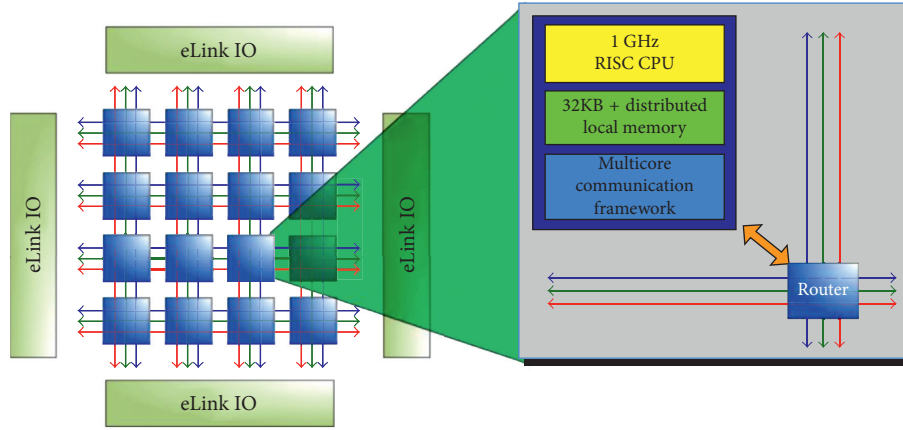


FIGURE 3: Implementation of the E16G301 Epiphany architecture [22].

it has to write the information about observed events in the external DDR memory of the board. This information is logged by the *host* processor (ARM).

- (ii) The physical distance between the E16G301 multicore and the *host* processor in the Parallella board is less than one centimeter. It was thus necessary to limit the neutron flux for avoiding particles affecting the *host* processor and other circuitries.

4.1. Experimental Setup. The DUT was placed at a distance of 38.5 ± 0.5 cm to the target. The neutron beam energy was 14 MeV with an estimated flux of $7.2 \times 10^4 \text{ n} \cdot \text{cm}^{-2} \cdot \text{s}^{-1}$ with an error of $\pm 0.1 \times 10^4 \text{ n} \cdot \text{cm}^{-2} \cdot \text{s}^{-1}$. Special attention was required to protect the rest of the platform components from radiation. For that, the E16G301 multicore was irradiated through a small window on a 5 cm thickness polypropylene block intended to protect the readout platform. The power supplied of the multicore platform was monitored by using a camera available in the casemate of the accelerator facility. In this way, the voltage and current parameters were controlled.

4.2. Intrinsic Sensitivity. This evaluation was performed by targeting the internal memory and accessible registers of each core of the E16G301 processor. The host processor of the Parallella board was in charge of filling the internal memory and registers of the multicore with a predefined pattern using the Epiphany SDK utilities E-READ and E-WRITE [25]. In this manner, the whole internal memory of the E16G301 multicore could be targeted. Table 2 summarizes the sensitive zones of the multicore processor.

Three static tests were performed with an exposure time of 1 hour each one, providing a fluence of $6.82 \times 10^8 \text{ n} \cdot \text{cm}^{-2}$ as per the neutron facility records. During the tests, 69 SBU and 7 MCU that produce bit-flips were detected. There were no observed errors in processor's registers. In addition, 5 SEFI that caused hangs were observed. Table 3 summarizes the test results. Note that the subscript number following MCU represents the multiplicity of the upset.

Table 4 shows a sample of data containing bit-flips caused by SBU and MCU produced in the local memory and logged during the experiment.

TABLE 2: Sensitive zones of the Epiphany E16G301 multicore processor.

Sensitive zone	Location	Capacity	Description
SRAM	Processor core	32 KB per core	Local memory
GPR	Processor core	64 registers of 32 bits per core	General-purpose register
SPR	Processor core	42 registers of 32 bits per core	Special-purpose register

TABLE 3: Results of the static radiation test campaigns.

SEE Type	Test 1	Test 2	Test 3	Consequences
SBU	29	17	23	Bit-flip
MCU (2)	1	5	1	Bit-flip
SEFI	3	2	0	Hangs
Total	33	24	24	—

At the end of the experiment, the static cross section σ_{STATIC} was estimated by applying (1). It provides the worst-case sensitivity of the device built in 65 nm CMOS technology.

$$\sigma_{\text{STATIC}} = \frac{81}{6.82 \times 10^8} = 1.29 \times 10^{-7} \text{ cm}^2/\text{dev.} \quad (2)$$

Due to the scarcity of experimental data, 95% confidence intervals were applied to this result. In this case, the most accurate way to calculate the uncertainty margins consists in using the relationship between the cumulative distribution functions of the Poisson and chi-squared distributions as described in [26]. Then, the lower and upper limits for the dynamic cross section are

$$0.94 \times 10^{-7} \text{ cm}^2/\text{dev} < \sigma_{\text{STATIC}} < 1.48 \times 10^{-7} \text{ cm}^2/\text{dev.} \quad (3)$$

Since the tested memory area of the multicore processor represents 4194304 bits, the 95% confidence interval for the static cross section per bit is estimated as

TABLE 4: Example of the obtained results in the static tests.

Pattern	Type	Core	Address	Data hex	Data binary
0x55AA55AA	SBU	3	0x7C84	0x55AA45AA	0b0101 0101 1010 1010 0100 0101 1010 1010
	SBU	7	0x52B4	0x55AA55AB	0b0101 0101 1010 1010 0101 0101 1010 1011
	MCU (2)	2	0x7110	0x55AA5DAA	0b0101 0101 1011 1010 0101 1101 1010 1010
			0x7130	0x55AA5DAA	0b0101 0101 1011 1010 0101 1101 1010 1010

TABLE 5: Results of the dynamic radiation test campaigns.

SEE Type	Test 1	Test 2	Test 3	Consequences
SEU	10	6	7	Silent faults
SEU	6	4	11	Erroneous results
SEU	1	0	0	Time-outs
SEFI	2	2	1	Hangs
Total	19	12	19	—

$$\sigma_{\text{STATIC_bit}} = [2.24 - 3.52] \times 10^{-14} \text{ cm}^2/\text{bit}. \quad (4)$$

4.3. *Dynamic Response.* This evaluation was carried out to obtain the dynamic cross section (σ_{DYN}) of an application running in the multicore processor. Three dynamic tests were performed with an exposure time of 1 hour each one providing a total fluence of $6.95 \times 10^8 \text{ n}\cdot\text{cm}^{-2}$ as per the accelerator records. The comparison between the obtained and correct results was performed inside the multicore processor. The duration of the matrix multiplication is $27597 \mu\text{s}$, and the comparison time is $1.44 \mu\text{s}$. Therefore, in one hour (3600 s), the application executes 130449 times, which multiplied by the comparison time gives 0.19 s (0.0052%) of loss of exposure time which is negligible. Table 5 summarizes the results of the dynamic radiation campaign.

From the results presented in Table 5, only erroneous results, time-outs, and hangs were taken into account to calculate the dynamic cross section as follows:

$$\sigma_{\text{DYNAMIC}} = \frac{27}{6.95 \times 10^8} = 3.88 \times 10^{-8} \text{ cm}^2/\text{dev}. \quad (5)$$

Silent errors were observed by reading input matrices aimed at detecting corrupted data caused by upset events which do not produce errors in the resulting matrix. They are presented for showing the total number of SEUs occurred in the dynamic test. As in the static case, uncertainty margins were added to the results. Then, the lower and upper limits for the dynamic cross section for a 95% confidence interval are as follows:

$$2.56 \times 10^{-8} \text{ cm}^2/\text{dev} < \sigma_{\text{DYN}} < 5.65 \times 10^{-8} \text{ cm}^2/\text{dev}. \quad (6)$$

From the consequences of the dynamic tests, erroneous results are the most critical since the program considers them as valid results affecting dramatically the reliability of the application. The reliability of the device can be evaluated by means of its failure rate. The failure rate (λ) of the device is estimated by extrapolating the dynamic cross section at avionic altitude (35,000 feet) where the neutron flux (ϕ) is about $2.99 \times 10^3 \text{ n}\cdot\text{cm}^{-2}\cdot\text{h}^{-1}$, by applying the following equation:

TABLE 6: Failure condition levels according to DO-178B/C [28, 29].

Level	Failure condition	Objectives	With independence	Failure rate
A	Catastrophic	66	25	$P \leq 10^{-9}/\text{h}$
B	Hazardous	65	14	$P \leq 10^{-7}/\text{h}$
C	Major	57	2	$P \leq 10^{-5}/\text{h}$
D	Minor	28	2	$P > 10^{-5}/\text{h}$
E	No effect	2	0	N/A

$$\lambda = \sigma * \phi,$$

$$\begin{aligned} \lambda &= [2.56 - 5.65] \times 10^{-8} \text{ cm}^2/\text{dev} * 2.99 \times 10^3 \text{ n}\cdot\text{cm}^{-2}\cdot\text{h}^{-1} \\ &= [7.65 - 16.89] \times 10^{-5}/\text{h}. \end{aligned} \quad (7)$$

As the reliability of multi-/manycore processors strongly depends on the implemented application (software), the failure rate of the device can be classified within the DO-178B/C (Software Considerations in Airborne Systems and Equipment Certification). The DO-178B/C is a guideline used as de facto standard for developing avionic software systems [27]. Table 6 shows the level of failure condition.

The failure conditions for avionic systems are described as follows:

- (i) *Catastrophic:* Failure may cause a crash. Error or loss of critical function required to safely fly and land the aircraft.
- (ii) *Hazardous:* Failure has a large negative impact on safety or performance or reduces the ability of the crew to operate the aircraft due to physical distress or a higher workload, or causes serious or fatal injuries among the passengers (safety-significant).
- (iii) *Major:* Failure is significant, but has a lesser impact than a hazardous failure (e.g., passenger discomfort) or significantly increases crew workload (safety related).
- (iv) *Minor:* Failure is noticeable, but has a lesser impact than a major failure (e.g., passenger inconvenience or a routine flight plan change).
- (v) *No Effect:* Failure has no impact on safety, aircraft operation, or crew workload.

Results show that the failure rate of the multicore executing a matrix multiplication as application falls in level D of the DO-178B/C. Therefore, the device is convenient for minor failure conditions, which includes several applications regarding data and image processing. In fact, the NASA's report, "Intelligent Hardware-Enable Sensor and Software

Safety and Health Management for Autonomous (UAS)” shows the use of Parallella board containing the Epiphany multicore for unmanned aircraft systems [30]. The current article is relevant since it supports the use of the Parallella board in aircraft applications by presenting experimental data concerning its radiation sensitivity.

5. Conclusions

Radiation experiments performed with 14 MeV neutrons are a useful technique for evaluating the intrinsic sensitivity of the multicore and dynamic response of the application. Results demonstrate that the Epiphany E16G301 multicore is suitable for embedded systems performing noncritical avionic applications. The fact that the Epiphany does not implement protection mechanisms has permitted a true estimation of the error rate, confirming that protection mechanisms affect testing as stated in [31].

Although the maximum flux provided by the radiation facility is 4.5×10^7 ($\text{n} \cdot \text{cm}^{-2} \cdot \text{s}^{-1}$), the applied neutron flux was limited to 7.2×10^4 $\text{n} \cdot \text{cm}^{-2} \cdot \text{s}^{-1}$ in order to avoid perturbations in the circuitry of the Parallella board. However, the applied flux is about eight orders of magnitude greater than the flux at avionic altitudes, which corresponds to almost 10 years of exposure time of the device to neutron radiation at 35,000 feet.

Despite the efforts for protecting the rest of components of the platform, the SD card containing the Linux OS was corrupted in one of the experiments. This was solved by replacing the tainted SD by a new one and repeating the test.

In future work, the Adapteva Epiphany multicore processor will be proposed to be used for image processing in a military aircraft. In parallel, another module containing the Epiphany processor will execute a memory-bound application in order to detect SEUs produced in real operating environment.

Data Availability

The data used to support the findings of this study are available from the corresponding author upon request.

Disclosure

The present paper is an extension of the abstract poster presented in the “Nano Science and Nanotechnology Week” held in Quito–Ecuador from 28/08/2017 to 01/09/2017.

Conflicts of Interest

The authors declare that they have no conflicts of interest.

Acknowledgments

The authors would like to thank Maud Baylac, Francesca Villa, and Solenne Rey from LPSC for their valuable support during radiation experiments presented in this work. This work has been supported by the Ecuadorian government through the Secretaría de Educación Superior, Ciencia, Tecnología e Innovación (SENESCYT) and the Universidad

de las Fuerzas Armadas ESPE (Grant no.PIC-2017-EXT-005). Radiation experiments in GENEPI2 at LPSC (CNRS/UGA) have been performed within the “Characterisation Program” of the IRT nanoelec and cofunded by the French government in the frame of the so-called “Programme d’Investissements d’Avenir” under the reference ANR-10-AIRT-05.

References

- [1] R. Hyman, K. Bhattacharya, and N. Ranganathan, “Redundancy mining for soft error detection in multicore processors,” *IEEE Transactions on Computers*, vol. 60, no. 8, pp. 1114–1125, 2011.
- [2] E. Kim and N. Shanbhag, “Soft N-modular redundancy,” *IEEE Transactions on Computers*, vol. 61, no. 3, pp. 323–336, 2012.
- [3] Certification Authorities Software Team (CAST), “Position paper cast-32 multi-core processors,” November 2016, https://www.faa.gov/aircraft/air_cert/design_approvals/air_software/cast/cast_papers/media/cast-32A.pdf.
- [4] R. Baumann, “Soft errors in advanced computer systems,” *IEEE Design and Test of Computers*, vol. 22, no. 3, pp. 258–266, 2005.
- [5] B. Vandana and M. Siva Mukar, “Study of VLSI bulk CMOS and SOI technologies,” *International Journal of Scientific and Research Publications*, vol. 3, no. 2, pp. 1–8, 2013.
- [6] G. Gasiot, V. Ferlet-Cavrois, J. Baggio et al., “SEU sensitivity of bulk and SOI technologies to 14 MeV neutrons,” *IEEE Transactions on Nuclear Science*, vol. 49, no. 6, pp. 3032–3037, 2002.
- [7] W. Hughes, *Single Event Effects Mitigation Techniques Report*, DOT/FAA/TC-15/62, Federal Aviation Administration, Washington, DC, USA, 2016.
- [8] P. Bieber, F. Boniol, M. Boyer, E. Noulard, and C. Pagetti, *New Challenges for Future Avionic Architectures*, Onera, Palaiseau, France, AerospaceLab, 2012.
- [9] P. Ramos, V. Vargas, R. Velazco, and N. E. Zergainoh, *Assessing the Static and Dynamic Sensitivity of a Commercial-Off-The-Shelf Multi-Core Processor for Non-Critical Avionic Applications*, Nano Science and Nanotechnology Week, Quito, Ecuador, 2017.
- [10] S. S. Stolt and E. Normand, “A multicore server SEE cross section model,” *IEEE Transactions on Nuclear Science*, vol. 59, no. 6, pp. 2803–2810, 2012.
- [11] S. Guertin, *Initial SEE Test of Maestro*, National Aeronautics and Space Administration, Jet Propulsion Laboratory, Pasadena, CA, USA, 2012, http://trs-new.jpl.nasa.gov/dspace/bitstream/2014/42682/1/12-2145_A1b.pdf.
- [12] T. Santini, P. Rech, G. Nazar, L. Carro, and F. R. Wagner, “Reducing embedded software radiation-induced failures through cache memories,” in *Proceedings of the 19th IEEE European Test Symposium (ETS)*, pp. 1–6, Paderborn, Germany, May 2014.
- [13] D. A. G. Oliveira, P. Rech, H. M. Quinn et al., “Modern GPUs radiation sensitivity evaluation and mitigation through duplication with comparison,” *IEEE Transactions on Nuclear Science*, vol. 61, no. 6, pp. 3115–3122, 2014.
- [14] P. Ramos, V. Vargas, M. Baylac et al., “Evaluating the SEE sensitivity of a 45 nm SOI multicore processor due to 14 MeV neutrons,” *IEEE Transactions on Nuclear Science*, vol. 63, no. 4, pp. 2193–2200, 2016.
- [15] V. Vargas, P. Ramos, V. Ray et al., “Radiation experiments on a 28 nm single-chip many-core processor and SEU error-rate

- prediction," *IEEE Transactions on Nuclear Science*, vol. 64, no. 1, pp. 483–490, 2017.
- [16] H. Quinn, "The use of accelerated radiation testing for avionics," *AIP Conference Proceedings*, vol. 1525, 2013.
- [17] S. Rezgui, R. Velazco, R. Ecoffet, S. Rodriguez, and J. Mingo, "Estimating error rates in processor-based architectures," *IEEE Transactions on Nuclear Science*, vol. 48, no. 5, pp. 1680–1687, 2001.
- [18] F. Miller, C. Weulersse, T. Carriere et al., "Investigation of 14 MeV neutron capabilities for SEU hardness evaluation," *IEEE Transactions on Nuclear Science*, vol. 60, no. 4, pp. 2789–2796, 2013.
- [19] JESD89A, *Measurement and Reporting of Alpha Particle and terrestrial Cosmic Ray-Induced Soft Errors in Semiconductor Devices*, JEDEC Solid State Technology Association, Arlington, VA, USA, December 2016, <http://www.jedec.org/sites/default/files/docs/jesd89a.pdf>.
- [20] P. Ramos, "Evaluation of the SEE sensitivity and methodology for error rate prediction of applications implemented in multi-core and manycore processors," Ph.D. thesis, TIMA laboratory, Grenoble, France, 2017, http://tima.univ-grenoble-alpes.fr/tima/en/mediatheque/PhDthesisresult_id452.html.
- [21] F. Villa, M. Baylac, S. Rey et al., "Accelerator-based neutron irradiation of integrated circuits at GENEPI2 (France)," in *Proceedings of the Radiation Effects Data Workshop*, pp. 1–5, Paris, France, July 2014.
- [22] ADAPTEVA, "E16G301 datasheet rev. 14.03.11," December 2016, http://www.adapteva.com/docs/e16g301_datasheet.pdf.
- [23] ADAPTEVA, "Epiphany architecture reference rev. 14.03.11," December 2016, http://www.adapteva.com/docs/epiphany_arch_ref.pdf.
- [24] G. Ballard, J. Demmel, O. Holtz, B. Lipshitz, and O. Schwartz, "Communication-optimal parallel algorithm for strassen's matrix multiplication," in *Proceedings of the 24th Annual ACM Symposium on Parallelism in Algorithms and Architectures*, pp. 193–204, Pittsburgh, PA, USA, June 2012.
- [25] ADAPTEVA, "Epiphany SDK Rev. 5.13.09.10," December 2016, http://www.adapteva.com/docs/epiphany_sdk_ref.pdf.
- [26] J. Autran, P. Munteanu, P. Roche, and G. Gasiot, "Real-time soft-error rate measurements: a review," *Microelectronics Reliability*, vol. 54, no. 8, pp. 1455–1476, 2014.
- [27] T. Ferrel and D. Ferrel, *RTCA DO-178B/EUROCAE ED-12B, Digital Avionics Handbook*, McGraw-Hill, New York, NY, USA, 3rd edition, 2014.
- [28] V. Hilderman and T. Baghai, *Avionics Certification: A Complete Guide to DO-178B (SW), DO-178C (Update), DO-254(HW)*, Avionics Communication Inc., Leesburg, VA, USA, 2013.
- [29] W. Youn, S. B. Hong, K. Ryooh Oh, and O. S. Ahn, "Software certification of safety-critical avionic systems: DO-178C and its impacts," *IEEE Aerospace and Electronic Systems*, vol. 30, no. 4, pp. 4–13, 2015.
- [30] K. Rozier, "Intelligent hardware-enable sensor and software safety and health management for autonomous UAS, NASA/TM-2015-218817," May 2015, <https://ntrs.nasa.gov/archive/nasa/casi.ntrs.nasa.gov/20150021506.pdf>.
- [31] K. LaBel and L. Cohn, *Radiation Testing and Evaluation Issues for Modern Integrated Circuits*, NASA/GSFC Code 561.4, 2005.

Research Article

Improvement of N-Acetylcysteine Loaded in PLGA Nanoparticles by Nanoprecipitation Method

Ruth Lancheros ¹, Carlos A. Guerrero,² and Rubén D. Godoy-Silva¹

¹Departamento de Ingeniería Química y Ambiental, Facultad de Ingeniería, Universidad Nacional de Colombia, Bogotá, Colombia

²Departamento de Ciencias Fisiológicas, Facultad de Medicina, Universidad Nacional de Colombia, Bogotá, Colombia

Correspondence should be addressed to Ruth Lancheros; rlancheros@unal.edu.co

Received 9 February 2018; Revised 21 May 2018; Accepted 7 June 2018; Published 5 July 2018

Academic Editor: Brajesh Kumar

Copyright © 2018 Ruth Lancheros et al. This is an open access article distributed under the Creative Commons Attribution License, which permits unrestricted use, distribution, and reproduction in any medium, provided the original work is properly cited.

N-Acetylcysteine (NAC) is a hydrophilic compound with a low bioavailability. It has been used as an effective antioxidant agent. This research seeks to enhance the entrapment of NAC in PLGA nanoparticles for drug delivery systems. The nanoparticles were made using the nanoprecipitation method and changing the following parameters: the solvent/nonsolvent nature, its viscosity, pH, NAC addition to the nonsolvent, the polymer concentration and molecular weight, and NAC concentration in the solvent. The results showed that an increase in the nonsolvent viscosity produces NAC concentration in the solvent, and the nonsolvent rises its entrapment in the nanoparticles. Nanoparticles with 235.5 ± 11.4 nm size with an entrapment efficiency of $0.4 \pm 0.04\%$ and a specific load of $3.14 \pm 0.33\%$ were obtained. The results suggest that besides efficiently entrapping hydrophobic compounds, the nanoprecipitation method also has a high potential as an alternative entrapment method for hydrophilic compounds as well. However, its use in the pharmaceutical industry, as a proper specific load vehicle, still depends on the improvement of the load capacity.

1. Introduction

N-Acetylcysteine (NAC) is a mucolytic, anti-inflammatory, and hepatoprotective agent used as a powerful antioxidant to protect cells [1, 2] and to treat diseases such as cancer, neuropsychiatric disorders, and cardiovascular diseases, among others [3, 4]. Despite all these benefits, NAC has a low bioavailability (6 to 8%), which limits its therapeutic effects. This happens because, once it enters the bloodstream, it joins the plasmatic proteins and creates disulfide bridges [5]. When supplied intravenously, nearly 30% of NAC is eliminated through urine and high doses can increase the blood pressure [5, 6]. Thus, the development of carriers to transport and stabilize NAC inside the body is a major concern when researching for new ways to increase its bioavailability. In this scenario, nanoparticles manufactured in materials such as PLGA, a biodegradable copolymer, are being developed [7–9].

Entrapping low molecular weight hydrophilic compounds, like NAC in PLGA nanoparticles, represents a challenge as the small size of the substance facilitates its migration and rapid release [7, 10]. This study aims at increasing NAC entrapment in nanoparticles fabricated by the nanoprecipitation method, as it constitutes a simple, economic, and easily scalable methodology [11, 12]. Even though this methodology is used mainly for liposoluble compounds, the literature presents successful cases of entrapment of hydrophilic compounds [13, 14]. As shown in Figure 1, this method consists in dissolving the active compound (NAC) and the polymer (PLGA) in the same solvent. This solution is brought into contact with a different solvent (called nonsolvent), in which the polymer is insoluble. The first solvent migrates into the nonsolvent because the latter is completely miscible in the former. This results in the polymer precipitation that gives form to nanoparticles. Thus, in this process, nanoparticles

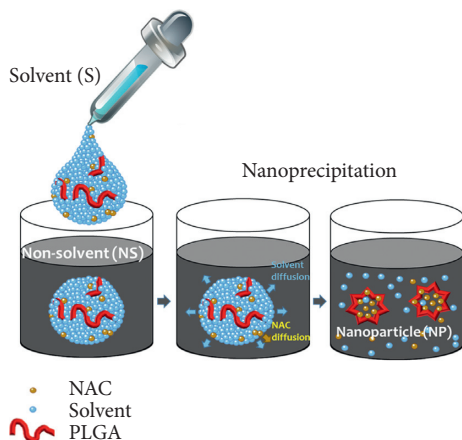


FIGURE 1: PLGA nanoparticle production scheme by nanoprecipitation methodology.

are expected to trap a considerable quantity of the active compound [15].

The quantity of the active compound that can be entrapped depends on factors such as the size of the molecules and the active compound solubility, as well as its affinity to the nonsolvent. If the active compound is highly soluble in the nonsolvent, it can migrate into the nonsolvent and reduce the quantity of compound trapped within the nanoparticles. Given that for medical purposes, the nanoparticles' diameter should not exceed 200 to 250 nm since a higher particle size can be retained by the reticuloendothelial system [16]. The strategies to increase the entrapment must focus on the two limiting conditions stated before.

There are multiple strategies reported in literature to enhance the entrapment of hydrophilic compounds in PLGA nanoparticles. For example, the nonsolvent, which is usually water, has been changed for another nonsolvent in which the active compound is less soluble. Some nonsolvents reported are caprylate and caprate triglyceride [17], cottonseed oil [13, 14], methanol, ethanol, and isopropanol [18]. It was found that cottonseed oil enhanced entrapment efficiency from 0.01 to 7.1% but increased the particle size (300 nm) and the polydispersity value (0.4). The use of alcohols as nonsolvents affects the particle size, obtaining the smaller size using methanol (102 nm) and increasing it with the hydrocarbon chain length. Bilati et al. reported no values of entrapment efficiency [18]. Another method employed is to make the active compound more hydrophobic by modifying water pH when it is used as a nonsolvent. Tewes et al. used an alkali pH (8.6) to turn doxorubicin more hydrophobic, increasing the entrapment efficiency from 67% (using neutral pH) to 95% [19]. Govender et al. reported similar results to enhance the entrapment of procaine hydrochloride from 11% using a pH of 5.8 to 58.5% with a pH value of 9.3 [20]. Peltonen et al. acidified the pH of sodium cromoglycate and enhanced the entrapment efficiency up to 70% [21]. Song and colleagues reported an increase of entrapment efficiency by changing the nonsolvent pH and increasing the molecular weight and the polymer concentration [22, 23].

The purpose was to develop a methodology to maximize the NAC entrapped inside PLGA nanoparticles (C_{NAC-S}), minimize the migration of active compound towards the nonsolvent (N_{NAC-NS}), and obtain a particle size under 250 nm. Using Fick's law for compound transport [24], we sought to decrease both the diffusivity (\mathcal{D}_{NAC-NS}) and the NAC concentration gradient between the inside and the outside of the nanoparticles ($\partial C_{NAC-NS}/\partial x$).

As explained in Figure 2, we increased PLGA molecular weight, viscosity of the nonsolvent, and the PLGA concentration to decrease the diffusivity (\mathcal{D}_{NAC-NS}). In this process, a variety of solvent/nonsolvent pairs were tested. The pH of the nonsolvent was varied and calcium ions were added to turn the active compound more hydrophobic. Additionally, NAC was added to the nonsolvent in order to decrease the concentration gradient ($\partial C_{NAC-NS}/\partial x$) between the NAC solvent and nonsolvent.

2. Materials and Methodology

2.1. Materials. Polymers employed in the preparation of nanoparticles: PLGA 50:50 Resomer RG 502 (Mw 7–17 kDa), RG 504 (Mw 38–54 kDa), and RG 505 (Mw 54–69 kDa) ester terminated were purchased at Sigma-Aldrich.

Surfactants: Stepan-Mild L3[®], Bio-Soft N1-7[®], and Makon NF-5[®] were acquired at Stepan. Pluronic F-127[®] Bioreagent was acquired at Sigma-Aldrich.

2.1.1. Solvents. Dimethylsulphoxide R.A. (DMSO) and ethyl acetate R.A. were acquired at Panreac. Acetone and methyl acetate R.A. were purchased from Merck.

2.1.2. Nonsolvents. Type II water, *n*-butanol, *n*-heptane, and amyl acetate were obtained from Merck; propylene glycol from Dow; and Neobee[®] 1053 from Stepan.

NAC handling and quantification: $FeCl_3 \cdot 6H_2O$ and dichloromethane were purchased from Merck; 2,4,6-tris-(2-pyridyl)-*s*-triazine (TPTZ) from Sigma-Aldrich; and HCl from J. Baker.

2.2. Preparation of Nanoparticles

2.2.1. Base Case. Nanoparticles formation was performed by the nanoprecipitation method using acetone as solvent and water as nonsolvent. 10 mg of PLGA RG 502 and 2 mg of NAC were dissolved in 1 mL of acetone in a glass vial. After the reactants' addition, the glass vial was immediately closed to prevent acetone evaporation. The vial was left for 2 h in dissolution at room temperature ($\sim 22^\circ C$) with sporadic shaking by manual inversion. Then, the solution was added manually (~ 1.5 ml/min) into 10 ml of water with Pluronic F-127 1% (w/v) as surfactant, and magnetically stirred. The final suspension was held in stirring during 10 minutes, enough time to allow the solvent to migrate towards the water and form the nanoparticles.

From the base case, several modifications were done in order to increase the entrapment of NAC by the nanoparticles. Figure 2 illustrates the strategy used to minimize

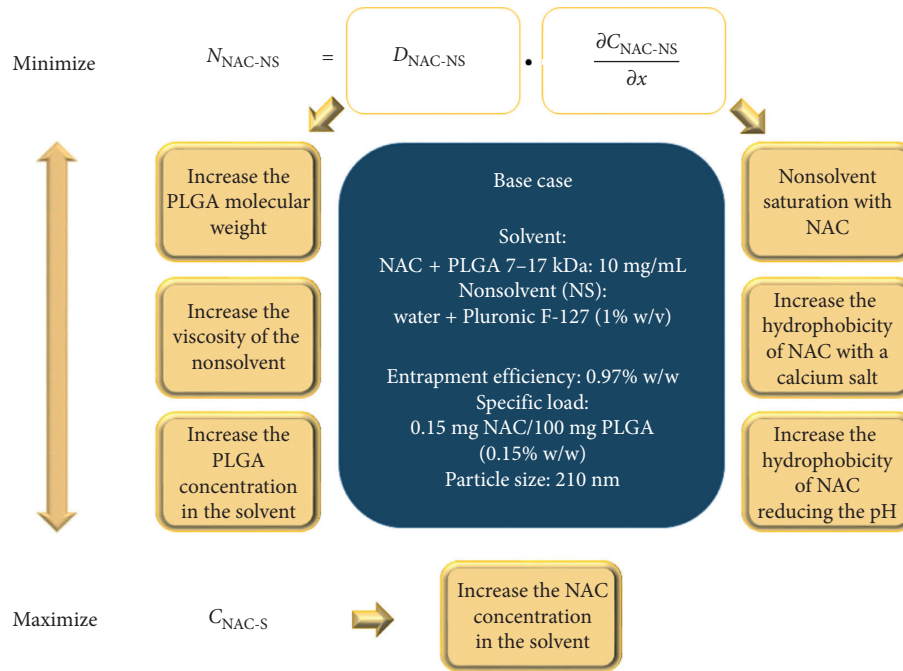


FIGURE 2: Strategies to increase the entrapped NAC in nanoparticles of PLGA.

TABLE 1: Solvent and nonsolvent effect on nanoparticle formation by nanoprecipitation method.

Dielectric constant (ϵ)	Nonsolvent	Particle size (nm)											
		Solvent											
		Ethyl acetate ($\epsilon = 6.0$)			Methyl acetate ($\epsilon = 6.7$)			Acetone ($\epsilon = 20.7$)			DMSO ($\epsilon = 48.9$)		
		No	AE	EL	No	AE	EL	No	AE	EL	No	AE	EL
2.0	Heptane	A	PS	PS	A	PS	PS	A	PS	PS	NM	NM	NM
3.0	Neobee 1053	A	A	PS	A	AS	PS	A	A	PS	NM	NM	NM
5.0	Amyl acetate	A	A	A	A	A	A	A	A	A	NM	NM	NM
17.1	Butanol	A	A	A	A	456.3 ± 15.9	A	A	287.7 ± 5.6	A	536.4 ± 22.3*	524 ± 22.2	A
32.0	Propylene glycol	A	A	A	A	A	A	A	A	A	696.8 ± 13.6*	2772 ± 861*	630.4 ± 7.8*

No: no surfactant used; AE: Bio-Soft N1-7; EL: Stepan-Mild L3; PS: partially soluble in the nonsolvent; A: aggregation; NM: not miscible; *microparticles present in the suspension.

NAC gradient concentration and diffusivity. The following variables were considered:

- (i) Solvent and nonsolvent identity: in the base case, we used acetone as the solvent and water as the nonsolvent with Pluronic F127 as a surfactant. As a strategy to avoid NAC diffusion into water, new couples different from acetone-water were used. The couples were selected according to four criteria: low toxicity (class 3 according to the specifications of the International Council for Harmonisation); miscibility; NAC insolubility in the nonsolvent; and similarity in the dielectric constant values (the higher the difference in the values of these constants, the higher will be the probability of nanoparticles aggregation [18]). Table 1 shows the different couples explored. The surfactant used in the base case was Pluronic F127, which is insoluble in all the nonsolvents used, so other surfactants were used. The surfactants chosen were nonionic to avoid reaction with NAC.
- (ii) Nonsolvent viscosity: diffusivity is inversely proportional to nonsolvent viscosity. Thus, to increase its diffusivity, we added propylene glycol, which is a solvent with a viscosity of 48.6 cP at 25°C. At this temperature, NAC is slightly soluble. In the test, a mixture of equal volumes of propylene glycol and water (6.12 cP) was used, and it was compared with the base case. In both cases, Pluronic F127 was added with a concentration of 1% w/v.
- (iii) Aqueous phase pH: NAC is protonated depending on the pH medium. The most hydrophobic form was reached at pH below 3.3 [25]. Tests were done at aqueous pH of 2.4 and 7.2. Given that NAC becomes unstable at higher levels, no tests at above pH 7.2 were done [26].

- (iv) Solvent and nonsolvent ratio (S:NS): different values were used: 1:2, 1:3, 1:4, 1:5, and 1:10. These values were derived from the literature [23, 27, 28].
- (v) NAC concentration in the solvent: diverse values of NAC were used according to the solvent capacity to dissolve it. 5, 10, and 25 mg/mL (solubility at 25°C~30 mg/mL) were used for acetone, and 2, 25, 50, 80, and 100 mg/mL (solubility at 25°C~100 mg/mL) for were used DMSO.
- (vi) NAC concentration in the nonsolvent: the nonsolvent was enriched with NAC in order to avoid its migration towards the nonsolvent by decreasing the concentration gradient. Thus, the concentration of NAC entrapped inside the nanoparticles increased. In this case, DMSO was used as solvent and NAC (80 mg/mL) was added to the nonsolvent (water + Pluronic F127).
- (vii) Solvent type: the quantity of NAC available to be entrapped inside the nanoparticles is limited by its solubility in the solvent. Although the base case uses acetone, diverse tests were done with DMSO and the mixture (1:1) of acetone-DMSO, due to the high solubility of NAC in DMSO.
- (viii) NAC-calcium salt formation: the neutralization of NAC with calcium hydroxide makes the molecule more hydrophobic [29]. The experiments were done adding the calcic salt of the N-acetylcysteine (NAC-Ca) to the solvent or the calcium chloride (1 mol of CaCl₂; 2 charged moles of NAC) to the nonsolvent (water + Pluronic F-127). The calcium-NAC salt was prepared by blending the NAC solution in water (90 mg/mL) up to pH 6 with calcium hydroxide (0.165 w/v%). Then, the mixture was lyophilized at -47°C and 10 Pa pressure for 32 h [29]. In this assay, the base case solvent was not used because the NAC calcic salt is not soluble in acetone. Therefore, the solvent used was acetone-DMSO in a volumetric proportion of 1:1. As control, NAC was used in the solvent.
- (ix) PLGA concentration: it has been reported that increasing the polymer concentration in the solvent rises the entrapment of the active compound and the particle size [30–32]. Even though the literature has reported values from 5 to 100 mg/ml [33–37], the PLGA concentrations used were 10 (base case) and 20 mg/mL since higher concentrations could increase particle size.
- (x) Polymer molecular weight (Mw): this variable can affect both the releasing velocity and the entrapment efficiency of the active compound [30, 38]. To evaluate this effect, different PLGA (50:50) polymers were used with molecular weight of 7–17 kDa, 38–54 kDa, and 54–59 kDa.

The aim of this research was to obtain nanoparticles with the lowest particle size and the highest entrapment

efficiency. Once all the variables were studied, a final assay was done using the better values found.

2.3. NAC Quantification. The extraction of NAC was carried out with the centrifugation (Hermle Z 233 M-2) of 1 mL of nanoparticle aqueous suspension at 20,000 g for 20 minutes to discard the supernatant. Later, the pellet was washed three times adding 0.7 mL of type II water. To dissolve the resultant pellet, 400 µL of DCM was added and the mixture was shaken with a vortex. The final solution was left at rest for 1 hour to guarantee the complete dissolution of the polymer. Afterward, 400 µL of water was added. The mixture was shaken one more time and centrifuged at 20,000 g for 3 minutes.

The NAC quantification was done in the superior phase (aqueous) by the spectrophotometry method, using an adaptation of Kukoc and Radic's protocol [39, 40]. For 60 µL of the aqueous phase, a reactant was prepared with a solution of 1.2 mL of acetate buffer (0.5 M) pH 3.6; 75 µL of aqueous Fe (III) (10 mM); 75 µL of aqueous solution of 2,4,6-tris-(2-pyridyl)-s-triazine (TPTZ) (10 mM); and 90 µL of water. The final mixture obtained was shaken and kept for 60 minutes at room temperature until a purple color was achieved.

Finally, the absorbance value was quantified at 593 nm wavelength. The same treatment was used as blank with type II water instead of the sample. Concentration was determined using a calibration curve with detection limits ranging between 5 and 140 µg/mL. The tests were carried out at least twice [40].

NAC entrapment efficiency (%NAC) was determined by dividing the NAC mass entrapped inside the nanoparticles by its original added weight in the solvent solution and multiplying the result by 100. The specific load (%w/w NAC/PLGA) was determined by dividing the NAC mass entrapped inside the nanoparticles by the added polymer mass in the solvent solution and multiplying the result by 100.

2.4. Determination of Particle Size, Polydispersity Index, and Zeta Potential. The particle size distribution was determined by the dynamic light scattering (DLS) with a Malvern Zetasizer ZS equipment at 25°C and a nanoparticle concentration of approximately 1 mg/mL. The polydispersity index (PDI) is a parameter obtained simultaneously with the particle size. This index provides information about the sample: values close to 0 indicate that the sample was monodispersed, while values close to 1 indicate that the sample was polydispersed. Zeta potential was determined by laser Doppler velocimetry and phase analysis light scattering using the same equipment.

2.5. Nanoparticle Morphology. The nanoparticle morphology was studied using transmission electronic microscopy (TEM) employing an FEI equipment (Tecnai 20 Twin, 200 kV), with a 120 kV voltage.

3. Results and Discussion

The first assay done under the base case conditions obtained nanoparticles with an average diameter of 210 ± 9 nm and PDI of 0.2 ± 0.04 . The NAC entrapment efficiency was $0.97 \pm 0.2\%$, and the specific load was $0.15 \pm 0.05\%$. Even though the particle size satisfied the expected range, the results showed significantly low entrapment efficiency and specific load levels. These results justify the modifications implemented during the procedure.

3.1. Solvent and Nonsolvent Identity. The NAC is a compound with high solubility in water (100 mg/ml [26]), which means that in this case, the use of water as nonsolvent would reduce its entrapment. A strategy to increase it was to replace water with another nonsolvent completely miscible with the organic solvent. In turn, the new nonsolvent should not solubilize NAC, so, several couples of solvents and nonsolvents were tested (Table 1). The results showed aggregation in the couples with low dielectric constant. Similar results were obtained by Dalpiaz et al. who experimented with acetone (solvent) and cottonseed oil (nonsolvent) to obtain nanoparticles with 200 nm size and a relatively high polydispersity index ranging between 0.3 and 0.4. Conversely, the results obtained from the DMSO and propylene glycol couple without surfactant showed particle sizes of 696.8 nm with a polydispersity index of 0.13. It is worth mentioning that both solvents have the highest dielectric constants (48.9 and 32, resp.). Although particles with the desired size were not achieved (below 250 nm), higher sizes and monodispersions were obtained ($PDI < 0.250$). This appears attractive for other applications, as preventing osteoblasts death in orthopedics applications by incorporating the particles into an acrylic bone cement [41], as an intravesical delivery system to treat bladder diseases [42], or in dryer power inhaler [43] among others.

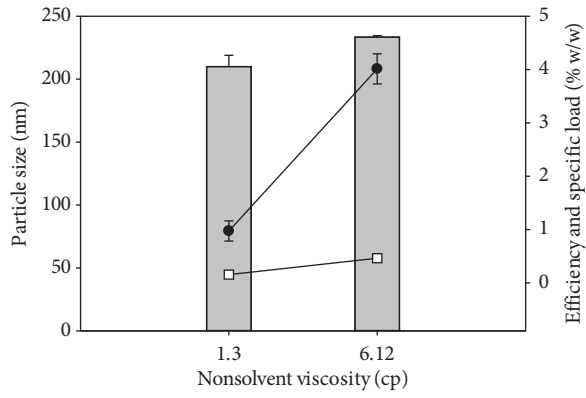
3.2. Nonsolvent Viscosity. Figure 3(a) shows the variation of particle size, efficiency, and specific load with the increase of the nonsolvent viscosity. As you can see, when the nonsolvent (propylene glycol/water 50 : 50) viscosity augmented, the particle size increased slightly (10%). This probably happened because the nanoparticle formation mechanism is given by the migration of the solvent towards to the nonsolvent, which turns the polymer insoluble. When water is enriched with propylene glycol, which is also a polar solvent completely miscible with acetone, the formation mechanism is not altered, showing similar results. In fact, the NAC solubility in water and in water with propylene glycol, it presents no considerable change. Regarding the retained NAC, both the entrapment efficiency and specific charge increased 4 and 3 times, respectively. In this research, we proposed that the higher the medium viscosity, the lower the diffusion of NAC from the acetone polymer solution towards the aqueous phase.

3.3. Aqueous Phase pH. Figure 3(b) shows the effect of the aqueous phase pH over particle size, efficiency, and specific load. Monodispersed nanoparticles with sizes below 250 nm were capable of entrapping NAC in a low percentage. The particle size increased in 18%, the entrapment efficiency in 17%, and the specific load in 18%. Although a higher entrapment of NAC and bigger particles at pH 2.4 than in the same test at neutral pH were observed, this difference could be found in the experimental error. Generally, no significant difference was found either in the entrapment (efficiency and specific charge) or the particle size. This indicates that even though the acid pH makes NAC molecule hydrophobic, the difference is not considerable. Similar results have been reported by Song et al. [23], who varied aqueous phase pH while entrapping vincristine and found that at pH higher than 7, the entrapment increases by 10% (approximately). It was also found that the particle size remains constant.

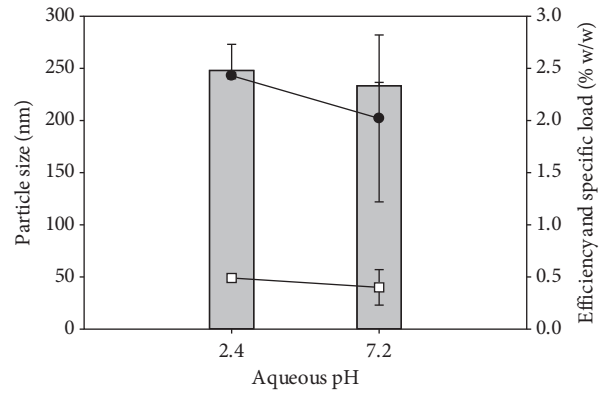
3.4. Solvent and Nonsolvent Ratio (S:NS). The influence of this variable in all the variable responses considered (%NAC, specific load, and particle size) can be observed in Figure 3(c). The particle size increases when a smaller volume is added (S : NS 1 : 2). This occurs because part of the solvent remains in the polymeric matrix, increasing its size. With higher volumes of nonsolvent, the particle size decreases and almost remains constant since 1 : 3. Additionally, entrapment efficiency and specific charge decrease while the aqueous phase volume rises. This is a consequence of the increment in the concentration gradient between the solvent and the nonsolvent. Similar results were reported by other authors [21, 24, 27]. Since low size nanoparticles and high entrapment efficiency are observed, it is concluded that the best ratio S:NS would be 1 : 3. Thus, for further tests, this ratio would be preferred.

3.5. NAC Concentration in the Solvent. The available amount of NAC to be entrapped varies according to the solvent capacity to dissolve it. In the case of acetone, the added concentration cannot be higher than 30 mg/mL (at room temperature $\approx 22^\circ\text{C}$), because at higher concentrations, the solubilization of the compound was not possible. However, the concentration used was higher (100 mg/mL) with DMSO.

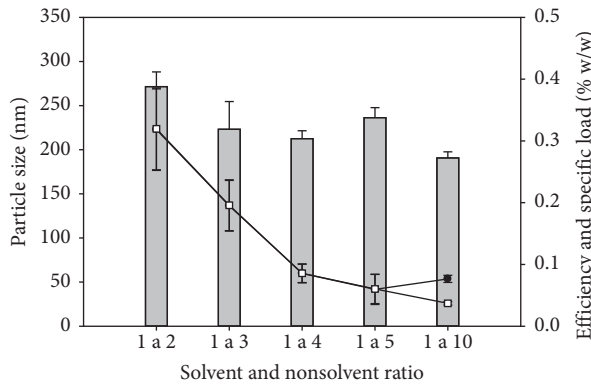
Figures 3(d) and 3(e) show that the particle size does not change significantly for any of the solvents used, and it is not affected by the NAC added. Conversely, it can be affirmed that the active compound does not interfere in the nanoparticle formation because its particle size remains constant, even with higher concentrations (100 mg/mL). The efficiency values are low. However, this behavior is different when it comes to the specific charge since it increases with the NAC amount added and gives a higher quantity of molecules to retain inside the polymeric matrix. The increment of the specific charge is even clearer in DMSO than in acetone, given that the polymer faces a higher amount of NAC. These results indicate that the polymeric matrix can retain a higher number of molecules inside when the quantity of available



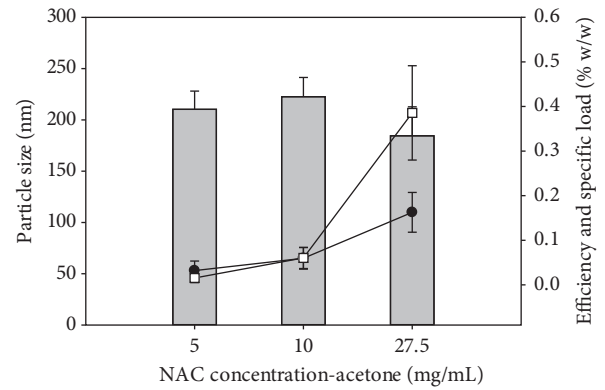
(a)



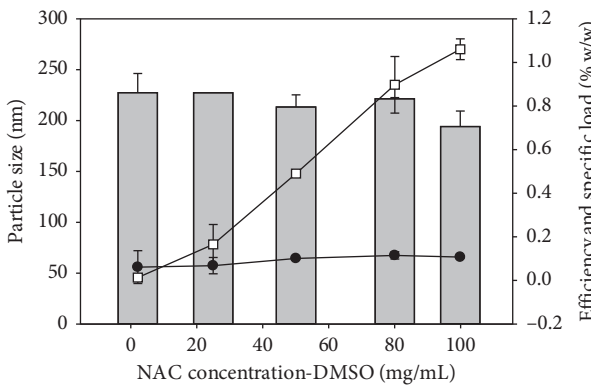
(b)



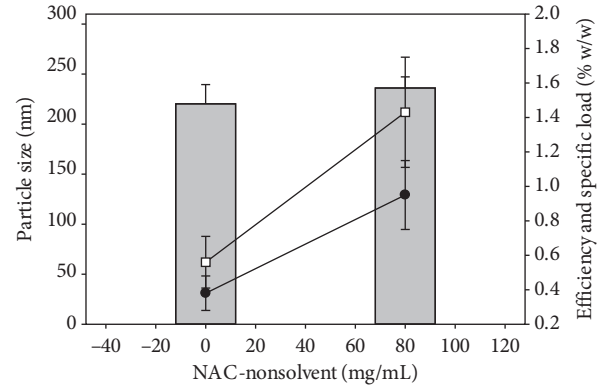
(c)



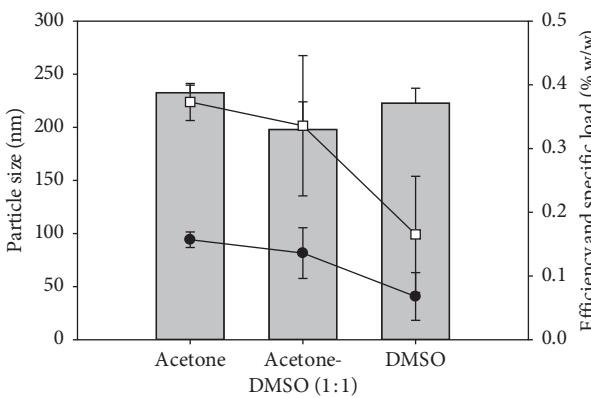
(d)



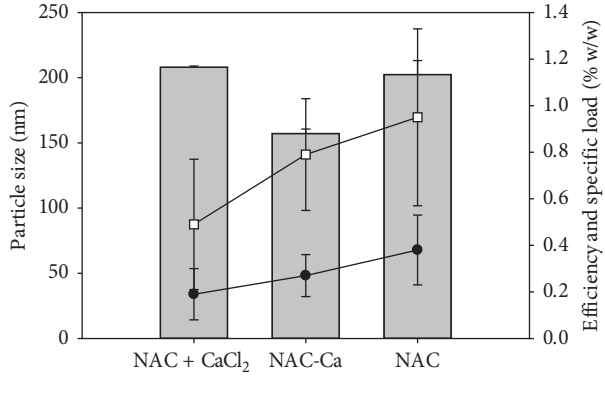
(e)



(f)



(g)



(h)

FIGURE 3: Continued.

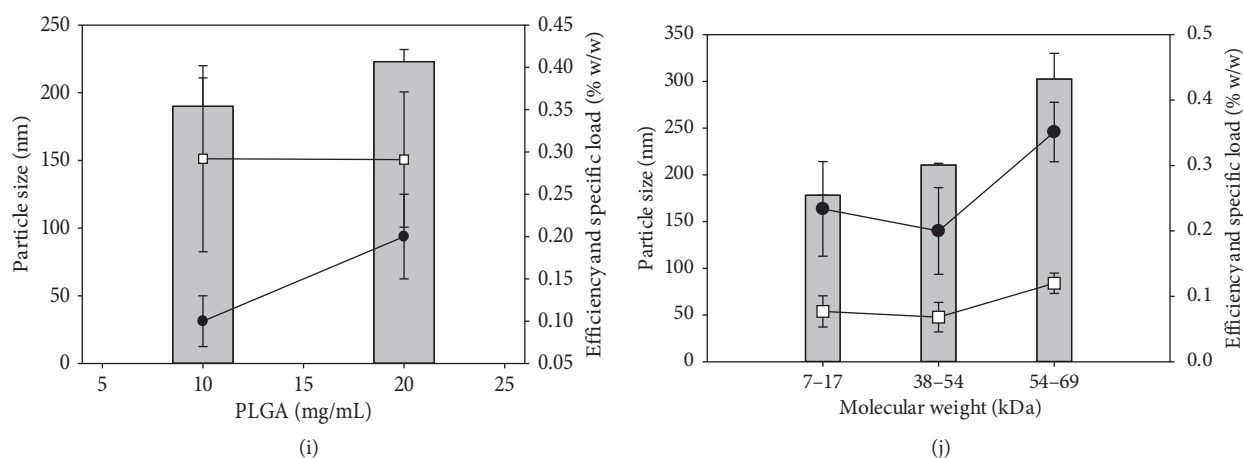


FIGURE 3: Effects of different variables on the average particle size (■), entrapment efficiency (●), and specific load (□) of PLGA nanoparticles loaded with NAC. (a) Nonsolvent viscosity, (b) aqueous phase pH, (c) solvent and nonsolvent ratio, (d) NAC concentration in acetone, (e) NAC concentration in DMSO, (f) NAC concentration in nonsolvent, (g) solvent type, (h) NAC-calcium salt, (i) polymer concentration, and (j) polymer molecular weight.

molecules is higher. Other researchers report similar results using different solvents [44, 45].

3.6. NAC Concentration in the Nonsolvent. In Figure 3(f), the particle size variation, the entrapment efficiency, and the specific load when the NAC is added to the nonsolvent can be observed. The particle size increased slightly (7%), while the entrapment efficiency and the specific load increased 2.5 times approximately. This indicates that the particle size is not significantly affected by the presence of NAC in the nonsolvent, probably due to the low entrapment. In addition, efficiency and specific load increased notably by the NAC presence in the nonsolvent inside the nanoparticles, which may result from the diminishing of the NAC concentration gradient.

Other authors report the addition of active compound to the nonsolvent as a strategy to increase the entrapment [46, 47]. For example, Avgoustakis et al. report similar values for cisplatin entrapment, which increases from 0.1% to 0.66% when saturating the nonsolvent [46]. Although NAC entrapment increases effectively when adding NAC to the nonsolvent (as much as twice), the NAC-enriched aqueous phase will not be used until the final test in order to describe the behavior of other variables.

3.7. Solvent Type. Different tests were done using DMSO, acetone, and a mixture (1:1) of both substances that have low-grade toxicity (class 3 in ICH classification). The aim of the tests with the mixture of solvents was to increase the acetone capacity of solubilizing NAC, considering that they complement each other. DMSO has proven to solubilize NAC in concentrations up to 100 mg/ml, but it presents a higher trend to agglomerate when resuspended after centrifugation. On the contrary, the particles produced with acetone remain in suspension. This can be verified when comparing the zeta potential (-33.4 mV for acetone and -9.8 mV for DMSO).

Figure 3(g) shows that the change of solvent does not affect the particle size, which achieved values ranging between 200 and 250 nm. Similar results including surfactants have been reported. For example, Song et al. found that when surfactant is employed, the particle size remains *quasi* constant [45].

Regarding efficiency and specific charge, a decrement when DMSO is used as solvent was observed. However, such a decrease is observed in acetone and in the mixture of solvents. This allows concluding that the use of a mixture of solvents would be the best option since it allows increasing the amount of NAC that can be added to the solvent, and its separation process by centrifugation would be less susceptible to agglomeration.

3.8. NAC-Calcium Salt Formation. The results of Figure 3(h) show the effect of adding calcium to NAC in order to make it more hydrophobic. When using the NAC salt, it is observed that the particle size decreases almost to 25%, but the efficiency and the specific charge are higher in the samples of NAC without calcium. These results suggest that the presence of calcium ions in the molecule of NAC does not affect the entrapment efficiency. These results contrast to those reported by Desai et al. [29], who improve the entrapment efficiency from 87.9% to 98.4% using salt of NAC-Ca, although the entrapment methodology for the active component is different.

3.9. PLGA Concentration. Results on Figure 3(i) show the effect of increasing the polymer concentration, regarding the particle size, the entrapment efficiency, and the specific load. As you can see, the particle size increased in 17%, while the entrapment efficiency increased almost twice, but the specific load remains without any variation. This happened because the polymer quantity added increased as well as the particle size; therefore, there is a higher capacity to entrap

the active compound inside the nanoparticles. As the specific load is related to the amount of added polymer, and it is increased, the final result is that the specific load remains constant. Similar results have been reported by other researchers [21, 27]. Mora-Huertas et al. report a bigger particle size than the one used in this research [31]. For this reason, the lowest concentration was chosen since it produces smaller particle size and the same specific load.

3.10. Polymer Molecular Weight. Figure 3(j) shows the effect of polymer molecular weight on the particle size, the entrapment efficiency, and the specific load. The particle size changes with the molecular weight. However, for values 7–17 kDa and 38–54 kDa, the change is negligible (18% compared to the value obtained for 7–17 kDa), while for the highest molecular weight (54–69 kDa) it increased almost 70%. Regarding the entrapment efficiency and the specific load, they both increased slightly with the increasing molecular weight, particularly with the higher value (both the entrapment efficiency and the specific load increased almost 50%, compared to the data obtained for 7–17 kDa). Other researchers have reported an increase in the efficiency and particle size with the molecular weight [23, 38, 48]. This indicates that the increase in the particle size happens due to the increase in the polymeric chain length. This would explain the slight increase for both the entrapment efficiency and specific load. It would be necessary to determine the variation of the pore size inside the nanoparticles with the change of molecular weight, to verify whether it is affected or not. Inasmuch as more porous particles are obtained, it would be easier for the compound to abandon the polymeric matrix.

3.10.1. Final Assay. Table 2 shows the effect of the variables studied on the particle size, the efficiency, and specific load. Accordingly, a final assay was proposed using the best found conditions. Water with propylene glycol (1 : 1) and Pluronic F127 was used as nonsolvent (surfactant 1% w/v); this nonsolvent was enriched with NAC (80 mg/mL). As solvent, a mixture of acetone and DMSO (1 : 1) with an NAC concentration of 80 mg/ml and 10 mg/ml of PLGA 38–54 kDa was used. As a result, spherical shape nanoparticles were obtained, which did not present aggregation (Figure 4). The histogram (Figure 5(a)) shows the different particle sizes obtained by TEM, and the Figure 5(b) shows the graph obtained by DLS. Based on micrographs of TEM, particle sizes vary from 76 to 180 nm with an average of 111.6 ± 24.8 (n = 43). These results differ from values obtained by DLS (235.5 ± 11.4 nm). It could be explained by the fact that TEM samples were dried as a preparation for TEM imaging, while DLS reported the hydrodynamic diameter that includes core plus any molecule attached on surface; this kind of difference between these techniques had been reported by other researchers [49, 50]. The nanoparticle zeta potential was -3.42 ± 0.5 mV, the entrapment efficiency was $0.4 \pm 0.04\%$, and the specific load was $3.14 \pm 0.33\%$. The latter increased almost 20 times compared with the data obtained for the base case. As a comparison, other research has reported

TABLE 2: Effect of variables on particle size, entrapment efficiency, and specific load.

Variable	Particle size	Efficiency	Specific load
Viscosity nonsolvent	=	+	+
pH	=	=	=
O/V volume ratio	-	-	-
Concentration NAC solvent	=	=	+
Concentration NAC nonsolvent	=	+	+
Solvent	=	=	=
Ca addition	-	=	=
PLGA concentration	+	+	=
PLGA molecular weight	+	=	=

higher and lower values for the specific load using similar molecules, which were made by the nanoprecipitation method: Lu et al. found 21% for doxorubicin trapped in mPEG-PLGA particles [51], Dalpiaz et al. reported a 7.4% for protamine [14], Govender et al. found 4.1% for Procaine loaded in PLGA nanoparticles [20], Yang et al. reported 2.59% for doxorubicin loaded in PEG-PLA particles [52], and Dalpiaz et al. found 0.26% for N⁶-cyclopentyladenosine. PLGA-NAC nanoparticles have also been obtained by other methods like electrospray with a drug load of 5% [53].

It is necessary to keep optimizing the process in order to obtain higher entrapments and increase the vehicle transport capacity. As a possibility, the NAC size could be increased, by joining this molecule to a bigger one and forming a bond that can be broken by an enzyme in the human body. Other alternative could be to find a solvent that generates smaller pores in order to increase the nanoparticle density and restrict the NAC migration to the nonsolvent or modify the copolymer adding a molecule to make the polymer more hydrophilic.

4. Conclusions

Different alternatives were evaluated in order to increase the entrapment of a hydrophilic low molecular weight compound such as NAC inside PLGA nanoparticles. It was found that the particle size was not affected by the nonsolvent viscosity, the type of solvent, or the NAC concentration in the solvent or nonsolvent. However, the ratio between the solvent and nonsolvent (S:NS), the polymer concentration and molecular weight, the use of calcium salt, and the use of different solvent-nonsolvent couples influence the particle size. It was also found that most of the solvent-nonsolvent couples tested presented agglomeration, except those formed by acetone and DMSO (solvents) with propylene glycol and butanol (nonsolvent), which have a high dielectric constant.

The specific charge and the entrapment efficiency were favored by the increase in the nonsolvent viscosity, the NAC concentration in the solvent, and the enrichment of nonsolvent with NAC. However, both of them decreased with higher volumes of nonsolvent (S:NS).

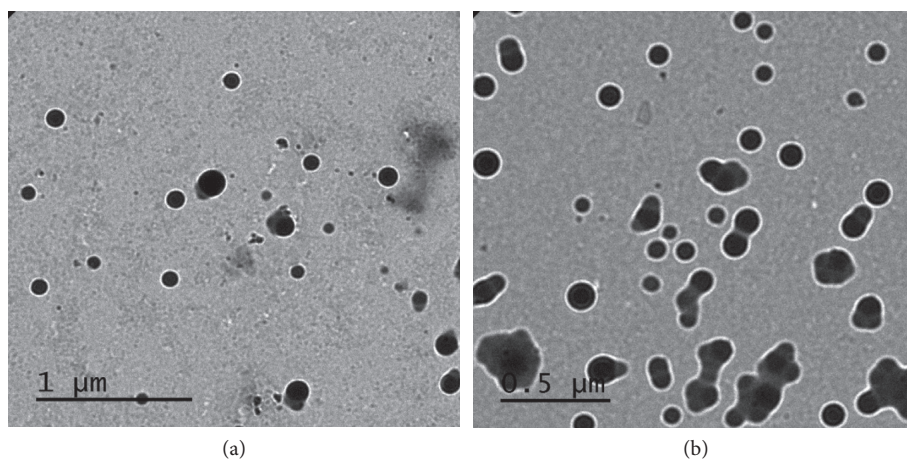


FIGURE 4: Transmission electron micrographs of PLGA-NAC nanoparticles.

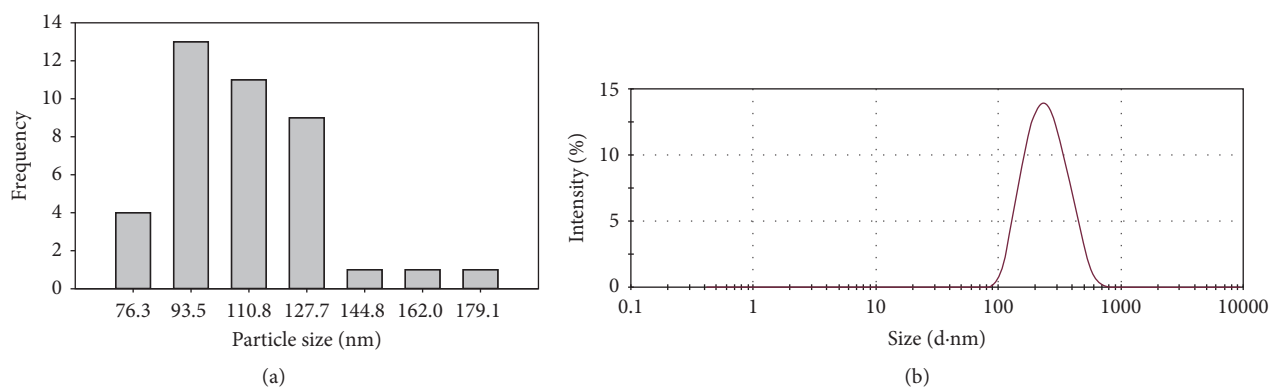


FIGURE 5: (a) Histogram with the distribution of particle size measure by TEM. (b) Distribution of particle size obtained by DLS.

A methodology that allows the NAC entrapped inside PLGA nanoparticles to increase, keeping the particle size below 250 nm and a specific load of 3.1% (20 times higher than the base case). Nevertheless, before using other strategies to increase the entrapment, different tests should be done in order to evaluate whether the current methodology affects or not the NAC biological activity.

Data Availability

All the data are available in <http://www.bdigital.unal.edu.co/55610/13/RuthJannethLancherosSalas.2016.pdf>.

Conflicts of Interest

The authors declare that they have no conflicts of interest.

Acknowledgments

This research was funded by Dirección de Investigación of Bogotá de la Universidad Nacional de Colombia Grant 202010018338 of 2012 and by Departamento Administrativo de Ciencia, Tecnología e Innovación-COLCIENCIAS Grant 110156935147.

References

- [1] H. Bulut and G. H. Sayar, "N-acetylcysteine in treatment of trichotillomania," *Journal of Neurobehavioral Sciences*, vol. 2, no. 3, p. 110, 2015.
- [2] L. Xue, J. Li, Y. Li et al., "N-acetylcysteine protects Chinese hamster ovary cells from oxidative injury and apoptosis induced by microcystin-LR," *International Journal of Clinical and Experimental Medicine*, vol. 8, no. 4, pp. 4911–4921, 2015.
- [3] M. Zafarullah, W. Q. Li, J. Sylvester, and M. Ahmad, "Molecular mechanisms of N-acetylcysteine actions," *Cellular and Molecular Life Sciences (CMLS)*, vol. 60, no. 1, pp. 6–20, 2003.
- [4] S. Naveed, A. Amray, A. Waqas, A. M. Chaudhary, and M. W. Azeem, "Use of N-acetylcysteine in psychiatric conditions among children and adolescents: a scoping review," *Cureus*, vol. 9, no. 11, 2017.
- [5] R. S. Navath, Y. E. Kurtoglu, B. Wang, S. Kannan, R. Romero, and R. M. Kannan, "Dendrimer–drug conjugates for tailored intracellular drug release based on glutathione levels," *Bioconjugate Chemistry*, vol. 19, no. 12, pp. 2446–2455, 2008.
- [6] B. Wang, R. S. Navath, R. Romero, S. Kannan, and R. Kannan, "Anti-inflammatory and anti-oxidant activity of anionic dendrimer-N-acetyl cysteine conjugates in activated microglial cells," *International Journal of Pharmaceutics*, vol. 377, no. 1–2, pp. 159–168, 2009.
- [7] F. Ramazani, W. Chen, C. F. Van Nostrum et al., "Strategies for encapsulation of small hydrophilic and amphiphilic drugs

- in PLGA microspheres: state-of-the-art and challenges,” *International Journal of Pharmaceutics*, vol. 499, pp. 358–367, 2016.
- [8] S. Sharma, A. Parmar, S. Kori, and R. Sandhir, “PLGA-based nanoparticles: a new paradigm in biomedical applications,” *TrAC Trends in Analytical Chemistry*, vol. 80, pp. 30–40, 2016.
- [9] S. Chou, S. Gunaseelan, M. Hussam et al., “A review of injectable and implantable biomaterials for treatment and repair of soft tissues in wound healing,” *Journal of Nanotechnology*, vol. 2017, Article ID 6341710, 15 pages, 2017.
- [10] S. Vrignaud, J.-P. Benoit, and P. Saulnier, “Strategies for the nanoencapsulation of hydrophilic molecules in polymer-based nanoparticles,” *Biomaterials*, vol. 32, no. 33, pp. 8593–604, 2011.
- [11] H. A. Almoustafa, M. A. Alshawsh, and Z. Chik, “Technical aspects of preparing PEG-PLGA nanoparticles as carrier for chemotherapeutic agents by nanoprecipitation method,” *International Journal of Pharmaceutics*, vol. 533, no. 1, pp. 275–284, 2017.
- [12] C. J. Martínez Rivas, M. Tarhini, W. Badri et al., “Nanoprecipitation process: from encapsulation to drug delivery,” *International Journal of Pharmaceutics*, vol. 532, no. 1, pp. 66–81, 2017.
- [13] A. Dalpiaz, E. Vighi, B. Pavan, and E. Leo, “Fabrication via a nonaqueous nanoprecipitation method, characterization and in vitro biological behavior of n 6-cyclopentyladenosine-loaded nanoparticles,” *Journal of Pharmaceutical Sciences*, vol. 98, no. 11, pp. 4272–4284, 2009.
- [14] A. Dalpiaz, F. Sacchetti, A. Baldisserotto et al., “Application of the “in-oil nanoprecipitation” method in the encapsulation of hydrophilic drugs in PLGA nanoparticles,” *Journal of Drug Delivery Science and Technology*, vol. 32, pp. 283–290, 2016.
- [15] K. Avgoustakis, “Pegylated poly(lactide) and poly(lactide-co-glycolide) nanoparticles: preparation, properties and possible applications in drug delivery,” *Current Drug Delivery*, vol. 1, no. 4, pp. 321–333, 2004.
- [16] D. E. Owens and N. Peppas, “Opsonization, biodistribution, and pharmacokinetics of polymeric nanoparticles,” *International Journal of Pharmaceutics*, vol. 307, no. 1, pp. 93–102, 2006.
- [17] H. Takeuchi, H. Yamamoto, and Y. Kawashima, “Mucoadhesive nanoparticulate systems for peptide drug delivery,” *Advanced Drug Delivery Reviews*, vol. 47, no. 1, pp. 39–54, 2001.
- [18] U. Bilati, E. Allemann, and E. Doelker, “Development of a nanoprecipitation method intended for the entrapment of hydrophilic drugs into nanoparticles,” *European Journal of Pharmaceutical Sciences*, vol. 24, no. 1, pp. 67–75, 2005.
- [19] F. Tewes, E. Munnier, B. Antoon et al., “Comparative study of doxorubicin-loaded poly(lactide-co-glycolide) nanoparticles prepared by single and double emulsion methods,” *European Journal of Pharmaceutics and Biopharmaceutics*, vol. 66, no. 3, pp. 488–492, 2007.
- [20] T. Govender, S. Stolnik, M. C. Garnett, L. Illum, and S. S. Davis, “PLGA nanoparticles prepared by nanoprecipitation: drug loading and release studies of a water soluble drug,” *Journal of Controlled Release*, vol. 57, no. 2, pp. 171–185, 1999.
- [21] L. Peltonen, J. Aitta, S. Hyvönen, M. Karjalainen, and J. Hirvonen, “Improved entrapment efficiency of hydrophilic drug substance during nanoprecipitation of poly(l)lactide nanoparticles,” *AAPS PharmSciTech*, vol. 5, no. 1, pp. 115–120, 2004.
- [22] X. Song, Y. Zhao, W. Wu et al., “PLGA nanoparticles simultaneously loaded with vincristine sulfate and verapamil hydrochloride: systematic study of particle size and drug entrapment efficiency,” *International Journal of Pharmaceutics*, vol. 350, no. 1-2, pp. 320–329, 2008.
- [23] X. Song, Y. Zhao, S. Hou et al., “Dual agents loaded PLGA nanoparticles: systematic study of particle size and drug entrapment efficiency,” *European Journal of Pharmaceutics and Biopharmaceutics*, vol. 69, no. 2, pp. 445–453, 2008.
- [24] T. Higuchi, “Mechanism of sustained-action medication,” *Journal of Pharmaceutical Sciences*, vol. 52, no. 12, pp. 1145–1149, 1963.
- [25] B. Noszál, D. Visky, and M. Kraszni, “Population, acid - base, and redox properties of N-acetylcysteine conformers,” *Journal of Medicinal Chemistry*, vol. 43, no. 11, pp. 2176–2182, 2000.
- [26] S. Aldrich Sigma, *Data Sheet, N-Acetyl-L-Cysteine*, 2012.
- [27] J. Cheng, B. A. Tepy, I. Sherifi et al., “Formulation of functionalized PLGA-PEG nanoparticles for in vivo targeted drug delivery,” *Biomaterials*, vol. 28, no. 5, pp. 869–876, 2007.
- [28] F. Danhier, N. Lecouturier, B. Vroman et al., “Paclitaxel-loaded PEGylated PLGA-based nanoparticles: in vitro and in vivo evaluation,” *Journal of Controlled Release*, vol. 133, no. 1, pp. 11–17, 2009.
- [29] K. Desai, S. Mallery, and S. Schwendeman, “Formulation and characterization of injectable poly(-lactide-co- glycolide) implants loaded with N-acetylcysteine, a MMP inhibitor,” *Pharmaceutical Research*, vol. 25, no. 3, pp. 586–597, 2008.
- [30] A. Budhian, S. J. Siegel, and K. I. Winey, “Haloperidol-loaded PLGA nanoparticles: systematic study of particle size and drug content,” *International Journal of Pharmaceutics*, vol. 336, no. 2, pp. 367–375, 2007.
- [31] C. E. Mora-Huertas, H. Fessi, and A. Elaissari, “Influence of process and formulation parameters on the formation of submicron particles by solvent displacement and emulsification-diffusion methods. Critical comparison,” *Advances in Colloid and Interface Science*, vol. 163, no. 2, pp. 90–122, 2011.
- [32] H.-Y. Kwon, J.-Y. Lee, S.-W. Choi, Y. Jang, and J.-H. Kim, “Preparation of PLGA nanoparticles containing estrogen by emulsification–diffusion method,” *Colloids and Surfaces A: Physicochemical and Engineering Aspects*, vol. 182, no. 1–3, pp. 123–130, 2001.
- [33] G. Dalwadi and B. Sunderland, “An ion pairing approach to increase the loading of hydrophilic and lipophilic drugs into PEGylated PLGA nanoparticles,” *European Journal of Pharmaceutics and Biopharmaceutics*, vol. 71, no. 2, pp. 231–242, 2009.
- [34] A. Beletsi, Z. Panagi, and K. Avgoustakis, “Biodistribution properties of nanoparticles based on mixtures of PLGA with PLGA-PEG diblock copolymers,” *International Journal of Pharmaceutics*, vol. 298, no. 1, pp. 233–241, 2005.
- [35] V. Saxena, M. Sadoqi, and J. Shao, “Indocyanine green-loaded biodegradable nanoparticles: preparation, physicochemical characterization and in vitro release,” *International Journal of Pharmaceutics*, vol. 278, no. 2, pp. 293–301, 2004.
- [36] E. Cenni, D. Granchi, S. Avnet et al., “Biocompatibility of poly (D,L-lactide-co-glycolide) nanoparticles conjugated with alendronate,” *Biomaterials*, vol. 29, no. 10, pp. 1400–1411, 2008.
- [37] F. N. Costa, A. L. Ibiapino, L. P. de Figueiredo et al., “Preliminary evaluation of the encapsulation of new antidiabetic sulphonylhydrazones and antitumor N-acylhydrazones derivatives using PLGA nanoparticles,” *Journal of Physics: Conference Series*, vol. 617, article 012015, 2015.
- [38] R. C. Mundargi, V. R. Babu, V. Rangaswamy, P. Patel, and T. M. Aminabhavi, “Nano/micro technologies for delivering

- macromolecular therapeutics using poly(D,L-lactide-co-glycolide) and its derivatives,” *Journal of Controlled Release*, vol. 125, no. 3, pp. 193–209, 2008.
- [39] L. Kukoc-Modun and N. Radić, “Kinetic spectrophotometric determination of N-acetyl-L-cysteine based on a coupled redox-complexation reaction,” *Analytical Sciences*, vol. 26, no. 4, pp. 491–495, 2010.
- [40] L. Kukoc-Modun and N. Radić, “Spectrophotometric determination of N-acetyl-L-cysteine and N-(2-mercaptopropionyl)-glycine in pharmaceutical preparations,” *International Journal of Analytical Chemistry*, vol. 2011, Article ID 140756, 6 pages, 2011.
- [41] H. Aita, N. Tsukimura, M. Yamada et al., “N-acetyl cysteine prevents polymethyl methacrylate bone cement extract-induced cell death and functional suppression of rat primary osteoblasts,” *Journal of Biomedical Materials Research Part A*, vol. 92, no. 1, pp. 285–296, 2009.
- [42] N. Denora, A. Lopodota, M. Perrone et al., “Spray-dried mucoadhesives for intravesical drug delivery using N-acetylcysteine-and glutathione-glycol chitosan conjugates,” *Acta Biomaterialia*, vol. 43, pp. 170–184, 2016.
- [43] M. D. Manniello, P. Del, R. P. Aquino, and P. Russo, “Clarithromycin and N-acetylcysteine co-spray-dried powders for pulmonary drug delivery: a focus on drug solubility,” *International Journal of Pharmaceutics*, vol. 533, no. 2, pp. 463–469, 2017.
- [44] B. Sinha, B. Mukherjee, and G. Pattnaik, “Poly-lactide-co-glycolide nanoparticles containing voriconazole for pulmonary delivery: in vitro and in vivo study,” *Nanomedicine: Nanotechnology, Biology and Medicine*, vol. 9, no. 1, pp. 94–104, 2013.
- [45] K. C. Song, H. S. Lee, I. Y. Choung, K. I. Cho, Y. Ahn, and E. J. Choi, “The effect of type of organic phase solvents on the particle size of poly(d,l-lactide-co-glycolide) nanoparticles,” *Colloids and Surfaces A: Physicochemical and Engineering Aspects*, vol. 276, no. 1–3, pp. 162–167, 2006.
- [46] K. Avgoustakis, A. Beletsi, Z. Panagi, P. Klepetsanis, A. G. Karydas, and D. S. Ithakissios, “PLGA-mPEG nanoparticles of cisplatin: in vitro nanoparticle degradation, in vitro drug release and in vivo drug residence in blood properties,” *Journal of Controlled Release*, vol. 79, no. 1–3, pp. 123–135, 2002.
- [47] D. Moreno, S. Zalba, I. Navarro, C. Tros de Ilarduya, and M. J. Garrido, “Pharmacodynamics of cisplatin-loaded PLGA nanoparticles administered to tumor-bearing mice,” *European Journal of Pharmaceutics and Biopharmaceutics*, vol. 74, no. 2, pp. 265–274, 2010.
- [48] G. Mittal, D. K. Sahana, V. Bhardwaj, and M. N. V. Ravi Kumar, “Estradiol loaded PLGA nanoparticles for oral administration: effect of polymer molecular weight and copolymer composition on release behavior in vitro and in vivo,” *Journal of Controlled Release*, vol. 119, no. 1, pp. 77–85, 2007.
- [49] E. Yoo, Y. Liu, C. A. Nwasike et al., “Surface characterization of nanoparticles using near-field light scattering,” *Beilstein Journal of Nanotechnology*, vol. 9, pp. 1228–1238, 2018.
- [50] K. L. Douglas and M. Tabrizian, “Effect of experimental parameters on the formation of alginate-chitosan nanoparticles and evaluation of their potential application as DNA carrier,” *Journal of Biomaterials Science, Polymer Edition*, vol. 16, no. 1, pp. 43–56, 2005.
- [51] P. Lu, Y. Chen, T. Ou et al., “Multifunctional hollow nanoparticles based on graft-diblock copolymers for doxorubicin delivery,” *Biomaterials*, vol. 32, no. 8, pp. 2213–2221, 2011.
- [52] Q. Yang, L. Tan, C. He et al., “Redox-responsive micelles self-assembled from dynamic covalent block copolymers for intracellular drug delivery,” *Acta Biomaterialia*, vol. 17, pp. 193–200, 2015.
- [53] A. Akbar, K. Zarchi, S. Abbasi et al., “Development and optimization of N-acetylcysteine-loaded poly (lactic-co-glycolic acid) nanoparticles by electrospray,” *International Journal of Biological Macromolecules*, vol. 72, pp. 764–770, 2015.

Research Article

Arsenic Retention on Technosols Prepared with Nanoparticles and Ferric Soil from Mine Drainage Water

Darío R. Bolaños-Guerrón ^{1,2} Viviana P. Sánchez-Gómez,² Johanna Paz,³
Andrés R. Izquierdo ^{1,4} Carina Stael,¹ and María Balseiro-Romero⁵

¹Centro de Nanociencia y Nanotecnología (CENCINAT), Universidad de las Fuerzas Armadas ESPE, Av. Gral. Rumiñahui s/n, P.O. Box 171-5-231B, Sangolquí, Ecuador

²Department of Earth Science and Constructions, Geographical and Environmental Engineering, Universidad de las Fuerzas Armadas ESPE, Sangolquí, Ecuador

³Department Life Science and Agriculture, Universidad de las Fuerzas Armadas ESPE, Sangolquí, Ecuador

⁴Grupo de Investigación en Microbiología y Ambiente (GIMA), Universidad de las Fuerzas Armadas ESPE, Sangolquí, Ecuador

⁵Department of Chemical Engineering, Centre for Research in Environmental Technologies (CRETUS), Universidade de Santiago de Compostela, Santiago, Spain

Correspondence should be addressed to Darío R. Bolaños-Guerrón; drbolanos@espe.edu.ec

Received 7 March 2018; Accepted 5 June 2018; Published 2 July 2018

Academic Editor: David Quesada

Copyright © 2018 Darío R. Bolaños-Guerrón et al. This is an open access article distributed under the Creative Commons Attribution License, which permits unrestricted use, distribution, and reproduction in any medium, provided the original work is properly cited.

Mining activities generate a large amount of solid waste and acid drains that contain heavy metals in high concentrations. In wastewater of gold mines from Southern Ecuador (Portovelo), arsenic concentrations between 4.8 and 27.5 $\mu\text{g/L}$ have been detected. In this context, the objective of this study is to prepare a technosol, which was used in the capture of arsenic dissolved in the acid drains. Technosol was elaborated using a clay-silty soil (iron-rich soil), collected in the mining area, and iron nanoparticles synthesized with the extract of orange peel. The technosol was experimentally characterized using adsorption isotherms and uptake kinetics. Besides, a mathematical model was developed using Vensim[®] to scale the process and predict the dynamic behavior of the adsorbent. Results indicate that adsorption behavior of technosol can be fitted to Langmuir isotherms ($R^2 > 0.9$), with 95% of adsorption of As from an input of 4.5 mg/L. The model will be useful to predict the time needed to remedy contaminated water and the duration of the adsorbent (until its saturation).

1. Introduction

Arsenic is a trace element of high toxicity and carcinogenicity, whose natural environmental distribution presents an enormous variability and ubiquity due to a combination of climate and geology but without a significant correlation [1, 2]. Arsenic concentrations in the environment may increase due to anthropogenic activities, being agriculture, mining, and petroleum refining, the main activities contributing to the contamination of soil and water resources [3].

Specifically, mine drainage water may present enormously high concentrations of heavy metals, with the consequent risks for the ecosystems and human health. This contaminated water

may leach and migrate (according to soil and geological properties and environmental conditions) to ground and spring water, becoming a potential contaminant of drinking water sources [4]. Therefore, the elimination of As from water bodies is considered one of the most important environmental challenges at a global level. All over the world, many studies have been carried out by the World Health Organization (WHO), the European Union (EU), and the United States Environmental Protection Agency (US EPA), among other international organizations, in order to establish the best water decontamination techniques according to toxicity and economical studies [5].

There are many available technologies to clean up As-contaminated water, whose efficiency and applicability will

mainly depend on the chemical form of As in water [3]. The techniques most commonly applied include oxidation to solid As(V) and filtration [3]; phytoremediation (mainly by phytoaccumulation and phytofiltration) [6]; coagulation-flocculation using ferric and aluminium salts [7]; adsorption on solid sorbents [8]; ion exchange using resins [9]; and membrane technologies (by micro- and nanofiltration or osmosis) [10].

Particularly, the immobilization (adsorption) of As in specific sorbents has been widely used due to its high versatility, easy operation and handling, and low costs. Furthermore, due to the development and application of novel materials with extremely high sorbent capacities, this technique can be applied with a significant efficiency. In this context, the use of nanosorbents has emerged as a promising alternative for the cleanup of As-contaminated water (particularly, zero valent and iron oxide nanoparticles), due to their distinctive and advantageous properties, such as the small size, high surface area, and high reactivity due to the large number of sorption active sites [11, 12].

On the contrary, the application of specifically “tailored” technosols (in this case, composed of soil components and nonharmful residues with sorption capacities for specific contaminants) has shown successful results on the restoration of degraded mining areas contaminated with a wide variety of trace metals and metalloids [13]. One of the main advantages of the use of “tailored” technosols is managing the increasing production of (nonharmful) residues, taking advantage of their properties to adsorb contaminants [14].

Adsorption is a very complex water remediation process that depends on a wide variety of parameters, including (a) water properties, such as pH, redox potential, and ionic composition of water (other ions present in water can compete with As for sorption sites); (b) As properties (particularly, the speciation or oxidation state); and (c) sorbent properties, such as the surface area, the size, the reactivity, and the number of sorption active sites [3]. Thus, modelling can be a very useful tool to help the researchers to design dynamic water remediation processes based on sorption, and models may be used to determine the amount and lifetime of the sorbent needed according to the volume and As concentration of the contaminated water to treat.

Within this context, the objective of the present work was to characterize the arsenic sorption capacity of a tailored technosol composed of a ferralsol with 25531 mg/kg of Fe (2% w/w, associated with Fe and Mn oxides) and multi-component nanoparticles synthesized from orange peel residues. An adsorption model was also developed to simulate the real application of those sorbents to the remediation of mine drainage water rich in As. The model proposed will allow scaling-up the remediation procedure from the laboratory to field application in a gold mining area in Portovelo (South Ecuador).

2. Materials and Methods

2.1. Soil and Water Sampling and On-Site Characterization. Water samples (acid discharges) were collected at three discharges of artesian gold-processing plants located in the

border of the Amarillo River (Figure 1), Portovelo town, Ecuador, the main collector of liquid wastes from the gold-processing artesian plants. pH, Eh, and electric conductivity were measured on-site using portable equipment (Mettler Toledo). Three zones were chosen for soil sampling taking in consideration their beneficial properties and the vicinity of the study area. All soil samples had a high content of iron oxides.

2.2. Soil Characterization. Chemical characterization of Cu, Cd, Zn, Cr, Pb, As, and Fe in soil was carried out by sequential digestion using methods 3111-B and 3114-C of the Standard Methods, with atomic absorption spectroscopy, AAnalyst 800 Atomic Absorption Spectrometer (Pelkin Elmer), using the air-acetylene flame method. Determination of arsenic was made with the FIAS injection system coupled to the atomic absorption spectrophotometer AAnalyst 800 Atomic Absorption Spectrometer (Pelkin Elmer).

Values of pH of soil were determined using the potentiometric method. For texture of soil, percentages of clay, silt, and soil sand were quantified, and to determine the granulometry of the soil, the method ASTM D422-6 was applied.

2.3. Synthesis of Nanoparticles. Fabrication of multicomponent nanoparticles (MCNPs) was achieved by mixing 5.0 mL of 1.0 M FeCl₃·6H₂O and 3.5 mL of 1.0 M Na₂SO₄ and purging the content with nitrogen for 15 min in a 1000 mL flask. Then, 20 mL of 0.8 M NaBH₄ and 20 mL of orange peel extract were added as coreductants. The mixture was homogenized with slow shaking at 30 rpm during 15 min at room temperature. During the evolution of the reaction, a color change from yellow to black was observed indicating the formation of MCNPs.

2.4. Preparation of Technosol. The technosol was prepared mixing 99.95% of a clay-silty soil (iron-rich soil) and 0.05% of dried MCNPs.

2.5. Sorption Isotherm Tests. Arsenic sorption was performed in batch tests using 5 g of technosol (4.9875 g of soil and 12.5 mg of nanoparticles). The sorbent material was mixed with 100 mL of artificially contaminated water, containing 10.9, 16.5, 80.6, 346.4, 2732.5, and 5286 µg/L of arsenic at pH 7. After 24 hours of agitation at 40 rpm, the treated samples were centrifuged and filtered, and the supernatant was analyzed for free arsenic using the same method as for water samples. The amount of arsenic sorbed on the technosol was determined by mass balance using the following equation [15]:

$$q = \frac{V}{m}(C_i - C_f), \quad (1)$$

where q is the concentration of As in the soil, V is the volume of water contaminated with As, m is the mass of soil, and C_i and C_f are the initial and final As concentrations, respectively.

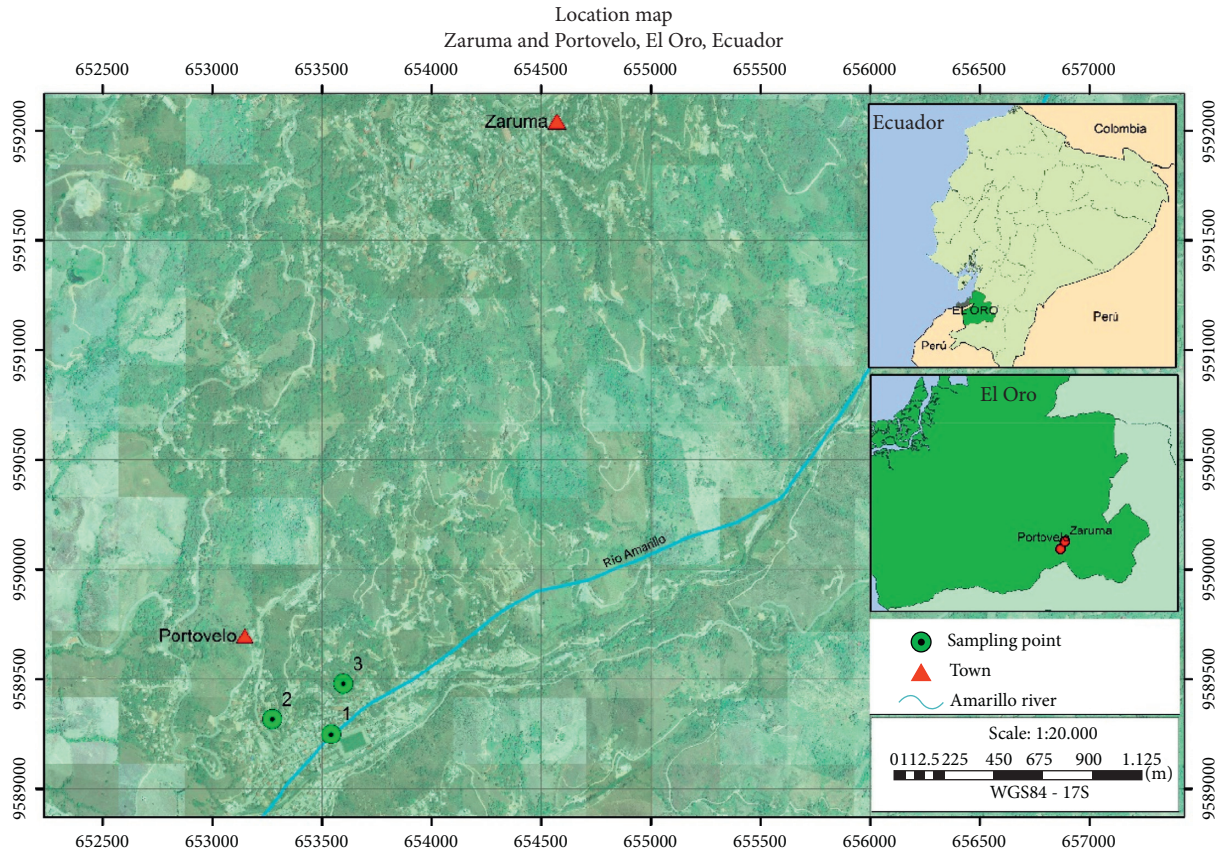


FIGURE 1: Location of study.

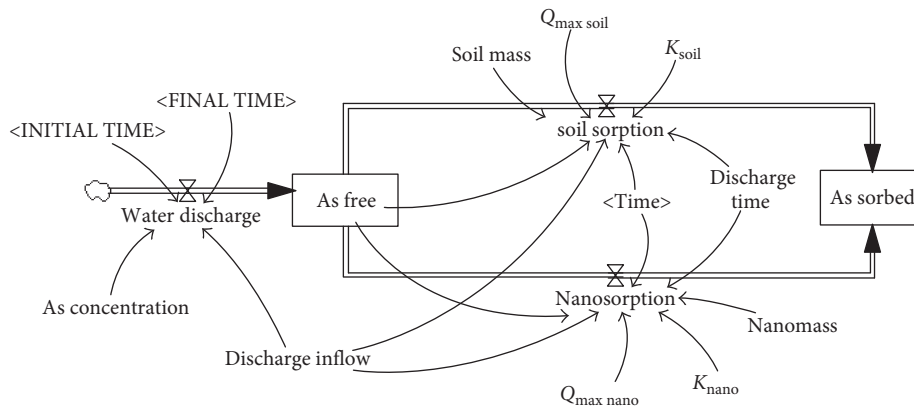


FIGURE 2: Stock-and-flow diagram of the model constructed using Vensim software.

2.6. *Kinetic Test.* The kinetics was performed with 5 g of technosol and 100 mL of artificially contaminated water at pH 7 and 20°C. During the test, two milliliters of the treated aqueous phase were centrifuged and filtered with 0.2 μm PVDF filters for arsenic analysis.

2.7. *Chemical Analysis.* Heavy metals were analyzed using an atomic absorption spectrometer AAnalyst 800 (Pelkin Elmer) (AA800) following standardized methods (i.e., Cu, Cd, Zn, Cr, Pb, Fe, and As). For arsenic analysis, AA800 was

coupled with a FIAS 110 (Flow Injection for Atomic Spectroscopy System) and the method 3114-C was used.

2.8. *Model Formulation Based on System Dynamics Methodology.* The system under study can be considered as a suspended-bed mixed reactor where the contaminated mine water enters and stays in contact with the sorbent until the complete water cleanup. Figure 2 shows the stock-and-flow diagram constructed using Vensim software (Ventana Systems, Inc.).

TABLE 1: Variables used for the formulation of the model, including the equations, and the determination or estimation methods.

	Variables	Equation/determination or estimation method
Stocks	As free (mg·As)	= MAX (Water discharge – soil sorption – nanosorption, 0) ¹
	As sorbed (mg·As)	= soil sorption + nanosorption
Flows	Water discharge (mg·As/h)	= discharge inflow · As concentration · PULSE TRAIN (INITIAL TIME, 72, 168, FINAL TIME) ²
	Soil sorption (mg·As/h)	= DELAY1 (($Q_{\max\text{soil}} \cdot K_{\text{soil}} \cdot \text{As free} / (1 + K_{\text{soil}} \cdot \text{As free})^2$) · (soil mass / discharge inflow · time), discharge time) ³
	Nano(particles) sorption (mg·As/h)	= DELAY1 (($Q_{\max\text{nano}} \cdot K_{\text{nano}} \cdot \text{As free} / (1 + K_{\text{nano}} \cdot \text{As free})^2$) · (nano mass / discharge inflow · time), discharge time) ³
Auxiliary	Time	Time of the simulation
	Initial time	0 h (initial time of the simulation)
	Final time	672 h (final time of the simulation)
	As concentration	4.5 mg/L (determination by AAS in real water discharge)
	Discharge inflow	3 L/h (field observation)
	$Q_{\max\text{soil/nano}}$; $K_{\text{soil/nano}}$ ⁴	Estimated from laboratory sorption experiments with soil and nanoparticles
	Soil mass ⁵	5 kg (estimated from laboratory experiments)
Nano(particles) mass ⁵	0.025 kg (estimated from laboratory experiments)	
	Discharge time	72 h (field observation)

¹The function MAX of Vensim allows us to have a concentration of As free which is always positive or 0 (never negative). ²The function PULSE TRAIN returns 1 value (presence of contaminated water discharge), starting at “INITIAL TIME” and ending at “FINAL TIME,” for 72 h, each 168 h. The rest of the time, it returns a value of 0 (absence of contaminated water discharge). ³The function DELAY1 returns a first order exponential delay of the adsorption on soil and nanoparticles during the residence time. These equations correspond to the derivation of Langmuir equations with respect to time. The second fraction of the equation is used to adjust the units. ⁴ Q_{\max} and K of soil and nanoparticles where the parameters calculated using the experiments included in this work. ⁵The ratio of mass of soil and nanoparticles corresponded to that used in the laboratory experimentation used in this work.

Based on system dynamics methodology, two stocks (or variables where positive or negative accumulation takes place; represented by squares) were considered within the reactor system: “As free” (i.e., mass of As remaining in the residual water which enters the reactor) and “As sorbed” (i.e., mass of As retained by technosol = soil + nanoparticles). The flows that modified those stocks (represented as double-lined arrows) are as follows: “water discharge” (discharge of As-contaminated water; inflow to “As-free” stock), “soil sorption,” and “nanosorption” (As sorption on soil and on nanoparticles, resp.; outflows from “As-free” stock and inflows to “As sorbed”). Note that there is no outflow from the system, since during the simulation time the reactor was not emptied. The rest of variables, namely, auxiliary variables, were connected to the variables that they help to calculate using single arrows. “INITIAL TIME,” “FINAL TIME,” and “Time,” intrinsically included in the modelling were considered shadow variables and were introduced in the model for the calculation of specific flows. The auxiliary parameters to simulate the system were estimated from field observations and calculations (As concentration in drainage water and the discharge inflow) and those calculated from the laboratory experiments described before (soil and nanoparticle mass and Q_{\max} and K of soil and nanoparticles) (Table 1).

Furthermore, several assumptions were considered to formulate the model. (i) The system is perfectly mixed, and therefore, the concentration of As in water is homogenous in

each water discharge, and all sorbent particles are in intimate contact with water. (ii) The discharge of residual and drainage water (“water discharge”) in the mine was supposed to be discontinuous and should be modelled as a “binary” discharge (presence or absence of inflow to the reactor). When a discharge of water occurs, the inflow to the reactor was supposed to be constant. According to field observations of the mine activity, the discharge of residual water occurs each week (each 168 h), and the water enters the reactor continuously for only 72 h (corresponding also to the “discharge time”) at a constant flow of 3 L/h (i.e., 216 L of contaminated water entered the tank at each discharge), after which it stops for 4 days, completing a discharge cycle of one-week duration. (iii) The maximum capacity of the reactor tank was assumed to be 1000 L. Therefore, it can hold a volume of water corresponding to maximum four consecutive discharge cycles (i.e., 864 L), then, during 4 weeks (672 h, which corresponds to the final time of the simulation). After a month, the reactor should be emptied and the water inside should be completely cleaned up. (iv) Sorption on technosol particles (including soil and nanoparticles) followed the Langmuir sorption model, and the partial derivative of that equation with respect to time was used to simulate sorption flows (Table 1). (v) A first order exponential delay was supposed to occur at the first moments of the contact between the contaminated water and the sorbent; that is, sorption is not immediate and is delayed while the complete contact between the contaminants and the sorbent

TABLE 2: Characterization of soil.

	Cu (mg/kg)	Cd (mg/Kg)	Zn (mg/kg)	Cr (mg/kg)	Pb (mg/kg)
F1: interchangeable	0.37	0.56	0.78	1.65	2.26
F2: linked to carbonates	1.23	0.5	2.11	0.96	5.7
F3: linked to Mn and Fe oxides	1.89	0	154.32	1.12	6.42
F4: linked to organic matter	3.54	0.15	5.27	2.78	1.67
F5: residual	4.5	0	6.94	0.75	3.21
Total	11.53	1.21	169.42	7.26	19.26

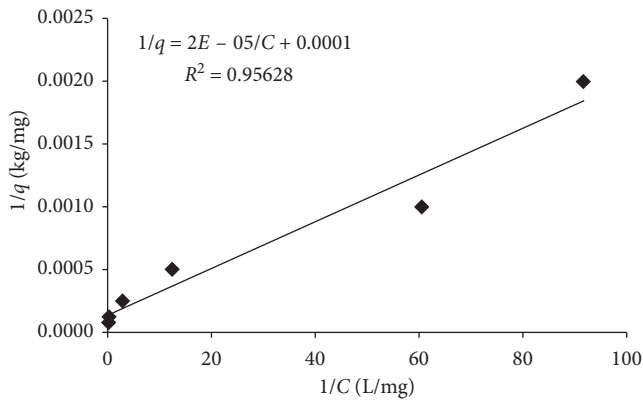


FIGURE 3: Langmuir isotherm for technosol (soil and MCNPs).

does not occur. (vi) The amount of technosol used in the reactor was 5 kg of soil and 0.025 kg of nanoparticles.

3. Results and Discussion

Mine drainage samples collected near to the Amarillo River presented a pH of 8.56 and an Eh of -107.50 mV. Under those conditions, arsenic is probably precipitating into the river basin. However, the variation of these parameters can easily lead to the release and mobilization of As to water, what is evidenced by the variation of As concentrations from 4.80, 8.60, and 27.46 $\mu\text{g/L}$. Aqueous samples had a very high EC (964 $\mu\text{S/cm}$). A clay-silty soil with pH of 5.34 and 20.25 meq/100 g soil of cation exchange capacity was chosen for preparing the technosol. Concentrations of metals in soil are shown in Table 2. Important to note that iron content was 25531.24 mg/kg with 432.88 mg/kg of Fe associated with oxides (i.e., 2% w/w). Sorption isotherm of the technosol is shown in Figure 3. It is observed that experimental data fit very well with the Langmuir model. The calculated Langmuir isotherm parameters are $Q_{\text{max}} = 7184.66$ mg/kg and $K = 7.5$ L/mg. Results of the kinetic tests of arsenic are shown in Figures 4(a) and 4(b). The experimental values fit a pseudo-second-order reaction shown below:

$$\frac{t}{q} = \frac{1}{k_2 q_e^2} + \frac{t}{q_e} \quad (2)$$

where k_2 (g/mg/min) is the pseudo-second-order rate constant, q_e is the amount of arsenic sorbed (mg/g) at the equilibrium, and q_t is the amount of the sorption at any time t (min). Good removal efficiency for arsenic was achieved with technosol (124 mg·As/kg) even though these tests were performed with heavy metals as competitor elements.

The fitting curve exhibits a good linearity with a correlation coefficient around the unity as shown in Figure 4. This trend suggests that chemical sorption is the main mechanism for the removal of arsenic from the mine drainage [16, 17].

3.1. Model Simulations. The sorption model was simulated using the equations and parameters described in Table 1. The model was simulated from 0 (“INITIAL TIME”) to 672 h (4 weeks) (“FINAL TIME”), and the variation of As mass in water (“As free”) and As mass sorbed on the technosol (“As sorbed”) was recorded. Note that these data are presented in Figure 5 as the concentration of As on the accumulated water in the reactor (mg/L) and the concentration of As sorbed on the technosol (mg/kg).

It can be observed that the concentration of As in water (“As free”) was decreased very fast and was maintained at approximately 0.17 mg/L at the first moments of the simulation (until 168 h, one week, during the first step of water discharge) (Figure 5), from when the concentration of As in water started to increase (up to 1.61 mg/L during the second discharge of water), following the discontinuity of the cycles of water discharge considered in the model (Table 1). On the contrary, a rapid increase of As concentration on the sorbent could be observed, but it started to slow down after the first week of treatment, mainly due to the saturation of the sorbent. Thus, near 96% of As of the first discharge of contaminated water was eliminated by sorption on technosol. The level of As in water after the treatment of two water discharges (up to 336 h) was observed to be very high (1.61 mg/L), indicating that the second discharge of water cannot be treated completely with the same sorbent under the same conditions to reach our final quality objectives.

Since both soil and nanoparticle sorption followed the Langmuir sorption model, “soil sorption” and “nanosorption” flows presented very similar patterns (Figure 6). It can be observed that As sorption increased until a maximum reached around the first 25 h, from when sorption slows down, indicating the beginning of the saturation of the sorbent sorption sites.

Therefore, we can assume that considering the contaminant concentration and inflow to the reactor (Table 1), the amount of sorbent included in the reactor (5 kg of soil and 0.025 kg of nanoparticles) will work for one entire contaminated water discharge (i.e., during the first cycle of 168 h) reducing the concentration of the effluent to nearly 0.17 mg/L. After that moment, the sorbent should be renovated at each discharge under the same operational

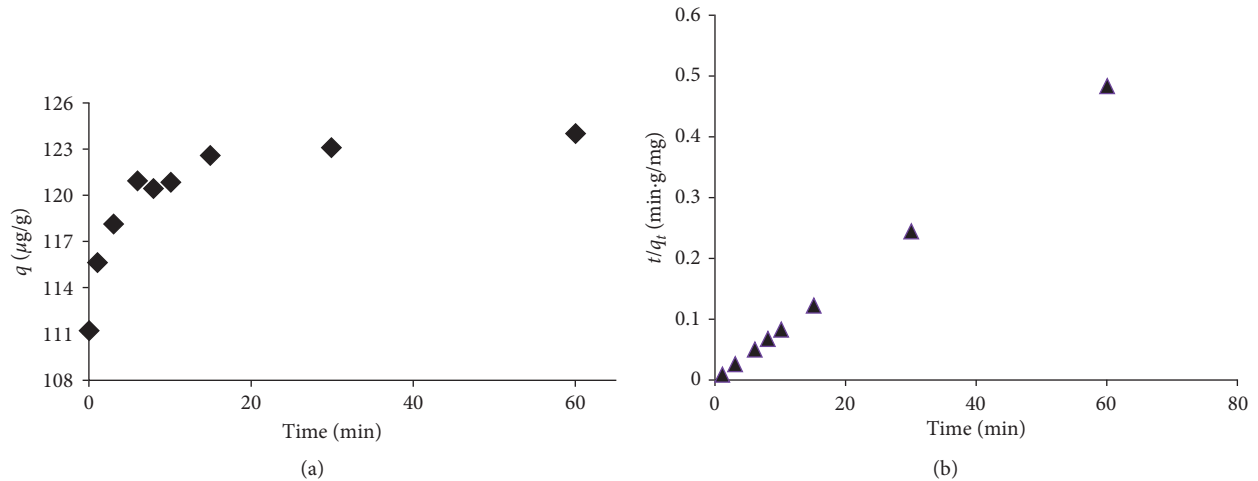


FIGURE 4: Arsenic retention kinetics of the technosol. (a) Sorbed in technosol versus time. (b) Pseudo-second-order fitting.

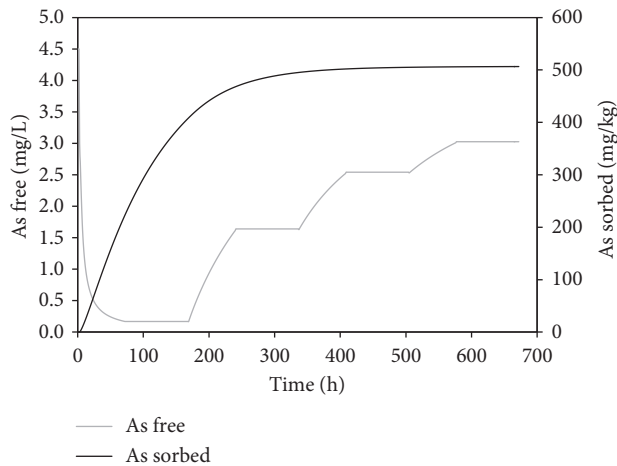


FIGURE 5: Simulation of the temporal modification of As concentration in accumulated water ("As free") and As concentration in the technosol ("As sorbed").

conditions; that is, the sorbent should be renovated 4 times, with each weekly water discharge, after emptying the tank after 4 weeks.

Considering those initial simulations, the model can be used to anticipate the behavior of the system if any of the initial conditions changed. Figure 7(a) shows the simulations of the behavior of the sorption process (in this case, the modification of the concentration of arsenic in water, "As free") when modifying the concentration of As in the water discharge (initially, 4.5 mg/L) to a lower and a higher value, respectively, 2 and 6 mg/L; and Figure 7(b) shows the response of increasing the mass of sorbent to 10 and 20 kg of soil + 0.05 and 0.1 kg of nanoparticles (i.e., twice and four times the initial value 5 kg of soil and 0.025 kg of nanoparticles, always changing one parameter at a time).

The simulations presented in Figure 7(a) indicate that if the concentration of As in the inflow decreased to 2 mg/L, it will take more time for the sorbent to saturate. Indeed, the concentration of As in the treated water was under 0.10 mg/L

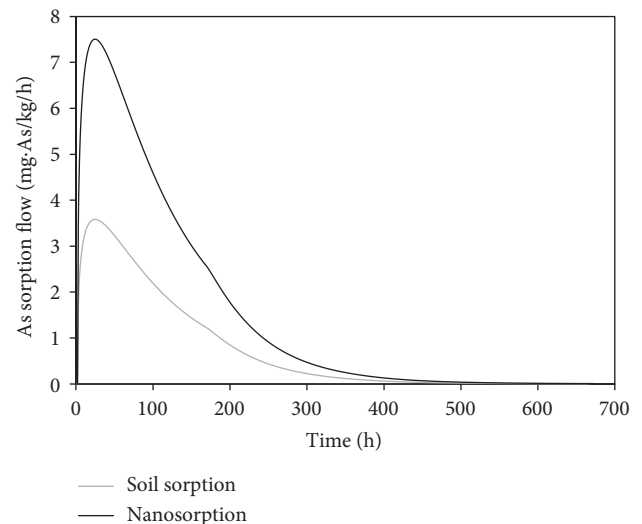


FIGURE 6: Simulation of As sorption flows on soil ("soil sorption") and nanoparticles ("nanosorption"), expressed here as mg As sorbed per kg of sorbent (soil or nanoparticles) and per hour.

until 338 days (approximately 2 weeks, i.e., 2 discharge cycles), from which it started to increase reaching a maximum of 0.57 mg/L at the end of the simulation. Therefore, in this case, the renovation of the sorbent could be done each 2 weeks (i.e., only 2 renovations during 4 weeks, after emptying the tank). On the contrary, at a higher As concentration (6 mg/L), the saturation was occurring very fast, and only half of the As entering can be eliminated during the first water discharge (up to 168 h). This indicated that under our specific conditions (water inflow and mass of sorbents), the reactor cannot efficiently clean up water contaminated with higher concentrations than that initially considered.

The simulations of As concentration in water, varying the mass of sorbent present in the reactor (Figure 7(b)), indicated that an increase in the mass of sorbent will decrease the amount of As present in water (i.e., that the

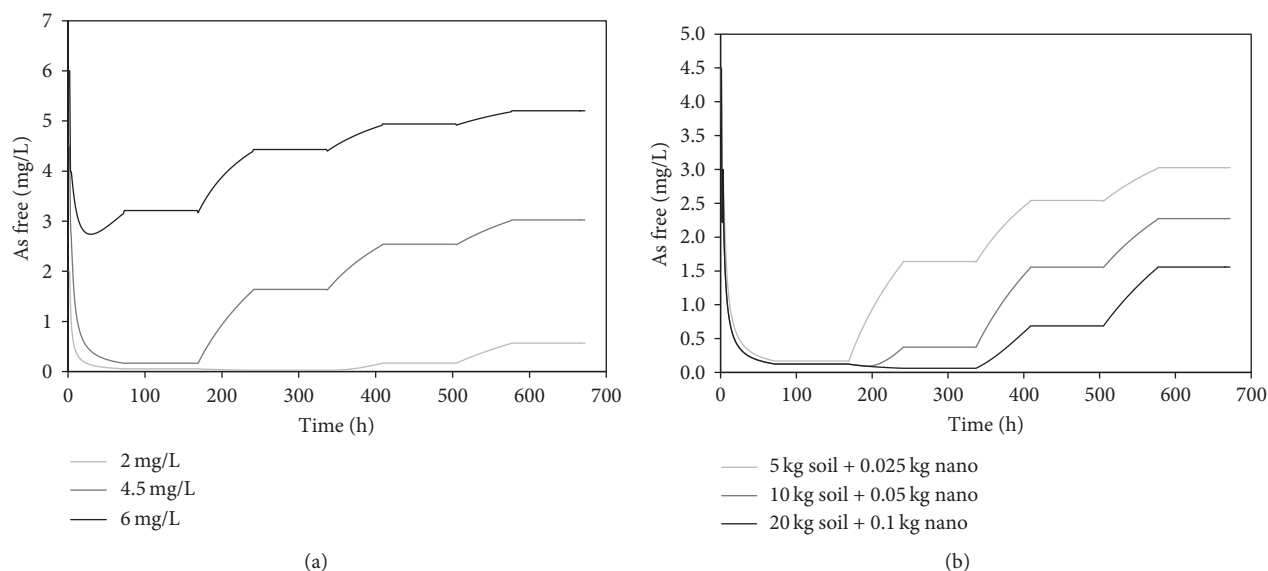


FIGURE 7: Simulation of As concentration in accumulated water (“As free”) using (a) different concentrations of As in discharge water (2, 4.5, and 6 mg/L) and (b) different amounts of sorbent in the reactor (5/10/20 kg of soil + 0.025/0.05/0.1 kg of nanoparticles).

amount of As sorbed increased). Also, the moment from when the sorbent started to saturate (and therefore the time of sorbent renovation) was longer when a higher mass of technosol was present: technosol started to be saturated at 168 h with 5 kg of soil + 0.025 kg of nanoparticles, at 192 h with 10 kg of soil + 0.05 kg of nanoparticles, and at 338 h with 20 kg of soil + 0.1 kg of nanoparticles. These results indicated that it is preferable to maintain a low proportion of sorbent in the reactor and carry out sequential renovations than increasing the amount of sorbent present. In the case of the initial simulations (Figure 5), the results indicated the need of renovating the sorbent weekly with each water discharge (i.e., 4 times before emptying the tank), which is a total of 20 kg of soil + 0.1 kg of nanoparticles. However, if that amount of soil was introduced from the beginning of the treatment (Figure 6), the model predicted that the sorbent should be renovated after 2 weeks (two discharge cycles). This could be caused by a hindered and slower sorption process by decreasing the proportion of water/soil (the contact between As-contaminated water and all the possible sorption sites was more difficult because of a hindered accessibility).

4. Conclusions

Technosol prepared with 99.95% of soil and 0.05% of nanoparticles showed a good efficiency for removing arsenic from mine drainage (124 mg·As/kg). Soil rich in iron (25531.24 mg/kg) could be the main component of the technosol for removing arsenic; however, nanoparticles may also play an important role in the formation of precipitates or inner sphere complexes with the metalloid. The process of arsenic sorption using a technosol showed a linear retention behavior approximately in first 10 min of treatment and reached steady state after 50 min. Results of

isothermal sorption fitted very well with the Langmuir model, and the maximum sorption capacity of the technosol is 7184.66 mg/kg.

A model of As retention from mine waters through the application of technosol, prepared with soil and MCNPs, was developed using the software Vensim PLE. It achieves elimination of more than 96% of As in water entering the remediation tank at each water discharge (216 L), using only 5 kg of soil and 0.025 kg of nanoparticles.

Further investigation is required to include new parameters to the model such as pH, influence of As speciation, and impact of other contaminants or other ions, which could compete for sorption sites. Furthermore, field experiments should be carried out to validate the model and test the real effect of soil + nanoparticles mixtures on arsenic sorption. This will help us to determine if sorption capacities are simply additive, synergistic, or even antagonistic.

Data Availability

Researchers who require the data of this research can contact the corresponding author.

Conflicts of Interest

The authors declare that they have no conflicts of interest.

Acknowledgments

This research was supported by the CRETUS Strategic Partnership (AGRUP2015/02), cofunded by FEDER (UE). Dr. Balseiro-Romero was granted by Banco Santander, within the program Becas Iberoamérica 2016, for a post-doctoral stay at the Nanoscience and Nanotechnology Center (Universidad de las Fuerzas Armadas ESPE).

Sampling was carried out, and thanks are due to the budget of the Vice-Rectorate of research of ESPE and laboratory tests with funds from CENCINAT. The authors thank Dr. Luis Cumbal for all his support in this project. The authors would also like to thank Eng. Nathaly Lopez for synthesis of nanoparticles.

References

- [1] J. Álvarez-Benedí, S. Bolado-Rodríguez, I. Cancillo-Carro, and C. Calvo-Revuelta, "Dinámica de adsorción-desorción de Arsénico (V) en los suelos de cultivo en Castilla y León," *Estudios de la Zona No Saturada del Suelo*, vol. 6, pp. 331–338, 2003.
- [2] D. Mohan and C. U. Pittman, "Arsenic removal from water/wastewater using adsorbents—a critical review," *Journal of Hazardous Materials*, vol. 142, no. 1–2, pp. 1–53, 2007.
- [3] R. Singh, S. Singh, P. Parihar, V. P. Singh, and S. M. Prasad, "Arsenic contamination, consequences and remediation techniques: a review," *Ecotoxicology and Environmental Safety*, vol. 112, pp. 247–270, 2015.
- [4] M. Argos, T. Kalra, P. Rathouz et al., "Arsenic exposure from drinking water, and all-cause and chronic-disease mortalities in Bangladesh (HEALS): a prospective cohort study," *The Lancet*, vol. 376, no. 9737, pp. 252–258, 2010.
- [5] F. Mejía-Zamudio, L. Valenzuela-García, S. Aguayo-Salinas, and D. Meza-Figueroa, "Arsenic adsorption in natural pre-treated zeolite with magnesium oxide," *Revista Internacional de Contaminación Ambiental*, vol. 25, no. 4, pp. 217–227, 2009.
- [6] Y. Huang, K. Miyauchi, C. Inoue, and G. Endo, "Development of suitable hydroponics system for phytoremediation of arsenic-contaminated water using an arsenic hyper-accumulator plant *Pteris vittata*," *Bioscience, Biotechnology and Biochemistry*, vol. 80, no. 3, pp. 614–618, 2016.
- [7] D. Lakshmanan, D. A. Clifford, and G. Samanta, "Comparative study of arsenic removal by iron using electro-coagulation and chemical coagulation," *Water Research*, vol. 44, no. 19, pp. 5641–5652, 2010.
- [8] C. Han, H. Li, H. Pu et al., "Synthesis and characterization of mesoporous alumina and their performances for removing arsenic(V)," *Chemical Engineering Journal*, vol. 20, pp. 1–9, 2013.
- [9] A. M. Donia, A. A. Atia, and D. H. Mabrouk, "Fast kinetic and efficient removal of As(V) from aqueous solution using anion exchange resins," *Journal of Hazardous Materials*, vol. 191, no. 1–3, pp. 1–7, 2011.
- [10] J. Iqbal, H. J. Kim, J. S. Yang, K. Baek, and J. W. Yang, "Removal of arsenic from groundwater by micellar-enhanced ultrafiltration (MEUF)," *Chemosphere*, vol. 66, no. 5, pp. 970–976, 2007.
- [11] J. Pérez-Esteban, B. Caballero-Mejía, A. Masaguer, and A. Moliner, "Effect of magnetite nanoparticles on heavy metals behavior in contaminated soils," in *Proceedings of the VII Congresso Ibérico das Ciências do Solo (CICS 2016)*, VI Congresso Nacional de Rega e Drenagem, pp. 419–422, Beja, Portugal, September 2016.
- [12] S. Lata and S. Samadder, "Removal of arsenic from water using nano adsorbents and challenges: a review," *Journal of Environmental Management*, vol. 166, pp. 387–406, 2016.
- [13] M. M. Jordán, E. García-Sánchez, M. B. Almendro-Candel et al., "Technosols designed for rehabilitation of mining activities using mine spoils and biosolids. Ion mobility and correlations using percolation columns," *CATENA*, vol. 148, pp. 74–80, 2017.
- [14] D. Bolaños, *Aplicación de Tecnosoles para la Recuperación de Suelos y Aguas Afectados por Actividades de Obras Civiles, Urbanas y Minería*, Universidad de Santiago de Compostela, Santiago, Spain, 2015.
- [15] B. M. Vandeborghht and R. E. Van Grieken, "Enrichment of trace metals in water by adsorption on activated carbon," *Analytical Chemistry*, vol. 49, no. 2, pp. 311–316, 1977.
- [16] Y. S. Ho and G. McKay, "The kinetics of sorption of basic dyes from aqueous solution by sphagnum moss peat," *Canadian Journal of Chemical Engineering*, vol. 76, no. 4, pp. 822–827, 1998.
- [17] K. G. Bhattacharyya and S. S. Gupta, "Adsorption of a few heavy metals on natural and modified kaolinite and montmorillonite: a review," *Advances in Colloid Interface Science*, vol. 140, no. 2, pp. 114–131, 2008.

Research Article

Computational Modeling of the Interaction of Silver Nanoparticles with the Lipid Layer of the Skin

Andrea Fabara,¹ Sebastián Cuesta ,² Fernanda Pilaquinga,^{3,4} and Lorena Meneses ²

¹Faculty of Chemistry, University of Strasbourg, Strasbourg, France

²Laboratory of Computational Chemistry, Pontificia Universidad Católica del Ecuador, Quito, Ecuador

³Laboratory of Nanotechnology, Pontificia Universidad Católica del Ecuador, Quito, Ecuador

⁴Department of Chemistry, University of the Balearic Islands, Palma de Mallorca, Balearic Islands, Spain

Correspondence should be addressed to Lorena Meneses; lmmeneses@puce.edu.ec

Received 6 February 2018; Revised 16 April 2018; Accepted 23 April 2018; Published 4 June 2018

Academic Editor: Rachid Seqqat

Copyright © 2018 Andrea Fabara et al. This is an open access article distributed under the Creative Commons Attribution License, which permits unrestricted use, distribution, and reproduction in any medium, provided the original work is properly cited.

Silver nanoparticles are recognized for numerous physical, biological, and pharmaceutical applications. Their main uses in the medical field comprise diagnostic and therapeutic applications. In this project, the interaction between silver nanoparticles and the lipid layer of the skin was studied in order to know how nanoparticles behave when they are in contact with the skin. Energies of the silver nanoparticles were calculated through the optimization of silver clusters using density functional theory implemented in the Gaussian program 09W. Biological molecules such as glucose, stearic acid, palmitic acid, and quercetin present in coated nanoparticles and in the skin were also optimized. The silver clusters containing 6 atoms were proven to be the most stable complexes. Moreover, a study of molecular orbital describing HOMO interactions of the clusters was performed showing that the electronic density was around the silver cluster. Molecular dynamics simulation was performed using Abalone program. Silver nanoparticles seemed to have very good clearance properties in our molecular dynamics simulation because over a certain period of time, the silver cluster got far away from the biological molecules.

1. Introduction

Silver nanoparticles have unique optical, electrical, and thermal properties. Present applications range from photovoltaics cells to biological and chemical sensors. Silver nanoparticles also present biological applications such as molecular diagnostics, photonic devices, nanomedicine drug delivery, imaging diagnostics, and biosensing [1, 2]. However, it is important to be sure about the possible consequences of their use.

Nanoparticles are being daily used, yet a concern rises due to the fact that their toxicity could put human health at risk [3]. Thus, to develop new nanoparticles and continue their use and development, more studies and evaluation have to be done. One of the possibilities in doing so is by investigating silver nanoparticles through quantum mechanics calculations.

Computational modeling is a powerful tool compared to experimental limitations. In a computational work, it is possible to manage each parameter separately and identify

the mechanism responsible for the experimental result. With a computational study, it is feasible to simulate interactions under different conditions that are not always possible to be studied in the lab [4]. All nanomaterials are size dependent because their physical and chemical properties will depend on the size of the nanoparticle. The composition, size, shape, and environment of nanoparticles can strongly influence their eventual application as they have excellent properties for antimicrobial coatings, textiles, keyboards, wound dressings, and biomedical devices [5, 6].

Theoretical studies on the affinity of silver ions with DNA at a molecular level were performed to determine the interaction of silver ions with a cytosine base and an adenosine base, using *ab initio* calculations and density functional theory (DFT) [7]. Also, a chemical reactivity analysis of biological molecules in the presence of silver ions in the DFT framework has been performed in order to find the molecular structure with the lowest energy, molecular orbitals, and chemical reactivity parameters [8].

Lipids are fundamental structural components of cell membranes. They are little oxidizable molecules serving as an energy reservoir for the cell. Lipids are key components of the skin cell membrane that need to be analyzed because when there is an attack from foreign agents, they become injured [9]. Lipids analyzed in this research were two saturated lipids, palmitic and stearic acids, present in the lipid layer of the skin. Stearic acid was chosen for the study because it was the second most common lipid after palmitic acid contributing to prove the stability of the silver complexes.

In this study, the interaction between silver nanoparticles and the lipid layer was investigated. Since an organic crystal structure is not available, a computational study was performed to evaluate the compounds and to determine structural information. This research aims to establish a quantitative structure-activity between the interaction of silver nanoparticles and the lipid layer of the skin (palmitic and stearic acids).

In previous works, small silver clusters were studied using DFT methods. Poteau and his team had studied the ground-state geometries and the binding energies per atom of small silver clusters, from 4 to 8 silver atoms. With their results, they managed to parameterize distance-dependent tight-binding Hamiltonian and accomplished good correlation between their model and ab initio calculations [10]. Another DFT study was done on small anionic, neutral, and cationic silver cluster hydrides using the PW91PW91 method. Here, binding energies showed different behaviors depending on the number of silver atoms; cationic clusters are the ones with lowest binding energies in clusters with an odd number of silver atoms while neutral clusters are the ones with an even number of silver atoms [11].

In other studies, silver nanoparticles coated with glucose and quercetin (a flavonoid) have been reported as green synthesis methodologies. Coated silver nanoparticles with *Piper aduncum* presented extraordinary healing properties [12, 13]. Quercetin, being the principal component of *Piper aduncum*, was chosen to interact with the silver clusters. Silver nanoparticles covered with quercetin proved to have therapeutic properties in addition to the antibacterial properties. However, silver nanoparticles covered with glucose did not show any healing characteristics except for antibacterial properties of the silver nanoparticles [12, 14, 15]. Thanks to their small size, large surface area, and versatile physicochemical properties, these coated silver nanoparticles could enter cells and organelles leading to the possibility of nanomedicine [15]. Therefore, we also proposed to determine the stability of these complexes, since the silver nanoparticles can be released once they have completed their therapeutic action.

2. Materials and Methods

The geometry optimization of silver clusters was carried out at the B3LYP/LANL2DZ level of theory, while palmitic acid, stearic acid, glucose, and quercetin geometries were carried out at the B3LYP/6-311G level of theory, implemented in the Gaussian 09W package of programs [16]. A computational modeling of silver clusters with the biological

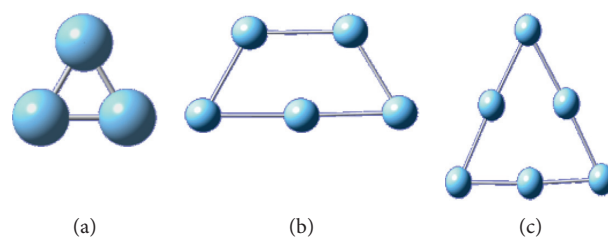


FIGURE 1: Silver cluster optimized and conserved: (a) cluster of 3 silver atoms, (b) cluster of 5 silver atoms, and (c) cluster of 6 silver atoms.

molecules was analyzed, and lower energy conformations were identified. The energy of the cluster interaction was calculated using the following equation:

$$\Delta I = E_{(Agc-BM)} - E_{Agc} - E_{BM}, \quad (1)$$

where ΔI = interaction energy, $E_{(Agc-BM)}$ = energy of the cluster-biomolecule complex, E_{Agc} = energy of the silver cluster, and E_{BM} = energy of the biomolecule.

Also, a study of the MO theory describing HOMO interactions of clusters was carried out.

Molecular dynamics using the Abalone program (a molecular simulation program with AMBER-ii force field) was performed to see how molecules interact for a given period of time (from 5 to 20 ps) [17]. To carry out the dynamics, a .pdb file with the optimized geometry of the cluster-biomolecule complex obtained from the DFT study was opened in the Abalone program. The option of molecular dynamics was selected; working conditions were set at 1 atm of pressure, 298.15 K of temperature, 2.0 fs time per step, and 5 or 20 ps of duration.

3. Results and Discussion

The methods within the framework of the density functional theory (DFT) were used to optimize the structure of the silver nanoparticles and also the stearic acid, palmitic acid, quercetin, and glucose. Vibrational frequencies at the ground state were calculated in order to ensure that they were at a minimum level.

3.1. Energetic Study. Different geometries and number of atoms were tested to form a silver nanoparticle. It took many tries using different numbers of silver atoms (3, 13, 30, 50, 64, 85, 100, 120, etc.) to form the silver nanoparticle with different geometries and shapes. However, the silver clusters were not correctly optimized because of the loss of geometry.

From all the geometries, the silver clusters with 3, 5, and 6 silver atoms were chosen to continue the study. Figure 1 shows the clusters of silver nanoparticles that were optimized and where sizes and geometries were conserved.

Once the silver clusters were optimized, the biological molecules were optimized as well. Figure 2 illustrates biological molecules that were analyzed: lipids such as palmitic acid and stearic acid, quercetin which is a flavonoid, and glucose a sugar.

Interaction between biological molecules (quercetin, glucose, palmitic acid, and stearic acid) and the three silver

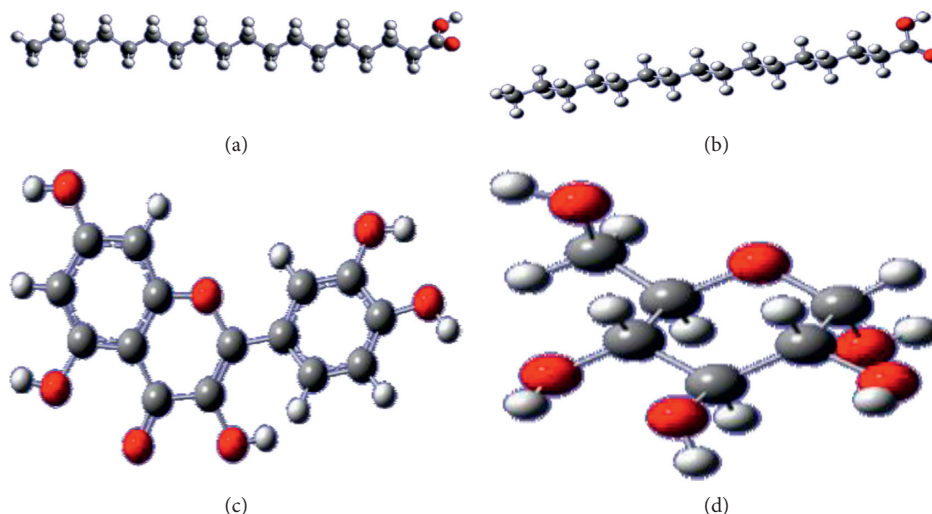


FIGURE 2: Biological molecules used in this study: (a) stearic acid, (b) palmitic acid, (c) quercetin, and (d) glucose.

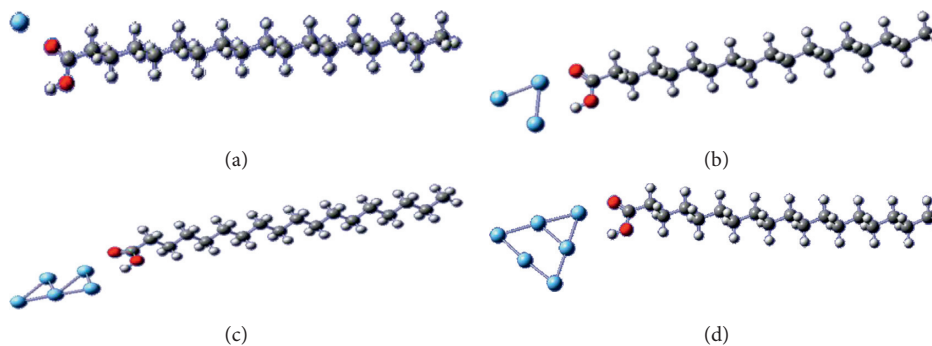


FIGURE 3: Optimized geometries of stearic acid with (a) a single silver atom, (b) cluster of 3 silver atoms, (c) cluster of 5 silver atoms, and (d) cluster of 6 silver atoms.

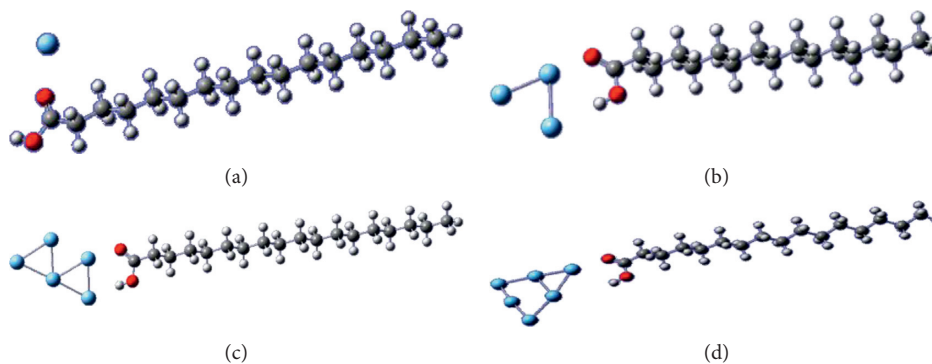


FIGURE 4: Optimized geometries of palmitic acid with (a) a single silver atom, (b) cluster of 3 silver atoms, (c) cluster of 5 silver atoms, and (d) cluster of 6 silver atoms.

clusters previously optimized was simulated. The optimized geometries of the interaction between the biomolecules with a single silver atom are also shown so as to find the differences between these and the cluster interactions. All of them were optimized in order to know if they could form a complex and to measure the distance of the cluster and the biomolecule. Based on the information provided by He and Zeng [18], the silver atom and the clusters were introduced

in a position in which they were close to the carboxyl group which is the hydrophilic part of the fatty acids, as shown in Figures 3 and 4. In this conformation, the complexes presented the lowest energy.

In Figures 5 and 6, the most stable complex between the silver atom and clusters with glucose and quercetin is shown. In this case, it can be seen that the clusters are close to the oxygen atoms of the molecules, also being the hydrophilic

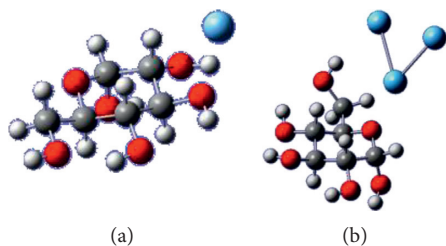


FIGURE 5: Optimized geometry of glucose with (a) a single silver atom and (b) the cluster of 3 silver atoms.

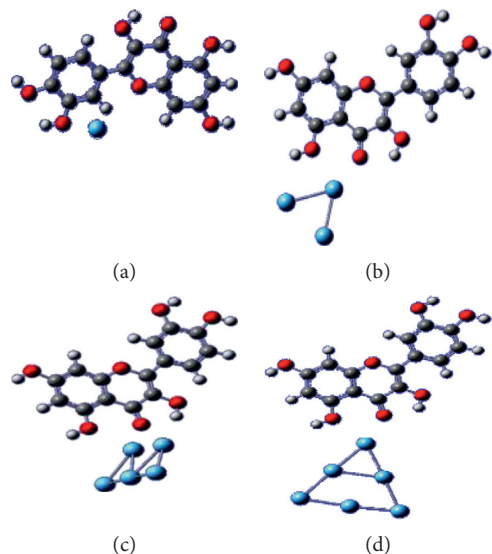


FIGURE 6: Optimized geometries of quercetin with (a) a single silver atom, (b) cluster of 3 silver atoms, (c) cluster of 5 silver atoms, and (d) cluster of 6 silver atoms.

parts. With glucose, it was not possible to obtain optimized geometries with 5 and 6 silver atom clusters.

In previous studies of reactivity analysis, it was found that the main interaction between palmitic acid and the silver ion was through the carboxylic acid of the lipid [8]. Besides, the interaction between biological molecules and silver clusters was through the hydroxyl groups as compared with the study between PVA and Ag55 nanocrystals [19]. Silver nanoparticles go through shape-dependent interaction with the lipid layer. While these interactions are being studied, these nanoparticles are being used more and more for their antibacterial and antimicrobial activities [20].

The interaction energies of the systems were calculated using (1) and are presented in Table 1.

The stabler structures are the ones with smaller energies; therefore, clusters of 6 silver atoms are considered as the most stable ones. On the contrary, when comparing these results with the ones obtained with a single silver atom, it could be seen that the systems with a single silver atom were the ones with the highest interaction energies. The different results obtained from the different clusters studied give a clear view of interaction energies, and therefore, the properties of the silver nanoparticles are size dependent.

TABLE 1: Interaction energies between the clusters of 1, 3, 5, and 6 atoms of silver, stearic acid, palmitic acid, and quercetin.

System	ΔI (kcal/mol)
Stearic acid 1 Ag	-2.79
Stearic acid cluster 3 Ag	-18.58
Stearic acid cluster 5 Ag	-8.51
Stearic acid cluster 6 Ag	-75.47
Palmitic acid 1 Ag	-3.41
Palmitic acid cluster 3 Ag	-18.65
Palmitic acid cluster 5 Ag	-8.53
Palmitic acid cluster 6 Ag	-75.43
Quercetin 1 Ag	-0.81
Quercetin cluster 3 Ag	-24.44
Quercetin cluster 5 Ag	-12.53
Quercetin cluster 6 Ag	-80.16
Glucose 1 Ag	-26.50

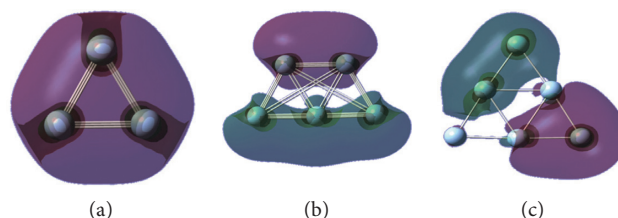


FIGURE 7: HOMO surfaces of clusters of (a) 3 silver atoms, (b) 5 silver atoms, and (c) 6 silver atoms.

According to our study, a silver nanoparticle with the size of our cluster of 6 silver atoms will have better properties due to its increased stability compared to small nanoparticles. The interaction energies between the metal clusters and the biological molecules suggest that nanoparticles will favorably bind to proteins and can be adsorbed with biomolecules as melamine [21, 22]. The energies also confirm that non-coated silver nanoparticles are less stable, thus presenting bigger energies. The silver cluster covered with the biological molecule was more stable than the silver nanoparticle alone. This was favorable because it improved bioavailability, as previously demonstrated by Kumar and Randhawa [23].

3.2. Molecular Orbital Study. Molecular orbitals are regions of space that contain the electron density defined by mathematical functions that describe the wave behavior that electrons can have on molecules. These functions can be used to calculate chemical and physical properties such as the probability of finding an electron in a region of space. The border molecular orbitals HOMO and LUMO (highest occupied molecular orbital and lowest unoccupied molecular orbital, resp.) allow for knowing the regions of space where the valence electrons are, that is, those that participate in bond formations. In this way, a study of border molecular orbitals allows us to see if there is a bond and where it is located.

In this investigation, a study of molecular orbitals (MO) describing HOMO interaction of the clusters and the biomolecules was carried out in order to know if there is a bond between the biomolecules and the clusters. In Figures 7–10,

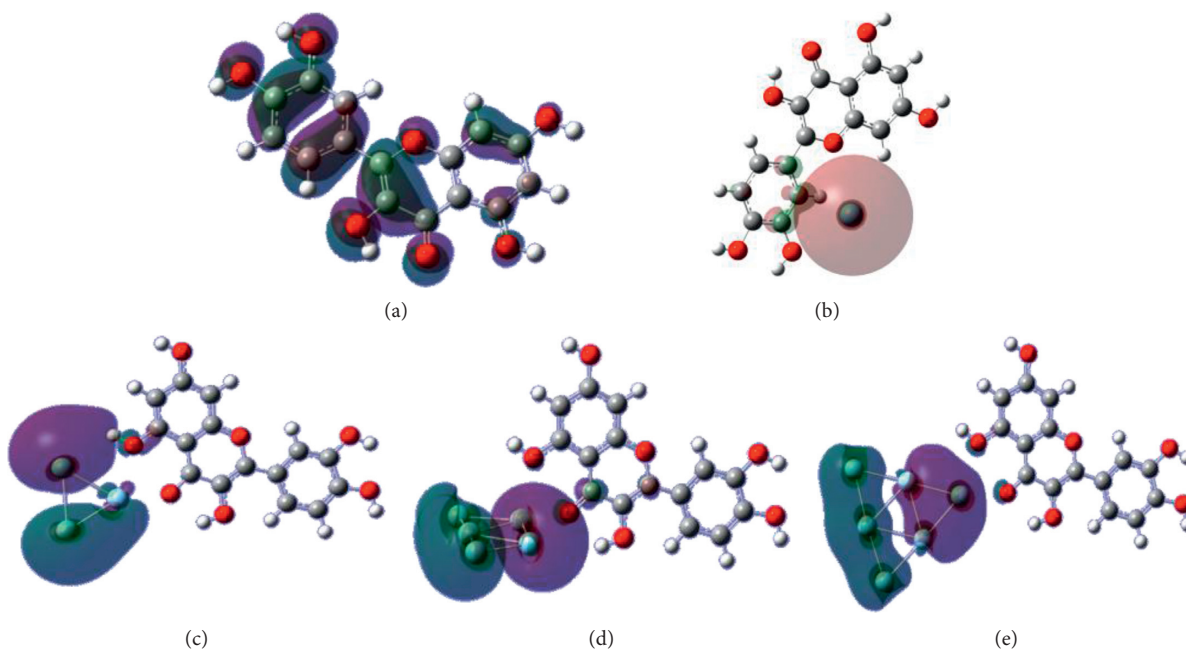


FIGURE 8: HOMO surfaces of (a) quercetin and the complex between quercetin with (b) a single silver atom, (c) cluster of 3 silver atoms, (d) cluster of 5 silver atoms, and (e) cluster of 6 silver atoms.

the red shapes correspond to bonding molecular orbitals, while the green shapes correspond to antibonding ones. Figure 7 illustrates the spatial and energetic properties of electrons that form orbitals in the silver clusters.

The shapes of the molecular orbitals from Figures 8–10 show that, in the stearic acid, palmitic acid, and quercetin, the energies surrounded the entire molecule. However, once the silver cluster was added, the molecular orbital energies changed and they were then located mainly around the cluster of 1, 3, 5, or 6 silver atoms.

In Figure 8(a), it can be seen that the energy of the HOMO is located completely around the quercetin molecule. However, when the single silver atom and the clusters of 3, 5, and 6 silver atoms are found near the quercetin molecule (Figures 8(b)–8(e)), the energy moves almost completely to the silver atoms, leaving small orbital regions around the oxygen atoms near the cluster. This indicates that there is a weak interaction between the cluster and the biomolecule. Given the simplicity of the study model, this can be considered as a bonding interaction.

In Figure 9(a), the energy of the HOMO is located completely around the stearic acid. When a single silver atom and the clusters of 3, 5, and 6 silver atoms are near the biomolecule (Figures 9(b)–9(e)), the energy again moves to the silver atoms, leaving small orbital regions around the oxygen atoms of the carboxylic acid.

This indicates that there is a weak interaction between the cluster and the biomolecule. With palmitic acid, the behavior is similar, as can be seen in Figure 10.

3.3. Molecular Dynamics Study. Molecular dynamics is a powerful tool in molecular modeling because it gives the opportunity to follow and understand the structure and

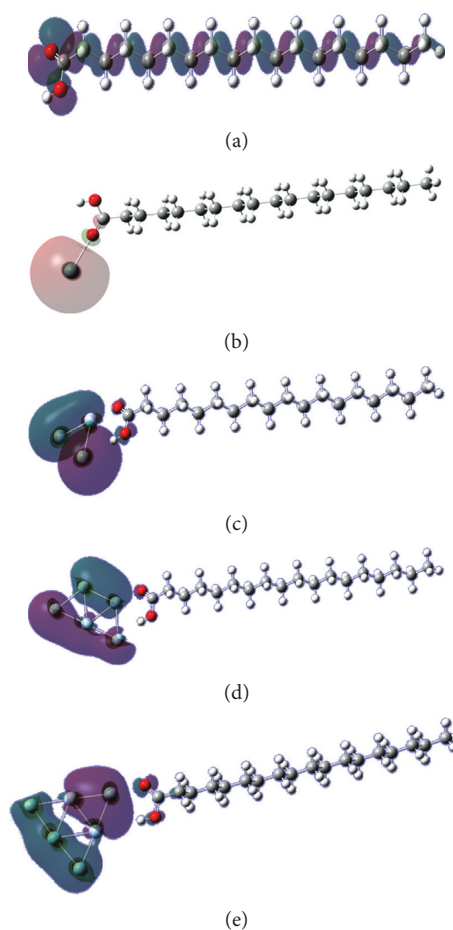


FIGURE 9: HOMO surfaces of (a) stearic acid and the complex between stearic acid with (b) a single silver atom, (c) cluster of 3 silver atoms, (d) cluster of 5 silver atoms, and (e) cluster of 6 silver atoms.

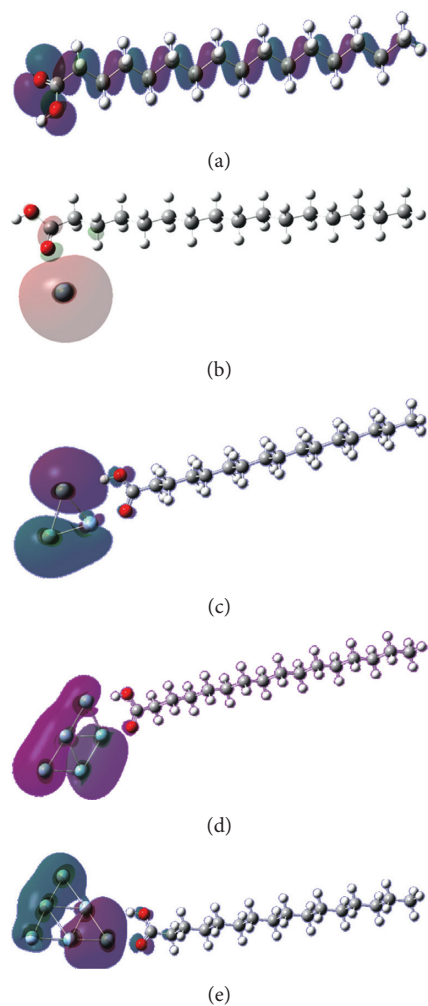


FIGURE 10: HOMO surfaces of (a) palmitic acid and the complex between palmitic acid with (b) a single silver atom, (c) cluster of 3 silver atoms, (d) cluster of 5 silver atoms, and (e) cluster of 6 silver atoms.

dynamics of molecules [24]. The Abalone program is used to simulate the natural motion of biological macromolecules. Silver nanoparticles have many interesting properties as previously mentioned. Nevertheless, silver nanoparticles reveal an extended retention in an organism which is cause for concern due to toxicity. For that reason, coated (*Piper aduncum*) silver nanoparticles with optimal clearance characteristics are very important because they minimize toxicity [12].

Furthermore, the Abalone program contributed by conducting the simulations of molecular dynamics in order to determine the interactions of biological molecules and the silver clusters for a fixed period of time, 5 and 20 ps. The molecules were allowed to move giving a view of the dynamical evolution of the system. At different times, distances increased between the cluster and the biological molecule as indicated in Figures 11–13.

Distances from the oxygen of the carboxylic acid to the first atom of the silver cluster were measured. The distance

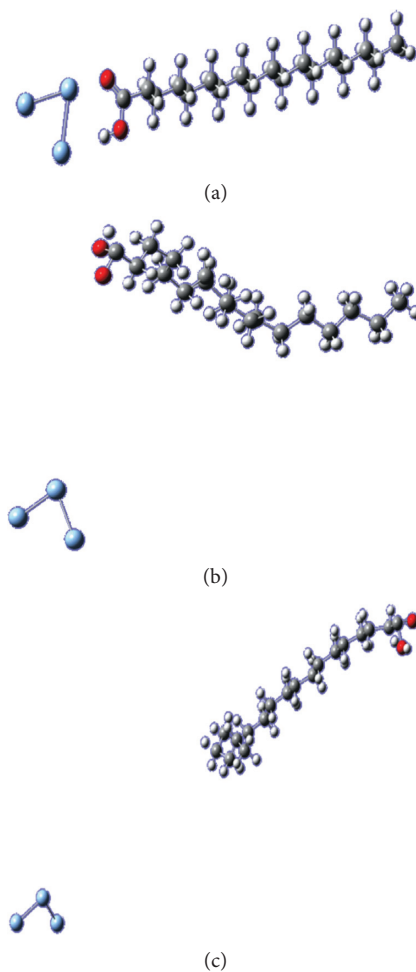


FIGURE 11: Molecular dynamics performed at 298.15 K. Stearic acid with 3 silver atoms cluster at (a) 0 ps, (b) 5 ps, and (c) 20 ps.

between stearic acid and the cluster of 3 silver atoms at the beginning of the dynamic was 2.33 Å. After 5 ps, the distance increased to 10.09 Å, and after 20 ps, it changed to 32.67 Å. Palmitic acid and the different clusters of 3, 5, and 6 silver atoms followed the same path as stearic acid. This meant that the cluster was moving away, while the distance kept increasing. These results indicate that the silver nanoparticles can go through the lipid layer of the skin, but they can also be easily separated reducing their toxicity.

In the case of the glucose, measured distances were calculated from the oxygen of the cycle to the first atom of the silver cluster. In Figure 12, the distances changed from 3.35 Å at the beginning of the dynamic to 61.53 Å after 20 ps. This shows that glucose does not have a strong interaction with the 3-atom silver cluster after a short period of time, and conversely, the silver cluster rapidly goes far away from the biomolecule, showing good clearance properties.

In Figure 13, distances were measured from the carbonyl oxygen of the quercetin to the first atom of the silver cluster. In the 3-atom silver cluster, the distances changed from 2.34 to 7.87 Å at the end of 20 ps. With the 5-atom silver cluster, the distances were higher, changing from 2.37 to 34.08 Å

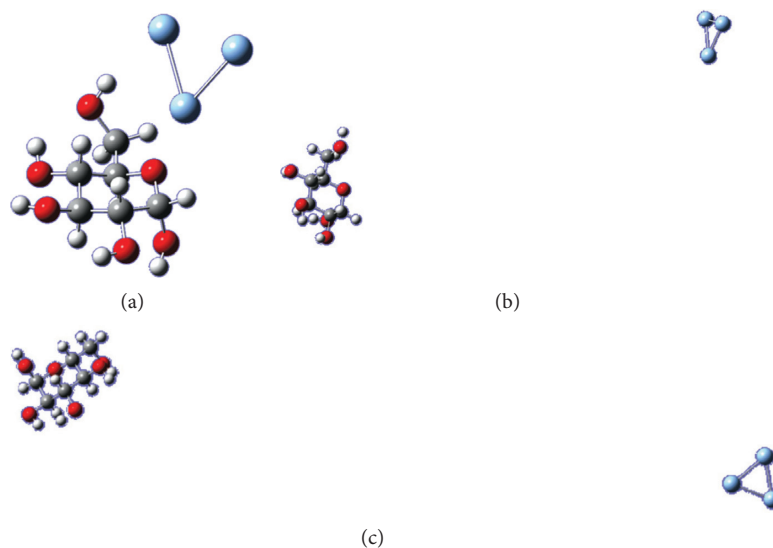


FIGURE 12: Molecular dynamics performed at 298.15 K. Glucose with 3-atom silver cluster at (a) 0 ps, (b) 5 ps, and (c) 20 ps.

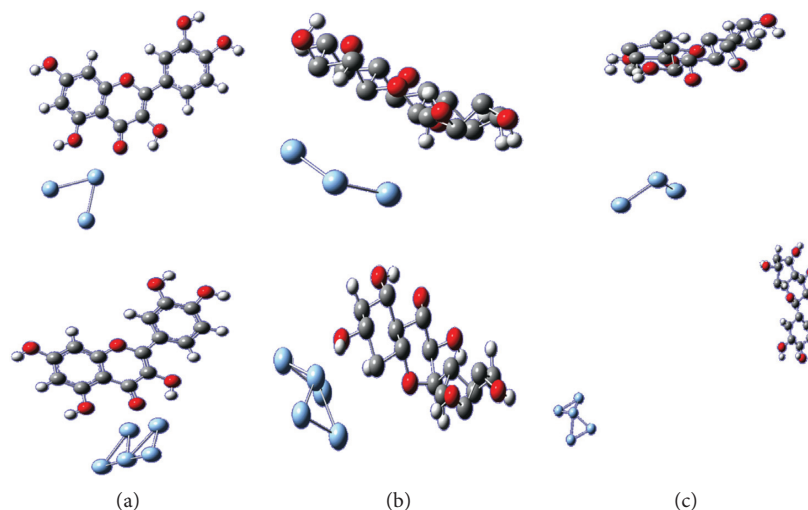


FIGURE 13: Molecular dynamics performed at 298.15 K. Quercetin with 3- and 5-atom silver clusters at (a) 0 ps, (b) 5 ps, and (c) 20 ps.

after the same period of time. This means that with small nanoparticles, there are major interactions between the nanoparticle and the biomolecule, and there is not a good clearance after short periods of time. On the contrary, with bigger nanoparticles, there is really great separation with the quercetin, showing excellent clearance properties. With the 6-atom silver cluster, the trend was the same as the 5-atom silver cluster [13].

To probe that the complex silver cluster-stearic acid has a bonding interaction, which was broken after 5 ps, a MO study on the molecular dynamics structures was done. In Figure 14, it can be seen that at 0 ps, the HOMO was located around the silver cluster, but a small shape is around the oxygen of the carboxylic part of the fatty acid. When the molecular dynamic moves to 5 ps, the HOMO was located completely around the silver cluster, and at 20 ps, this was maintained. This shows that there was an orbital

interaction between the stearic acid and the silver cluster when they were 2.33 Å away from each other. The complex was broken when the distance increased to 10.09 Å and further.

In the case of the quercetin with 3-atom silver clusters (Figure 15), it can be seen that at 0 ps, the HOMO was located around the silver cluster and a small part above the oxygen of the hydroxyl group. When the molecular dynamics moves to 5 ps, the HOMO was located completely around the silver cluster, and at 20 ps, some of the orbital energy is again located at the biomolecule. This shows that there was an orbital interaction between the quercetin and the silver cluster when they have around 2.34 Å of separation distance. The complex was broken when the distance increased. Finally, at 7.87 Å, the interaction returned although the molecules were away from each other. This confirms that with small nanoparticles, there are major

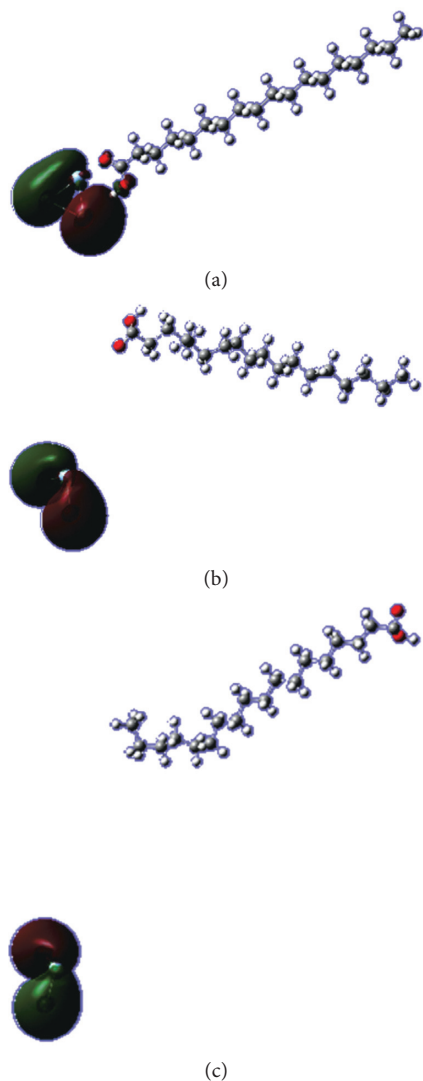


FIGURE 14: HOMO surfaces from molecular dynamics. Stearic acid with 3-atom silver cluster at (a) 0 ps, (b) 5 ps, and (c) 20 ps.

interactions between the nanoparticle and the biomolecule and there is not a good clearance after short periods of time.

The results illustrate that, for biological molecules, the cluster stays near 5 ps which is important in the case of introducing the coated nanoparticle in an organism because the complex has to stay stable for a minimum period of time. However, at 20 ps, the cluster moves far away from the biological molecules. This is really interesting because the intention is that once the coated molecule is introduced into the organism, the complex would be separated and it would be eliminated very easily with optimal clearance characteristics.

In order to prove that the dynamic goes well with the biomolecules studied, a file with the crystal structure of FGF Receptor 2 Tyrosine Kinase Domain Harboring the D650V Activating Mutation was chosen for the interaction with the 3-atom silver cluster. The biomolecule was obtained from the RCSB Protein Data Bank [25].

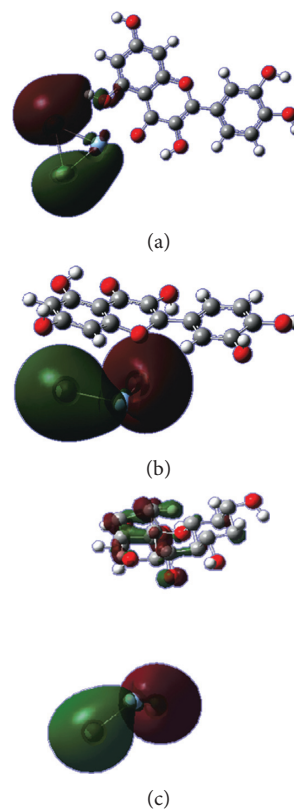


FIGURE 15: HOMO surfaces from molecular dynamics. Quercetin with 3-atom silver clusters at (a) 0 ps, (b) 5 ps, and (c) 20 ps.

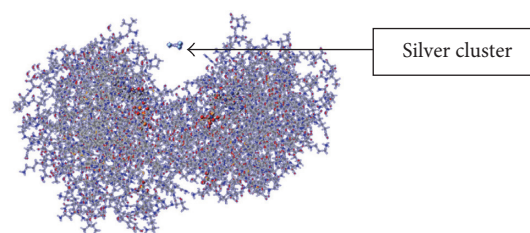


FIGURE 16: Interaction between the crystal structure of FGF Receptor 2 Tyrosine Kinase Domain Harboring the D650V Activating Mutation and the 3-atom silver cluster.

After a dynamical evolution of 5, 20, and 100 ps, there is no movement of the cluster. The system is very stable and does not move at all as shown in Figure 16. This demonstrates that there is an important difference in stability between our systems and this system.

4. Conclusion

A computational modeling of the silver nanoparticles and the biological molecules including glucose, stearic acid, palmitic acid, and quercetin was performed. The lowest energy conformations were identified, and the clusters of 6 silver atoms were the most stable complexes. Moreover, the study of MO describing HOMO cluster interaction contributed to find that the electronic density was around the silver cluster. Finally, molecular dynamics was performed

using the Abalone program to observe how silver clusters interact with biological molecules for a given period of time, 5 and 20 ps. Molecular dynamics showed that, over a certain period of time, the silver cluster moved far away from the biological molecule. This means that the quercetin-coated silver nanoparticles could have good clearance properties. With respect to the interaction with the lipid layer of the skin, it can be preliminarily said that because the interaction of the silver nanoparticles with the fatty acids is not strong after a period of time, it is possible to reduce their toxicity by skin contact. In future experimental work, it would be interesting to do a full characterization of the coated silver nanoparticles and studies of cytotoxicity.

Data Availability

Data described in the manuscript are available from the authors.

Conflicts of Interest

The authors declare that they have no conflicts of interest.

Acknowledgments

Andrea Fabara would like to thank Pontificia Universidad Católica del Ecuador for all the facilities provided in the realization of their master's thesis. This research was supported by DGA-PUCE Project N13438 (2016-2017).

References

- [1] R. Li, R. Chen, P. Chen, Y. Wen, P. C. Ke, and S. S. Cho, "Computational and experimental characterizations of silver nanoparticle-apolipoprotein biocorona," *Journal of Physical Chemistry B*, vol. 117, no. 43, pp. 13451-13456, 2013.
- [2] J. Romann, J. Wei, and M. P. Pileni, "Computational matching of surface plasmon resonance: interactions between silver nanoparticles and ligands," *Journal of Physical Chemistry C*, vol. 119, no. 20, pp. 11094-11099, 2015.
- [3] N. Lewinski, V. Colvin, and R. Drezek, "Cytotoxicity of nanoparticles," *Small*, vol. 4, no. 1, pp. 26-49, 2008.
- [4] C. You, C. Han, X. Wang et al., "The progress of silver nanoparticles in the antibacterial mechanism, clinical application and cytotoxicity," *Molecular Biology Reports*, vol. 39, no. 9, pp. 9193-9201, 2012.
- [5] E. Saion, E. Gharibshahi, and K. Naghavi, "Size-controlled and optical properties of monodispersed silver nanoparticles synthesized by the radiolytic reduction method," *International Journal of Molecular Sciences*, vol. 14, no. 4, pp. 7880-7896, 2013.
- [6] S. Pal, Y. K. Tak, and J. M. Song, "Does the antibacterial activity of silver nanoparticles depend on the shape of the nanoparticle? A study of the Gram-negative bacterium *Escherichia coli*," *Applied and Environmental Microbiology*, vol. 73, no. 6, pp. 1712-1720, 2007.
- [7] J. Wu, Y. Fu, Z. He et al., "Growth mechanisms of fluorescent silver clusters regulated by polymorphic DNA templates: a DFT study," *Journal of Physical Chemistry B*, vol. 116, no. 5, pp. 1655-1665, 2012.
- [8] L. L. Landeros-Martinez, E. Orrantia-Borunda, and N. Flores-Holguin, "DFT chemical reactivity analysis of biological molecules in the presence of silver ion," *Organic Chemistry: Current Research*, vol. 4, no. 4, pp. 1-6, 2015.
- [9] J. Q. Lin, Y. G. Zheng, H. W. Zhang, and Z. Chen, "A simulation study on nanoscale holes generated by gold nanoparticles on negative lipid bilayers," *Langmuir*, vol. 27, no. 13, pp. 8323-8332, 2011.
- [10] R. Poteau, J. L. Heully, and F. Spiegelmann, "Structure, stability, and vibrational properties of small silver cluster," *Zeitschrift für Physik D Atoms*, vol. 40, no. 1, pp. 479-482, 1997.
- [11] S. Zhao, Z. Liu, Z. Li, W. Wang, and K. Fan, "Density functional study of small neutral and charged silver cluster hydrides," *Journal of Physical Chemistry A*, vol. 110, no. 40, pp. 11537-11542, 2006.
- [12] Y. Santorum, *Síntesis y caracterización de nanopartículas de plata empleando el extracto de las hojas de matico (Piper aduncum) como un agente reductor*, Undergraduate thesis, Pontificia Universidad Católica del Ecuador, Quito, Ecuador, 2017.
- [13] N. Santorum, A. Fabara, F. Pilaquinga, S. Ampudia, E. Jara, and L. Meneses, "Experimental and computational characterization of silver nanoparticles using matico (*Piper aduncum*) leaves extract as reducing agent," *Periódico Tchê Química*, vol. 15, no. 29, pp. 309-318, 2018.
- [14] P. Raveendran, J. Fu, and S. L. Wallen, "A simple and "green" method for the synthesis of Au, Ag, and Au-Ag alloy nanoparticles," *Green Chemistry*, vol. 8, no. 1, pp. 34-38, 2006.
- [15] A. Desireddy, B. E. Conn, J. Guo et al., "Ultrastable silver nanoparticles," *Nature*, vol. 501, no. 7467, pp. 399-402, 2013.
- [16] M. J. Frisch, G. W. Trucks, H. B. Schlegel et al., *Gaussian 09, Revision A.02*, Gaussian, Inc., Wallingford, CT, USA, 2009.
- [17] *Agile Molecule*, 2006, <http://www.biomolecular-modeling.com/Abalone/abalone-ii.html>.
- [18] Y. He and T. Zeng, "First-principles study and model of dielectric functions of silver nanoparticles," *Journal of Physical Chemistry C*, vol. 114, no. 42, pp. 18023-18030, 2010.
- [19] H. L. Chou, C. M. Wu, F. D. Lin, and J. Rick, "Interactions between silver nanoparticles and polyvinyl alcohol nanofibers," *AIP Advances*, vol. 4, no. 8, p. 087111, 2014.
- [20] S. Prabhu and E. K. Poulouse, "Silver nanoparticles: mechanism of antimicrobial action, synthesis, medical applications, and toxicity effects," *International Nano Letters*, vol. 2, no. 32, pp. 1-10, 2012.
- [21] C. M. Aikens, "Modelling small gold and silver nanoparticles with electronic structure methods," *Molecular Simulation*, vol. 38, no. 8-9, pp. 607-614, 2012.
- [22] X. Chen, Y. Hu, J. Gao, Y. Zhang, and S. Li, "Interaction of melamine molecules with silver nanoparticles explored by surface-enhanced Raman scattering and density functional theory calculations," *Applied Spectroscopy*, vol. 67, no. 5, pp. 491-497, 2013.
- [23] S. Kumar and J. K. Randhawa, "Solid lipid nanoparticles of stearic acid for the drug delivery of paliperidone," *RSC Advances*, vol. 5, no. 84, pp. 68743-68750, 2015.
- [24] E. Lindahl, "Molecular dynamics simulations," *Methods in Molecular Biology*, vol. 1215, pp. 3-26, 2015.
- [25] H. Berman, J. Westbrook, Z. Feng et al., "The protein data bank," *Nucleic Acids Research*, vol. 28, no. 1, pp. 235-242, 2000.

Research Article

Improvement of Cochineal Extract (*Dactylopius coccus* Costa) Properties Based on the Green Synthesis of Silver Nanoparticles for Application in Organic Devices

Carina Stael, Ricardo Cruz, Blanca Naranjo, Alexis Debut , and Yolanda Angulo 

Centro de Nanociencia y Nanotecnología, Universidad de las Fuerzas Armadas ESPE, Av. Gral. Rumiñahui S/N, P.O. Box 171-5-231B, Sangolquí, Ecuador

Correspondence should be addressed to Yolanda Angulo; yrangulo@espe.edu.ec

Received 18 October 2017; Revised 11 January 2018; Accepted 7 February 2018; Published 21 May 2018

Academic Editor: Lee Blaney

Copyright © 2018 Carina Stael et al. This is an open access article distributed under the Creative Commons Attribution License, which permits unrestricted use, distribution, and reproduction in any medium, provided the original work is properly cited.

The UV-Vis absorption and conductivity properties of the organic sample cochineal (*Dactylopius coccus* Costa) were modified by using it as a reducing agent in the biosynthesis of silver nanoparticles. This was done in a straightforward way in order to allow its possible application in organic devices. The biosynthesized solution exhibited a hybrid material with a UV-Vis absorbance range from 205 to 650 nm. The sizes of silver nanoparticles of the hybrid material were between 5 and 10 nm. X-ray diffraction (XRD) revealed silver structures, when samples were dried at 100°C. At 40°C, the structures detected were chlorargyrite (AgCl) and silver oxide (Ag₂O). The nucleation and subsequent growth of the hybrid thin film on the substrates indicated an increase of clusters and roughness in comparison to thin films made solely from cochineal. The thin films of hybrid materials showed an improvement of 40% in their electrical potential. The stability at room temperature demonstrated that the hybrid material could be useful as a potential candidate for photoactive thin films in organic devices.

1. Introduction

Organic semiconductors have witnessed considerable development in recent years, with increasing research activity on this class of materials and their potential applications. The interest in this area is to obtain new organic compounds with improved, more efficient properties for the manufacture of organic, light-emitting diodes (OLEDs) [1], organic photovoltaic cells (OPVs) [2, 3], and thin film transistors (TFTs) [4]. The biosynthesis of new hybrid structures using natural organic compounds for development of photo-reactive compounds is straightforward and significantly reduces the cost of organic devices.

Cochineal insects (*Dactylopius coccus* C.) from the city of Loja, Ecuador, were used here to form a new hybrid structure. Cochineal is not only the main red dye used in Central America, but it was also used in Ecuador and Peru by the Incas, before the Spanish conquest. Cochineal is made up of 80% carminic acid (CA). In the 16th century, it was exported to Europe and began to replace the domestic kermes insect

(*Kermes vermilio*) [5, 6]. Cochineal insects are nowadays widely used in the food industry to replace synthetic colorants, and its antioxidant properties have been well known for a long time [7, 8].

In this study, we observed the increased UV-Vis spectral absorbance and electrical conductivity of the natural pigment through biosynthetic silver nanoparticles [5]. To improve the optical and electrical properties of cochineal, it was used as the reducing agent during the biosynthesis of silver nanoparticles (AgNPs) without submitting the cochineal to any kind of separation of its primary compounds. The cochineal extract was used as the reducing agent for the biosynthesis of AgNPs, since green synthesis of the AgNPs has been an easy, affordable, inexpensive technique and is potentially not harmful to human health and the environment [9–14]. Different volumes of cochineal dye (pH = 12, [5]) in 1 ml of AgNO₃ solution (10 mM, pH = 5.6) were analyzed with UV-Vis spectrometry, Commission Internationale de l'Éclairage (CIE) chromaticity diagram, cyclic voltammetry (CV), scanning transmission electron microscopy (STEM), energy dispersive X-ray spectroscopy

(EDS), dynamic light scattering (DLS), and X-ray diffraction (XRD). The surface morphology and electrical properties of the thin films were analyzed using atomic force microscopy (AFM). This suite of analytical tools facilitated the study of the thin films from multiple perspectives and explained their increased conductivity properties.

2. Materials and Methods

2.1. Materials. *Dactylopius coccus* Costa samples were obtained from the city of Loja, Ecuador. The insects, which were found in the tuna (fruit) of *Opuntia ficus-indica*, secrete a white and cottony substance that serves to protect them from external, environmental conditions. The interesting property of these insects is that they generate a natural red pigment inside their body. The goal of this research was to improve the properties of the cochineal by the synthesis of silver nanoparticles. The silver nitrate and all the solvents used in the sample preparation were obtained from Sigma-Aldrich (Missouri, United States).

2.2. Hybrid Material Synthesis. Ten grams (10.0 g) of the cochineal sample was dissolved in 3.0 L of methanol and distilled water (9:1, resp.). This solution was evaporated using a Rotavapor (Buchi R-220) at 40°C and a pressure of 44000 Pa before being vacuum-filtered (a filter paper of 0.45 μm). For the reduction of AgNO₃, the pigment was diluted with NaOH to obtain a pH of 12 [9]. For the biosynthesis of AgNPs, different volumes (0.1 ml and 0.4 ml) of the alkaline solution (cochineal at pH 12) were diluted with 1 ml of AgNO₃ solution (10 mM; pH = 5.6), and this mixture was incubated for 1 h at 40°C.

2.3. Physical and Chemical Characterization of the Hybrid Material. The stability of the nanoparticles in solution at room temperature was measured after 8 days using UV-Vis spectrometry (Analytik Jena S600). CIE chromaticity diagram was analyzed using OSRAM Sylvania, Inc. (2009) software. Cyclic voltammetry was done using a three-electrode system (Metrohm Autolab PGSTAT 128N). The working electrode was a carbon electrode; a calomel (Hg/HgCl) electrode was used as reference and a platinum strand served as the auxiliary electrode. The analyses were conducted in a background electrolyte solution of 0.1 M KCl. Prior to each analysis, dissolved oxygen in the KCl solution was removed by bubbling with N₂ (g) for 15 min. The voltammetry scan rate was 0.05 V·s⁻¹ at room temperature in the range from -1.2 to 1.2 V of the standard hydrogen electrode versus saturated calomel electrode (SHE versus SCE).

Particle size and morphology of the samples were analyzed by a scanning transmission electron microscope (TESCAN MIRA3) operating at an accelerating voltage of 25 kV equipped with a Bruker EDS XFlash 6130 detector. Dynamic light scattering (Horiba LB-550) was used to determine the hydrodynamic diameter of the AgNPs. All DLS measurements were performed at a 25°C fixed temperature.

Organic layers were grown onto quartz, silicon, and indium tin oxide (ITO)/glass substrates for the optical spectroscopy and morphology study of the samples' thin films. Before spin coating (40°C) the thin films, the substrates were cleaned with detergent, rinsed with deionized water, sonicated

in organic solvents and acetone, and rinsed with alcohol before being dried in a N₂ (g) stream. X-ray patterns of the thin films from different samples were collected on an Empryan diffractometer (PANalytical) in the Bragg-Brentano configuration at 40 kV and 45 A with monochromatic X-rays of Cu K-alpha wavelength ($\lambda = 1.541 \text{ \AA}$). The morphology in the ScanAsyst mode and surface conductivity in the conductive atomic force microscopy mode of the thin films were studied with a Bruker Icon atomic force microscope.

3. Results and Discussion

3.1. Hybrid Material Characterization. The UV-Vis absorption spectra of the cochineal solutions were obtained at pH 3.8 and 12.0 (Figure 1(a)). This pH change improves the cochineal reducing properties, which are conducive for the formation of AgNPs. Both solutions were stable at room temperature throughout the analysis. The inset in Figure 1(a) shows the corresponding CIE chromaticity diagram. The chromaticity of the solutions changed as a function of pH (inset in Figure 1(a); pH 3.2: $x = 0.318$, $y = 0.346$; pH 12.0: $x = 0.304$, $y = 0.372$). Gaussian fitting of the curves (Figure 1(b), pH 3.2: $\chi^2 = 0.14$; Figure 1(c), pH 12: $\chi^2 = 0.04$) shows a red shift in their wavelengths and a decrease in their half width at half maximum (HWHM). These changes are due to the predominance of carminic acid in cochineal, which has an anthraquinone nucleus. When diluted in distilled water (pH = 3.8) or in methanol (pH = 12), maximum absorption peaks can be observed in three bands: 243~243.5 nm, 280~282 nm, and 324~331 nm, respectively, with a slight bathochromic shift, but with a strong hypsochromic shift at a wavelength from 383.6 nm to 302.5 nm. This effect is caused not only by the carboxyl group in the C2 position but also by the deprotonation of hydroxyls in positions C3, C5, C6, and C8, which are stable at pH 12 and responsible for the hydroxyanthraquinone chromophore properties. The red color of the molecule is explained by the degree of oxidation of the anthraquinone nucleus with the maximum absorbance at 496 nm [15–17], similar to the one found in the analyzed extract.

Figures 2(a) and 2(b) show absorption spectra of the biosynthesis of silver nanoparticles (AgNPs) from the cochineal extract, and the difference of the two spectra is the volume of cochineal. Insets in Figures 2(a) and 2(b) show the time-dependent stability of AgNPs (Figure 2(a): $\lambda = 443 \text{ nm}$; Figure 2(b): $\lambda = 428.5 \text{ nm}$). From Figure 2(a), one can observe that the sample prepared with 0.1 ml of the cochineal extract in 1 ml of silver nitrate reached stability at 72 h. On the contrary, Figure 2(b) shows faster kinetics for the biosynthesis of AgNPs from 0.4 ml of the cochineal extracts in 1 ml of silver nitrate, reaching stability around 24 h. The faster reaction kinetics of the last sample (0.4 ml of the cochineal extract in 1 ml of AgNO₃) likely stems from the fourfold increase in the reducing agent volume.

Figure 3(a) shows the UV-Vis spectra of the cochineal extract at pH 12.0 and after the biosynthesis of AgNPs on the eighth day. The inset in Figure 3(a) shows the CIE chromaticity diagram for the extracts at pH 12 ($x = 0.251$, $y = 0.406$) and the biosynthesis of AgNPs with 0.1 ml ($x = 0.255$, $y = 0.238$) and 0.4 ml ($x = 0.275$, $y = 0.315$) of the cochineal extract. The results show that the biosynthesis of

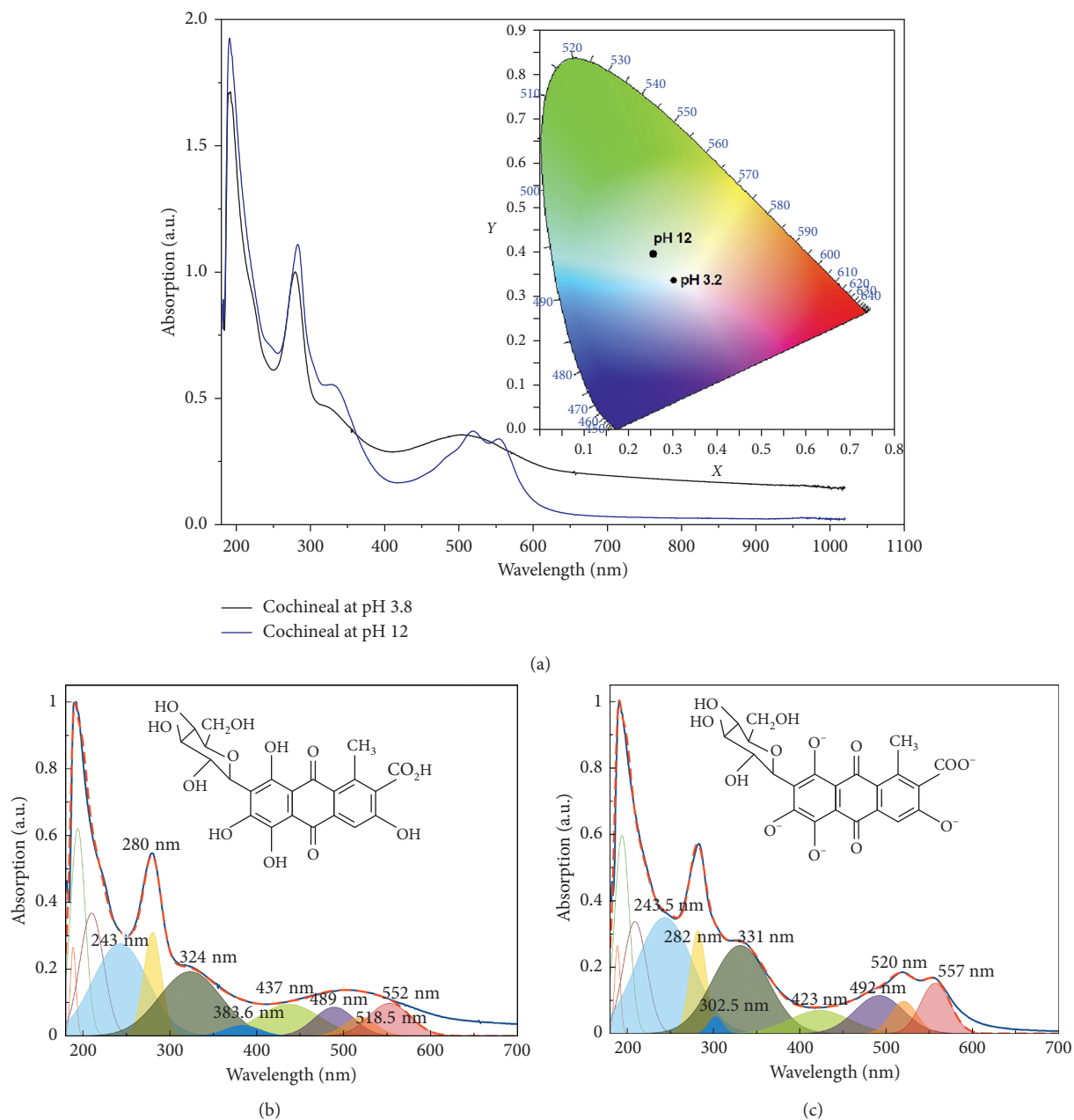


FIGURE 1: (a) UV-Vis spectra of cochineal pigment at pH 3.8 (black) and 12.0 (blue) with corresponding CIE chromaticity diagram (inset). Linear least-squares models (red dashed lines) of Gaussian components of cochineal pigment spectra (solid blue lines) at pH 3.8 (b) and 12.0 (c). Insets in (b) and (c) show the chemical structures of cochineal pigment at pH 3.8 and pH 12.0.

AgNPs with 0.4 ml of the cochineal extract has greater spectral absorbance in the UV-Vis region, indicating a possible candidate for photoactive thin films of organic solar cells [18–21].

According to Mie’s theory, optical properties of metal nanoparticles are dominated by localized surface plasmon resonance (LSPR), and the profile of LSPR bands depends on the shape of the particle [21, 22]. The AgNP mixture with 0.4 ml of the cochineal extract presented a single surface plasmon absorption band at 428.5 nm (Figure 3(c) and Table 1); however, the AgNP mixture with 0.1 ml of the cochineal extract presented two plasmon bands at 443 nm with a weak shoulder

peak at 379 nm (Figure 3(b) and Table 1), possibly suggesting nonspherical (irregularly shaped) particles [22, 23]. Hence, the two plasmon bands (at 379 nm and 433 nm; Table 1) presented by the Gaussian fit shown in Figure 3(b) (0.1 ml of the cochineal extract) imply the nonspherical nanoparticles [21, 22–24]. The nanoparticles formed with 0.4 ml of the cochineal extract are more likely being spherical in shape because only one band was observed at 428.5 nm (Figure 3(c) and Table 1). As the number of plasmon bands observed is indicative of the shape of the nanoparticles, those nanoparticles formed in the presence of 0.4 ml of the cochineal extract had a higher probability of being spherical in shape [21].

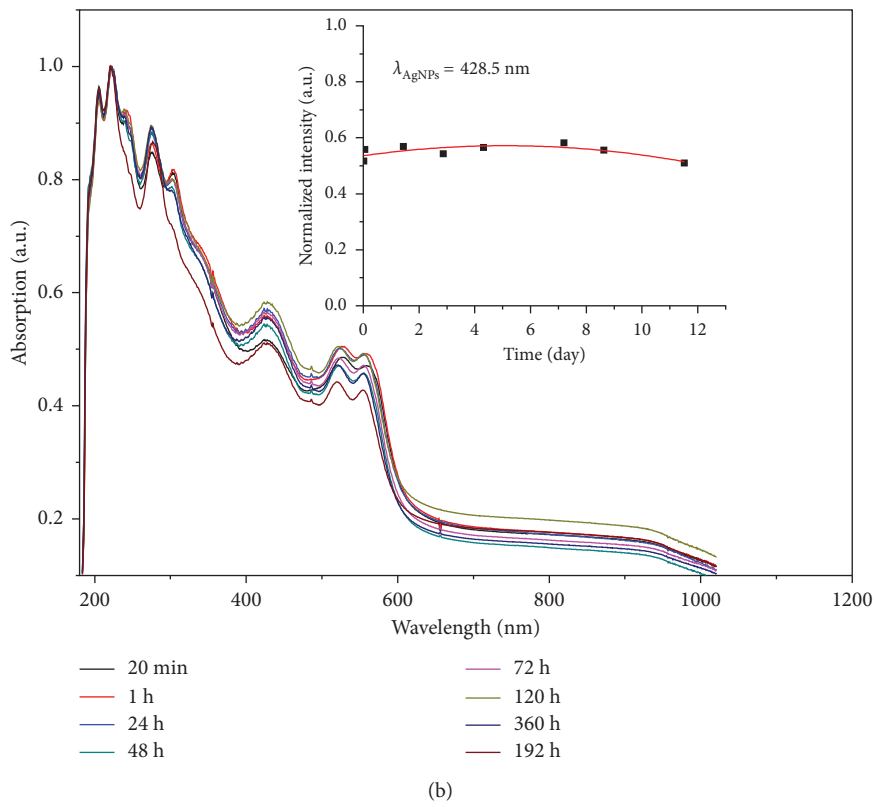
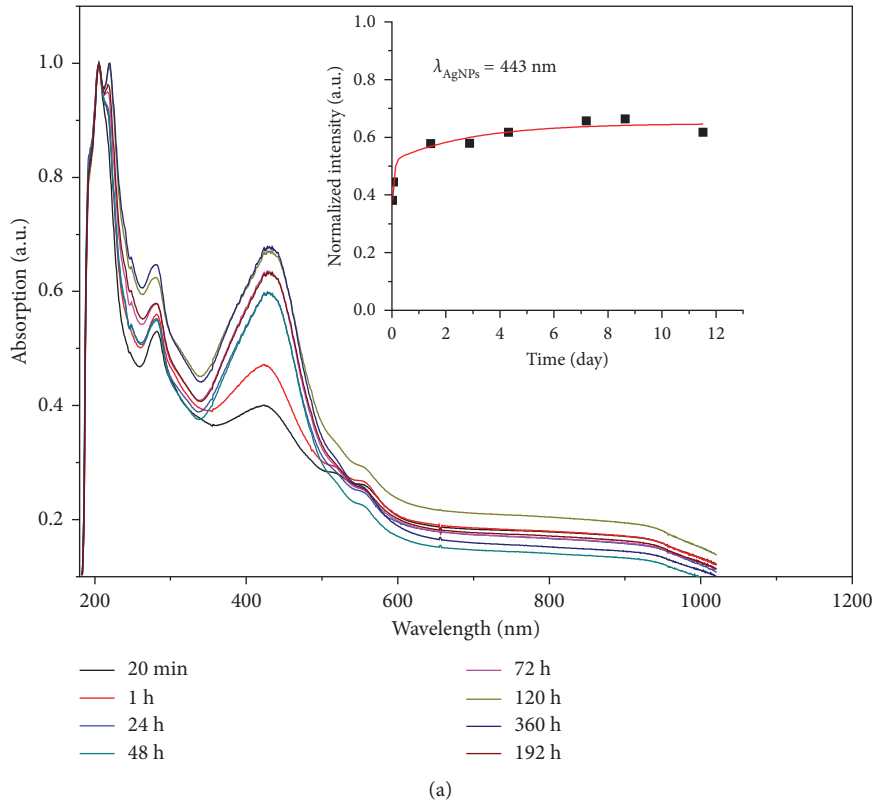


FIGURE 2: UV-Vis spectra collected over time during the formation of AgNPs in (a) 0.1 ml and (b) 0.4 ml of cochineal pigment solution. Insets follow the intensity of the absorbance peak over time (0.1 ml of cochineal extract: 443 nm and 0.4 ml cochineal extract: 428.5 nm).

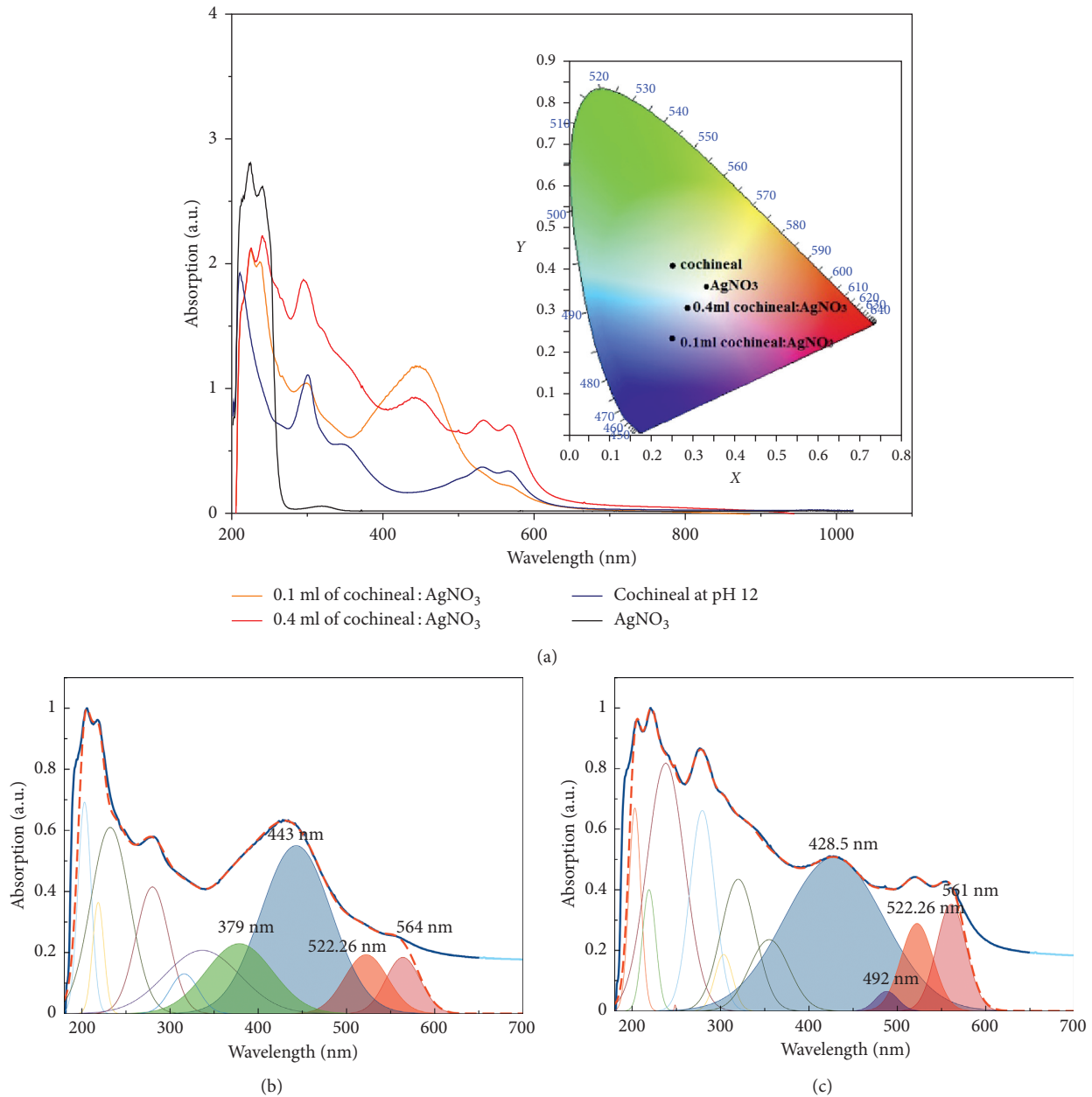


FIGURE 3: (a) Comparison of UV-Vis spectra of cochineal pigment (pH 12.0), silver nitrate, and AgNPs synthesized from (b) 0.1 ml and (c) 0.4 ml of the cochineal extract. The inset in (a) shows the corresponding CIE chromaticity diagram: cochineal pigment (pH 12.0, $x=0.251$, $y=0.406$), AgNPs (0.1 ml of the cochineal extract, $x=0.255$, $y=0.238$), and AgNPs (0.4 ml of the cochineal extract, $x=0.275$, $y=0.315$). Linear least-squares models (dashed red lines) of UV-Vis spectra (solid blue lines) with Gaussian components are shown in (b) AgNPs (0.1 ml of the cochineal extract) and (c) AgNPs (0.4 ml of the cochineal extract).

3.2. Physical and Chemical Characterization of the Hybrid Material. The spherical AgNPs were also indicated by a STEM image in the sample synthesized from 0.4 ml of the cochineal extract (Figure 4(b)) in agreement with the suggested results obtained of the LSPR bands. In the other sample, Figure 4(a) shows a diffuse image with very small particle sizes and, therefore, inconclusive results about the true morphology of the particles. EDS (Figure 4(c)) analysis confirmed that the particles were composed of silver when synthesized from cochineal solutions. The weight percentage of Ag in each sample (0.1 ml and 0.4 ml of the cochineal

extract) was similar because the volume of silver nitrate in the reagent was the same (Table 2). The size distribution of the different AgNPs ranged between 5 and 15 nm using DLS (Figure 4(d)).

The X-ray pattern was recorded from the same batch of samples (Figure 5). The inset in Figure 5 shows AgNPs synthesis with 0.4 mL of the cochineal extract, which was dried at 100°C as well as a graphical representation of the scattering of X-rays in the film. When the thin film was dried at 40°C, chlorargyrite (AgCl), silver oxide (Ag₂O), and other structures were observed (Table 3). The reason is that the

TABLE 1: Wavelength analysis of the half width at half maximum (HWHM) of cochineal at pH 12 and biosynthetic AgNPs at different initial volumes (0.1 and 0.4 ml) of the cochineal extract.

Number	Cochineal at pH 12		0.4 ml of the cochineal extract in 10 ml of AgNO ₃		0.1 ml of the cochineal extract in 10 ml of AgNO ₃	
	Wavelength (nm)	Spectral width (HWHM) (nm)	Wavelength (nm)	Spectral width (HWHM) (nm)	Wavelength (nm)	Spectral width (HWHM) (nm)
1	203.02	8.72	203.02	7.90	203.02	8.70
2	273.58	14.69	279.30	16.70	280.00	22.00
3	303.17	20.56	303.50	12.00	—	—
4	—	—	—	—	379.00	44.5
5	—	—	428.50	66.00	433.00	47.00
6	489.59	22.20	489.00	15.00	—	—
7	525.75	21.63	522.26	21.50	522.26	29.00
8	569.58	27.10	561.00	19.80	564.00	23.00

The wavelengths correspond to the formation of silver nanoparticles and of the natural pigment (cochineal) [21–23].

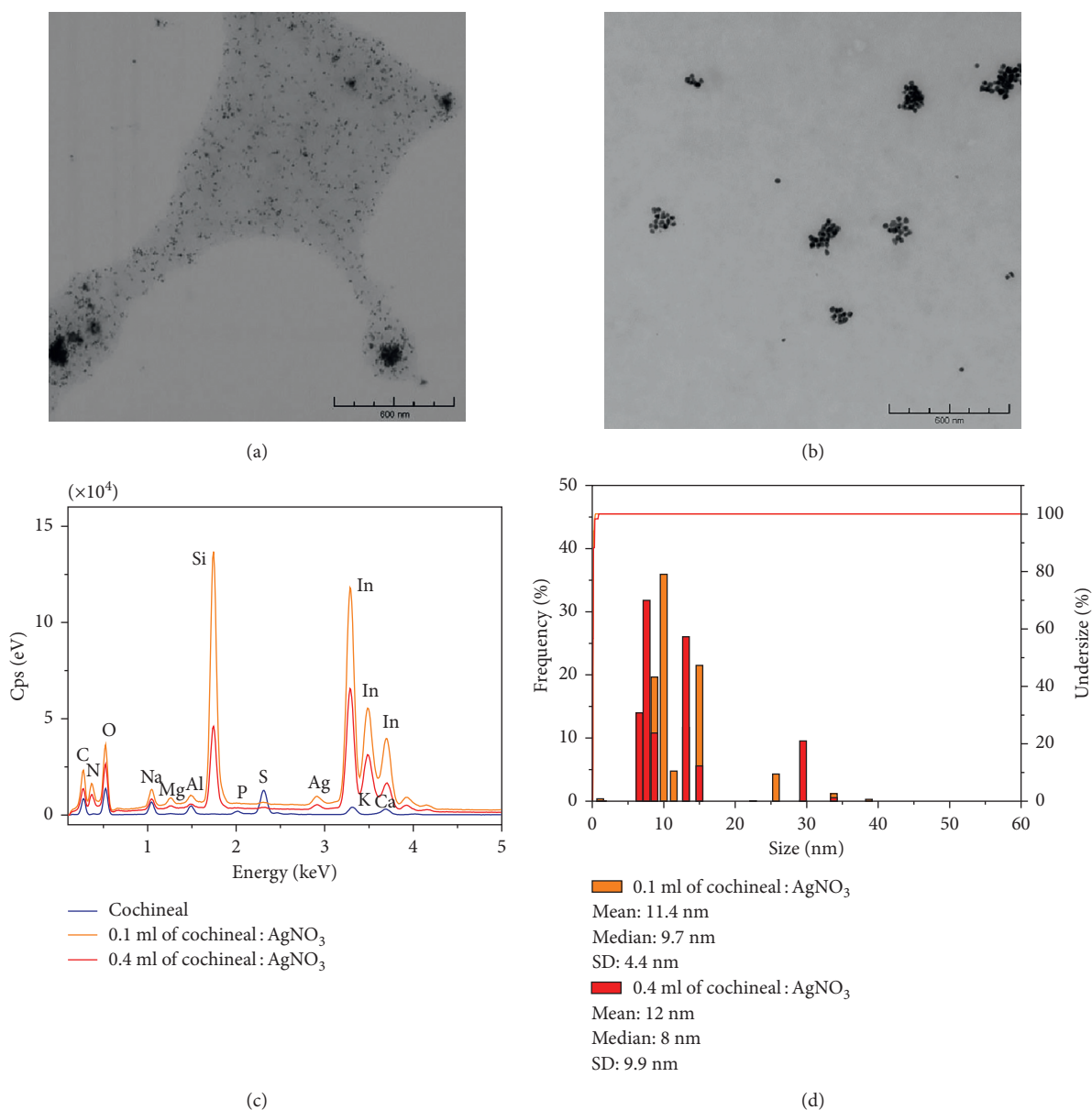


FIGURE 4: Scanning transmission electron micrographs of AgNPs synthesized from 0.1 ml (a) and 0.4 ml (b) of the cochineal extract and their (c) EDS spectra and (d) DLS analyses.

TABLE 2: Major elemental composition (weight percent) of cochineal pigment and AgNPs synthesized from 0.1 and 0.4 ml of the cochineal extract.

Elements	wt. %		
	Cochineal at pH 3.8	0.1 ml of the cochineal extract	0.4 ml of the cochineal extract
Ag	—	0.89 ± 0.05	0.83 ± 0.02
Na	0.21 ± 0.04	1.29 ± 0.11	1.50 ± 0.13
Mg	0.40 ± 0.05	0.37 ± 0.04	0.35 ± 0.05
Al	0.42 ± 0.03	0.30 ± 0.03	0.31 ± 0.04
S	6.18 ± 0.25	—	0.02 ± 0.01

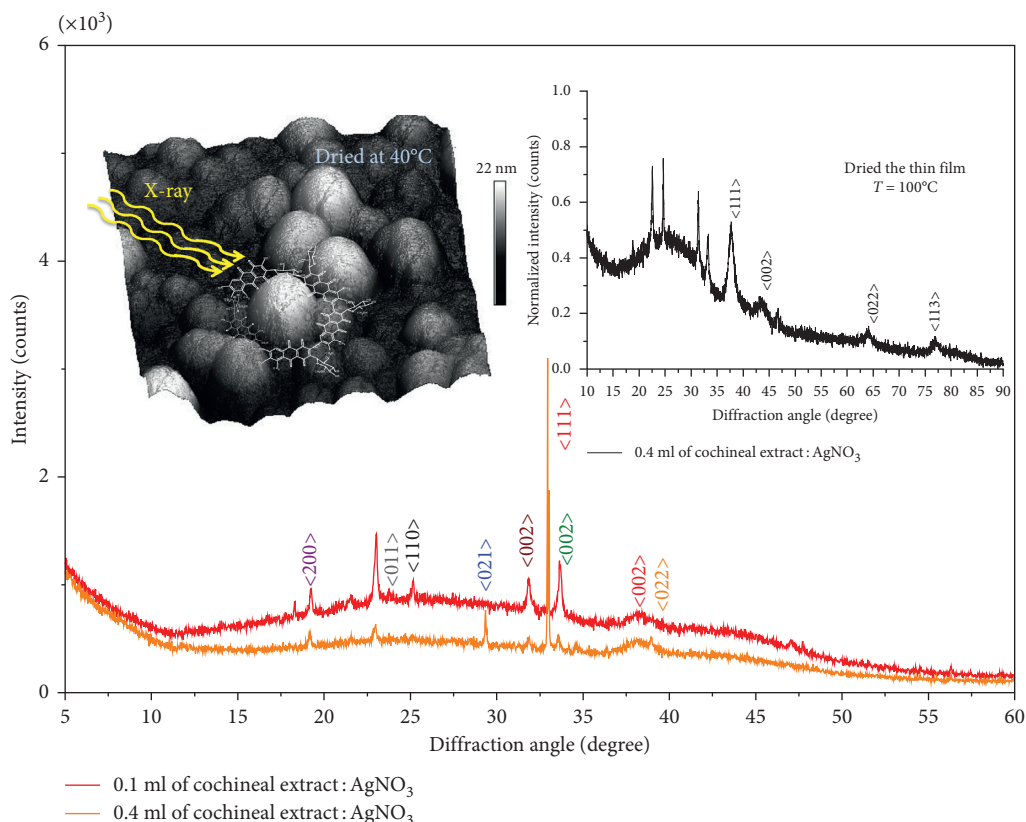


FIGURE 5: XRD patterns of AgNP thin films (0.1 and 0.4 ml of cochineal extract solution) dried at 40°C. Inset shows the schematic representation of X radiation in the thin film and the XRD pattern of AgNPs synthesized with 0.4 ml of the cochineal extract (same batch) but dried at 100°C confirming the formation of face centre cubic silver.

TABLE 3: Crystal structure analysis of AgNPs synthesized from 0.1 and 0.4 ml of the cochineal extract dried at 40 and 100°C.

Name	Crystal system	<hkl>	Color	%	
				0.1 ml Dried at 40°C	0.4 ml Dried at 100°C
Chlorargyrite	Cubic	<002>	Green	2.1	3.2
Silver oxide	Cubic	<111> <002>	Red	0.3	3.7
Sodium sulfide	Cubic	<022>	Orange	14.6	12.2
Sulfur helical	Hexagonal	<110>	Black	15.2	26.1
Ice	Tetragonal	<021>	Blue	36.3	21.4
Halite	Cubic	<002>	Wine	11.0	10.8
Aluminium trihydroxide	Monoclinic	<200>	Violet	2.2	2.1
Potassium	Cubic	<001>	Plum	2.1	2.5
Silver	Cubic	<111>			
		<002>			
		<022>			42.3
		<113>			

Values are obtained by Rietveld analysis.

organic matrix which surrounds the AgNPs produces increased scattering of X-rays, limiting observation of the silver crystals. When the thin film was dried at 100°C, silver crystals were detected (Table 3) [25–28]. The clear detection of silver crystals was observed due to the degradation of organic compounds at that temperature. The relation detected by XRD for the two volumes of the cochineal extract of 0.4 ml and 0.1 ml for AgCl and Ag₂O shows that the AgNPs formation was greater at the higher cochineal volume, which was confirmed by STEM micrographs, the physical-chemical analysis by EDS, and UV-Vis absorption spectroscopy.

3.3. Cyclic Voltammetry Characterization. Figure 6 shows the cyclic voltammogram of the cochineal pigment and of the two hybrid materials within a potential window of –1.0 to 1.2 V. The cochineal extract exhibited no reduction peak; however, three oxidation peaks were observed at –0.14, –0.32, and –0.61 V in the aqueous medium. Curves b (0.1 ml of the cochineal extract) and c (0.4 ml of the cochineal extract) exhibit the reduction of AgNO₃ by oxidation of the cochineal pigment with concomitant formation of AgNPs. The two curves (b and c) exhibit the oxidation (+0.88 V) and reduction (–0.18 V) of the cochineal extract. 0.4 ml of the cochineal extract sample (curve c) also shows a reduction event occurring at –0.66 V. Curves b (0.1 ml of the cochineal extract) and c (0.4 ml of the cochineal extract) exhibit the reduction of the Ag⁺ ions to elemental Ag⁰ by cochineal oxidation leading to stable AgNPs; however, the two curves also show the contribution of AgNO₃. Likewise, the oxidation of Ag⁺ to Ag₂O is observed, especially in 0.1 ml of the cochineal extract sample in which the amount of reductant to AgNO₃ ratio was smaller. These results show that a higher volume of cochineal is required to avoid the formation of Ag₂O and ascertain the reduction of AgNO₃ with reasonable reaction kinetics [29, 30].

The reduction of AgNO₃ is probably due to electron transfer from carboxyl/hydroxyl groups of cochineal to Ag⁺ resulting in stable AgNPs. The energy gap and ionization potential of the biosynthesis of AgNPs from cochineal were estimated with optical and electrochemical techniques [31]. Based on these values, the highest occupied molecular orbital (HOMO) and lowest unoccupied molecular orbital (LUMO) energy levels could be determined (Table 4). These results show that the AgNPs synthesized from 0.4 ml of the cochineal extract have a smaller energy gap and thus have better photon absorbance (2.169 eV) than the corresponding AgNPs synthesized from 0.1 ml of the cochineal extract (2.669 eV) in the UV-Vis region.

3.4. AFM and Electrical Measurements. Figures 7(a)–7(d) show AFM images from the samples of the cochineal pigment and AgNPs (0.4 ml and 0.1 ml of the cochineal extract) on silicon. The roughness of the clusters was calculated to be 2.06 ± 0.19 nm (Figure 7(a), cochineal pigment), 5.94 ± 1.30 nm (Figure 7(b), 0.4 ml of the cochineal extract sample), and 2.96 ± 0.35 nm (Figure 7(c), 0.1 ml of the cochineal extract sample). Figure 7(d) shows an enlargement of the AFM image of AgNPs synthesized from 0.4 ml of the

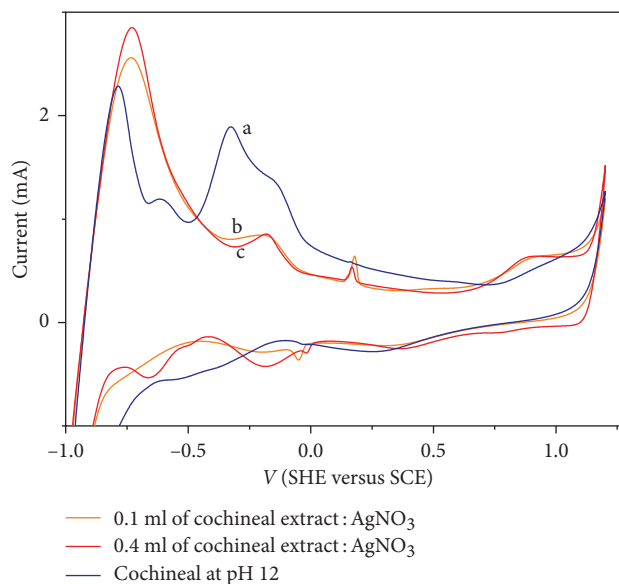


FIGURE 6: Cyclic voltammogram of cochineal pigment and AgNPs synthesized from 0.1 and 0.4 ml of the cochineal extract. SHE = saturated hydrogen electrode; SCE = saturated calomel electrode.

TABLE 4: Energy levels of cochineal pigment (pH 12.0) and AgNPs (0.1 and 0.4 ml of the cochineal extract).

Energy	Cochineal at pH 12	0.4 ml of the cochineal extract in 10 ml of AgNO ₃	0.1 ml of the cochineal extract in 10 ml of AgNO ₃
HOMO (eV)	-5.178 ± 0.001	-5.074 ± 0.002	-5.049 ± 0.004
LUMO (eV)	-3.055 ± 0.002	-2.905 ± 0.003	-2.380 ± 0.002

cochineal extract on a silicon substrate. The differences between the nanoparticles from the two ((Figure 7(b), 0.1 ml of the cochineal extract) and (Figure 7(c), 0.4 ml of the cochineal extract)) are clearly observed by the surface roughness being less in the case of AgNPs with 0.1 ml of the cochineal extract compared to 0.4 ml of the cochineal extract, which might contribute to the size increase of the AgNPs due to cochineal adsorption. Studies show that, to obtain a good efficiency of a hybrid device, it must have roughness around 2 nm [32]. In this case, the 0.4 ml sample of the cochineal extract that exceeds this value due to the size of the AgNPs must undergo an optimization of the spin-coating technique. This finding is in agreement with the size distributions shown in Figure 4(d). The effect of the potential size regulation is demonstrated in Figure 7(e) for thin films of the cochineal pigment and AgNPs (0.4 and 0.1 ml of the cochineal extract). The potential offset is positive indicating the level of conductivity possible for each sample for application in organic devices.

4. Conclusion

This work demonstrates that, despite maintaining reaction time, temperature, and silver nitrate concentration, a change

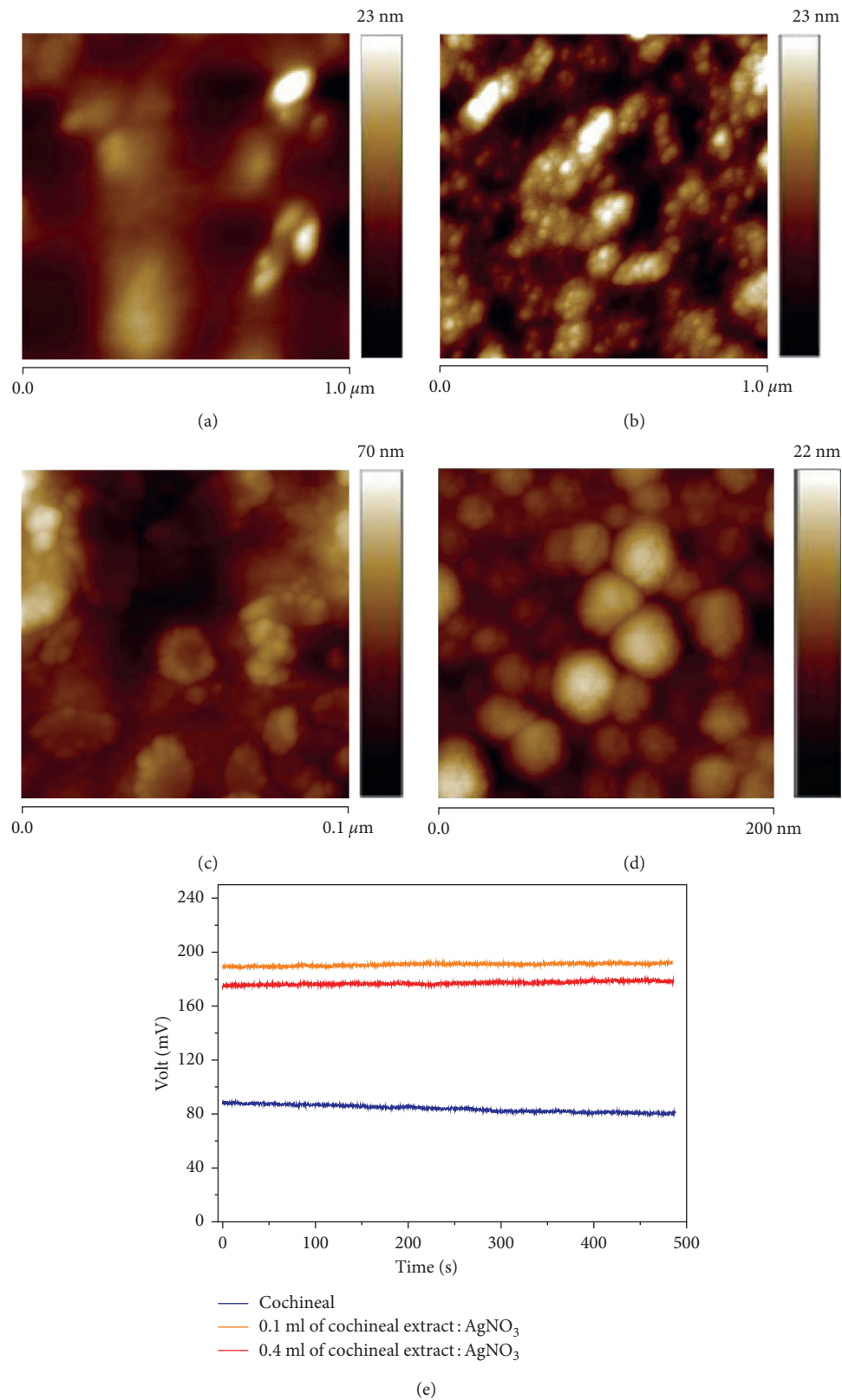


FIGURE 7: Atomic force micrographs of $1 \times 1 \mu\text{m}^2$ thin films (on glass) of (a) cochineal pigment and AgNPs synthesized with (b) 0.1 ml and (c) 0.4 ml of cochineal extract solution. (d) Atomic force micrograph of $200 \times 200 \text{ nm}^2$ from the same batch as shown in (c). Electric potential curves (e) as a function of time of cochineal pigment and AgNPs (0.1 and 0.4 ml of the cochineal extract).

of the LSPR band of AgNPs was observed as a function of the amount of cochineal applied. The higher cochineal concentration (0.4 ml of the cochineal extract) generated spherical AgNPs of 5 to 10 nm and good stability at room temperature. The trace of Ag₂O observed in the sample (electrochemistry and XRD) probably stems from the concentration of cochineal used in the preparation process. If a slightly lowered concentration was used, incomplete reduction of silver nitrate is likely. Coating AgNPs with the cochineal pigment through direct biosynthesis improved the absorption spectrum in the UV-Vis range of the nanoparticles. The AgNPs in turn improve the electrical properties of the cochineal pigment converting it into a promising photoactive layer of organic solar cells.

Conflicts of Interest

The authors declare that they have no conflicts of interest.

Acknowledgments

This work was supported by a research grant (Grant no. 2014-PIT-034) of Universidad de las Fuerzas Armadas ESPE.

Supplementary Materials

Graphical abstract is included in this manuscript as a supplementary file. (*Supplementary Materials*)

References

- [1] G. Krucaite, L. Liu, D. Tavgeniene et al., "Electroactive polymers containing 3-arylcabazoyl units as hole transporting materials for OLEDs," *Optical Materials*, vol. 42, pp. 94–98, 2015.
- [2] H. Duan, J. Yang, L. Fu et al., "Interface modification of organic photovoltaics by combining molybdenum oxide (MoOx) and molecular template layer," *Thin Solid Films*, vol. 574, pp. 146–151, 2015.
- [3] C. Chappaz-Gillot, S. Berson, R. Salazar et al., "Polymer solar cells with electrodeposited CuSC nanowires as new efficient hole transporting layer," *Solar Energy Materials and Solar Cells*, vol. 120, pp. 163–167, 2014.
- [4] G. Lopinski, N. Du, G. Dubey et al., "Cyanoethylated pullulan as a high-k solution processable polymer gate dielectric for SWCNT TFTs," *Organic Electronics*, vol. 42, pp. 329–336, 2017.
- [5] B. Kumar, K. Smita, Y. Angulo, and L. Cumbal, "Green synthesis of silver nanoparticles using natural dyes of cochineal," *Journal of Cluster Science*, vol. 27, no. 2, pp. 703–713, 2016.
- [6] M. Schoeser and J. Macdonald, *Silk*, Yale University Press, New Haven, CT, USA, 2007.
- [7] M. González, M. Gloria Lobo, J. Méndez, and A. Carnero, "Food control, detection of colour adulteration in cochineals by spectrophotometric determination of yellow and red pigment groups," *Food Control*, vol. 16, no. 2, pp. 105–112, 2005.
- [8] M. Shahid, S.-U. Islam, and F. Mohammad, "Recent advancements in natural dye applications: a review," *Journal of Cleaner Production*, vol. 53, pp. 310–331, 2013.
- [9] B. Kumar, Y. Angulo, K. Smita, L. Cumbal, and A. Debut, "Capuli cherry-mediated green synthesis of silver nanoparticles under white solar and blue LED light," *Particuology*, vol. 24, pp. 123–128, 2016.
- [10] B. Kumar, K. Smita, L. Cumbal, and A. Debut, "Ficus carica (fig) fruit mediated green synthesis of silver nanoparticles and its antioxidant activity: a comparison of thermal and ultrasonication approach," *BioNanoScience*, vol. 6, no. 1, pp. 15–21, 2016.
- [11] B. Kumar, K. Smita, L. Cumbal, A. Debut, and R. N. Pathak, "Ionic liquid based silica tuned silver nanoparticles: novel approach for fabrication," *Synthesis and Reactivity in Inorganic, Metal-Organic, and Nano-Metal Chemistry*, vol. 46, no. 8, pp. 1265–1271, 2016.
- [12] K. S. Vizuete, B. Kumar, K. Guzmán, A. Debut, and L. Cumbal, "Shora (*Capparis petiolaris*) fruit mediated green synthesis and application of silver nanoparticles," *Green Processing and Synthesis*, vol. 6, no. 1, pp. 23–30, 2017.
- [13] M. E. Borges, R. L. Tejera, L. Díaz, P. Esparza, and E. Ibáñez, "Natural dyes extraction from cochineal (*Dactylopius coccus*). New extraction methods," *Food Chemistry*, vol. 132, no. 4, pp. 1855–1860, 2012.
- [14] E. A. González, E. M. García, and M. A. Nazareno, "Free radical scavenging capacity and antioxidant activity of cochineal (*Dactylopius coccus* C.) extracts," *Food Chemistry*, vol. 119, no. 1, pp. 358–362, 2010.
- [15] K. Do, C. Kim, K. Song, S. J. Yun, J. K. Lee, and J. Ko, "Efficient planar organic semiconductors containing fused triphenylamine for solution processed small molecule organic solar cells," *Solar Energy Materials and Solar Cells*, vol. 115, pp. 52–57, 2013.
- [16] V. Shanmugam, S. Manoharan, S. Anandan, and R. Murugan, "Performance of dye-sensitized solar cells fabricated with extracts from fruits of ivy gourd and flowers of red frangipani as sensitizers," *Spectrochemical Acta Part A: Molecular and Biomolecular Spectroscopy*, vol. 104, pp. 35–40, 2013.
- [17] M. R. Narayan, "Review: dye sensitized solar cells based on natural photosensitizers," *Renewable and Sustainable Energy Reviews*, vol. 16, pp. 208–215, 2012.
- [18] T. Huang and X.-H. N. Xu, "Synthesis and characterization of tunable rainbow colored colloidal silver nanoparticles using single-nanoparticle plasmonic microscopy and spectroscopy," *Journal of Materials Chemistry*, vol. 20, no. 44, pp. 9867–9876, 2010.
- [19] V. Dal Lago, L. F. de Oliveira, K. D. A. Goncalves, J. Kobarg, and M. B. Cardoso, "Size-selective silver nanoparticles: future of biomedical devices with enhanced bactericidal properties," *Journal of Materials Chemistry*, vol. 21, no. 33, pp. 12267–12273, 2011.
- [20] B. Chudasama, A. K. Vala, N. Andhariya, R. V. Mehta, and R. V. Upadhyay, "Highly bacterial resistant silver nanoparticles: synthesis and antibacterial activities," *Journal of Nanoparticle Research*, vol. 12, no. 5, pp. 1677–1685, 2010.
- [21] J. F. Affonso de Oliveira and M. B. Cardoso, "Partial aggregation of silver nanoparticles induced by capping and reducing agents competition," *Langmuir*, vol. 30, no. 17, pp. 4879–4886, 2014.
- [22] G. Favaro, C. Miliari, A. Romani, and M. Vagnini, "Role of protolytic interactions in photo-aging processes of carminic acid and carminic lake in solution and painted layers," *Journal of the Chemical Society, Perkin Transactions*, vol. 2, no. 1, pp. 192–197, 2002.
- [23] E. H. Anouar, C. P. Osman, J.-F. F. Weber, and N. H. Ismail, "UV/Visible spectra of a series of natural and synthesised anthraquinones: experimental and quantum chemical approaches," *SpringerPlus*, vol. 3, p. 233, 2014.

- [24] D. de Marcano and M. Hasegawa, *Fitoquímica Brgánica*, Editorial Consejo de Desarrollo Científico y Humanístico, Venezuela, 1st edition, 1991.
- [25] M. Šuleková, A. Hudák, and M. Smrcová, “The determination of food dyes in vitamins by RP-HPLC,” *Molecules*, vol. 21, no. 10, p. 1368, 2016.
- [26] P. Magudapathy, P. Gangopadhyay, B. K. Panigrahi, K. G. M. Nair, and S. Dhara, “Electrical transport studies of Ag nanoclusters embedded in glass matrix,” *Physica B: Condensed Matter*, vol. 299, no. 1-2, pp. 142–146, 2001.
- [27] S. Talekar, A. Joshi, R. Chougale, A. Nakhe, and R. Bhojwani, “Immobilized enzyme mediated synthesis of silver nanoparticles using cross-linked enzyme aggregates (CLEAs) of NADH-dependent nitrate reductase,” *Nano-Structures and Nano-Objects*, vol. 6, pp. 23–33, 2016.
- [28] D. K. Lee and Y. S. Kang, “Synthesis of silver nanocrystallites by a new thermal decomposition method and their characterization,” *ETRI Journal*, vol. 26, no. 3, pp. 252–256, 2004.
- [29] J. Tian, S. Liu, Y. Zhang et al., “Environmentally friendly, one-pot synthesis of Ag nanoparticle-decorated reduced graphene oxide composites and their application to photocurrent generation,” *Inorganic Chemistry*, vol. 51, no. 8, pp. 4742–4746, 2012.
- [30] R. M. Thangavelu, D. Gunasekaran, M. I. Jesse, S. U. Mohammed Riyaz, D. Sundarajan, and K. Krishnan, “Nanobiotechnology approach using plant rooting hormone synthesized silver nanoparticle as “nanobullets” for the dynamic applications in horticulture—an in vitro and ex vitro study,” *Arabian Journal of Chemistry*, vol. 11, no. 1, pp. 48–61, 2016.
- [31] W.G. Quirino, C. Legnani, R. M. B. dos Santos et al., “Electroluminescent devices based on rare-earth tetrakis β -diketonate complexes,” *Thin Solid Films*, vol. 517, no. 3, pp. 1096–1100, 2008.
- [32] C.-C. Chen, S. H. Chang, L.-C. Chen et al., “Improving the efficiency of inverted mixed-organic-cation perovskite absorber based photovoltaics by tailing the surface roughness of PEDOT: PSS thin film,” *Solar Energy*, vol. 134, pp. 445–451, 2016.

Research Article

Larvicidal Activity of Silver Nanoparticles Synthesized Using Extracts of *Ambrosia arborescens* (Asteraceae) to Control *Aedes aegypti* L. (Diptera: Culicidae)

Bianca Morejón,¹ Fernanda Pilaquina,^{2,3} Flavia Domenech,² Danny Ganchala,² Alexis Debut ,⁴ and Marco Neira ¹

¹Exact and Natural Sciences Department, Center for Research on Health in Latin America, Pontificia Universidad Católica del Ecuador, Quito, Ecuador

²Exact and Natural Sciences Department, Laboratory of Nanotechnology, Pontificia Universidad Católica del Ecuador, Quito, Ecuador

³Department of Chemistry, University of the Balearic Islands, Palma de Mallorca, Balearic Islands, Spain

⁴Universidad de las Fuerzas Armadas ESPE, Sangolquí, Ecuador

Correspondence should be addressed to Marco Neira; mvneira@puce.edu.ec

Received 1 November 2017; Accepted 4 March 2018; Published 18 April 2018

Academic Editor: David Quesada

Copyright © 2018 Bianca Morejón et al. This is an open access article distributed under the Creative Commons Attribution License, which permits unrestricted use, distribution, and reproduction in any medium, provided the original work is properly cited.

The mosquito species *Aedes aegypti* is the primary vector of dengue, chikungunya, and Zika infections worldwide. Since effective vaccines or drugs are not available for the prevention and/or treatment of these pathologies, vector control has been adopted as the main approach to reduce their transmission. To control *Aedes* populations, the most commonly used tool is the application of chemical insecticides and, despite their effectiveness, indiscriminate use of these chemicals has led to high operational costs, appearance of resistant populations, and adverse nontarget effects. Plant-derived insecticides may be an eco-friendly, cost-effective, and safe biocontrol alternative. The present study was carried out to evaluate the larvicidal activity of leaf extracts of *Ambrosia arborescens* and green-synthesized silver nanoparticles (AgNPs) using aqueous extracts obtained from this plant against third instar larvae of *Ae. aegypti*. To test this, larvae were exposed for 24 h to the aqueous plant extract at 1500, 3000, 4500, and 6000 ppm and the plant-synthesized AgNPs at 0.2, 0.3, 0.4, and 0.5 ppm. In laboratory assays, AgNPs were more toxic ($LC_{50} = 0.28$ ppm; $LC_{90} = 0.43$ ppm) than the plant extract ($LC_{50} = 1844.61$ ppm; $LC_{90} = 6043.95$ ppm). These results suggest that *A. arborescens* aqueous extract and green-synthesized silver nanoparticles produced from those extracts have the potential to be developed into suitable alternative tools useful for the control of *Ae. aegypti* populations.

1. Introduction

Over the last decades, climate change, population growth, deforestation, habitat invasion, and insecticide resistance have contributed to the emergence, reemergence, and dispersion of several vector-borne diseases. Among these, those transmitted by the mosquito *Aedes aegypti* (Diptera: Culicidae), which include dengue fever, yellow fever, chikungunya, and Zika, represent some of the major challenges of public health in a vast region of our planet, affecting the lives of hundreds of millions of people every year [1, 2].

Originally native to Africa, *Ae. aegypti* is a strongly anthropophilic and sinanthropic species which, due to its capacity to thrive in human settlements, has been able to expand its distribution all along the tropical and subtropical regions of the globe [3]. Female *Ae. aegypti* become arbovirus vectors after ingesting an infectious blood meal. Once the pathogen starts being secreted with the insect's saliva, the mosquito becomes infective and will transmit the pathogen every time it blood feeds on a susceptible host, for the rest of its life [4, 5].

With the exception of yellow fever, for which an efficient vaccine has been available since the 1940's [6], no vaccine is

currently commercially available against the viral diseases transmitted by *Ae. aegypti*. Therefore, prevention of these diseases is mainly achieved through mosquito population control. Traditionally, most control programs have relied heavily on the use of chemical pesticides, targeting both adults and larvae [7, 8]. Unfortunately, the persistent and in some cases indiscriminate use of these chemicals has resulted in a reduction of their efficacy due to the dramatic emergence of resistant insect populations during the last decades [9].

Larvicides are among the main tools in our arsenal to control mosquito populations. The most widely used larvicides are organophosphates such as temephos, growth inhibitors, and bacterial insecticides such as *Bacillus thuringiensis israelensis* (Bti) and *Bacillus sphaericus* [8, 10, 11]. Because larvicides must be applied to either natural or artificial bodies of water, they must be harmless to fish and other nontarget organisms, including humans, potentially associated with these water reservoirs [12]. Therefore, the development of new biodegradable, eco-friendly, and specific larvicides is of paramount importance for future control strategies.

Larvicides derived from botanical extracts constitute a new and promising category of pesticide, due to their reduced toxicity for nontarget species and low environmental pollution [13]. Unlike conventional insecticides, which normally contain one specific active agent, plant-derived larvicides usually contain a combination of several chemical compounds that work synergistically, targeting different biological processes and therefore reducing the likelihood of resistance development in their targets [14]. An interesting alternative to strictly botanic larvicides is the production of silver nanoparticles (AgNPs) synthesized using plant extracts as reducing, stabilizing, and capping agents [15]. This technology combines the microbicide properties of silver, the insecticidal activity of the selected plant, and a high efficiency due to the favorable surface area to volume ratio due to the small size of the particles (1–100 nm) [16, 17]. In combination, these characteristics allow AgNPs to achieve their insecticide effect at very low concentrations (often ≥ 30 mg/L) [14].

Due to its location, geography, and climate, Ecuador is widely regarded as a hotspot for biodiversity [18]. Among the large variety of plant species present in this country, at least 34 have been reported to be used as insecticides by local populations [19]. Among these, *Ambrosia arborescens* (Mill.) stands out as a species used by various populations for insecticidal purposes, including the elimination of fleas, lice, flies, and other insects [19]. This plant, commonly known as “marco,” “marku,” “altamisa,” or “artemisia,” is a species native to Ecuador that belongs to the family Asteraceae and is found in the Andean region of the country, between 2000 and 3500 m.a.s.l [20]. The plant can range in size from a subshrub to a small tree and presents a pungent odor, and its stems contain an aqueous bitter latex [21].

In this context, we attempted to evaluate the potential of *A. arborescens* as a larvicide against *Ae. aegypti*, both as an aqueous extract and in combination with AgNPs.



FIGURE 1: *Ambrosia arborescens* (Mill.) voucher.

2. Materials and Methods

2.1. Plant Specimens. Fresh leaves of *A. arborescens* were collected in a small, family-owned farm in the Calacalí parish (geographic coordinates: 78°30'55.7"S, 00°00'32.7"O), which is located approximately 17 km north of Ecuador's capital city, Quito, at an altitude of 2980 m.a.s.l. The plot where the plant was growing had not received any kind of pesticide or fertilizer for at least one year previous to our collection date (R. Zambrano, personal communication).

A botanical voucher specimen (Figure 1) was prepared and deposited at the Center for Research on Health in Latin America (CISEAL) as a reference.

2.2. Preparation of *A. arborescens* Extract. The leaves of *A. arborescens* were cleaned of any visible debris and dried in shade for seven days at room temperature. Subsequently, they were dried in an oven at 40°C for 48 hours; dried sample was ground in a mortar. To prepare the extract, 1 g of vegetable material and 20 mL of distilled water were added. The mixture was placed under constant stirring for one hour at 60°C \pm 1°C; after this time, the extract was filtered and stored at 4°C until use.

2.3. Synthesis of Silver Nanoparticles. The best conditions were previously optimized using 1 mM silver nitrate Sigma-Aldrich® solution. Twenty mL of this solution was taken, and 2 mL of the extract of *A. arborescens* were added dropwise. Two to three drops of 1% NaOH were added to adjust the pH to 8. This mixture was stirred for 50 minutes at a temperature of 50°C \pm 1°C. The colloidal solution was cooled and stored in amber containers at 4°C for further analysis.

2.4. Characterization of Silver Nanoparticles

2.4.1. UV-Vis Spectroscopy. The nanoparticles were analyzed on a Cary 60 double beam spectrophotometer from Agilent Technologies. The resolution of the equipment was one nm, and the measurement range was from 350 to 800 nm. Dilutions 1 to 10 were made with distilled water from colloidal solutions obtained from the synthesis process.

2.4.2. FTIR Spectroscopy. Infrared spectroscopy analyses were performed on a Spectrum BX PerkinElmer with ATR Miracle Pike coupling under 4 cm^{-1} resolution conditions, ranging from 4000 cm^{-1} to 500 cm^{-1} , and ten scans per sample. Both the extract and the synthesized nanoparticles were dried in the oven at 60°C for 24 hours.

2.4.3. STEM Analysis. The STEM analysis was carried out on a FEG-SEM Tescan Mira 3 device, using a voltage of 30 kV. Nanoparticles were observed in colloidal solution.

2.4.4. SEM-EDX Analysis. SEM analysis was performed in a Phenom ProX scanning electron microscope equipped with an EDX-detector operating at 10 kV and ProSuite-EDS software. Nanoparticles were read in solid state over a pin of carbon.

2.4.5. Flame Atomic Absorption Spectroscopy for Silver Quantification. The silver content was analyzed on a PerkinElmer AAnalyst 400 atomic absorption spectrophotometer. A flux of 10.0 L/min of air and 2.5 L/min of acetylene were used for the flame. For the reading of the samples, once the performance of the method was verified, and a 1 : 100 dilution with distilled water of the obtained colloidal solutions was made.

2.4.6. Mosquito Rearing. The strain of *Ae. aegypti* used for this work was collected in 2015 in the Ecuadorian city of Puerto Francisco de Orellana, Orellana Province, and has since been continuously maintained under standard insectary conditions ($28 \pm 1^\circ\text{C}$ temperature, $80 \pm 10\%$ relative humidity, and 12 h light/12 h darkness photoperiod) at CISEAL [22].

Eggs were hatched in water that had been previously boiled and allowed to cool down to room temperature. Larvae were fed on finely ground fish food flakes, following the feeding regime developed by Carvalho et al. [23]. The larvae were maintained at the aforementioned standard insectary conditions until reaching the 3rd instar, when they were used for experimentation [24].

2.4.7. Larvicidal Assays. In order to test the larvicidal activity of the aqueous extract and the plant-synthesized AgNPs of *A. arborescens*, we followed the protocol proposed by the WHO [24]. Briefly, each bioassay consisted of a set of four experimental groups (one for each concentration tested) and a control group. Within each one of these

groups, the basic testing unit (i.e., technical replicate) was a plastic well containing 25 third instar larvae in either 200 mL of the test solution at the desired concentration (for experimental groups) or distilled water (for control groups). Each group contained four technical replicates, for a total of 500 larvae per bioassay ((100 larvae per concentration \times 4 concentrations) + (100 larvae per control group)). The entire bioassay was repeated five times.

During bioassays, larvae were maintained at standard insectary conditions ($28 \pm 1^\circ\text{C}$ temperature, $80 \pm 10\%$ relative humidity, and 12 h light/12 h darkness photoperiod) [22]. No food was provided during this period. Mortality was recorded 24 hours after the beginning of each bioassay. Specimens were considered as dead when, following stimulation by touch, they either did not move at all or moved sluggishly and were unable to rise towards the surface of the rearing medium [24].

To establish the concentration that results lethal to 50% of individuals (LC_{50}), concentration gradients were established for both the aqueous plant extract and the plant-synthesized AgNPs. The upper and lower limits of these gradients were established by preliminary experiments (data not shown). Concentrations tested for the aqueous plant extract were 1500, 3000, 4500, and 6000 ppm. Concentrations tested for the plant-synthesized AgNPs tests were 0.2, 0.3, 0.4, and 0.5 ppm.

2.4.8. Data Analysis. Using the mortality results obtained from the five bioassay replicates, we calculated the mean mortality per dose. With these values, we performed dose-mortality regressions using a log-probit model [25] in order to calculate the LC_{50} and LC_{90} values. Calculations were done using the R-software for statistical computing [26], and codes within the package MASS containing the material are discussed in [27].

3. Results

3.1. UV-Vis Spectroscopy. Parameters for this assay were previously optimized using 1.0 mM silver nitrate heated at 50°C for 50 minutes, at pH 8, with 2 mL of aqueous *A. arborescens* extract [28]. The UV spectrum of the synthesized nanoparticles is shown in Figure 2. The wavelength of maximum absorbance was 414 nm, and this value, according to Pradeep's description [29], corresponds to an average nanoparticle-core shell size of 10 to 14 nm. It can be evidenced by the shape of the spectrum that there is a high dispersion of particle size, since the peak is wide but symmetrical. Peak spreading may also indicate that there are wide spaces between the nanoparticles [30].

3.2. FTIR Spectroscopy. Fourier transform infrared spectroscopy (FTIR) was used to verify that the silver nanoparticles were indeed coated with the *A. arborescens* extract used for their synthesis. This is important because the extract does not only act as a reducing agent, but its organic fraction overlays or functionalize nanoparticles. Thus, the compounds responsible for the reduction of silver nitrate can be

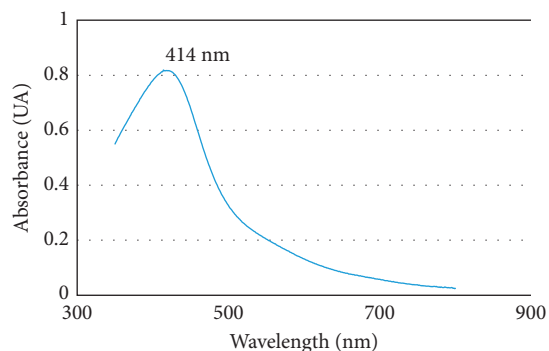


FIGURE 2: UV-Vis spectra of silver nanoparticles in optimal conditions.

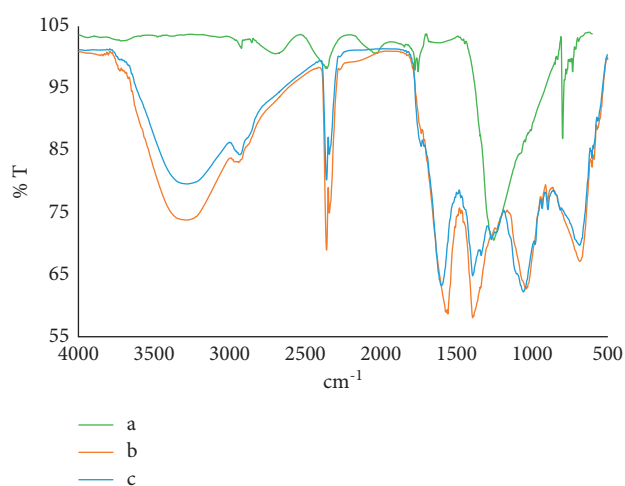


FIGURE 3: FTIR spectra of silver nitrate (a), *A. arborescens* extract (b), and silver nanoparticles-*A. arborescens* extract (c).

identified. In Figure 3, we compare the spectra of silver nitrate, *A. arborescens* extract, and nanoparticles synthesized with *A. arborescens* extract.

The similarity between the spectra of the synthesized nanoparticles and the extract indicates that the organic residue of the extract is kept intact. Similar bands are present in both spectra around 1570 cm^{-1} corresponding to the stretching of the C=C group of the aromatic rings, in addition to a band at approximately 1050 cm^{-1} of CO bonds within the alcohols. These data confirm the adequate coating of nanoparticles with the extract. Once again, the extract not only fulfills the function of reducing agent but also acts as a stabilizing medium. This saves additional use of other reagents.

In the spectra of the *A. arborescens* extract, there is a band at 1337.47 cm^{-1} that corresponds to the O-H bond characteristic of the phenolic compounds [31]. In the nanoparticle spectra, this band is not present; however, the high intensity band around 3280 cm^{-1} is maintained. This difference occurs because the OH groups of the phenolic compounds do not react in their entirety. Rais [32] indicates that only one out of four hydroxyl groups react, which is why the band of the OH groups at 3200 cm^{-1} is not affected

by the reaction. The remaining hydroxyl groups are attached to the nanoparticles by electrostatic attraction, coating them. A colorimetric test using FeCl_3 showed the color difference between the extract and the silver nanoparticles-*A. arborescens* extract.

3.3. STEM Analysis. As shown in Figure 4, the silver nanoparticles obtained are spherical and dispersed with an average size of $14 \pm 6\text{ nm}$. STEM image shows the action of aqueous extract on the nanoparticles as a stabilization agent. Anandalakshmi et al. [33] reported similar results in terms of particle size with diameters of 13 to 61 nm; this study was carried out with natural extract whose predominant components were polyphenols, which is why it resembles the synthesis performed with *A. arborescens* extract. Ndikau et al. [34] not only got similar size particles but also they found out that silver nanoparticles synthesized with plant extracts have smaller sizes than those synthesized with sodium citrate.

In STEM, a direct projection of the nanoparticles was observed and due to the low diffraction of the conjugated molecule these do not appear on the electron microscope images and so you only observe the core shell of the nanoparticles. This is quite useful in green chemistry as normally the UV-Vis methods give an overestimation of the nanoparticle size and then the difference in size between UV-Vis and STEM gives the average size value of the capping agent. A complete description of this effect and an extensive list of relevant references can be found in [35].

3.4. SEM-EDX. Figure 5 shows the micrograph of silver nanoparticles-*A. arborescens* extract powder measured by SEM. The image shows the dispersion of the nanoparticles onto the carbon pin. EDX spectrum shows three peaks of silver located below 4 kV. The rest of elements are present in the organic *A. arborescens* extracts, confirmed by FAAS.

3.5. Flame Atomic Absorption Spectroscopy for Silver Quantification. The silver content of silver nanoparticles synthesis with *A. arborescens* extract was determined in order to verify that the silver content did not change to determine the yield of the reaction. The amount of theoretical silver that should be obtained was calculated as a function of the amount of silver nitrate in the initial solution and the volume of extract added. An average concentration of 90.73 ppm silver in the synthesized nanoparticles was obtained compared with initial 98.01 ppm present in the silver nitrate. This amount of silver equals a reaction yield of 92.52%, which is acceptable for synthesis on a smaller scale. In his doctoral thesis, Li [36] tested different phenols and mixtures of phenols as reducing agents and obtained yields in the range of 75 to 90%.

3.6. Larvicidal Activity of Aqueous Extract and Synthesized AgNPs. Mortality values observed following all bioassays are shown in Table 1. Both the aqueous extract and the plant-synthesized AgNPs showed a dose-dependent toxic effect against *Ae. aegypti* larvae. No mortality was observed in the control groups.

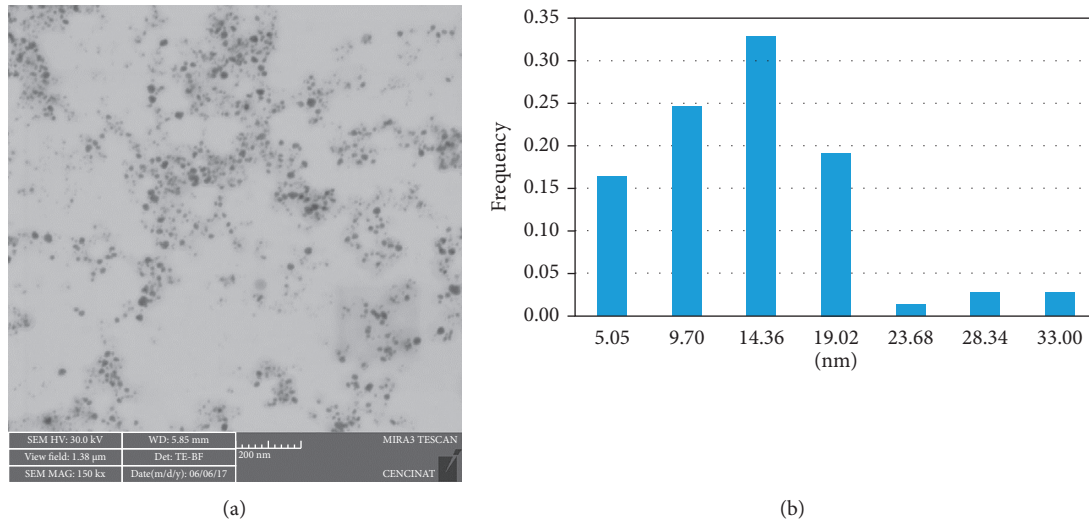


FIGURE 4: STEM image (a) and frequency histogram (b) of average shape of silver nanoparticles-*A. arborescens* extract.

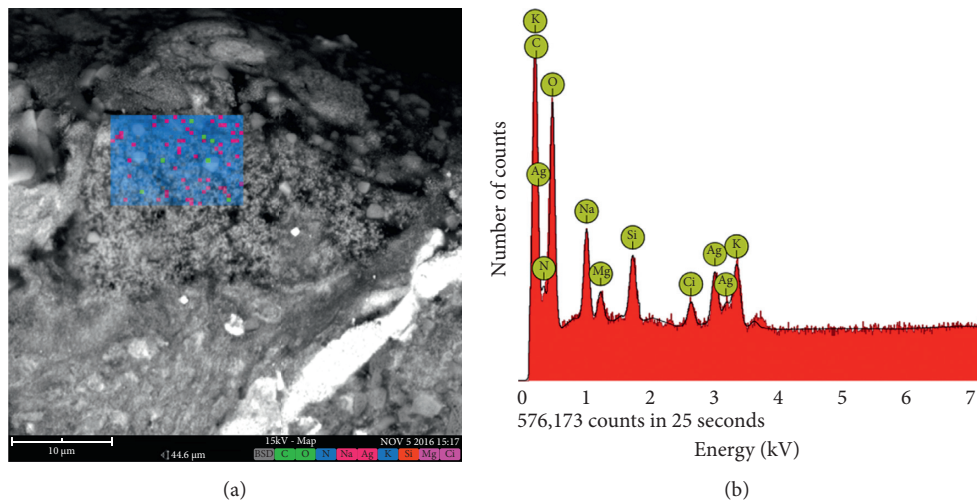


FIGURE 5: SEM micrograph (a) and EDX spectrum (b) of silver nanoparticles-*A. arborescens* extract.

TABLE 1: Larvicidal activity of aqueous extracts and silver nanoparticles synthesized using *Ambrosia arborescens* against *Aedes aegypti* third instar larvae.

Treatment	Dose (ppm)	Larval mortality ^a ± SD
Plant aqueous extract	1500	43.4 ± 4.9
	3000	66.6 ± 2.1
	4500	81.2 ± 0.8
	6000	92.8 ± 1.3
Control	0	0 ± 0.0
	0.2	17.6 ± 3.2
AgNPs	0.3	60.6 ± 3.2
	0.4	82.6 ± 3.1
	0.5	96.4 ± 1.8
Control	0	0 ± 0.0

SD: standard deviation; ^avalues are mean ± SD of five trials.

The LC_{50} and LC_{90} values of the aqueous extract were 1844.61 ppm and 6043.95 ppm, respectively (Table 2). However, the combination of this extract with silver nanoparticles

greatly potentiated its toxicity to *Ae. aegypti* larvae: LC_{50} and LC_{90} values for plant-synthesized AgNPs were 0.28 ppm and 0.43 ppm (Table 2), respectively. χ^2 value was not significant at $p \leq 0.05$ level.

Furthermore, exposure to aqueous extract at a concentration of 6000 ppm resulted in an average mortality of 97% of individuals, while exposure to 0.5 ppm plant-synthesized AgNPs resulted in an average mortality of 93.4% of individuals (Table 1).

4. Discussion

Our study suggests that the leaves of *A. arborescens* contain water-soluble chemicals which are toxic to *Ae. aegypti* larvae. Furthermore, our results show that the toxicity of such chemicals is greatly enhanced when they are combined with AgNPs.

It has been reported that plants belonging to the Asteraceae family can present an elevated toxicity due to the

TABLE 2: Probit values of plant aqueous extracts and silver nanoparticles synthesized using leaves of *Ambrosia arborescens* against *Aedes aegypti* third instar larvae.

Treatment	LC ₅₀ (ppm)	95% fiducial limits (LCL–UCL)	LC ₉₀ (ppm)	95% fiducial limits (LCL–UCL)	χ^2
Plant aqueous extract	1844.61	1489.16–2146.46	6043.95	5031.51–7970.18	2.01 ^{NS}
AgNPs	0.28	0.26–0.29	0.43	0.41–0.48	0.9 ^{NS}

LC₅₀: lethal concentration that kills 50% of the exposed larvae; LC₉₀: lethal concentration that kills 90% of the exposed larvae; LCL: lower confidence limit; UCL: upper confidence limit; χ^2 : chi-square test; ^{NS}not significant at $p \leq 0.05$ level.

presence of a wide range of defensive chemical agents against herbivores, such as sesquiterpenic lactones, monoterpenes, terpenoids, and polyacetylenic resins [37]. Within this family, the genus *Ambrosia* presents a remarkable physiological plasticity that allows it to adapt to a wide range of environmental conditions [38], a characteristic that might be explained, at least partially, by the secondary metabolites produced by the species of this taxon [39]. All members of the *Ambrosia* genus present a high content of sesquiterpenic lactones which possesses antibacterial, cytotoxic, and antifungal properties [40, 41]. Regarding *A. arborescens*, former studies have reported damsines, coronophelines, and psilostachynes as the main sesquiterpenic lactones in this species [39, 42, 43]. It seems plausible that the lethal effect observed is, at least in part, due to these kinds of compounds.

Several studies have reported on the larvicidal activity of plants of the Asteraceae family against *Ae. aegypti*. For example, Govindarajan and Karuppannan [44] used the methanolic extract of *Eclipta alba* against third instar larvae, obtaining a LC₅₀ of 127.64 ppm. Alvarez et al. [45] reported that the LC₅₀ of the ethereal extracts of *Heli oppositifolia* and *Jaegeria hirta* are 41 ppm and 24 ppm, respectively. Sukhthankar et al. [46] used a methanolic extract of the leaves of *Chromolaena odorata*, obtaining a LC₅₀ of 138 ppm, and Tennyson et al. [47] tested hexane and ethyl acetate extracts of *Ageratum houstonianum*, obtaining LC₅₀ values of 8889.13 ppm and 1952.12 ppm, respectively. Furthermore, and as far as we are aware, only two previous reports exist regarding the toxicity of plants within the *Ambrosia* genus against mosquito larvae: (a) Eisa [48] tested the aqueous extract of *A. maritima* leaves against field-collected *Culex* larvae, obtaining a LC₅₀ of 1349 ppm, and (b) De La Torre et al. [49] tested the ethereal extract made with the aerial parts of *A. confertifolia* against *Ae. aegypti*, obtaining a LC₅₀ of 185.6 ppm.

In this context, the LC₅₀ value of 1844.61 ppm observed in our study for *A. arborescens* aqueous extract is within the range observed with similar plant extracts against mosquito larvae. However, one of the most interesting and striking aspects of our study was the exponential potentiation of the lethal effect we observed when the aqueous extract was used to synthesize AgNPs, reaching a LC₅₀ of 0.28 ppm, which represents a >6 000-fold increase in toxicity. Although this is consistent with other reports which have reported an enhanced efficiency of plant-synthesized AgNPs in comparison with the plant extracts by themselves [50], it is worth mentioning that the LC₅₀ reported in our work is, as far as we are aware, the lowest reported for AgNPs synthesized from any member of the Asteraceae family [51, 52].

The physiological basis for the high toxicity of plant-synthesized AgNPs remains an open question. It has been

suggested that a key factor is their ability to permeate through the invertebrate exoskeleton and penetrate into the insect's cells, where they bind macromolecules such as proteins and DNA, altering their structure and therefore their functionality [53, 54]. Interestingly, it has also been reported that doses of plant-synthesized AgNPs which result lethal to several species of mosquito larvae have little or no effect on other nontarget species, including other aquatic arthropod species and fish [55, 56], suggesting that at least some mosquito species are particularly susceptible to the lethal effect of AgNPs. At the moment, the reasons behind this phenomenon remain unknown.

It is, therefore, important to stress that more research is needed to identify the mechanisms by which AgNPs exert their toxic effect on their intended target species. This information will be crucial to establish whether the use of nanoparticles for mosquito control could have any unintended negative impact on either the environment or the health of the human population. Furthermore, any field application of this technology must be preceded by extensive laboratory and semifield research, exploring aspects such as residuality, bioaccumulation, and long-term effects of exposure to AgNPs on relevant biological systems.

5. Conclusions

In summary, our study shows that the aqueous extract obtained from the leaves of *A. arborescens* presents a clear insecticidal effect against *Ae. aegypti* larvae. Furthermore, this effect is greatly potentiated when this extract is used for the synthesis of AgNPs.

Therefore, our results suggest that *A. arborescens* has the potential to be used for the development of novel pesticides. However, the said development must be complemented by studies aimed at defining key aspects, such as the nature of the specific molecules responsible for the insecticidal effect observed, the potential effects of these chemicals in both the environment and in human health, and the field logistics required for the use of such a novel insecticide.

Conflicts of Interest

The authors declare that there are no conflicts of interest regarding the publication of this paper.

Authors' Contributions

Bianca Morejón conducted the bibliographical research that lead to the selection of *Ambrosia arborescens* for this work, performed all bioassays, and analyzed experimental results.

Marco Neira supervised the experimental design and performance of bioassays and contributed to the analysis of experimental results. Fernanda Pilaquinga, Flavia Domenech, and Danny Ganchala performed the synthesis and characterization of silver nanoparticles. Alexis Debut performed STEM analysis. Bianca Morejón, Marco Neira, Fernanda Pilaquinga, and Flavia Domenech wrote the manuscript. All authors reviewed and approved this manuscript. Bianca Morejón and Fernanda Pilaquinga contributed equally to this work.

Acknowledgments

This research was supported in part by PUCE's Research Grants N13409 and N13438. The authors would also like to thank Mr. Ricardo Zambrano for his help in obtaining suitable plant samples and Dr. Svetlana Ivanova from the University of Sevilla for her support in the characterization of nanoparticles.

References

- [1] World Health Organization (WHO), "Dengue y dengue grave," 2016, <http://www.who.int/mediacentre/factsheets/fs117/en/>.
- [2] S. Bhatt, P. Gething, O. Brady et al., "The global distribution and burden of dengue," *Nature*, vol. 496, no. 7446, pp. 504–507, 2013.
- [3] G. Cook and A. Zumla, *Manson's Tropical Diseases*, Saunders, Philadelphia, PA, USA, 2008.
- [4] R. Chamberlain and W. Sudia, "Mechanism of transmission of viruses by mosquitoes," *Annual Review of Entomology*, vol. 6, no. 1, pp. 371–390, 1961.
- [5] T. Sardar, S. Rana, and J. Chattopadhyay, "A mathematical model of dengue transmission with memory," *Communications on Nonlinear Science and Numeric Simulation*, vol. 22, no. 1, pp. 511–525, 2015.
- [6] J. Frierson, "The yellow fever vaccine: a history," *Yale Journal of Biology and Medicine*, vol. 83, no. 2, pp. 77–85, 2010.
- [7] WHO and TDR, *Dengue Guidelines for Diagnosis, Treatment, Prevention and Control*, WHO Publications, Geneva, Switzerland, 2009.
- [8] J. Bisset, M. Rodríguez, and D. Fernández, "Selection of insensitive acetylcholinesterase as a resistance mechanism in *Aedes aegypti* (Diptera: Culicidae) from Santiago de Cuba," *Journal of Medical Entomology*, vol. 43, no. 6, pp. 1185–1189, 2006.
- [9] M. Govindarajan, A. Jebanesan, and D. Reetha, "Larvicidal effect of extracellular secondary metabolites of different fungi against the mosquito, *Culex quinquefasciatus* Say," *Tropical Biomedicine*, vol. 22, no. 1, pp. 1–3, 2005.
- [10] J. da Silva and J. Mendes, "Susceptibility of *Aedes aegypti* (L) to the insect growth regulators diflubenzuron and methoprene in Uberlândia, State of Minas Gerais," *Revista da Sociedade Brasileira de Medicina Tropical*, vol. 40, no. 6, pp. 612–616, 2007.
- [11] S. Poopathi and S. Abidha, "Mosquitocidal bacterial toxins (*Bacillus sphaericus* and *Bacillus thuringiensis* serovar israelensis): mode of action, cytopathological effects and mechanism of resistance," *Journal of Physiology and Pathophysiology*, vol. 1, no. 3, pp. 22–38, 2010.
- [12] T. Hurst, B. Kay, P. Ryan, and M. Brown, "Sublethal effects of mosquito larvicides on swimming performance of larvivoracious fish *Melanotaenia duboulayi*; (Atheriniformes: Melanotaeniidae)," *Journal of Economic Entomology*, vol. 100, no. 1, pp. 61–65, 2007.
- [13] P. Thiyagarajan, P. Kumar, K. Kovendan, and K. Murugan, "Effect of medicinal plant and microbial insecticides for the sustainable mosquito vector control," *Acta Biologica Indica*, vol. 3, no. 1, pp. 527–535, 2014.
- [14] G. Benelli, A. Caselli, and A. Canale, "Nanoparticles for mosquito control: challenges and constraints," *Journal of King Saud University-Science*, vol. 29, no. 4, pp. 424–435, 2017.
- [15] A. Priyadarshini, K. Murugan, C. Panneerselvam, S. Ponarulselvam, J. Hwang, and M. Nicoletti, "Biolarvicidal and pupicidal potential of silver nanoparticles synthesized using *Euphorbia hirta* against *Anopheles stephensi* Liston (Diptera: Culicidae)," *Parasitology Research*, vol. 111, no. 3, pp. 997–1006, 2012.
- [16] H. Borase, C. Patil, R. Patil et al., "Phyto-synthesized silver nanoparticles: a potent mosquito biolarvicidal agent," *Journal of Nanomedicine & Biotherapeutic Discovery*, vol. 3, no. 1, 2013.
- [17] U. Muthukumaran, M. Govindarajan, M. Rajeswary, and S. Hoti, "Synthesis and characterization of silver nanoparticles using *Gmelina asiatica* leaf extract against filariasis, dengue, and malaria vector mosquitoes," *Parasitology Research*, vol. 114, no. 5, pp. 1817–1827, 2015.
- [18] N. Myers, R. Mittermeier, C. Mittermeier, G. da Fonseca, and J. Kent, "Biodiversity hotspots for conservation priorities," *Nature*, vol. 403, no. 6772, pp. 853–858, 2010.
- [19] L. De La Torre, H. Navarrete, P. Muriel, M. Macía, and H. Balslev, *Enciclopedia de las Plantas Útiles del Ecuador*, Herbario QCA de la Escuela de Ciencias Biológicas de la Pontificia Universidad Católica del Ecuador & Herbario AAU del Departamento de Ciencias Biológicas de la Universidad de Aarhus, Quito, Ecuador, 2008.
- [20] P. Jørgensen and S. León-Yáñez, "Catalogue of the vascular plants of Ecuador," *Monographs on Systematic Botany from Missouri Botanical Garden*, vol. 75, pp. 1–1182, 1999.
- [21] C. Ruales, *Plantas de Quito-La Vegetación Original de una Ciudad Siempre Verde*, Universidad San Francisco de Quito, Quito, Ecuador, 2013.
- [22] E. Gerberg, D. Barnard, and R. Ward, *Manual for Mosquito Rearing and Experimental Techniques*, American Mosquito Control Association, Inc., Lake Charles, LA, USA, 1994.
- [23] D. Carvalho, D. Nimmo, N. Naish et al., "Mass production of genetically modified *Aedes aegypti* for field releases in Brazil," *Journal of Visualized Experiments*, no. 83, p. e3579, 2014.
- [24] WHO, *Guidelines for Laboratory and Field Testing of Mosquito Larvicides*, World Health Organization, Geneva, Switzerland, 2005.
- [25] D. Finney, *Probit Analysis*, Cambridge University Press, Cambridge, UK, 1971.
- [26] R Core Team, *R: A Language and Environment for Statistical Computing*, Foundation for Statistical Computing, Vienna, Austria, 2013.
- [27] W. Venables and B. Ripley, *Modern Applied Statistics with S*, Springer, New York, NY, USA, 4th edition, 2002.
- [28] F. Domenech, *Síntesis y caracterización de nanopartículas de plata usando extracto de hojas de *Ambrosia arborescens* (marco) como reductor químico*, B. Sc. thesis, Pontificia Universidad Católica del Ecuador, Quito, Ecuador, 2017.
- [29] T. Pradeep, *A Textbook of Nanoscience and Nanotechnology*, McGraw Hill, New Delhi, India, 2012.
- [30] M. Aguilar, *Síntesis y caracterización de nanopartículas de plata: efecto sobre *Collectotrichum gloesporioides**, Doctoral dissertation, Instituto Politécnico Nacional de México, Mexico City, Mexico, 2009.

- [31] S. Trifunski, M. Munteanu, V. Agotici, S. Pintea, and R. Gligor, "Determination of flavonoid and polyphenol compounds in viscum album and allium sativum extracts," *International Current Pharmaceutical Journal*, vol. 4, no. 5, pp. 382–385, 2015.
- [32] M. Rais, "Preparation of silver nanoparticles," Patent WO2012074355 A1, 2012, <https://www.google.com/patents/WO2012074355A1?cl=en>.
- [33] K. Anandalakshmi, J. Venugobal, and V. Ramasamy, "Characterization of silver nanoparticles by green synthesis method using *Petalium murex* leaf extract and their antibacterial activity," *Applied Nanoscience*, vol. 6, no. 3, pp. 399–408, 2015.
- [34] M. Ndikau, N. Noah, D. Andala, and E. Masika, "Green synthesis and characterization of silver nanoparticles using *Citrullus lanatus* fruit rind extract," *International Journal of Analytical Chemistry*, vol. 2017, Article ID 8108504, 9 pages, 2017.
- [35] S. Ramesh, M. Grijalva, A. Debut, B. De la Torre, A. Albericio, and L. Cumbal, "Peptides conjugated to silver nanoparticles in biomedicine—a "value-added" phenomenon," *Biomaterials Science*, vol. 4, no. 12, pp. 1713–1725, 2016.
- [36] V. Li, *Advancing silver nanostructures towards antibacterial applications*, Doctoral dissertation, Royal Melbourne Institute of Technology, Melbourne, Australia, 2014.
- [37] J. Mauseth, *Botany: An Introduction to Plant Biology*, Jones and Bartlett Publishers, Burlington, MA, USA, 2003.
- [38] A. Parkhomenko, E. Oganessian, O. Andreeva, E. Dorkina, E. Paukova, and Z. Agadzhanian, "Pharmacologically active substances from *Ambrosia artemisiifolia*. Part 2," *Pharmaceutical Chemistry Journal*, vol. 40, no. 11, pp. 627–632, 2006.
- [39] M. Vera, *Estudio Fitoquímico de una Planta de la Flora del Ecuador: Ambrosia arborescens*, Escuela Politécnica del Ejército, Quito, Ecuador, 2008.
- [40] O. Spring, J. Kupka, B. Maier, and A. Hager, "Biological activities of sesquiterpene lactones from *Helianthus annuus*: antimicrobial and cytotoxic properties; influence on DNA, RNA, and protein synthesis," *Zeitschrift für Naturforsch C*, vol. 37, no. 11–12, pp. 1087–1091, 1982.
- [41] M. Neerman, "Sesquiterpene lactones: a diverse class of compounds found in essential oils possessing antibacterial and antifungal properties," *International Journal of Aromatherapy*, vol. 13, no. 2–3, pp. 114–120, 2003.
- [42] W. Herz, G. Anderson, S. Gibaja, and D. Raulais, "Sesquiterpene lactones of some *Ambrosia* species," *Phytochemistry*, vol. 8, no. 5, pp. 877–881, 1969.
- [43] M. De Leo, M. Vera, B. Naranjo, N. De Tommasi, and A. Braca, "Sesquiterpenes and diterpenes from *Ambrosia arborescens*," *Phytochemistry*, vol. 71, no. 7, pp. 804–809, 2010.
- [44] M. Govindarajan and P. Karuppanan, "Mosquito larvicidal and ovicidal properties of *Eclipta alba* (L.) Hassk (*Asteraceae*) against chikungunya vector, *Aedes aegypti* (Linn.) (Diptera: Culicidae)," *Asian Pacific Journal of Tropical Medicine*, vol. 4, no. 1, pp. 24–28, 2011.
- [45] J. Álvarez, I. Duarte, O. Aguirre, and J. Jiménez, "Control del vector del dengue utilizando fracciones etéreas de dos plantas (*Asteraceae*) como larvicidas," *Revista de Salud Pública*, vol. 15, no. 2, pp. 227–236, 2013.
- [46] J. Sukhthankar, H. Kumar, M. Godinho, and A. Kumar, "Larvicidal activity of methanolic leaf extracts of plant, *Chromolaena odorata* L. (*Asteraceae*) against vector mosquitoes," *International Journal of Mosquito Research*, vol. 33, no. 13, pp. 33–38, 2014.
- [47] S. Tennyson, J. Ravindran, A. Eapen, and J. William, "Larvicidal activity of *Ageratum houstonianum* Mill. (*Asteraceae*) leaf extracts against *Anopheles stephensi*, *Aedes aegypti* and *Culex quinquefasciatus* (Diptera: Culicidae)," *Asian Pacific Journal of Tropical Diseases*, vol. 5, pp. S73–S76, 2015.
- [48] A. Eisa, *Toxicity of Ambrosia maritima L. leaves aqueous extract and abate aqueous solutions, on Culex species*, University of Khartoum, Khartoum, Sudan, 2010.
- [49] Y. De La Torre, F. Martínez, A. Flores, N. De Torres, and R. Salazar, "Larvicidal and cytotoxic activities of extracts from 11 native plants from northeastern Mexico," *Journal of Medical Entomology*, vol. 50, no. 2, pp. 310–313, 2013.
- [50] G. Benelli, "Plant-mediated biosynthesis of nanoparticles as an emerging tool against mosquitoes of medical and veterinary importance: a review," *Parasitology Research*, vol. 115, no. 1, pp. 23–34, 2016.
- [51] G. Rajakumar and A. Rahuman, "Larvicidal activity of synthesized silver nanoparticles using *Eclipta prostrata* leaf extract against filariasis and malaria vectors," *Acta Tropica*, vol. 118, no. 3, pp. 196–203, 2011.
- [52] M. Nalini, M. Lena, P. Sumathi, and C. Sundaravadivelan, "Effect of phyto-synthesized silver nanoparticles on developmental stages of malaria vector, *Anopheles stephensi* and dengue vector, *Aedes aegypti*," *Egyptian Journal of Basic and Applied Sciences*, vol. 4, no. 3, pp. 212–218, 2017.
- [53] J. Subramaniam, K. Murugan, C. Panneerselvam et al., "Eco-friendly control of malaria and arbovirus vectors using the mosquitofish *Gambusia affinis* and ultra-low dosages of *Mimusops elengi*-synthesized silver nanoparticles: towards an integrative approach?," *Environmental Science and Pollution Research*, vol. 22, no. 24, pp. 20067–20083, 2015.
- [54] N. Arjunan, K. Murugan, C. Rejeeth, P. Madhiyazhagan, and D. Barnard, "Green synthesis of silver nanoparticles for the control of mosquito vectors of malaria, filariasis, and dengue," *Vector Borne Zoonotic Diseases*, vol. 12, no. 3, pp. 262–268, 2012.
- [55] K. Haldar, B. Haldar, and G. Chandra, "Fabrication, characterization and mosquito larvicidal bioassay of silver nanoparticles synthesized from aqueous fruit extract of putranjiva, *Drypetes roxburghii* (Wall.)," *Parasitology Research*, vol. 112, no. 4, pp. 1451–1459, 2013.
- [56] A. Rawani, A. Ghosh, and G. Chandra, "Mosquito larvicidal and antimicrobial activity of synthesized nano-crystalline silver particles using leaves and green berry extract of *Solanum nigrum* L. (*Solanaceae*: Solanales)," *Acta Tropica*, vol. 128, no. 3, pp. 613–622, 2013.

Research Article

Biosynthesis of Multicomponent Nanoparticles with Extract of Mortiño (*Vaccinium floribundum* Kunth) Berry: Application on Heavy Metals Removal from Water and Immobilization in Soils

Mayra Abril,¹ Hugo Ruiz,² and Luis H. Cumbal ^{1,2}

¹Departamento de Ciencias de la Vida, Universidad de las Fuerzas Armadas ESPE, Av. Gral. Rumiñahui s/n, P.O. Box 171-5-231B, Sangolquí, Ecuador

²Centro de Nanociencia y Nanotecnología, Universidad de las Fuerzas Armadas ESPE, Av. Gral. Rumiñahui s/n, P.O. Box 171-5-231B, Sangolquí, Ecuador

Correspondence should be addressed to Luis H. Cumbal; lhcumbal@espe.edu.ec

Received 19 October 2017; Accepted 31 January 2018; Published 1 April 2018

Academic Editor: Andrey E. Miroshnichenko

Copyright © 2018 Mayra Abril et al. This is an open access article distributed under the Creative Commons Attribution License, which permits unrestricted use, distribution, and reproduction in any medium, provided the original work is properly cited.

Through preparation of multicomponent nanoparticles (MCNPs) using ferric chloride (FeCl_3), sodium sulfate (Na_2SO_4), and the extract of mortiño fruit (*Vaccinium floribundum* Kunth), we dramatically improved the removal/immobilization of heavy metals from water and in soils. As-prepared nanoparticles were spherical measuring approximately 12 nm in diameter and contained iron oxides and iron sulfides in the crystal structure. Removal of copper and zinc from water using MCNPs showed high efficiencies (>99%) at pH above 6 and a ratio of 0.5 mL of the extract:10 mL 0.5 M $\text{FeCl}_3 \cdot 6\text{H}_2\text{O}$:10 mL 0.035 M Na_2SO_4 . The physisorption process followed by chemisorption was regarded as the removal mechanism of Cu and Zn from water. While, when MCNPs were used to treat soils contaminated with heavy metals, more than 95% of immobilization was accomplished for all metals. Nevertheless, the distribution of the metallic elements changed in the soil fractions after treatment. Results indicate that immobilization of metals after the injection of nanoparticles into soils was effective. Metals did not leach out when soils were drained with rain, drinking, and deionized water but fairly leached out under acidic water drainage.

1. Introduction

In this century, the applications of nanotechnology are increasing, particularly those related to the use of nanoparticles (NPs). All NPs show outstanding physical, mechanical, optical, catalytic, and chemical properties due to a variety of morphologies, sizes, and reactivities [1–3]. Even though the current NPs have found broader and potential applications in the fields of medicine, energy, cosmetics, environmental remediation, and catalysis, an enormous amount of hazardous chemicals have been used in their synthesis [4]. A massive quantity of fabricated nanoparticles includes only a single element, but more beneficial properties can be attained when the nanoparticles contain two or more dissimilar elements that altogether form multicomponent nanoparticles (MCNPs). The inclusion of two or more components can add supplementary

functionality to the particles, such as antimicrobial activity, chemical-mechanical polishing [5], magnetic capability [6], and others. Among the MCNPs prepared up to now, Fe/FeS nanoparticles were formed by the interaction between dissolved iron species and hydrogen sulfide using sodium borohydride (NaBH_4) as a reducing agent at room temperature [7]. Using this procedure of fabrication, the FeS precipitates on the Fe^0 surface. These nanoparticles were successfully used in the removal of trichloroethylene and pesticides from water. Similar nanoparticles were prepared using sodium sulfate instead of dithionite to selectively immobilize heavy metals from the aqueous phase [8]. In both studies, the performance of the MCNPs was excellent; however, researchers used NaBH_4 as the reducing agent. This chemical is expensive, hazardous, and harmful to the ecosystem [9, 10]. On the contrary, in this research, we exploit green nanoscience to

reduce the risks of using nanomaterials on human health and the environment.

With the evolution of green chemistry, ecofriendly dispersing agents such as polymers and oligomers have increasingly been used for the stabilization of multicomponent nanoparticles [5]. Natural products like plant extracts have attracted attention for this purpose because they are easy to handle, readily available, low cost, and highly biocompatible, and their own polyphenols (e.g., flavonoids and flavones), carotenoids, reducing sugars, glucosinolates, terpenoids, glutathiones, metallothioneins, and so on are ecological [11–14].

Mortiño (*Vaccinium floribundum*), sometimes called Andean berry, belongs to the Ericaceae family. The fruit is round, is bluish black in color, and is about 8 mm in diameter. The berry grows in a shrub 1.5 m tall, with lanceolate leaves 2 cm long possessing a serrated edge. In Ecuador, it grows in high altitudes, between 3400 and 3800 meters above the sea level. It is a well-known fruit because of its high antioxidant activity for the presence of anthocyanins (delphinine, peonidin, malvidin, and cyanidin) and other phenolic compounds (quercetin, myricetin, gallic acid, ellagic acids, hydroxycinnamic and hydroxybenzoic acid derivatives, and others) in very high concentrations. The berry is consumed fresh, dried, in sausages, jellies, and jams, and in a special beverage called “colada morada” [15, 16]. Furthermore, mortiño contains a high content of glucose and fructose. In this research, we use the mortiño berry extract (MBE) as a reducing and stabilizing agent in the synthesis of MCNPs.

2. Experimental Section

2.1. Materials. Chemicals purchased from Fisher Scientific were ferric chloride ($\text{FeCl}_3 \cdot 6\text{H}_2\text{O}$, 99.8%), sodium sulfate (Na_2SO_4 , 99.9%), ascorbic acid (USP/FCC), hydrochloric acid (HCl, 37.3%), nitric acid (HNO_3 , 69.5%), sodium hydroxide (NaOH, 98%), and buffer solution (0.2 M sodium acetate, 96%) and from HiMedia were potassium iodide (KIO_3 , 99%). Fresh and ripe mortiño berries were purchased in a nearby popular market. Millipore Milli-Q water was used in all experiments.

2.2. Preparation of the Mortiño Extract. First, fresh mortiño berries were washed with Milli-Q and cut into small pieces. Then, 300 grams of crushed mortiño fruit were immersed in 300 mL of 99.6% ethanol for 2 days. The resultant solution was filtered using the Whatman no.1 paper and dried at 40°C under reduced pressure and then freeze-dried for 24 hours to give a dark reddish gummy extract.

2.3. Biosynthesis of Multicomponent Nanoparticles. 10 mL of 0.5 M $\text{FeCl}_3 \cdot 6\text{H}_2\text{O}$ was used as an iron source. The pH of the solution was adjusted to 8.7 with 0.1 M NaOH, and the resulting suspension was centrifuged at 3000 rpm for 10 min. The supernatant was discarded, and 10 mL of 0.035 M Na_2SO_4 was added to the Fe precipitate. Afterwards, the mixture was stirred, and the concentrated fruit extract was

added, keeping a ratio of 10:10:0.5 (v/v/v) for ferric chloride, sodium sulfate, and MBE.

2.4. Characterization. The particle size distribution of MCNPs was determined using the HORIBA, DLS Version LB-550 program. Transmission electron microscope images were digitally recorded (Tecnai G2 Spirit TWIN, FEL, Holland). XRD studies on thin films of the nanoparticle were carried out using a diffractometer (EMPYREAN, PANalytical) with a θ - 2θ configuration (generator-detector), wherein a copper X-ray tube emitted a wavelength of $\lambda = 1.54 \text{ \AA}$. FTIR-ATR spectra were recorded on a Spectrum Two IR spectrometer (PerkinElmer, USA) to detect the different functional groups involved in the capture of heavy metals by the multicomponent nanoparticles. The UV-Vis spectrum was obtained using a spectrophotometer (Analytik Jena SPECORD S6008, Germany).

2.5. Removal of Heavy Metals. Batch kinetic tests for heavy metal removal from the liquid phase after treatment with nanoparticles were carried out using 100 mL Boeco bottles under the oxidant environment and pH 6.5 ± 0.2 . The removal was initiated by mixing 1 mL of MCNPs with 10 mL of artificially contaminated water, which resulted in concentrations of 5.2 mg/L Cu^{2+} , 4.95 mg/L Zn^{2+} , 4.05 mg/L Mn^{2+} , 2.51 mg/L Ni^{2+} , 2.98 mg/L Cd^{2+} , and 1.12 mg/L Cr^{6+} . Bottles were placed in a water bath and agitated for 2.5 h at 25°C. During the test, six samples of 2 mL of the treated aqueous phase were filtered with a 0.2 μm PVDF filter for heavy metal analyses at 5, 20, 40, 60, 120, and 150 min.

2.6. Soil Characterization. Cation exchange capacity of the soil was performed using the 9081 EPA method. Briefly, the soil sample was saturated with a solution of 1.0 N of sodium acetate to replace cations bound to the soil with sodium ions at pH 8.2. The sample was then placed on a rotary shaker at 40 rpm for 1.0 h and centrifuged for 5 min, and the supernatant decanted. The precipitate was washed 5 times with 99% isopropyl alcohol. Then, 100 mL of 1.0 N ammonium acetate at pH 7 was added, and the content was placed on the rotary shaker at 40 rpm for another hour and centrifuged. A sample of 1 mL was taken from the supernatant diluted with 9.0 mL of ammonium acetate and filtered with a membrane of 0.45 μm , and the sodium concentration was analyzed by atomic absorption. The organic matter contained in the soil was measured using the method reported by [17]. After oven-drying of soil to constant weight (12–24 h at 105°C), 10 g of dry soil was weighed in a porcelain dish (DW_{105}) and placed in a Wild Barfield muffle, model MI 254, at 550°C for six hours. After total calcination, the sample was allowed to cool down and weighed again, and the value was recorded (DW_{550}). The organic matter content was estimated with the following equation:

$$\text{OM} = \frac{\text{DW}_{105} - \text{DW}_{550}}{\text{DW}_{105}} * 100. \quad (1)$$

For the doping of soil with heavy metals, deionized water containing different concentrations of Cu^{2+} , Zn^{2+} , Ni^{2+} , Mn^{2+} ,

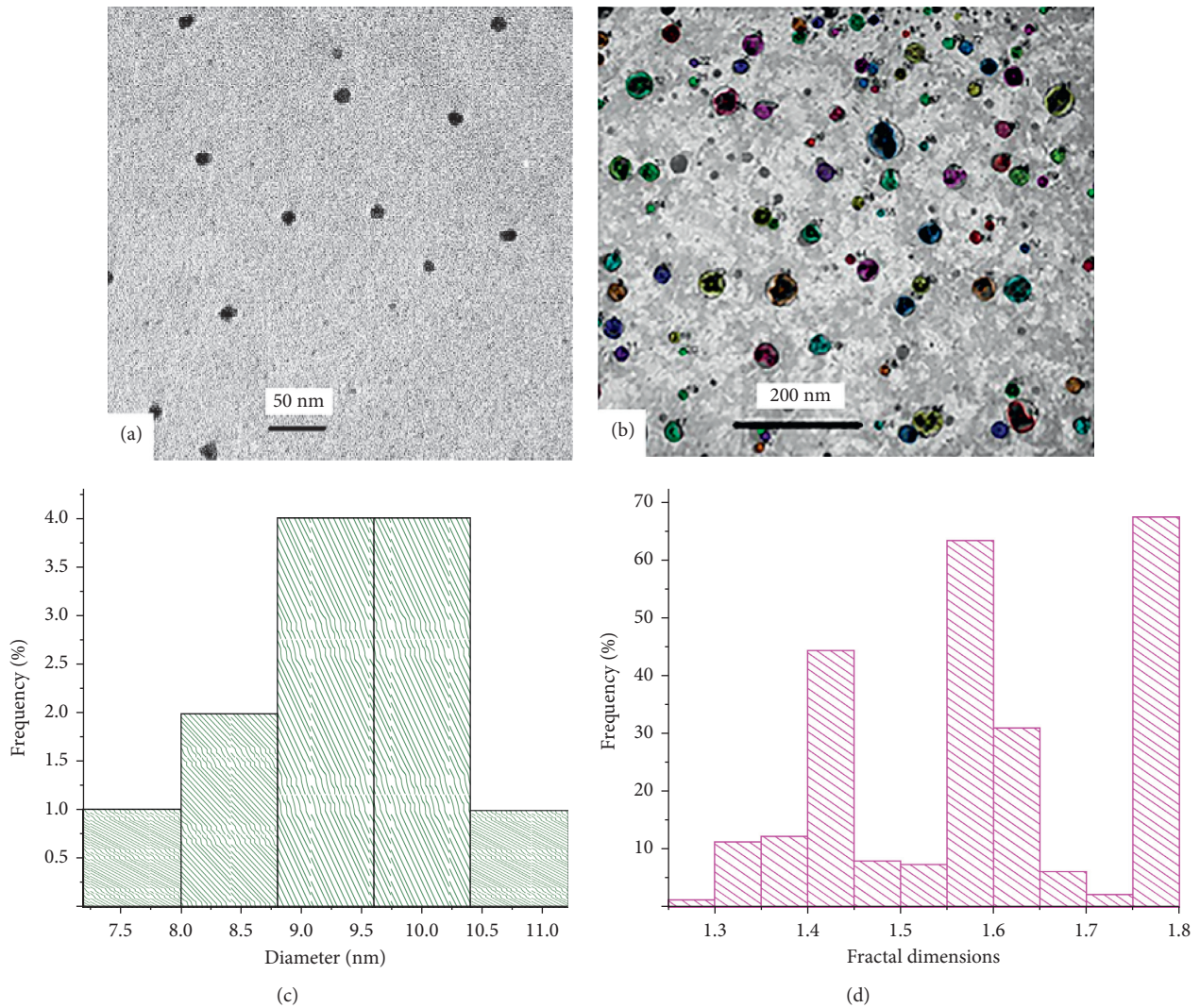


FIGURE 1: Multicomponent nanoparticles synthesized with the mortiño berry extract: (a) TEM image, (b) TEM image analyzed with MATLAB software, (c) DLS size distribution, and (d) fractal roughness.

Cd^{2+} , and Cr^{6+} was used to saturate 521.8 g of soil taken from a mining site with a continuous agitation for four days. Afterwards, the soil sample was centrifuged at 3000 rpm for 10 min, and the supernatant was separated. The remaining solids were washed twice with distilled water to remove the soluble fraction of heavy metals. Finally, the supernatant and washed fractions were filtered through a membrane filter of $0.45\ \mu\text{m}$, and the dissolved metal concentrations were measured using an atomic absorption spectrometer by the flame method. Doped soil reached concentrations of 636 mg/kg Cu^{2+} , 737 mg/kg Zn^{2+} , 21.2 mg/kg Ni^{2+} , 408 mg/kg Mn^{2+} , 19.2 mg/kg Cd^{2+} , and 195 mg/kg Cr^{6+} .

2.7. Immobilization Tests. Experiments of immobilization of heavy metals were performed by adding dropwise different volumes of MCNPs at $\text{pH } 6.5 \pm 0.2$ (5, 10, 15, and 20 mL) into a glass chromatographic column packed with 2.0 g of previously doped soils. Concentrations of heavy

metals in soil samples, before and after treatment, were obtained using a sequential extraction method [18]. The extraction was performed consecutively on an initial weight of 1.0 g of soil, following a three-step procedure: Step 1: for the exchangeable-weakly sorbed, 20 mL of 0.11 M acetic acid was added to 1.0 g of soil sample in a Falcon tube and shaken for 16 h at room temperature. The extract was then separated from the solid residue by centrifugation at 3000 rpm for 20 min, and the supernatant liquid was filtrated with a $0.45\ \mu\text{m}$ membrane. Subsequently, the filtrate was chemically analyzed by atomic absorption to measure concentration of heavy metals. The solid residue was washed by adding 20 mL of deionized water, shaken for 15 min, and centrifuged at 3000 rpm for 20 min. Step 2: heavy metals bound to Fe/Mn oxides were extracted by adding 40 mL of 0.1 M hydroxylamine hydrochloride to the residue from Step 1 and resuspended by mechanical shaking for 16 h at room temperature. The separation of the extract, filtration of the supernatant, analysis of the filtrate, and rinsing of residues were carried out

as indicated in Step 1. In Step 3: heavy metals strongly bound or incorporated into organic matter or other oxidizable species. The residue from Step 2 was treated twice with 10 mL of 8.8 M hydrogen peroxide (H_2O_2). Then, the digestion was allowed to proceed at room temperature for 1.0 h with occasional manual agitation, followed by digestion for another hour at $85 \pm 1^\circ\text{C}$ in a water bath. During the digestion, the Falcon tube was loosely capped to avoid loss of hydrogen peroxide. Next, the tube was uncapped, and heating was continued until the volume decreased to approximately 2-3 mL. An additional 10 mL of peroxide was added to the tube, capped, and digested at $85 \pm 1^\circ\text{C}$ for 1.0 h. Heating continued as before until the volume was reduced to 2-3 mL. Finally, 25 mL of 1.0 M ammonium acetate was added to the cold mixture and shaken for 16 h at room temperature. The separation of the extract, filtration of the supernatant, analysis of the filtrate, and rinsing of residues were carried out as described in Step 1. Heavy metals sorbed or carbonate-bound were discarded in this study because the amount of carbonates in soil were insignificant.

2.8. Chemical and Physical Analyses. Almost all heavy metals (Cu^{2+} , Cd^{2+} , Ni^{2+} , Mn^{2+} , and Zn^{2+}) were analyzed with an atomic absorption spectrometer, PerkinElmer AA 800, using APHA standardized methods. Calibration curves with a correlation index $R \geq 99\%$ were run before analyzing each sample. For the analysis of anions such as CrO_4^{2-} (Cr^{6+}), an ion chromatograph Dionex ICS 1100, equipped with a guard column AG14 and an analytical column AS14, both of 4 mm, and a sample loop of $50 \mu\text{L}$, was used. A solution of 35 mM sodium hydroxide was used as the eluent solution.

3. Results and Discussion

3.1. Characterization of Multicomponent Nanoparticles. A TEM image showed a spherical morphological structure (Figure 1(a)). The nanoparticle size distribution was obtained with a dynamic light scattering (DLS). The Gaussian distribution with an average size of polydispersed nanoparticles lies in a range of $9.5 \pm 1.5 \text{ nm}$ in diameter (Figure 1(c)). The size of the nanoparticles was similar to that obtained with TEM. Roughness of nanoparticles was estimated using MATLAB software developed by Arroyo et al. [19]. This software calculated roughness as a fractal dimension (Figures 1(b) and 1(d)), and the value was given as 1.8 ($D_s = 1.8$). Gagnepain and Roques-Carnes exploited this technique to characterize the uniformity of surfaces for profiles in two dimensions, with D_s falling within a range between 1 and 2, in which 1 corresponds to a smooth surface and 2 to a highly rough surface [20]. Recently, in the fabrication of Fe/FeS nanoparticles was evidenced an enhancement in roughness of the particles' surfaces [7, 8]. Evidently, a high roughness favors the reactivity of the nanoparticle due to the increase of its surface area, thus promoting the formation of more reactive sites [7, 21]. Figure 2(a) shows the UV-Vis spectrum of the mortiño berry extract. Two broad peaks between 240 and 340 nm and 480 and 530 nm were observed, which are related to the presence of gallic acid, vanillic acid, hydroxybenzoic acid,

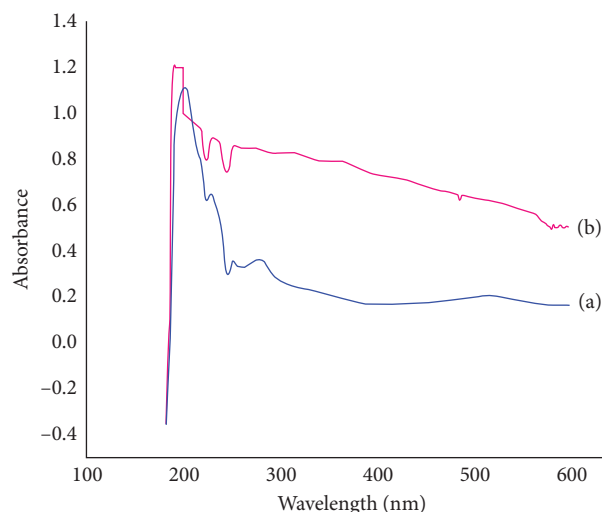


FIGURE 2: UV-Vis spectra of (a) the mortiño berry extract and (b) as-prepared multicomponent nanoparticles.

caffeic/ferulic acid, chlorogenic acid, coumaric acid, myricetin, quercetin, delphinidin, and cyanidin [15, 16, 22].

The as-synthesized multicomponent nanoparticles (Figure 2(b)) showed a broad contribution in the visible light, in addition to the strong band at $\sim 200 \text{ nm}$ and the small one at $\sim 240 \text{ nm}$. As reported by Sherman and Waite [23], species based on iron oxides and hydroxides have four predominant regions of absorption: ligand to metal charge transfer (250–400 nm) along with contribution of Fe^{3+} ligand field transition (290–310 nm), pair excitation process (400–600 nm) of magnetically coupled Fe^{3+} ions, and two strong absorption bands near 640 and 900 nm of ligand field transitions of Fe^{3+} cation in the octahedral environment. The peak found at 290 nm is related to the formation of iron oxide nanoparticles [24] mediated by complex polyphenols contained in the mortiño extract. Recently, these polyphenols induced the reduction of silver ions to metallic silver during the synthesis of the silver-graphene nanocomposite [22]. A peak at 270 nm corresponding to the oxidized polyphenols can also be shown. This peak emerges on the as-synthesized nanoparticle spectrum due to the limitations of the antioxidant activity of the fruit extract. Additionally, peaks from 210 to 260 nm are seen in the two analyzed samples, and it is suggested that they resemble the presence of polyphenols. Markova et al. [25] bio-synthesized nanoparticles with green tea leaves and compared with nanoparticles synthesized with sodium borohydride. Nanoparticles prepared with green tea leaves showed peaks at 210, 220, and 270 nm, whereas in the inorganic samples (nanoparticles with sodium borohydride), these peaks do not show up. Moreover, XRD analyses revealed that the as-synthesized nanoparticles contain iron oxides in the core and a small amount of iron sulfide on the surface as shown in Figure 3. Peaks at 35.54° and 75.3° matched to iron oxides and the peak at 34.03° corresponded to iron sulfide. Benitez in 2010 found iron oxides linked to peaks at 31° and 45.5° [26]. Nevertheless, the displacement of the positions of peaks observed in the study is due to the synthesis protocol. Lastly, FTIR measurements were carried out to understand the

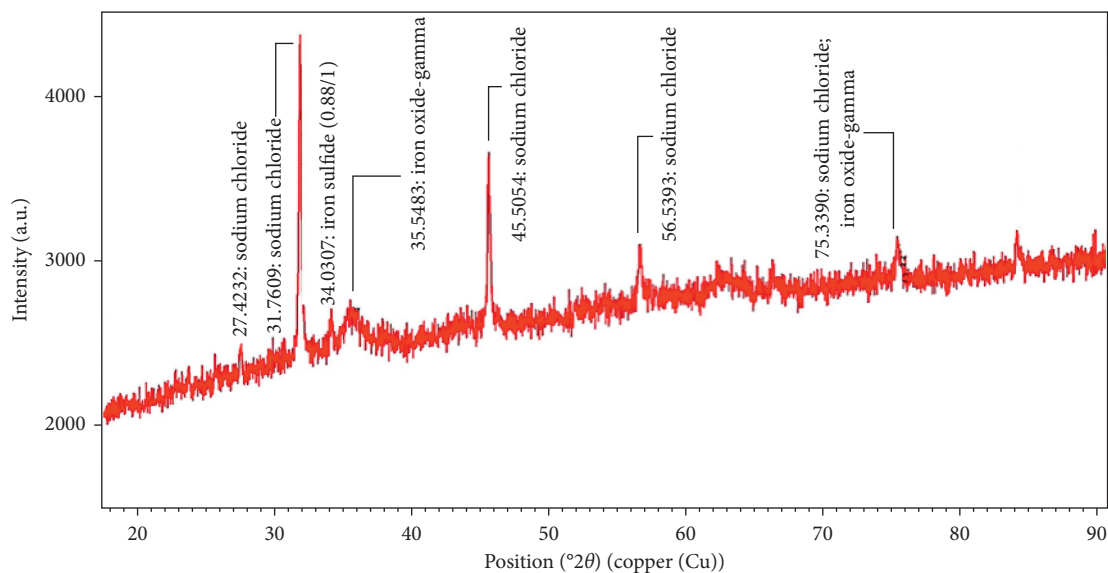


FIGURE 3: XRD spectrum of multicomponent nanoparticles.

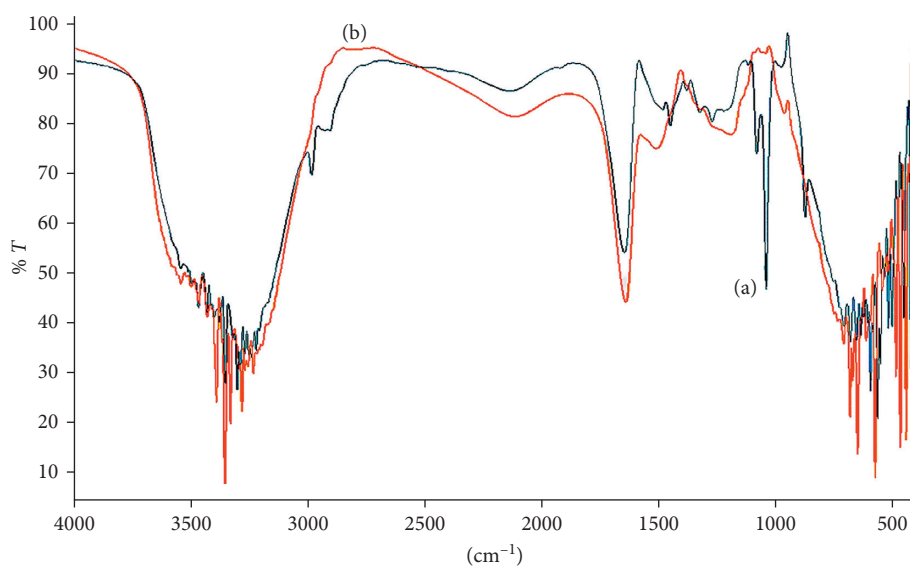


FIGURE 4: FTIR spectra of (a) the mortiño berry extract and (b) as-prepared multicomponent nanoparticles.

participation of the MBE molecules in the formation of nanoparticles. As seen in Figure 4(a), peaks in the range of $3650\text{--}3200\text{ cm}^{-1}$ are related to the vibrations of the -OH groups of the phenolic moiety of MBE, and positions from 1620 to 1690 cm^{-1} are attributed to the aldehydes (C=O) of an ester sugar. These peaks in conjunction with the 1089 cm^{-1} peak (CO stretching) represent the amount of carbon that belongs to the extract. Conversely, the peaks observed at positions 577 and $489\text{--}826\text{ cm}^{-1}$ are characteristic of the vibrations produced by iron oxides (FeO) and sulphides (S-S), respectively (Figure 4(b)). Herlekar and Palanisamy et al. studied the formation of peaks for Fe-O ($636.16\text{--}550\text{ cm}^{-1}$) using the FTIR technique [27, 28]. The peak appearing in the spectrum of multicomponent nanoparticles (577 cm^{-1}) is in between the given peaks, while peaks at 489 and 826 cm^{-1} are

attributed to the vibrations of sulphides. A previous study locates FTIR peaks at 480 cm^{-1} and 600 cm^{-1} for the sulfide group [29]. Therefore, it can be suggested that multicomponent nanoparticles were actually formed.

3.2. Kinetic Study. Figure 5 shows results of kinetic tests for the removal of heavy metals from artificially contaminated water using multicomponent nanoparticles ($\text{Fe}_x\text{O}/\text{FeS}$). It is observed that most of metals achieved maximum removal after 5 min (99.8% Cu, 99.5% Zn, 99.6% Ni, 71.4% Mn, 99.6% Cd, and 99% Cr), showing a sharp slope and then reaching the steady state at around 60 min.

Also, it is seen that there is no difference in the removal rate for each metal. It is remarkable to mention that kinetic

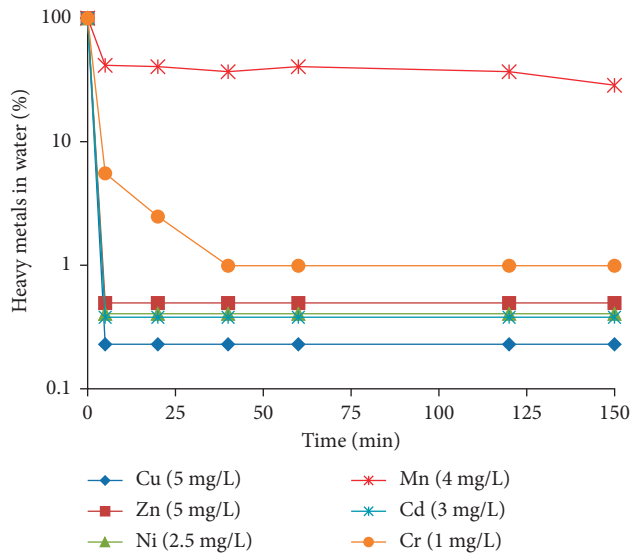


FIGURE 5: Kinetic profiles of heavy metals in artificially contaminated water treated with multicomponent nanoparticles.

data for the adsorption of heavy metals fit very well a pseudo-second-order model (2) as seen in Figure 6:

$$\frac{t}{q_t} = \frac{1}{k_2 q_e^2} + \frac{1}{q_e} t, \quad (2)$$

where k_2 (g/mg·h) is the pseudo-second-order rate constant, q_e is the amount of metal adsorbed (mg/g) at equilibrium, and q_t is the amount of the adsorption (mg/g) at any time t (h) [30]. All fitting curves showed good linearity with a correlation factor equal to unity ($R^2 = 1$). As observed in Figure 5, there was not any change in the concentration of heavy metals in the time period between 5 and 60 min. This implies that chemisorption is the principal mechanism for the uptake of heavy metals [31–33]. However, the electronegativity and the hydrated ionic size of the metallic elements play the role in the selectivity of the adsorption [34]. For example, in our study, the hydrated radius of Mn^{2+} is larger than that of Cu^{2+} ($\text{Mn}^{2+} r_H = 0.438$ nm and $\text{Cu}^{2+} r_H = 0.419$ nm) [35] difficulting coulombic interactions of Mn with the reactive sites of nanoparticles. Also, Mn is the element with the least electronegativity in the series of the studied metals ($\text{Mn} = 1.55$) [36]. Therefore, its tendency to attract electrons is less, which in turn decreases the interactions with the nanoparticles. Also, precipitate formation of metallic sulfides speeds up the removal of heavy metals from water [37–40]. In previous studies of our group, it is reported that multicomponent nanoparticles of zerovalent iron and iron sulfide (Fe/FeS) rapidly removed heavy metals from an artificially prepared mine tailing due to processes of physisorption and chemisorption [8].

3.3. Simultaneous Immobilization of Heavy Metals in Fixed-Bed Columns. A simultaneous immobilization of heavy metals was performed in a fixed-bed column packed with 2.0 g of soil (properties in Table S1) and treated with MCNPs. In Figure 7 is shown that immobilization of heavy metals is

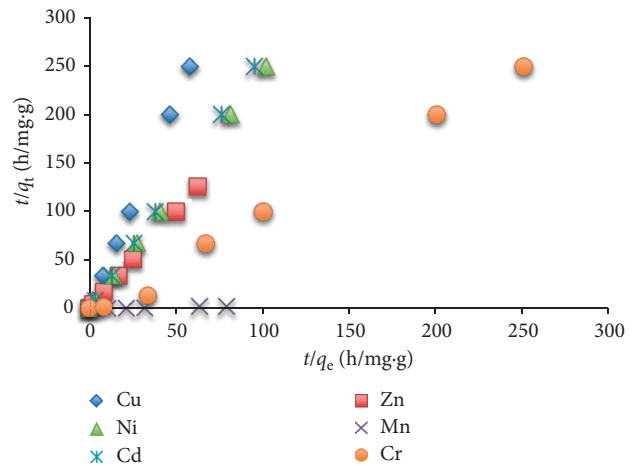


FIGURE 6: Pseudo-second order kinetics for the uptake of heavy metals from water.

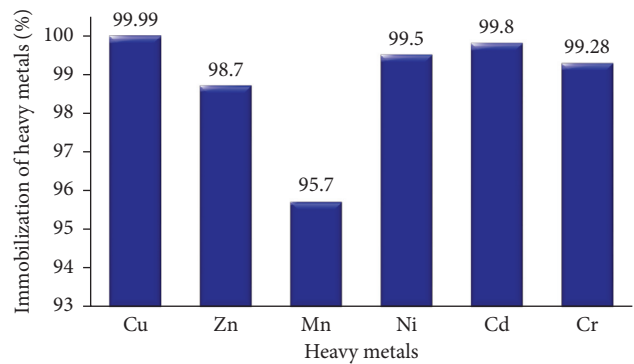


FIGURE 7: Heavy metal immobilization in 2 g of soil at pH 6.58 using 5 mL of MCNPs

higher than 95%. However, the distribution of heavy metals in the soil fractions changed after treatment. Nickel, copper, cadmium, chromium, zinc, and manganese (Figures 8(a)–8(f)) decreased in concentration in the exchangeable phase (22.1%, 9%, 7.9%, 2.6%, 1.82%, and 0.6%, resp.), while Ni^{2+} , Cu^{2+} , and Cd^{2+} showed an increase in concentration in the oxidable fraction (9.1%, 3.37%, and 2.6%, resp.) (Figures 8(a)–8(c)).

On the contrary, concentrations of Ni^{2+} and Cd^{2+} (Figures 8(a) and 8(c)) were higher than those of Cu^{2+} and Cr^{6+} (Figures 8(b) and 8(d)) in the reducible phase after treatment of soils. The drop in the exchangeable fraction could be related to a rapid capture of the toxic cations from soil by MCNPs, forming metallic sulfide precipitates and therefore increasing the oxidable phase. In harmony with Figure 3, multicomponent nanoparticles contain FeS and iron oxides. Once FeS thin film contacted with free heavy metals in the pore water of soil samples, S^{2-} promptly reacted with the toxic metals, forming chemically stable sulfides [41–43] because their solubility products favored the reaction ($K_{\text{sp,Cu}} = \sim 10^{-47}$; $K_{\text{sp,Cd}} = \sim 10^{-29}$; and $K_{\text{sp,Ni}} = \sim 10^{-12}$) [44]. Additionally, concentration of ions with E^0 values close to Fe^{2+} ($E^0 = -0.44$ V) may be lowered much less to reducible forms ($\text{Ni}^{2+} = -0.25$ V, $\text{Cd}^{2+} = -0.4$ V)

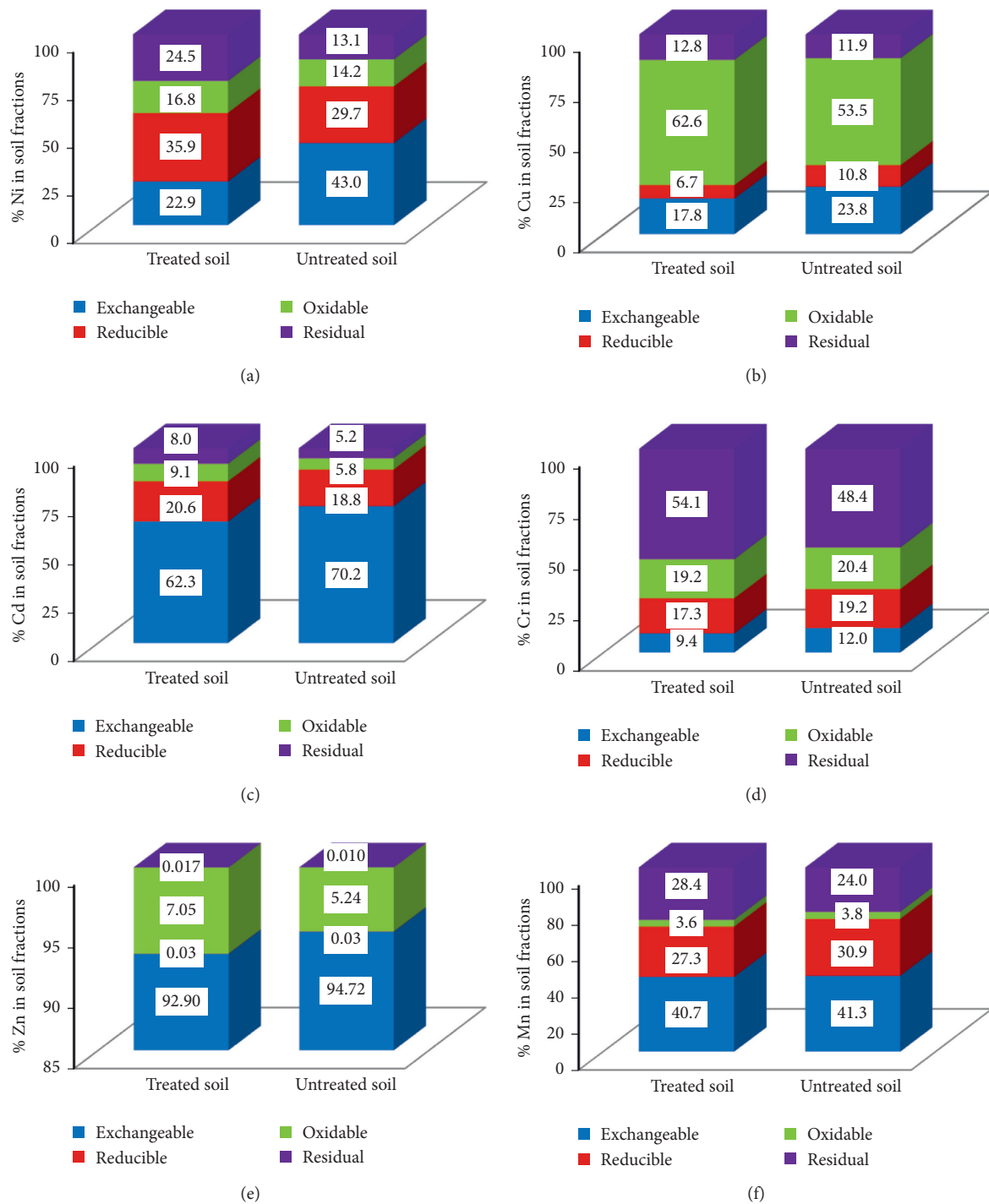


FIGURE 8: Distribution of heavy metals in soils after treatment (T) using 2 g of soil and 5 mL of MCNPs at pH 6.58 and without treatment (UT): (a) Ni, (b) Cu, (c) Cd, (d) Cr, (e) Zn, and (f) Mn.

compared to that of ions with higher reduction potential ($\text{Cu}^{2+} = +0.337 \text{ V}$ and $\text{Cr}^{6+} = +1.33 \text{ V}$) [45]. As result, Ni^{2+} and Cd^{2+} are increased in the reducible fraction, whereas Cu^{2+} and Cr^{6+} (CrO_4^{2-}) decreased. As indicated before, MCNPs also contain iron oxides in the core. These metallic oxides in the pore water could easily release Fe^{2+} or form hydrated iron oxides [46]. Also, Fe^{2+} ions from the ionization

of FeS were in the pore water. Hence, both sources of Fe^{2+} could trigger reduction of toxic metallic ions.

3.4. Leaching of Heavy Metals from Treated Soils. Leaching test results of soils treated with nanoparticles and without treatment under different extractive solutions are observed

TABLE 1: Percentage of heavy metals leaching from soil samples.

Metal	Rainwater		Drinking water		Deionized water		Acidified water	
	T	UT	T	UT	T	UT	T	UT
Cu	0	3.0	0.1	1.3	0.2	4.2	16.0	47.1
Zn	0.6	17.0	0.9	17.2	1.4	19.6	46.5	89.6
Ni	5.2	8.9	1.5	5.0	1.4	3.6	53.8	88.4
Mn	1.7	3.7	4.6	5.3	1.8	4.7	64.5	70.9
Cd	0.0	0.6	0.0	0.1	0.0	0.3	2.0	5.7
Cr	15.8	16.3	13.3	23.7	17.1	21.7	19.4	46.4

T: treated soil with MCNPs; UT: untreated soil with MCNPs.

in Table 1. In general, concentration of heavy metals in the aqueous phase (free metals) is lower for soils treated with MCNPs. However, when acidic water (pH \sim 2) was used as the extracting fluid, the release of heavy metals from soils increased. Zn²⁺, Cr⁶⁺, and Mn²⁺ were the most soluble metals in the extractant medium. Acidic liquids reacting with soils are more aggressive initiating accelerated leaching of heavy metals [47, 48]. At pH < 5, the mobility of metals is improved as a result of the higher concentration of competing protons [49, 50].

4. Conclusion

Kinetic tests revealed a high reactivity of the multicomponent nanoparticles for the removal of heavy metals from artificially contaminated water. This removal is regarded to both physisorption and chemisorption processes. The initial uptake is a physical phenomenon, and it requires only five minutes to remove more than 90% of all heavy metals existing in the aqueous phase. The completion of the reaction takes around 60 min without any leaching of metallic elements due to a chemisorption uptake. On the other hand, the effluent of the column packed with contaminated soils treated with MCNPs showed minimal concentration of heavy metals after five days. All heavy metals were well immobilized within the soil matrix. Nevertheless, the distribution in the soil fractions varies after treatment. In general, the amount of heavy metals in the exchangeable phase decreased, while copper, cadmium, and nickel increased in the oxidizable fraction. In contrast, concentrations of nickel and cadmium were higher than those of copper and chromium in the reducible phase. As reported, immobilization of the toxic metals in soil was a successful procedure; metals do not leach even when flowing rainwater, drinking water, and deionized water through the soil. Yet, leaching of heavy metals is moderate when acidic water is used as an extracting solution.

Conflicts of Interest

The authors declare that they have no conflicts of interest.

Acknowledgments

The authors thank Dr. Alexis Debut for the TEM images, Dr. Carlos Arroyo for allowing us to use his software for estimating the fractal dimension of roughness, and

Mr. Gustavo Martínez for preparing the graphical material. Thanks also to the Universidad de las Fuerzas Armadas for providing funds through a research project.

Supplementary Materials

Table S1: the chemical and physical properties of soil without treatment. (*Supplementary Materials*)

References

- [1] R. G. Chaudhuri and S. Paria, "Core/shell nanoparticles: classes, properties, synthesis mechanisms, characterization, and applications," *Chemical Reviews*, vol. 112, no. 4, pp. 2373–2433, 2011.
- [2] B. Issa, I. M. Obaidat, B. A. Albiss, and Y. Haik, "Magnetic nanoparticles: surface effects and properties related to biomedicine applications," *International Journal of Molecular Sciences*, vol. 14, no. 11, pp. 21266–21305, 2013.
- [3] J. Tian, J. Xu, F. Zhu, T. Lu, C. Su, and G. Ouyang, "Application of nanomaterials in sample preparation," *Journal of Chromatography A*, vol. 1300, pp. 2–16, 2013.
- [4] J. E. Hutchison, "Greener nanoscience: a proactive approach to advancing applications and reducing implications of nanotechnology," *ACS Nano*, vol. 2, no. 3, pp. 395–402, 2008.
- [5] B. Zhou, S. Parasher, and M. Rueter, "Multicomponent nanoparticles formed using a dispersing agent," US Patent no. 7,632,775, December 2009.
- [6] H. Zeng and S. Sun, "Syntheses, properties, and potential applications of multicomponent magnetic nanoparticles," *Advanced Functional Materials*, vol. 18, no. 3, pp. 391–400, 2008.
- [7] E. J. Kim, J. H. Kim, A. M. Azad, and Y. S. Chang, "Facile synthesis and characterization of Fe/FeS nanoparticles for environmental applications," *ACS Applied Materials & Interfaces*, vol. 3, no. 5, pp. 1457–1462, 2011.
- [8] L. H. Cumbal, A. Debut, D. Delgado, C. Bastidas, and C. Stael, "Synthesis of multicomponent nanoparticles for immobilization of heavy metals in aqueous phase," *Nano World Journal*, vol. 1, no. 4, pp. 103–109, 2015.
- [9] D. N. Tran, S. Kabiri, and D. Losic, "A green approach for the reduction of graphene oxide nanosheets using non-aromatic amino acids," *Carbon*, vol. 76, pp. 193–202, 2014.
- [10] S. F. Adil, M. E. Assal, M. Khan, A. Al-Warthan, M. R. H. Siddiqui, and L. M. Liz-Marzán, "Biogenic synthesis of metallic nanoparticles and prospects toward green chemistry," *Dalton Transactions*, vol. 44, no. 21, pp. 9709–9717, 2015.
- [11] S. Iravani, "Green synthesis of metal nanoparticles using plants," *Green Chemistry*, vol. 13, no. 10, pp. 2638–2650, 2011.
- [12] M. J. Firdhouse and P. Lalitha, "Phyto-reduction of graphene oxide using the aqueous extract of *Eichhornia crassipes* (Mart.) Solms," *International Nano Letters*, vol. 4, no. 4, pp. 103–108, 2014.
- [13] T. Kuila, S. Bose, P. Khanra, A. K. Mishra, N. H. Kim, and J. H. Lee, "A green approach for the reduction of graphene oxide by wild carrot root," *Carbon*, vol. 50, no. 3, pp. 914–921, 2012.
- [14] A. H. Al-Marri, M. Khan, M. Khan et al., "Pulicaria glutinosa extract: a toolbox to synthesize highly reduced graphene oxide-silver nanocomposites," *International Journal of Molecular Sciences*, vol. 16, no. 1, pp. 1131–1142, 2015.
- [15] C. Vasco, K. Riihinen, J. Ruales, and A. Kamal-Eldin, "Chemical composition and phenolic compound profile of

- mortiño (*Vaccinium floribundum* Kunth),” *Journal of Agricultural and Food Chemistry*, vol. 57, no. 18, pp. 8274–8281, 2009.
- [16] G. A. Garzón, C. E. Narváez, K. M. Riedl, and S. J. Schwartz, “Chemical composition, anthocyanins, non-anthocyanin phenolics and antioxidant activity of wild bilberry (*Vaccinium meridionale* Swartz) from Colombia,” *Food Chemistry*, vol. 122, no. 4, pp. 980–986, 2010.
- [17] O. Heiri, A. F. Lotter, and G. Lemcke, “Loss on ignition as a method for estimating organic and carbonate content in sediments: reproducibility and comparability of results,” *Journal of Paleolimnology*, vol. 25, no. 1, pp. 101–110, 2001.
- [18] A. M. Ure, P. Quevauviller, H. Muntau, and B. Griepink, “Speciation of heavy metals in soils and sediments. An account of the improvement and harmonization of extraction techniques undertaken under the auspices of the BCR of the Commission of the European Communities,” *International Journal of Environmental Analytical Chemistry*, vol. 51, no. 1–4, pp. 135–151, 1993.
- [19] C. R. Arroyo, A. Vaca, A. Debut, and L. Cumbal, “Reliable tools for quantifying the morphological properties at the nanoscale,” *Biology and Medicine*, vol. 8, no. 3, pp. 1–7, 2016.
- [20] J. J. Gagnepain and C. Roques-Carmes, “Fractal approach to two-dimensional and three-dimensional surface roughness,” *Wear*, vol. 109, no. 1–4, pp. 119–126, 1986.
- [21] E. Malkoc and Y. Nuhoglu, “Removal of Ni(II) ions from aqueous solutions using waste of tea factory: adsorption on a fixed-bed column,” *Journal of Hazardous Materials*, vol. 135, no. 1–3, pp. 328–336, 2006.
- [22] K. S. Vizuete, B. Kumar, A. V. Vaca, A. Debut, and L. Cumbal, “Mortiño (*Vaccinium floribundum* Kunth) berry assisted green synthesis and photocatalytic performance of silver-graphene nanocomposite,” *Journal of Photochemistry and Photobiology A: Chemistry*, vol. 329, pp. 273–279, 2016.
- [23] D. M. Sherman and T. D. Waite, “Electronic spectra of Fe³⁺ oxides and oxide hydroxides in the near IR to near UV,” *American Mineralogist*, vol. 70, pp. 1262–1269, 1985.
- [24] H. Muthukumar and M. Matheswaran, “*Amaranthus spinosus* leaf extract mediated FeO nanoparticles: physicochemical traits, photocatalytic and antioxidant activity,” *ACS Sustainable Chemistry & Engineering*, vol. 3, no. 12, pp. 3149–3156, 2015.
- [25] Z. Markova, P. Novak, J. Kaslik et al., “Iron(II, III)–polyphenol complex nanoparticles derived from green tea with remarkable ecotoxicological impact,” *ACS Sustainable Chemistry & Engineering*, vol. 2, no. 7, pp. 1674–1680, 2014.
- [26] M. J. Benitez, D. Mishra, P. Szary et al., “Structural and magnetic characterization of self-assembled iron oxide nanoparticle arrays,” *Journal of Physics: Condensed Matter*, vol. 23, no. 12, p. 126003, 2011.
- [27] M. B. Herlekar, “Biological synthesis of iron oxide nanoparticles using agro-wastes and feasibility for municipal wastewater treatment,” in *Proceedings of the 47th Indian Water Works Association (IWWA) Convention*, Kolkata, West Bengal, India, January–February 2015.
- [28] K. L. Palanisamy, V. Devabharathi, and N. M. Sundaram, “The utility of magnetic iron oxide nanoparticles stabilized by carrier oils in removal of heavy metals from waste water,” *International Journal of Research in Applied, Natural and Social Sciences*, vol. 1, no. 4, pp. 15–22, 2013.
- [29] F. L. Pua, C. H. Chia, S. Zakari et al., “Preparation of transition metal sulfide nanoparticles via hydrothermal route,” *Sains Malaysiana*, vol. 39, no. 2, pp. 243–248, 2010.
- [30] J. Gong, T. Liu, X. Wang, X. Hu, and L. Zhang, “Efficient removal of heavy metal ions from aqueous systems with the assembly of anisotropic layered double hydroxide nanocrystals@carbon nanosphere,” *Environmental Science & Technology*, vol. 45, no. 14, pp. 6181–6187, 2011.
- [31] S. D. Comber, M. J. Gardner, A. M. Gunn, and C. Whalley, “Kinetics of trace metal sorption to estuarine suspended particulate matter,” *Chemosphere*, vol. 33, no. 6, pp. 1027–1040, 1996.
- [32] Y. S. Ho and G. McKay, “The kinetics of sorption of divalent metal ions onto sphagnum moss peat,” *Water Research*, vol. 34, no. 3, pp. 735–742, 2000.
- [33] Y. S. Ho, J. C. Ng, and G. McKay, “Removal of lead(II) from effluents by sorption on peat using second-order kinetics,” *Separation Science and Technology*, vol. 36, no. 2, pp. 241–261, 2001.
- [34] E. Sočo and J. Kalembkiewicz, “Removal of copper(II) and zinc(II) ions from aqueous solution by chemical treatment of coal fly ash,” *Croatia Chemica Acta*, vol. 88, no. 3, pp. 267–279, 2015.
- [35] E. R. Nightingale, “Phenomenological theory of ion solvation. Effective radii of hydrated ions,” *Journal of Physical Chemistry*, vol. 63, no. 9, pp. 1381–1387, 1959.
- [36] A. L. Allred, “Electronegativity values from thermochemical data,” *Journal of Inorganic and Nuclear Chemistry*, vol. 17, no. 3–4, pp. 215–221, 1961.
- [37] D. T. Rickard, “Kinetics and mechanism of pyrite formation at low temperatures,” *American Journal of Science*, vol. 275, no. 6, pp. 636–652, 1975.
- [38] G. W. Luther, “Pyrite synthesis via polysulfide compounds,” *Geochimica et Cosmochimica Acta*, vol. 55, no. 10, pp. 2839–2849, 1991.
- [39] D. Rickard and G. W. Luther, “Kinetics of pyrite formation by the H₂S oxidation of iron(II) monosulfide in aqueous solutions between 25 and 125°C: the mechanism,” *Geochimica et Cosmochimica Acta*, vol. 61, no. 1, pp. 135–147, 1997.
- [40] D. Rickard, “Kinetics of pyrite formation by the H₂S oxidation of iron(II) monosulfide in aqueous solutions between 25 and 125°C: the rate equation,” *Geochimica et Cosmochimica Acta*, vol. 61, no. 1, pp. 115–134, 1997.
- [41] J. G. Dean, F. L. Bosqui, and K. H. Lanouette, “Removing heavy metals from waste water,” *Environmental Science & Technology*, vol. 6, no. 6, pp. 518–522, 1972.
- [42] R. G. Lidzey, J. H. P. Watson, and D. C. Ellwood, “The removal of the pertechnetate ion and actinides from radioactive waste streams at Hanford, Washington, USA and Sellafield, Cumbria, UK: the role of iron-sulfide-containing adsorbent materials,” *Nuclear Engineering and Design*, vol. 226, no. 3, pp. 375–385, 2003.
- [43] R. D. Ludwig, R. G. McGregor, D. W. Blowes, S. G. Benner, and K. Mountjoy, “A permeable reactive barrier for treatment of heavy metals,” *Ground Water*, vol. 40, no. 1, pp. 59–66, 2002.
- [44] R. Chang and K. A. Goldsby, *General Chemistry: The Essential Concepts*, McGraw-Hill, New York, NY, USA, 7th edition, 2014.
- [45] J. E. Macdonald and J. G. C. Veinot, “Removal of residual metal catalysts with iron/iron oxide nanoparticles from coordinating environments,” *Langmuir*, vol. 24, no. 14, pp. 7169–7177, 2008.
- [46] A. K. Gupta and M. Gupta, “Synthesis and surface engineering of iron oxide nanoparticles for biomedical applications,” *Biomaterials*, vol. 26, no. 18, pp. 3995–4021, 2005.

- [47] J. J. Dijkstra, J. C. L. Meeussen, and R. N. J. Comans, "Leaching of heavy metals from contaminated soils: an experimental and modeling study," *Environmental Science & Technology*, vol. 38, no. 16, pp. 4390–4395, 2004.
- [48] S. A. Zheng, X. Zheng, and C. Chen, "Leaching behavior of heavy metals and transformation of their speciation in polluted soil receiving simulated acid rain," *PLoS One*, vol. 7, no. 11, Article ID e49664, 2012.
- [49] E. O. E. Agbenyeku, E. Muzenda, and M. L. Msibi, "Chemical alterations in three clayey soils from percolation and interaction with acid mine drainage (AMD)," *South African Journal of Chemical Engineering*, vol. 21, pp. 28–36, 2016.
- [50] P. H. T. Beckett, "The use of extractants in studies on trace metals in soils, sewage sludges, and sludge-treated soils," in *Advances in Soil Science*, pp. 143–176, Springer, New York, NY, USA, 1989.

Research Article

Curcumin-Loaded Mixed Micelles: Preparation, Characterization, and *In Vitro* Antitumor Activity

Suping Ji,¹ Xiao Lin,¹ Enjiang Yu,¹ Chengyang Dian,¹ Xiong Yan,¹ Liangyao Li,¹ Meimei Zhang,³ Wenchang Zhao,¹ and Linghui Dian ^{1,2}

¹School of Pharmaceutical Sciences, Guangdong Medical University, Dongguan 523808, China

²Guangdong Key Laboratory for Research and Development of Natural Drugs, Guangdong Medical University, Zhanjiang 524023, China

³Affiliated Cancer Hospital and Institute of Guangzhou Medical University, Guangzhou 511436, China

Correspondence should be addressed to Linghui Dian; 605911308@qq.com

Received 17 October 2017; Accepted 25 December 2017; Published 15 March 2018

Academic Editor: Rachid Seqqat

Copyright © 2018 Suping Ji et al. This is an open access article distributed under the Creative Commons Attribution License, which permits unrestricted use, distribution, and reproduction in any medium, provided the original work is properly cited.

The objective of this study was to prepare curcumin-loaded mixed Soluplus/TPGS micelles (Cur-TPGS-PMs) for oral administration. The Cur-TPGS-PMs showed a mean size of 65.54 ± 2.57 nm, drug encapsulation efficiency over 85%, and drug loading of 8.17%. The Cur-TPGS-PMs were found to be stable in various pH media (pH 1.2 for 2 h, pH 6.8 for 2 h, and pH 7.4 for 6 h). The X-ray diffraction (XRD) patterns illustrated that curcumin was in the amorphous or molecular state within PMs. The *In vitro* release test indicated that Cur-TPGS-PMs possessed a significant sustained-release property. The cell viability in MCF-7 cells was found to be relatively lower in Cur-TPGS-PM-treated cells as compared to free Cur-treated cells. CLSM imaging revealed that mixed micelles were efficiently absorbed into the cytoplasm region of MCF-7 cells. Therefore, Cur-TPGS-PMs could have the significant value for the chronic breast cancer therapy.

1. Introduction

Curcumin (Cur), obtained from the rhizomes of *Curcuma longa* L., turmeric, is the most widely used phytoconstituent in food industry. It has a wide spectrum of pharmacological activities, such as anti-inflammatory, anticancer, and other pharmacological activities [1]. Numerous experimental results had unequivocally demonstrated that curcumin could induce arrest and/or apoptosis of human cancer cells of a variety of solid tumors at, for example, colorectal, lung, breast, pancreatic, and prostate carcinomas [2–6]. Recently, a clinical trial performed in patients with familial adenomatous polyposis has confirmed that curcumin could decrease the progression of cancer at a variety of organ sites, showing the potentiality of chemoprevention [7]. Furthermore, considerable studies suggested that curcumin was an efficacious and safe compound for cancer therapy and chemoprevention. However, its limited aqueous solubility and degradation at alkaline pH hinder its bioavailability [8, 9]. Following oral

administration (up to 8 g per day), the compound is poorly absorbed with only trace appearing in the blood [10]. One of the attempts to improve its bioavailability is utilizing proper delivery vehicles to maximize the absorption of curcumin in the upper gastrointestinal tract. The nanodrug delivery system has a good prospect in oral administration, especially polymeric micelles. Polymeric micelles comprise inner and outer domains which are denominated “core” and “shell” respectively, which offer outstanding advantages to promote oral absorption of the chemotherapy drug through encapsulating with a hydrophobic drug in the cores [11, 12]. It can deliver the drug to the desired site at the concentration exceeding its intrinsic water solubility and protect the unstable drug from direct contacting with the gastrointestinal (GI) contents inducing chemical degradation and metabolism. Meanwhile, the encapsulated drug was sustained released, with direct uptake by cells. It should be emphasized that mixed micelles have received much attention due to increasing physical stability, improving drug-loading capacities, and enhancing

antidilution ability compared with polymeric micelles for drug delivery [13]. Mixed micelles can self-assemble with two or more similar structures and performance block copolymers. Mixed micelles can provide multiple functionality micelles by constituent copolymers. Therefore, a mixed micelle was developed with Soluplus and D- α -tocopheryl polyethylene glycol 1000 succinate (TPGS 1000) for curcumin delivery.

Soluplus is an amphiphilic polyvinyl caprolactam-polyvinyl acetate-polyethylene glycol graft copolymer introduced by BASF recently. This graft copolymer has a polyethylene glycol (PEG) backbone as a hydrophilic part and vinylcaprolactam/vinyl acetate side chains as a hydrophobic structure. It can form micelles in aqueous solution above the CMC of 10^{-8} M [14]. Though Soluplus could improve the oral bioavailability of poorly soluble drugs by producing solid solutions [15], so far there is no systemic research on preparation of drug-loaded Soluplus micelles.

D- α -tocopheryl polyethylene glycol 1000 succinate (TPGS 1000), known as an attracting surfactant, has been used in many pharmaceutical nanoformulations, which can not only increase drug solubility and stability, enhance drug encapsulation efficiency, and prolong the time of drug retention in the blood but also improve the oral bioavailability of anticancer drugs and overcome the multidrug resistance by inhibiting P-gp efflux pumps [16]. Therefore, TPGS 1000-incorporating nanomicelle systems could successfully promote the oral absorption of anticancer drugs [17, 18].

The objective of this study was to develop a mixed micelle delivery system by using Soluplus and TPGS, which could solubilize curcumin *in vitro* to reach the clinically relevant concentration and deliver the drug in a controlled manner. Hence, we tried to develop Cur-TPGS-PMs to enhance its antitumor activity. After assessing the feasibility of preparation, we prepared and characterized the physicochemical properties of Cur-TPGS-PMs including particle size analysis, zeta potential measurement, drug entrapment efficiency, pH stability, and *in vitro* drug release behavior. Moreover, the toxicity and cell uptake of Cur-TPGS-PMs with MCF-7 breast cancer cells were further investigated comparing with free Cur. These results showed the promise of potential applications of delivering curcumin as a mixed micelle for cancer therapy.

2. Materials and Methods

2.1. Materials. Soluplus® (an amphiphilic polyvinyl caprolactam-polyvinyl acetate-polyethylene glycol graft copolymer) was generously presented by BASF Auxiliary Chem. Co., Ltd. (Shanghai, China). D- α -tocopherol polyethylene glycol 1000 succinate (TPGS 1000) was obtained from Eastman Chemical Company (USA). Curcumin (Cur) was provided by Sigma-Aldrich (USA). High-pressure liquid chromatography- (HPLC-) grade methanol was bought from Fisher Scientific (Beijing, China). Other chemical reagents received were used without further purification. Milli-Q grade water purified through a Millipore system (ELGA LabWater, Sartorius, UK) was used during this study.

2.2. Preparation of Micelles. Mixed micelles containing curcumin were prepared by an ameliorated film dispersion

method [19]. Accordingly, curcumin and Soluplus were mixed into methanol. The mixed solution was evaporated under reduced pressure by a rotary evaporator at 35°C, and then, a thin film with curcumin was achieved. The thin film was hydrated with deionized water containing TPGS, followed by moderate stirring for 2 h. The curcumin-mixed Soluplus with TPGS-mixed micelles (abbreviated as Cur-TPGS-PMs) was obtained by filtration of the micelle through a 0.22 μ m polycarbonate membrane to separate nonencapsulated curcumin. In addition, curcumin Soluplus micelles (short form Cur-PMs) were prepared using the same protocol of curcumin-mixed Soluplus micelles except that TPGS were not used in the procedure, and used as the control.

2.2.1. Effect of TPGS Concentration. In order to select a suitable TPGS concentration for preparing the desirable Cur-TPGS-PMs, different concentrations (0.005%, 0.015%, 0.03%, and 0.04%) were investigated. Particle size and zeta potential were selected as the optimum condition for the Cur-TPGS-PM formulation.

2.2.2. Effect of Stirring Time. The stirring time for preparing the desirable Cur-TPGS-PMs was optimized. Particle size and zeta potential were selected as the optimum condition for the Cur-TPGS-PM formulation.

2.2.3. Effect of Stirring Rate. The stirring rate for preparing the desirable Cur-TPGS-PMs was investigated. Particle size and zeta potential were selected as the optimum condition for the Cur-TPGS-PM formulation.

2.2.4. Effect of Drug Loading. Cur-TPGS-PMs were prepared using different theoretical ratios of curcumin to polymer, that is, 0.5 : 10, 1 : 10, and 1.5 : 10, on the basis of the preliminary experiment to determine the optimum percentage of curcumin in the Soluplus matrix and its effects on particle size, polydispersity index (PDI), zeta potential, and encapsulation efficiency. The magnetic stirring time (2 h), stabilizer concentration (0.03% of TPGS), and aqueous ratio were kept constant.

2.3. Particle Size and Zeta Potential. Particle size is one of the important indexes in the evaluation of nanodosage forms. The average particle size and size distribution of Cur-TPGS-PMs were determined by the Malvern Instruments Zetasizer Nano ZS90 (Malvern Instruments, Malvern, UK) laser particle size analyzer. Double dilution of the formulations with distilled water was analyzed for particle size and zeta potential before each measurement. The mean Z-average diameter and polydispersity index (PDI) were obtained through cumulate analysis software. Each test was performed in triplicate.

2.4. Transmission Electron Microscopy (TEM). The morphological characteristics of Cur-TPGS-PMs were viewed by a transmission electron microscope (TEM, H66009IV, Hitachi, Japan). Cur-TPGS-PMs were diluted with distilled

water and dropped on a copper grid covered with nitrocellulose. Samples were stained with oleic acid and dried at room temperature of 25°C before examination.

2.5. Characterization by X-Ray Diffraction (XRD). XRD analysis was carried out to determine the crystallinity of curcumin in PMs by an X-ray powder diffractometer (D-MAX 2200 VPC, Rigaku, Japan) operating with the voltage of 40 kV and the current of 25 mA. Data were collected in the 2θ range of 5–50 degrees at a scan rate of 0.9 min⁻¹. A lyophilized powder sample was put on a glass plate to spread a flat surface for measurement. XRD patterns were obtained for free Cur, void PMs, physical mixture of void PMs and Cur, and Cur-TPGS-PMs.

2.6. pH-Dependent Stability Studies. The stability of Cur-TPGS-PMs was investigated under different pH (pH 1.2, pH 6.8, and pH 7.4) conditions that could impact their particle size and drug release properties. Briefly, 1 mL of Cur-TPGS-PM colloidal solution was added into different pH solutions. The Cur-TPGS-PMs were incubated in pH 1.2 for 2 h, pH 6.8 for 2 h, and pH 7.4 for 6 h, respectively. The particle size and PDI were assessed after the incubation of Cur-TPGS-PMs with different pH solutions [20, 21].

2.7. In Vitro Release. The curcumin release from the Cur-TPGS-PM system was performed using a dialysis method. Dialysis bags (14000 MWCO, Millipore, Boston, MA, USA) were soaked in double-distilled water for 24 h before the experiment. Briefly, 1 mL of Cur-TPGS-PM colloidal solution, Cur-PM colloidal solution, or Cur suspension solution (equivalent to 1 mg of Cur) was loaded into dialysis bags. The bags were in turn placed in a 150 mL pH 1.2 for 2 h and then in pH 7.4 release media until 48 h. The flask was placed in a water bath at 37 ± 0.5°C under a shaking rate at 100 rpm. 5 mL of the release sample was withdrawn and replaced with the same volume of the fresh medium to maintain a sink condition at the specific time points of 0.5, 1.0, 1.5, 2.0, 4.0, 8.0, 12.0, 24.0, 36.0, and 48.0 h. The release samples were analyzed for curcumin content using a high-performance liquid chromatography (HPLC), and the release test on each sample was performed in triplicate.

The content of curcumin was assayed by an HPLC system (Shimadzu, Kyoto, Japan), which was equipped with an SPD-10A ultraviolet detector, LC-10AT pump. Curcumin separation was carried out on a column (Hypersil C₁₈, 4.6 × 250 mm, 5 μm, Yilite, China) with a mobile phase made up of methanol, water, and acetic acid (76 : 23 : 1, v/v/v). The flow rate was maintained at 1 mL/min. The absorbance of curcumin was measured at a wavelength of 421 nm.

2.8. Cell Culture. The MCF-7 cells (obtained from the American Type Culture Collection) were grown in an RPMI-1640 medium with 10% (v/v) heat-inactivated fetal bovine serum (FBS) and 1% antibiotics (100 U/ml penicillin and 100 μg/ml streptomycin). The cells were maintained at 37°C with 5% CO₂ in a humidified incubator.

2.9. Cell Uptake Studies. To evaluate MCF-7 cellular uptake quantitatively, the MCF-7 cells were seeded into 6-well culture plates at a density of 3 × 10⁵ cells/well under 5% CO₂ at 37°C for 24 h. Free Cur, Cur-PMs, and Cur-TPGS-PMs were applied to 6-well culture plates for 4 h. The final concentration of Cur was 10 μM. The culture medium was used as a blank control. The cells were washed 3 times with PBS (pH 7.4), fixed with 4% paraformaldehyde (v/v) for 15 min under 5% CO₂ at 37°C, and trypsinized with 0.25% trypsinase and collected. The harvested cells were estimated with an FACScan flow cytometry to measure the fluorescence intensity of Cur for assessing the quantity of cellular uptake (excitation wavelength = 488 nm, emission wavelength = 560 nm).

MCF-7 cells were seeded into 6-well culture slides (BD Falcon) with densities being approximately 3 × 10⁵ per well and allowed to culture for 24 h. The cells were incubated with free Cur, Cur-PMs, and Cur-TPGS-PMs for 4 h at a final concentration of 20 μM Cur. Then, the cells were washed with cold PBS (pH 7.4) three times to remove extracellular particles. The cell nuclei were stained with Hoechst 333342 (5 mg/mL) for 30 min. Then, the cells were washed twice with PBS and observed with a laser scanning confocal microscope (Leica SP2, Heidelberg, Germany).

2.10. Cytotoxicity Assay. MCF-7 cells were seeded into 96-well culture plates at a density of 1 × 10⁴ cells/well and cultured for 24 h under 5% CO₂ at 37°C. When reaching approximately 80% confluence, the medium was then replaced with fresh culture media and different concentrations of free Cur, Cur-PMs, and Cur-TPGS-PMs for 48 h, respectively. The final concentration of curcumin was in between 0 and 20 μM, and blank PMs were added as parallel controls. Blank culture medium was used as a blank control. After incubation for 48 h, the cytotoxic effects were estimated by a sulforhodamine B (SRB, Sigma-Aldrich) staining assay [22]. Briefly, the culture medium was removed. The cells were fixed with trichloroacetic acid, washed with deionized water, and stained with SRB. The measuring absorbance was at 540 nm with a microplate reader (Model 680 microplate reader; Bio-Rad Laboratories, Hercules, CA, USA). The survivals of MCF-7 cells were evaluated using the following formula: survival% = (A_{540 nm} for the treated cells/A_{540 nm} for the control cells) × 100%, where A_{540 nm} denotes the absorbance at 540 nm. Each test was performed in triplicate.

2.11. Statistical Analysis. Data are reported as the mean ± SD (standard deviation). One-way analysis of variance was used to assess the significance among groups, after which post hoc tests with the Bonferroni correction were used for multiple comparisons between individuals. A value of *P* less than 0.05 was evaluated to be statistically significant.

3. Results

3.1. Preparation of Mixed Micelles. Different process variables including stabilizer concentration, magnetic stirring time, magnetic stirring rate, and theoretical drug loading were optimized for the preparation of Cur-TPGS-PMs.

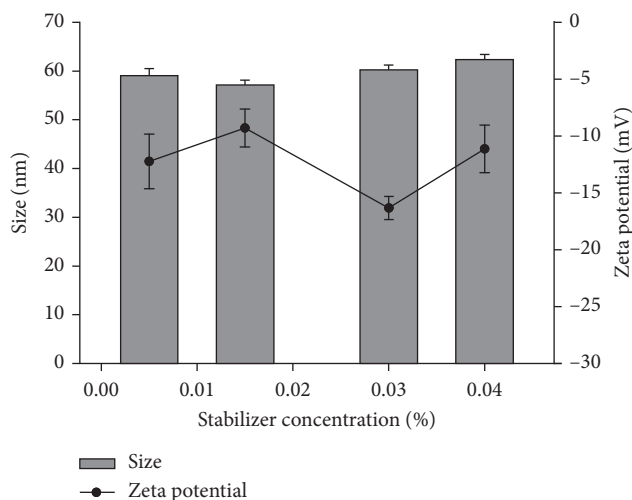


FIGURE 1: Effect of TPGS concentration on the size and zeta potential of Cur-TPGS-PMs.

3.1.1. Effect of Stabilizer Concentration. The effects of TPGS concentration on the particle size and zeta potential of Cur-TPGS-PMs are shown in Figure 1. As the concentration of TPGS increased (0.005–0.04%), no significant difference was found in the particle size. The particle size was less than 100 nm which was acceptable. While the concentration of TPGS was 0.03%, the absolute value of the zeta potential was the maximum, contributing to the stability of mixed micelles. Therefore, 0.03% TPGS (w/v) was optimized for the preparation of Cur-TPGS-PMs.

3.1.2. Effect of Stirring Time. Cur-TPGS-PMs were prepared by magnetic stirring for particle size reduction. Figure 2 shows the decrease in the particle size upon increasing the stirring time up to 2 h. Magnetic stirring of 2 h brought about the smaller particle size (59.32 ± 1.01 nm), and the absolute value of the zeta potential was the maximum. So, magnetic stirring of 2 h was selected for further research.

3.1.3. Effect of Stirring Rate. The effects of stirring rate on the particle size and zeta potential of Cur-TPGS-PMs were also studied. Figure 3 indicates that the effects of stirring rate on the particle size and zeta potential were negligible. When the stirring rate was 600 rpm, the zeta potential of Cur-TPGS-PMs reached the largest absolute value. So, the optimal magnetic stirring rate was set at 600 rpm for further research.

3.1.4. Optimum of Drug Loading. The single film dispersion method was implemented for encapsulation of water-insoluble curcumin in mixed micelles. Cur-TPGS-PMs were prepared with different theoretical ratios of curcumin to Soluplus, that is, 0.5:10, 1:10, and 1.5:10, to determine the optimum percentage of curcumin in nanocarriers. As shown in Table 1, the drug loading affected significantly the particle size and encapsulation efficiency of Cur-TPGS-PMs. With the increase of drug loading, the particle size increased and the encapsulation efficiency decreased significantly. The reason for

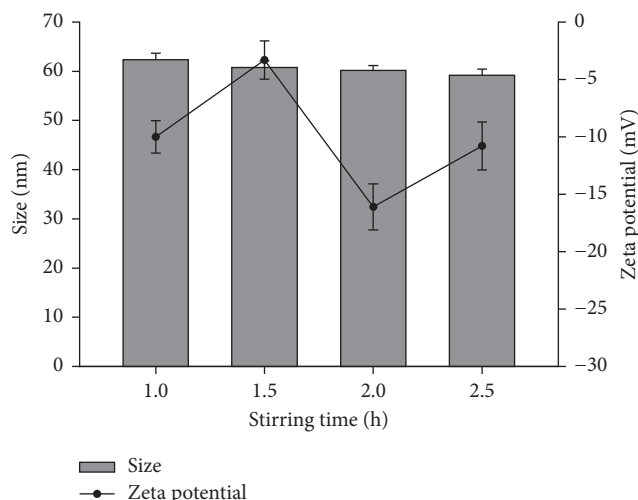


FIGURE 2: Effect of stirring time on the size and zeta potential of Cur-TPGS-PMs.

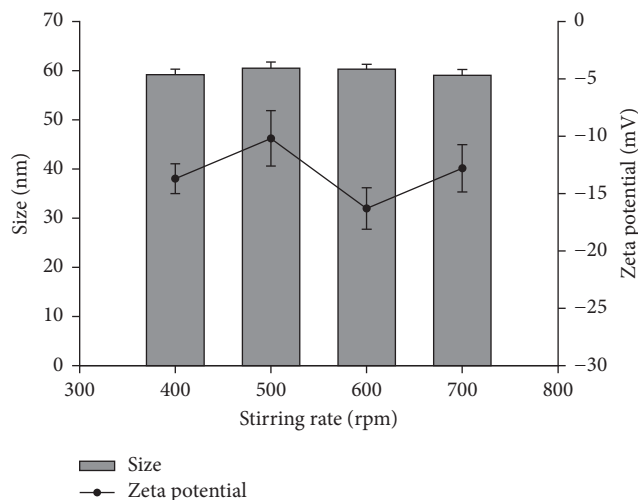


FIGURE 3: Effect of stirring rate on the size and zeta potential of Cur-TPGS-PMs.

that was more drug loading which expanded the core of micelles, leading to the increase of the particle size. Along with the improvement of ratios of drug to polymer, the encapsulation efficiency (EE) of Cur-TPGS-PMs declined markedly. It might be attributed to some amount of the polymer that could encapsulate a certain amount of drugs in mixed micelles. When the drug/Soluplus ratio was above 1.5:10, the micellar structure could break down. Therefore, the favorable drug loading in mixed micelle formulation was drug/Soluplus ratio at 1:10, in which the drug loading was superior and the Cur-TPGS-PMs had small particle size and uniform distribution.

3.2. Characterization of Cur-TPGS-PMs

3.2.1. Particle Size and Morphology. The average particle size of Cur-TPGS-PMs was 65.54 ± 2.57 nm (Figure 4(a)), and

TABLE 1: Effect of dosage on the size and zeta potential of Cur-TPGS-PMs (mean \pm SD, $n = 3$).

Curcumin : Soluplus	Particle size (nm)	PDI	Zeta potential (mV)	EE (%)
0.5 : 10	60.76 \pm 1.02	0.02 \pm 0.01	-12.21 \pm 1.95	93.17 \pm 0.92
1.0 : 10	67.13 \pm 2.01	0.09 \pm 0.02	-14.50 \pm 3.46	90.26 \pm 1.38
1.5 : 10	506.41 \pm 5.02	0.42 \pm 0.35	-9.01 \pm 6.08	51.34 \pm 2.94

Note. PDI, polydispersity index; SD, standard deviation; EE, encapsulation efficiency.

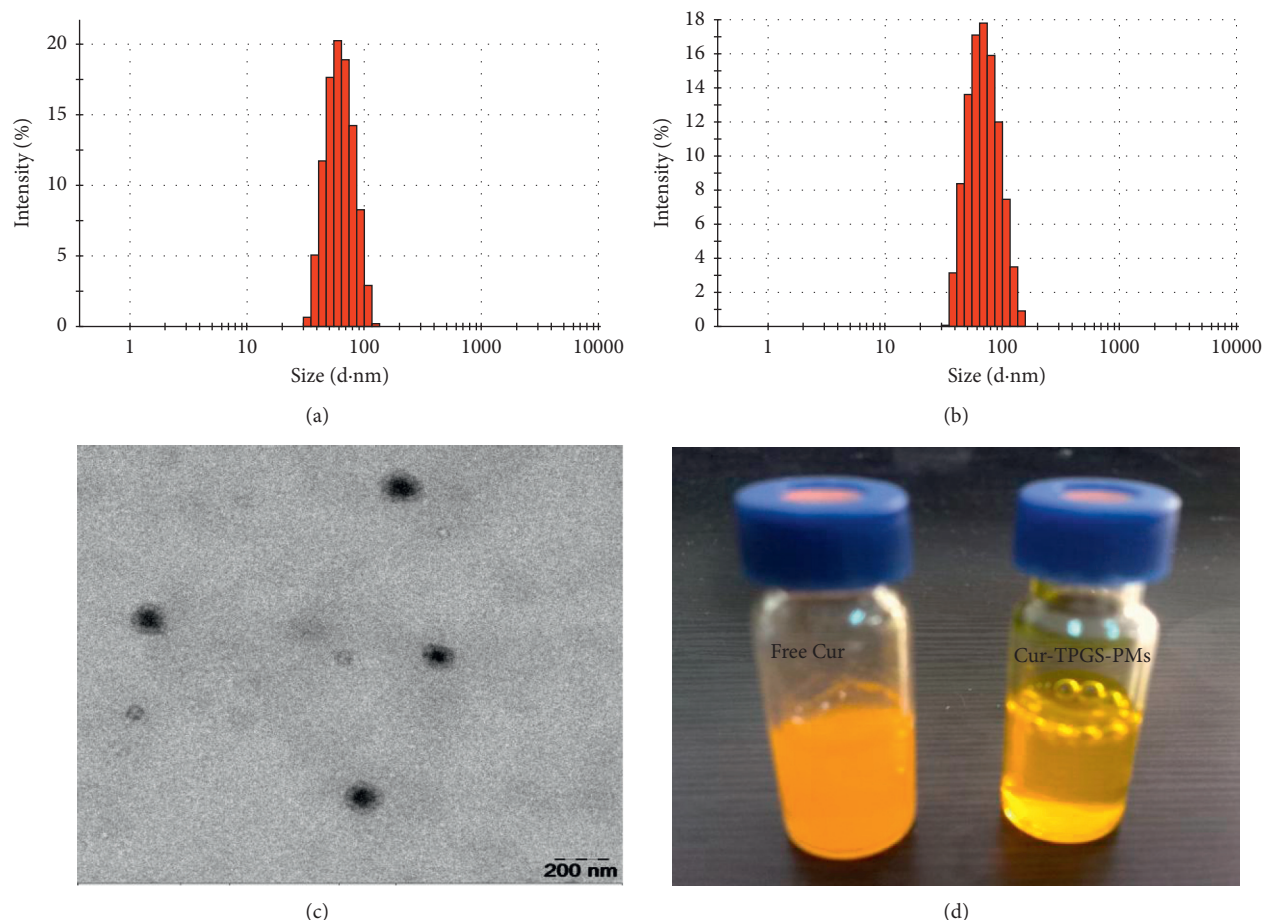


FIGURE 4: Particle size of blank-TPGS-PMs (a), particle size of Cur-TPGS-PMs (b), TEM image of Cur-TPGS-PMs (c), and colloidal solution of Cur-TPGS-PMs (right), in comparison with free Cur in water (left) (d).

the polydispersity index was 0.114 ± 0.027 . Studies indicate that a favorable particle size range for oral absorption was advantageous to the proleptic tissue distribution and passive targeting ability of micelles *in vivo* [23, 24]. It was well known that nanoparticles with the sizes ranging from 10 nm to 100 nm could show an optimum cellular and nuclear uptake in epithelial and smooth muscle cells [17]. Therefore, Cur-TPGS-PMs in small size were easier to be taken in intestines and could avoid rapid metabolism and elimination, with the stability and long circulation time guaranteed. Besides, the nanosized micelles were accounted for the enhanced permeability and retention (EPR) effect, that is, passive targeting ability. Thus, Cur-TPGS-PMs in small size with enhanced permeability and retention were suitable for tumor specific accumulation.

The average zeta potential measured was -14.90 ± 2.50 mV with negative surface charge, which certainly increased the stability of Cur-TPGS-PMs in dispersion. The electrostatic repulsion and steric hindrance, as well as hydrophilic interactions between hydrophilic chains of the mixed micelle system, could prevent the aggregation of the micelles and provide important effects on stability of the colloid system [25].

The mixed micelles presented a perfectly monodispersed, spheroidal shape, and obvious core-shell structure with no conglutination under TEM (Figure 4(b)). With respect to the surface morphology, aqueous solution of Cur-TPGS-PMs was clear and transparent (Figure 4(c), right). In contrast, the equivalent amount of curcumin dispersed in water appeared turbid, nontransparent, and insoluble (Figure 4(c), left). Based on the amphiphilic property and block structure of

carrier materials, it was deduced that the large hydrophobic chain area of Soluplus formed the core, and with the larger hydrophilic area, PEG distributed around the micelle core as an outer shell.

3.2.2. X-Ray Diffraction (XRD). XRD is a very useful technique to determine the status of the drug in carriers. The highly hydrophobic curcumin tends to crystallize from aqueous solution. If nanosized crystals are formed inside the matrix of Cur-TPGS-PMs, the drug elution from the PMs will be hindered. X-ray diffraction (XRD) analysis was performed to determine the physical status of curcumin encapsulated in Cur-TPGS-PMs as compared with that of free Cur. As shown in XRD patterns (Figure 5), free Cur appeared to be several crystal peaks that were characteristic of a crystalline structure in the 2θ range of $10\text{--}30^\circ$ [26]. The physical mixture of curcumin and void PMs also exhibited a lot of distinct peaks, suggesting that curcumin was crystalline in the mixture. No characteristic peaks of curcumin were seen in Cur-TPGS-PMs, which hinted that the drug was molecularly dispersed or entrapped at an amorphous state in the micelles. In comparison with void PMs, the variation of position and spikes of the peaks in the XRD pattern of Cur-TPGS-PMs implied that minor interactions occurred between curcumin molecules and the polymer matrix during mixing.

3.2.3. pH-Dependent Stability Studies. Table 2 shows the stability of Cur-TPGS-PMs in different pH. It was obvious that the particle size and PDI of Cur-TPGS-PMs had no significant change in pH 6.8 or pH 7.4 after incubation for 2 h or 6 h. Although the particle size and PDI became larger (approximately 80 nm) in pH 1.2 after incubation for 2 h, it was still in the best size range for oral absorption. Therefore, Cur-TPGS-PMs would prevent them from aggregation under various pH circumstances to promote their intestinal absorption.

3.2.4. In Vitro Release. To verify the potential of carriers to deliver the loaded drug, it is essential to assess the release profile of curcumin *in vitro* from the mixed micelle formulations. The *in vitro* release behaviors of tested formulations were observed in the pH 1.2 for 2 h and then in the pH 7.4 until 48 h. As shown in Figure 6, the accumulative release of curcumin from free Cur, Cur-PMs, and Cur-TPGS-PMs in pH 1.2 was about 3.21%, 1.06%, and 1.61% for 2 h, respectively. In the following release media (pH 7.4), the release rates of free Cur were less than 20% after 48 h. From Figure 6, the releases of Cur-PMs and Cur-TPGS-PMs showed the sustained-release characteristics. The accumulative release rates of free Cur, Cur-PMs, and Cur-TPGS-PMs for 48 h were $19.64 \pm 1.65\%$, $24.91 \pm 2.62\%$, and $32.11 \pm 2.22\%$, respectively.

It could be concluded from abovementioned results that most of curcumin was embedded in the hydrophobic core by hydrophobic interaction or hydrogen bonds, and the curcumin in the surface of the particles was little [19]. The released mechanism of curcumin from micelles might be related to the drug diffusion and the disintegration of the

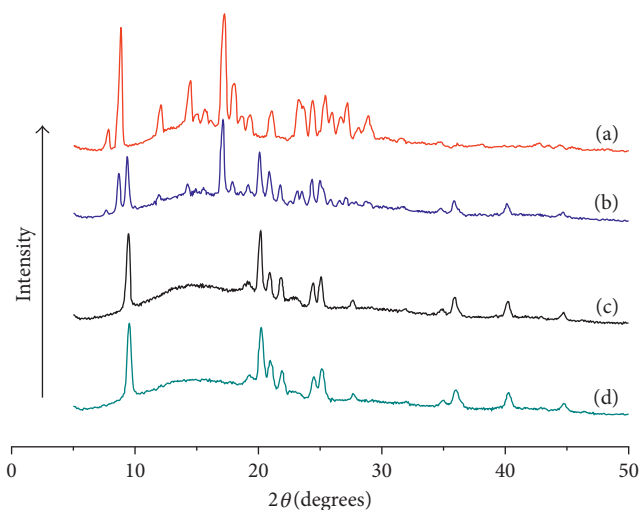


FIGURE 5: XRD patterns of free Cur (a), physical mixture of PMs and Cur (b), Cur-TPGS-PMs (c), and void PMs (d).

polymer material [27]. Curcumin was physically entrapped in the hydrophobic core of the mixed micelles that restricts its release from the micelles. Firstly, the media gradually got into the micellar interior to dissolve curcumin, and the dissolved drug spread to the media slowly. Then, the carrier material was slowly corroded and degraded, which resulted in the slow release of curcumin. Furthermore, the release of the drug from Cur-TPGS-PMs was faster than that from Cur-PMs. This is because the addition of TPGS in the formulation of Cur-TPGS-PMs increased the proportion of PEO, which was propitious to water molecules in the hydrophobic core of the mixed micelles, resulting in faster release of curcumin in Cur-TPGS-PMs.

In short, the fabricated formulation of Cur-TPGS-PMs possessed evidently a sustained-release profile, which may reduce the side effects of drugs, lessen the times of administration, decrease the fluctuations of blood drug concentration, and improve patient compliance.

3.3. Cellular Uptake. The fluorescence intensity of Cur was further quantitatively demonstrated by flow cytometry (Figure 2(b)). Results indicated that the mean fluorescence intensities after treatment with culture medium, free Cur, Cur-PMs, and Cur-TPGS-PMs for 4 h were 494 ± 5.24 , 563.47 ± 34.31 , 972.04 ± 84.42 , and 1219.43 ± 391.37 , respectively.

Cellular uptake was also determined by a confocal fluorescence microscope. The cell nucleus was stained with Hoechst 333342, and the micelles loaded with curcumin exhibited the green fluorescence. The various formulations were treated with MCF-7 cells for 4 h. Figure 7 shows the confocal microscopic images of MCF-7 cells at 4 h after applying free Cur, Cur-PMs, and Cur-TPGS-PMs, respectively. Free Cur, Cur-PMs, and Cur-TPGS-PMs all showed definite uptake in the MCF-7 cells; however, the intensity of green fluorescence in the cell cytoplasm was evidently different. As shown in Figure 7, the highly hydrophobic free Cur was difficultly diffused into MCF-7 cells, leading to little cellular

TABLE 2: Effect of pH on the particle size and PDI of Cur-TPGS-PMs (mean \pm SD, $n = 3$).

Medium	Initial		Final	
	Particle size (nm)	PDI	Particle size (nm)	PDI
pH 1.2	65.54 \pm 2.57	0.11 \pm 0.04	79.48 \pm 2.64	0.22 \pm 0.03
pH 6.8	65.54 \pm 2.57	0.11 \pm 0.04	65.47 \pm 2.16	0.11 \pm 0.05
pH 7.4	65.54 \pm 2.57	0.11 \pm 0.04	65.23 \pm 1.98	0.11 \pm 0.04

Note. PDI, polydispersity index; SD, standard deviation.

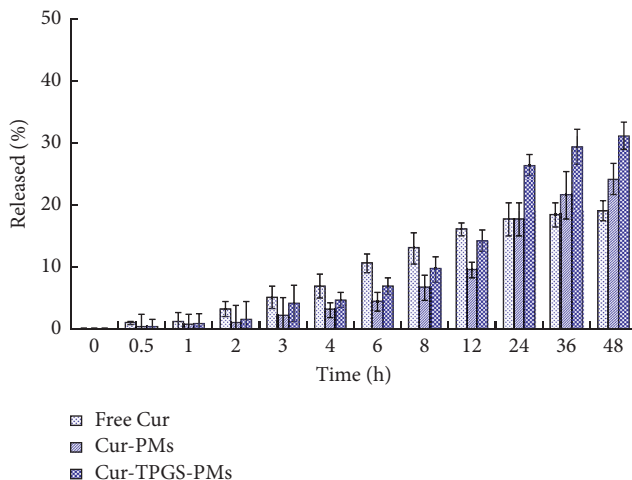


FIGURE 6: Curcumin release rates (%) of free Cur, Cur-PMs, and Cur-TPGS-PMs in pH 1.2 for 2 h and pH 7.4.

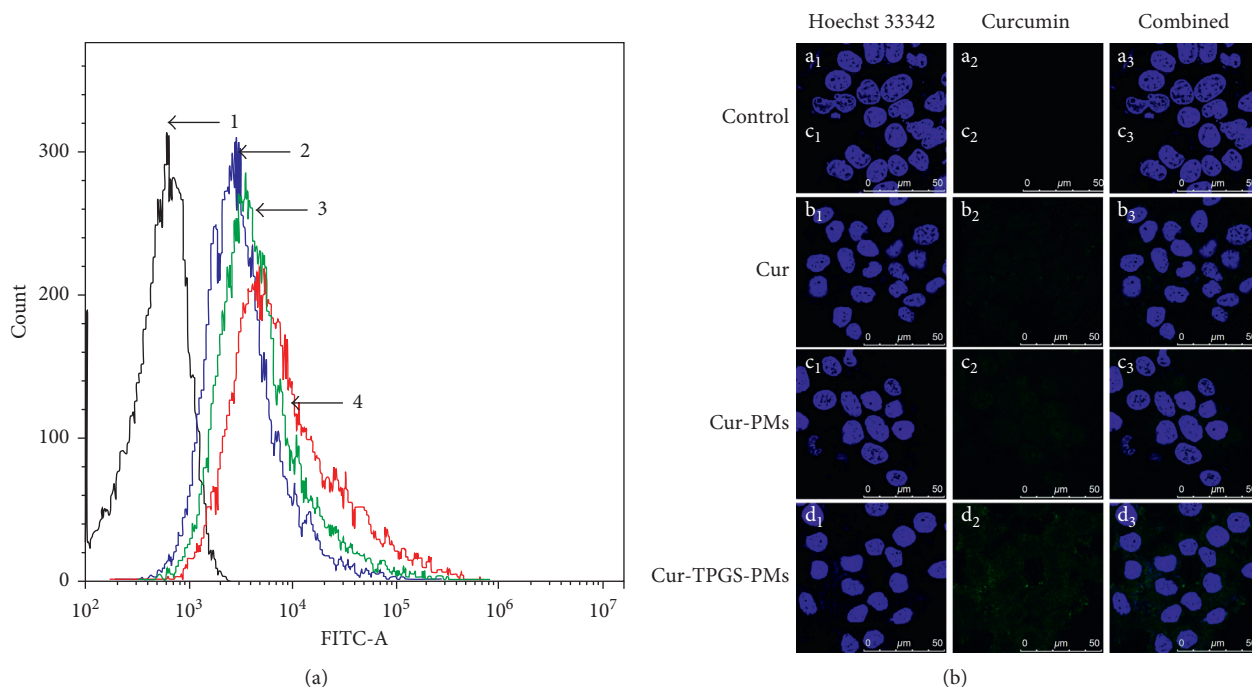


FIGURE 7: Intracellular uptake by MCF-7/Adr cells after treating with varying formulations by flow cytometry (a) and laser scanning confocal microscopy (b).

accumulation. The weak fluorescence in the free Cur-treated group could be attributed to the poor cellular internalization process because of only passive accumulation in the cells.

However, the overlaying images of Cur-TPGS-PMs in the cell cytoplasm displayed stronger green fluorescence of curcumin than that of free Cur and Cur-PM-treated cells. Here, TPGS

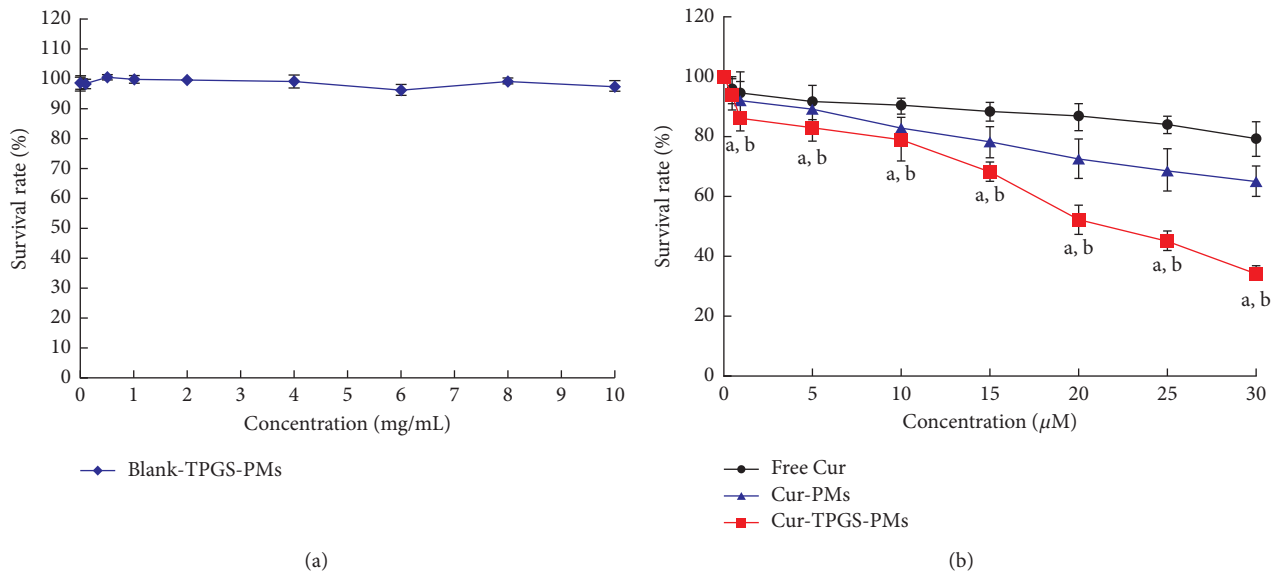


FIGURE 8: Survival rates of MCF-7 cells after treating with varying formulations. Data are presented as mean \pm SD ($n = 3$; $P < 0.05$). (a) Blank-TPGS-PMs. (b) Free Cur; Cur-PMs; Cur-TPGS-PMs.

played an important part in improving the cellular uptake of curcumin. The cellular uptake of Cur-TPGS-PMs could be accelerated because they can be nonspecifically internalized into cells via endocytosis or phagocytosis [28]. Second, when Cur-TPGS-PMs attached to the cell membrane, the interactions between micelles and cell membranes can affect the structure and properties of lipid bilayers as well as functions of the biomacromolecules on the biomembrane, such as ion channels [29]. Therefore, the attachment of Cur-TPGS-PMs to the cell membrane is not as simple as physical adsorption. The homeostasis of cells can be consequently altered, which further contributed to the cytotoxicity of Cur-TPGS-PMs. Third, Cur-TPGS-PMs, possessing a markedly increased solubility and dissolution rate, could induce higher molecular concentration around the cells. The increased antitumor effect may also be associated with the more efficient uptake of tumor cells to the drug delivered.

3.4. Cellular Cytotoxicity. The cellular toxicity of free Cur, Cur-PMs, and Cur-TPGS-PMs was taken on MCF-7 breast cancer cells, which were sensitive and inhibited by curcumin [30]. Cell proliferation was assessed by SRB at the same concentration gradient (0.01–20 μM). Figure 8 shows the cell survival rate after treatment with various concentrations of three kinds of formulations. The results indicated that free Cur, Cur-PMs, and Cur-TPGS-PMs showed a similar effect on cell viability after incubation for 48 h. Free Cur did not show significant inhibition in MCF-7. The cell viability was relatively higher in free Cur-treated cells in comparison with Cur-TPGS-PM-treated cells. However, Cur-TPGS-PMs showed the highest inhibition rates on the proliferation of MCF-7 cells at various concentration points. The half-maximal inhibitory concentration (IC₅₀ value) on MCF-7 cells for free Cur, Cur-PMs, and Cur-TPGS-PMs was

54.5, 28.6, and 10.3 μM , respectively. It was shown that IC₅₀ values of Cur-TPGS-PMs were the lowest among tested formulations. Meanwhile, the empty micelles, just containing TPGS and Soluplus, showed negligible effect on MCF-7 cell survival, which indicated that carrier materials were safe (Figure 8). In short, the results suggested that Cur-TPGS-PMs significantly improved the antitumor efficacy of curcumin.

4. Conclusions

In this study, curcumin was loaded within Soluplus-based mixed micelles using a modified film dispersion method. The Cur-TPGS-PMs with narrow size distribution had good entrapment efficiency, sustained-release character, and excellent long-term physical stability. The Cur-TPGS-PMs provide a promising preparation with efficient delivery of curcumin for therapeutic treatment in the near future. The anticancer activity of curcumin has been an extensive research, and it has been indicated as a potential agent for both prevention and treatment of a great variety of different cancers, including breast cancer, lung cancer, and sarcoma [3]. Moreover, this study explored an interesting alternative approach for design and fabrication of mixed micelles as delivery systems for curcumin.

Disclosure

The authors alone are responsible for the content and writing of this article.

Conflicts of Interest

The authors report no conflicts of interest.

Acknowledgments

The authors gratefully acknowledge Science and Technology Planning Project of Guangdong Province (2014A020212296), Administration of Traditional Chinese Medicine of Guangdong Province, China (20161140, 20151258), Medical Scientific Research Foundation of Guangdong Province, China (A2016076, A2017106), Social Development Key Project of Dongguan (2017507152463), Key cultivation project of Guangdong Medical University (Z2016002), and National Natural Science Foundation of China (81473401) for the financial support. The study was supported in part by the Central Finance Fund to Develop Local Universities (Construction of Tumor Nano-Pharmaceutics Innovative Team, 2016).

References

- [1] R. C. Srimal, "Turmeric: a brief review of medicinal properties," *Fitoterapia*, vol. 68, pp. 483–493, 1997.
- [2] R. K. Maheshwari, A. K. Singh, J. Gaddipati, and R. C. Srimal, "Multiple biological activities of curcumin: a short review," *Life Sciences*, vol. 78, no. 18, pp. 2081–2087, 2006.
- [3] A. Duvoix, R. Blasius, S. Delhalle et al., "Chemopreventive and therapeutic effects of curcumin," *Cancer Letters*, vol. 223, no. 2, pp. 181–190, 2005.
- [4] B. B. Aggarwal, A. Kumar, and A. C. Bharti, "Anticancer potential of curcumin: preclinical and clinical studies," *Anticancer Research*, vol. 23, no. 1, pp. 363–398, 2003.
- [5] Z. Wang, Y. Zhang, S. Banerjee et al., "Notch-1 down-regulation by curcumin is associated with the inhibition of cell growth and the induction of apoptosis in pancreatic cancer cells," *Cancer*, vol. 106, no. 11, pp. 2503–2513, 2006.
- [6] S. L. Ari, L. Strier, D. Kazanov et al., "Celecoxib and curcumin synergistically inhibit the growth of colorectal cancer cells," *Clinical Cancer Research*, vol. 11, no. 18, pp. 6738–6744, 2005.
- [7] C. M. Correa, D. A. Shoskes, P. Sanchez et al., "Combination treatment with curcumin and quercetin of adenomas in familial adenomatous polyposis," *Clinical Gastroenterology and Hepatology*, vol. 4, no. 8, pp. 1035–1038, 2006.
- [8] H. H. Tonnesen and J. Karlsen, "Studies on curcumin and curcuminoids," *Zeitschrift für Lebensmittel-Untersuchung und Forschung*, vol. 180, no. 5, pp. 402–404, 1985.
- [9] Y. J. Wang, M. H. Pan, A. L. Cheng et al., "Stability of curcumin in buffer solutions and characterization of its degradation products," *Journal of Pharmaceutical and Biomedical Analysis*, vol. 15, no. 12, pp. 1867–1876, 1997.
- [10] A. L. Cheng, J. K. Lin, M. M. Hsu et al., "Phase I chemoprevention clinical trial of curcumin, a chemopreventive agent, in patients with high risk or pre-malignant lesions," *Anticancer Research*, vol. 21, no. 4, pp. 2895–2900, 2001.
- [11] K. Kataoka, A. Harada, and Y. Nagasaki, "Block copolymer micelles for drug delivery: design, characterization and biological significance," *Advanced Drug Delivery Reviews*, vol. 64, pp. 37–48, 2012.
- [12] L. Bromberg, "Polymeric micelles in oral chemotherapy," *Journal of Controlled Release*, vol. 128, no. 2, pp. 89–112, 2008.
- [13] A. B. E. Attia, Z. Y. Ong, J. L. Hedrick et al., "Mixed micelles self-assembled from block copolymers for drug delivery," *Current Opinion in Colloid and Interface Science*, vol. 16, no. 3, pp. 182–194, 2011.
- [14] S. Ali, N. Langley, D. Djuric, and K. Kolter, "Eye on excipients," <https://industries.basf.com/bin/bws/documentDownload.en.8805804190165>.
- [15] R. N. Shamma and M. Basha, "Soluplus®: a novel polymeric solubilizer for optimization of carvedilol solid dispersions: formulation design and effect of method of preparation," *Powder Technology*, vol. 237, pp. 406–414, 2013.
- [16] Y. Y. Guo, J. Luo, S. W. Tan et al., "The applications of Vitamin E TPGS in drug delivery," *European Journal of Pharmaceutical Sciences*, vol. 49, no. 2, pp. 175–186, 2013.
- [17] S. S. Feng, L. Mei, P. Anitha, C. W. Gan, and W. Zhou, "Poly (lactide)-vitamin E derivative/montmorillonite nanoparticle formulations for the oral delivery of Docetaxel," *Biomaterials*, vol. 30, no. 19, pp. 3297–3306, 2009.
- [18] M. J. Shieh, C. Y. Hsu, L. Y. Huang, H.-Y. Chen, F.-H. Huang, and P.-S. Lai, "Reversal of doxorubicin-resistance by multifunctional nanoparticles in MCF-7/ADR cells," *Journal of Controlled Release*, vol. 152, no. 3, pp. 418–425, 2011.
- [19] L. H. Dian, E. J. Yu, X. N. Chen et al., "Enhancing oral bio-availability of quercetin using novel soluplus polymeric micelles," *Nanoscale Research Letters*, vol. 9, no. 1, pp. 648–659, 2014.
- [20] D. R. Kalaria, G. Sharma, V. Beniwal, and M. N. V. Ravi Kumar, "Design of biodegradable nanoparticles for oral delivery of doxorubicin: in vivo pharmacokinetics and toxicity studies in rats," *Pharmaceutical Research*, vol. 26, no. 3, pp. 492–501, 2009.
- [21] E. Zimmermann and R. H. Müller, "Electrolyte- and pH-stabilities of aqueous solid lipid nanoparticle (SLN) dispersions in artificial gastrointestinal media," *European Journal of Pharmaceutics and Biopharmaceutics*, vol. 52, no. 2, pp. 203–210, 2001.
- [22] X. Y. Li, Y. Zhao, M. G. Sun et al., "Multifunctional liposomes loaded with paclitaxel and artemether for treatment of invasive brain glioma," *Biomaterials*, vol. 35, no. 21, pp. 5591–5604, 2014.
- [23] H. Cabral, Y. Matsumoto, K. Mizuno et al., "Accumulation of sub-100 nm polymeric micelles in poorly permeable tumours depends on size," *Nature Nanotechnology*, vol. 6, no. 12, pp. 815–823, 2011.
- [24] Z. Popovic, W. Liu, V. P. Chauhan et al., "A nanoparticle size series for in vivo fluorescence imaging," *Angewandte Chemie International Edition*, vol. 49, no. 46, pp. 8649–8652, 2010.
- [25] M. Larsson, A. Hill, and J. Duffy, "Suspension stability: why particle size, zeta potential and rheology are important," *Annual Transactions of the Nordic Rheology Society*, vol. 20, pp. 209–214, 2012.
- [26] K. Hu, X. Huang, Y. Gao, X. Huang, H. Xiao, and D. J. McClements, "Core-shell biopolymer nanoparticle delivery systems: synthesis and characterization of curcumin fortified zein-pectin nanoparticles," *Food Chemistry*, vol. 182, pp. 275–281, 2015.
- [27] L. C. Chen, Y. C. Chen, C. Y. Su, W.-P. Wong, M.-T. Sheu, and H.-O. Ho, "Development and characterization of lecithin-based self-assembling mixed polymeric micellar (saMPMs) drug delivery systems for curcumin," *Scientific Reports*, vol. 6, no. 1, pp. 37122–37133, 2016.
- [28] H. Hillaireau and P. Couvreur, "Nanocarriers' entry into the cell: relevance to drug delivery," *Cellular and Molecular Life Sciences*, vol. 66, no. 17, pp. 2873–2896, 2009.
- [29] Z. Sezgin, N. Yuksel, and T. Baykara, "Investigation of pluronic and PEG-PE micelles as carriers of meso-tetraphenyl porphine for oral administration," *International Journal of Pharmaceutics*, vol. 332, no. 1–2, pp. 161–167, 2007.
- [30] F. S. T. Mirakabad, A. Akbarzadeh, and M. Milani, "A comparison between the cytotoxic effects of free curcumin and curcumin-loaded PLGA-PEG nanoparticles on the MCF-7 human breast cancer cell line," *Artificial Cells, Nanomedicine, and Biotechnology*, vol. 44, no. 1, pp. 423–430, 2014.